ABSTRACT

Title of Dissertation:	IMPROVING SWAT MODELING AND INTEGRATING OBSERVATIONAL ANALYSIS TO ASSESS THE IMPACTS OF CLIMATE AND LAND USE CHANGE ON HYDROLOGICAL PROCESSES IN THE UNITED STATES
	Sijal Dangol Doctor of Philosophy, 2023
Dissertation directed by:	Professor Xin-Zhong Liang Department of Atmospheric and Oceanic Science

Climate and land use have been changing significantly. Climate and land use changes are intricately linked to the hydrological processes that have a significant impact on water resources. The availability of water resources is crucial for food and energy production. In the U.S., about 42% of water is used for agricultural irrigation to improve the productivity of grain crops, including corn and soybeans. About 30% of the corn produced in the U.S. is used for ethanol production, which raises serious concerns regarding the food-fuel competition and detrimental environmental impacts. The expansion of corn production competes for water resources, as corn requires irrigation. To address these issues, the cultivation of bioenergy crops on marginal lands is proposed as a solution that also alleviates water demand, as they do not require irrigation. This cultivation

could involve complex interactions among climate, crops, and hydrological processes, which may lead to significant environmental consequences. This necessitates an understanding of how land use and climate changes will affect hydrological processes and, subsequently, food production.

To understand these processes, I use the hydrological model, Soil and Water Assessment Tool (SWAT). SWAT has a distinct advantage in its capability to simulate water and sediment transport, crop growth, agricultural management, and land management practices, and has specialized extensions for groundwater simulation (SWAT-MODFLOW). In this study, I focus on large agricultural watersheds in the U.S. Northern High Plains (NHP) Aquifer region. The NHP is a vast and critical agricultural area that relies heavily on groundwater irrigation, which has resulted in streamflow and groundwater level decline.

Although the SWAT model can quantify the environmental impacts of climate and land use changes, its utility is limited by: (1) deficiencies in the auto-irrigation algorithms in SWAT that continue irrigation during the non-growing season, (2) optimization of the SWAT model with streamflow data only, without considering other hydrological components such as evapotranspiration and soil moisture, (3) failure to explicitly account for shoot and root biomass development when simulating bioenergy crops, and (4) standalone climate and land use change simulation that do not consider the influence of climate-crop feedback on hydrological processes.

To provide an accurate assessment of the impact of climate and land use changes on hydrological processes in the NHP, my first effort involved improving the irrigation algorithms in both SWAT and its extension SWAT-MODFLOW to provide an improved representation of irrigational water use conditions. The use of SWAT-MODFLOW provides an improved representation of hydrological processes, particularly when considering the significant role of groundwater dynamics in the overall water budget of the NHP. The modified SWAT and SWAT-

MODFLOW were applied to the NHP which exhibited improved performance in simulating groundwater irrigation volume, groundwater level, and streamflow in the NHP. I also examined the effects of groundwater irrigation on the water cycle. Based on simulation results from SWAT-MODLFOW, historical irrigation has increased surface runoff, evapotranspiration, soil moisture, and groundwater recharge by 21.3%, 4.0%, 2.5%, and 1.5%, respectively. Irrigation also improved crop water productivity by nearly 27.2% for corn and 23.8% for soybean.

To optimize the SWAT model for addressing climate and land use change issues in the NHP, I tried to identify the best approach to calibrate the SWAT. Traditionally, SWAT is calibrated using streamflow only. I hypothesize that calibrating SWAT with streamflow only, without considering broad hydrological processes like evapotranspiration and soil moisture causes model overfitting. I utilized the best available remotely sensed data, including Atmosphere–Land Exchange Inverse (ALEXI) Evapotranspiration (ET), Moderate Resolution Imaging Spectroradiometer (MODIS) ET, and Soil MERGE (SMERGE), to examine if multi-variate calibration could improve model performance. Contrary to my hypothesis, using remotely sensed data does not improve model performance because of two reasons: (a) remotely sensed data may lack physical constraints and has large uncertainty, and (b) SWAT may not provide an accurate representation of hydrological processes due to deficiencies in its model algorithms. Further investigation is required to address these issues.

SWAT utilizes standalone climate change data without considering climate-crop feedback in environmental impact assessments of climate and land use change scenarios. To address this gap, I used another tool, the Climate-Weather and Research Forecasting (CWRF) model, both in standalone mode and coupled with the BioCro model. This approach incorporates the climate-crop feedback associated with the cultivation of perennial grasses on marginal lands. The climate data from these two scenarios: (i) Climate-only without climate-crop feedback, and (ii) Climate-crop feedback turned on, were used in SWAT to investigate hydrological responses to simulated climate-crop feedback in the NHP. The incorporation of climate-crop feedback produced cooler and wetter conditions in the NHP. These changes in temperature and precipitation have substantial environmental consequences. The cultivation of miscanthus on marginal lands increases evapotranspiration and decreases surface runoff, soil moisture, and percolation. At the watershed scale, surface runoff substantially increases during the growing season, both in the present (1985-2014) and the future (2031-2060). The differences in the extent of marginal land use for miscanthus cultivation between the Platte (4%) and Republican (20%) River basins result in different responses in streamflow and nitrogen loading. For example, in the future, annual streamflow and nitrogen loading increases by 5.5% and 2.3%, respectively, in the Platte River basin. In contrast, the Republican River basin exhibits negligible changes in annual streamflow and an 8.6% decrease in nitrogen loading during this period. These results highlight the importance of including climate-crop feedback in addition to the impact from land use change when assessing the impacts of climate and land use changes on hydrological processes.

The SWAT model does not explicitly account for shoot and root biomass development. I integrated the grass growth sub-model from the DAYCENT into SWAT (SWAT–GRASS$_D$) and further modified it by considering the impact of leaf area index (LAI) on potential biomass production (SWAT–GRASS$_M$). Based on testing at eight sites in the U.S. Midwest, SWAT–GRASS$_M$ generally outperformed both SWAT and SWAT–GRASS$_D$ in simulating switchgrass biomass yield and the seasonal development of LAI. Additionally, SWAT–GRASS$_M$ can more realistically represent root development, which is key for the allocation of accumulated biomass and nutrients between aboveground and belowground biomass pools.

From these model experiments and analyses, I realized that there are still a lot of model and data gaps that need to be addressed. Consequently, the results of the impacts of the climate and land use changes on hydrological processes could be subjective due to inherent model deficiencies and calibration issues because of uncertainty in observed data.

I, therefore, revisited the observed data screening approaches to identify near-natural streamflow data that are representative of actual watershed processes. Assuming that the hydrologic response of the watershed is primarily driven by precipitation and runoff processes, I applied lagged correlation analysis between precipitation and streamflow at various temporal scales, complemented by a systematic screening process using basin properties to select streamgages with near-natural streamflow. The screening method introduced here is objective and easy to implement in other data-sparse regions. The selected streamgages serve as valuable calibration and validation points for hydrological models, thereby it could help enhance the accuracy and confidence in model projections.

In summary, my work improved the SWAT auto-irrigation algorithm for a better representation of irrigation water use and integrated the DAYCENT grass growth sub-model to enhance biomass yield predictions. The hydrological consequences of land use change for miscanthus cultivation highlighted the importance of incorporating climate-crop feedback into hydrological modeling. This integration had a substantial impact on the hydrological processes in the NHP. Despite the model improvements through changes in model algorithms and optimization, my work reveals that model and data gaps result in subjectivity in the study's findings. To address this, I propose an objective screening process for streamgage selection that reflects natural watershed processes. The enhancements introduced to the modeling framework, coupled with the objective streamgage screening approach, will assist water resource managers and the regional hydrologic modeling community in the credible assessment of the hydrological impacts resulting from climate and land use changes.

IMPROVING SWAT MODELING AND INTEGRATING OBSERVATIONAL ANALYSIS TO ASSESS THE IMPACTS OF CLIMATE AND LAND USE CHANGE ON HYDROLOGICAL PROCESSES IN THE UNITED STATES

by

Sijal Dangol

Dissertation submitted to the Faculty of the Graduate School of the
University of Maryland, College Park, in partial fulfillment
of the requirements for the degree of
Doctor of Philosophy
2023

Advisory Committee:
Professor Xin-Zhong Liang, Chair/Advisor
Professor Fernando Miralles-Wilhelm
Dr. Xuesong Zhang, Co-Advisor
Professor Raghu Gopalrao Murtugudde
Professor James Carton
Associate Professor Kuishuang Feng, Dean's Representative

Dedication

My dissertation is dedicated to my aunt, Mangala Dangol, my uncle, Surya Man Dangol, my parents, Chandra Man and Sharmila Dangol, my wife, Samira Shrestha, and my brothers, Sijan and Sajan Dangol, for always supporting and believing in me throughout this journey of my doctoral studies.

Acknowledgements

I would like to express my sincere gratitude to my advisors, Dr. Xin-Zhong Liang, Dr. Xuesong Zhang, and Dr. Fernando Miralles-Wilhelm, for their support, guidance, encouragement, and patience throughout this journey. I feel very forutunate to have worked with Dr. Xin-Zhong Liang and Dr. Xuesong Zhang who have played huge role to bring out the best in me as a researcher. I am grateful for always finding time from their busy schedule to help draft all my manuscripts and provide constructive comments. Specially, I want to thank Dr. Xuesong Zhang who guided me in enhancing the SWAT model.

I would like to sincerely thank all the members of CWRF Earth System Science group in ESSIC for their continued support and encouragement. Many thanks to Dr. Chao Sun, Dr. Yufeng He, and Vitaly Kholodovsky for their support and feedback to my research questions and findings. I am grateful to the AOSC department for their continued support throughout this journey. I would like to thank all my friends, colleagues, and mentors in the UMD Global STEWARDS program for their support.

Finally, I am grateful to my uncle and aunt who have been the pillar of my life and believing in me. To, my wife Samira Shrestha, I am thankful for your sacrifices and providing me strength to walk through this journey for the last seven years.

Table of Contents

List of Tables

List of Figures

List of Abbreviations

ALEXI	Atmosphere–Land Exchange Inverse
ALMANAC	Agricultural Land Management Alternatives with Numerical Assessment Criteria
CDL	Cropland Data Layer
CESM	Community Earth System Model
CMIP6	Coupled Model Intercomparison Project Phase 6
CONUS	Contiguous United States
CSSP	Conjunctive Surface Subsurface Process Model
CWRF	Climate Weather Research and Forecasting Model
DAYCENT	Daily CENTURY
DEM	Digital Elevation Model
DHRU	Disaggregated Hydrological Response Unit
DISALEXI	Disaggregated ALEXI algorithm
DNDC	DeNitrification-DeComposition
DSSAT	Decision Support System for Agrotechnology Transfer
ECS	Equilibrium Climate Sensitivity
EISA	Energy Independence and Security Act
EPIC	Environmental Policy Integrated Climate
ET	Evaporation Transpiration
GAGES	Geospatial Attributes of Gages for Evaluating
GCM	Global Climate Model
GHCND	Global Historical Climatology Network Daily

GLBRC	Great Lakes Bioenergy Research Center
HCDN	Hydro-Climatic Data Network
HRU	Hydrological Response Unit
KGE	Kling-Gupta Efficiency
LAI	Leaf Area Index
LAR	Leaf Area Ratio
MODIS	Moderate Resolution Imaging Spectroradiometer
MPI-ESM1.2	Max Planck Institute Earth System
NADP	National Atmospheric Deposition Program
NAAR	North American Regional Reanalysis
NHP	Northern High Plains
NLDAS	National Land Data Assimilation
NRMSE	Normalize Root Mean Square Error
NSE	Nash-Sutcliffe Efficiency
PBIAS	Percent Bias
PRISM	Parameter-elevation Regressions on Independent Slopes Model
RFS	Renewable Fuel Standard
RMSE	Root Mean Square Error
RSR	Root-Shoot Ratio
SSP	Shared Socioeconomic Pathway
SMERGE	Soil MERGE
SRTM	Shuttle Radar Topography Mission
SSURGO	Soil Survey Geographic Database

STATSGO	State Soil Geographic Database
SUFI-2	Sequential Uncertainty Fitting algorithm version 2
SWAT	Soil and Water Assessment Tool
SWAT-C	Soil and Water Assessment Tool -Carbon
SWAT-CUP	Soil and Water Assessment Tool -Calibration and Uncertainty Programs
USDA	United States Department of Agriculture
USGS	United States Geological Survey
WRF	Weather Research and Forecasting

Chapter 1: Introduction

1.1 Background and motivations

The food-energy-water (FEW) nexus is a complex and interrelated system that underpins the sustainability of human societies (Cai et al., 2018; Smidt et al., 2016; Zhang et al., 2018). Understanding the intricate connections and dependencies between food production, energy use, and water availability, and how changes in one component can impact the others is crucial for addressing pressing challenges related to food-energy-water security, environmental degradation, and climate change (Cai et al., 2018; Scanlon et al., 2017).

The current trend of non-renewable fossil fuel use is environmentally unsustainable, which has substantially increased CO2 emissions resulting in a warmer climate. Furthermore, the enhanced global energy demand has resulted in concerns regarding energy security and the need for sustainable carbon-negative or carbon-neutral energy sources (Antar et al., 2021). One potential approach to address this issue is the use of bioenergy. The government level policies such as the Renewable Fuel Standard (RFS), were established by the U.S. Energy Independence and Security Act (EISA) 2007 (Schnepf and Yacobucci, 2013; U.S. EPA, 2022) for renewable biofuel production, which requires an increase in biofuel to 36 billion gallons by 2022. However, the wide use of grain crops for biofuel production in the U.S. has raised serious concerns regarding the competition between food and fuel and detrimental environmental impacts (Lark et al., 2022; Searchinger et al., 2008; Zhang et al., 2010). For example, about 38% of corn grown in the U.S. was used for ethanol production

(Golden et al., 2018), which accounts for 98 percent of ethanol production in the U.S. (Dohlman et al., 2022). On the other hand, this has also led to the rapid expansion of croplands (corn/soybean) to marginal lands/grassland for bioenergy production from 2008 to 2011 in the U.S., with hotspots over northern Missouri and Ogallala aquifer region (Lark et al., 2015). The cropland expansion over the water-stressed Ogallala aquifer region followed by increased irrigation demand further raises concerns about water use and sustainability. Globally, 70% of freshwater is used for irrigation (FAO, 2011; Rost et al., 2008) and nearly 18% of the world's agricultural land is irrigated, which produces about 40% of global agricultural products (Garces-Restrepo et al., 2007). The expansion of water-intensive corn production in this region and the continuous use of nonrenewable groundwater may further threaten the environment and agricultural production. While acknowledging the significance of complexities involved in addressing uncertainties within the FEW nexus systems, few studies offer a comprehensive approach to assess the synergies and trade-offs from the FEW nexus perspectives and their implications for regional FEW sustainability.

1.1.1 Effects of climate and land use change on food, energy, and water resources

Human activities have led to the continued increase in carbon dioxide emission in conjunction with the agricultural intensification and expansion of cropland in the last century (Fischer et al., 2001; IPCC, 2023). These activities have disturbed the energy system at the local and global scale causing an increase in atmospheric temperature and changes in large-scale atmospheric circulation (Trenberth, 2011). The changes in energy distribution and general atmospheric circulation could lead to spatial and temporal variability in regional precipitation and evapotranspiration that may have severe consequences on water use and water management, especially in semi-arid regions (Sivakumar, 2011). Additionally, the hydrological cycle is projected to intensify in response to a warming climate in the future (IPCC, 2023; Oki and Kanae, 2006). Specifically, climate change is likely to increase the duration, frequency, and intensity of floods and droughts in the future (IPCC, 2023), which would have a significant impact on water resources and agricultural production.

Land use change together with climate change further complicates the response of the hydrological cycle. Agriculture, land use change, and climate change are linked together and have a strong influence on the availability of water resources, which presents a significant challenge to the sustainability of water resources (Trenberth, 2011) and agricultural production systems (Kukal and Irmak, 2018). Changes in precipitation and temperature pattern in combination with land use changes influence the hydrological processes such as surface runoff, evapotranspiration, groundwater recharge, and streamflow (Schilling et al., 2008a; Sivakumar, 2011; Van Liew et al., 2012). In addition, it has been found that climate variability may have a spatially variable influence on crop yield depending on the crop types and locations (Kukal and Irmak, 2018; Paul et al., 2020). The increased water stress during crop growth as a result of a warming climate can be offset through irrigation (Kukal and Irmak, 2018; Paul et al., 2020; Troy et al., 2015). However, prolonged irrigation could have an adverse impact on crop yield due to nutrient runoff (Paul et al., 2020). Climate variability, crop water requirement, availability of water resources, and water management strategies are factors limiting irrigation and agricultural productivity (Kukal and Irmak, 2018; Marek et al., 2017; Troy et al., 2015). Hence, appropriate agricultural water management strategies are required to minimize the increased risks associated with climate change and land-use change.

The last few decades have been marked by significant land-use change through deforestation, expansion of agricultural land, and subsequent increase in irrigation (Carruthers et al., 1997; Lark et al., 2015; Yasarer et al., 2020). Tilman et al. (2011) examined the future food demand based on current trends and projected a 100-110% global crop demand increment by 2050 which would be supplemented through 1 billion ha of land obtained from land clearing or pre-existing cultivated land. The intensification of agriculture and land-use change in combination with the variability and intensification of extreme events (floods/droughts/rainfall) is anticipated to have dramatic effects on hydrological processes with possible implications on regional agricultural water use and management practices (Tilman et al., 2011; Troy et al., 2015; Zhang et al., 2016).

Bioenergy has been promoted as one of the carbon-neutral or carbon-negative energy sources that could partially substitute fossil fuels, which is expected to make a significant contribution to meeting greenhouse gas reduction targets (Chum et al., 2011). However, bioenergy production can lead to land-use change that may cause food insecurity and have unintended environmental consequences (Qin et al., 2012; Searchinger et al., 2008). The economic and land-use policies are directed towards increasing bioenergy production from dedicated energy crop production. Current economic and energy policies have influenced land use change decisions made by farmers (Wallander et al., 2011) leading to the expansion of corn production for biofuel (Lark et al., 2015; Wallander et al., 2011). Climate change in combination with land use change will lead to increased stress on water resources and agricultural production (Piao et al., 2010; Taylor et al., 2013).

The land-use change and climate change are likely to have a significant effect on the regional climate patterns and hydrological cycle that may affect the availability of water resources. In this context, there is a need for efforts to reduce the impact of land use change and climate change on water resources. Given the complex and interconnected nature of food, energy, water, and the climate system, an integrated climate-food-energy-water assessment is necessary to investigate the effects of climate change, land use change, and water management strategies on hydrological processes.

1.1.2 Hydrological responses to land-atmosphere feedback from bioenergy crop production

Multiple studies examining the local direct impact of bioenergy crop production on basin scale or regional scale, without considering the land-atmosphere feedback on regional climate, have shown that land use change to perennial bioenergy crops could enhance ET and infiltration, reduce surface runoff, soil moisture, and streamflow, and improve the water quality (Guo et al., 2018; Schilling et al., 2008; Wu et al., 2012). For example, Feng et al. (2018) simulated streamflow reduction by 16% when marginal land was converted to switchgrass, and by 23% when converted to Miscanthus. Similarly, Hickman et al. (2010) and McIsaac et al. (2010) also found the reduction of streamflow under bioenergy crop scenarios mainly because of higher infiltration and evapotranspiration, and lower soil moisture. However, in terms of water quality, Ng et al. (2010) reported a 10% land use change from cropland to miscanthus decreases nitrate loading by 6.4%. Song et al. (2016) found that bioenergy crop cultivation reduces nitrogen leaching relative to row crops and herbaceous plants when grown without applying N fertilizer. They also reported the variable response of soil water content depending on the location and land use change for bioenergy crop production. For instance, they found that switchgrass reduced soil moisture content when grown over croplands and forests but decreased when grown on grassland. Meanwhile, miscanthus resulted in an overall decrease in soil water from high water use. These findings suggest that the production of bioenergy feedstock can greatly affect groundwater depletion in water-limited watersheds/regions.

When the land-atmosphere interactions associated with bioenergy crop cultivation on marginal land are considered, the regional climate feedback lowers the minimum and maximum temperature by 0.4 and 0.9 °C in the summer months and increases precipitation in the U.S. (He et al., 2022). A land-atmosphere feedback impact assessment on crop and biomass yield of corn, soybean, and switchgrass by Brown et al. (2000) found that the higher temperatures lead to rapid accumulation of heat units, which speeds up the vegetation growth, shortens the growing season, and increases temperature stress that results in reduced yield for corn and soybean. In contrast, they found that the switchgrass biomass yield improved in warmer climates. Whereas, precipitation increases improved crop yield by reducing the water stress in Kansas and Nebraska. Also, precipitation increase leads to higher runoff from the cropland but not from switchgrass. The results from these studies highlight the complex land-vegetation-atmosphere interactions and the changes in water fluxes due to differences in vegetation phenology.

The US Great Plains region, already a biofuel-producing area, is an intensively farmed region with a large portion of the landscape covered by rangeland, pastureland, and wetlands of low productivity (Cai et al., 2011). The large area of marginal land around the US Great Plains has been identified to be suitable for bioenergy feedstock production (Cai et al., 2011; Gelfand et al., 2013). The state government's support for ethanol production combined with national policies such as the Food, Conservation, and Energy Act of 2008 provides favorable conditions to produce bioenergy crops in marginal land (Harris et al., 2008). A study by Lark et al. (2015) indicated the rapid expansion of croplands (corn/soybean) to marginal lands/grassland for bioenergy production from 2008 to 2011 in the U.S.

Given the prospects of large-scale cultivation of bioenergy crops in the U.S., further research is required to comprehend the hydrological effects of converting landscapes to perennial bioenergy crops. The utilization of refined hydrologic models, like the one implemented in this study, can provide clearer scientific insights and better inform policymakers. Models are crucial for assessing system-level responses to bioenergy production scenarios, considering site-specific characteristics and drivers that influence system behavior. Previous studies have explored the impacts of bioenergy production on system behavior, but the capability of these models to accurately simulate the hydrologic response of climate feedback under new bioenergy cropping systems in changing climate remains unassessed.

Previous studies have mainly been conducted for watersheds or river basins in an energy-limited region where precipitation is sufficient to sustain crop growth (e.g., Mississippi River basins, Illinois aquifer). However, watersheds or river basins in semiarid regions, with a large area of marginal land available for bioenergy feedstock productions have received little attention. The US Northern High Plains Aquifer region (NHP), already a biofuel-producing area, is representative of such a semiarid region. The NHP is an intensively farmed region with a large portion of the landscape covered by rangeland, pastureland, and wetlands. The large area of marginal land around the NHP has been identified to be suitable for bioenergy feedstock production (Gelfand et al., 2013a). The state government's support for ethanol production combined with national policies such as the Food, Conservation, and Energy Act of 2008 provides favorable conditions to produce bioenergy crops in marginal land (Harris et al., 2008). However, changes in land use and management practices induced by bioenergy crop production can affect the hydrological processes of the region. For this region, many earlier studies have evaluated the hydrological response (ET, surface runoff, water yield, and soil moisture content) to potential land use change scenarios for bioenergy crop production. The land use change scenarios consist of conversion to bioenergy crops from food crops (e.g., corn, maize, soybean, sorghum) or grassland or a combination of both in fertile and marginal land that includes application of fertilizer for optimum growth (Davis et al., 2012; Dolan et al., 2020a; Gelfand et al., 2013a; Qin et al., 2015; Wu et al., 2012a). These studies show that depending on the choice of bioenergy feedstocks, type of land use expansion or conversion, management practices (e.g., use of tillage, fertilizer, and irrigation), and climatic condition, the effect on hydrological processes could be different. Generally, land use change to perennial bioenergy crops may enhance ET and infiltration and reduce surface runoff, soil moisture, and streamflow (Guo et al., 2018a; Schilling et al., 2008a; Wu et al., 2012a).

Their analysis of ET, surface runoff, soil moisture and water yield, and soil moisture content has been limited to regions with abundant precipitation. There are still knowledge gaps concerning changes in the spatio-temporal distribution of water resources and the hydrological cycle associated with bioenergy feedstock production under rainfed conditions in marginal land over semi-arid regions such as the US Great Plains. Therefore, investigating the surface and subsurface processes in such water-stressed intensively cultivated regions is crucial for effective water resource management.

1.1.3 Overview of the Northern High Plains aquifer region

The Northern High Plains aquifer region is a vast and critical agricultural area spanning across parts of Colorado, Kansas, Nebraska, and Wyoming. The NHP is known for its intensive agricultural practices, including large-scale irrigation and the use of fertilizers and pesticides (Peterson et al., 2020). Its agricultural productivity heavily relies on groundwater resources, primarily sourced from the U.S. High Plains aquifer also known as the Ogallala aquifer, one of the largest aquifers in the world (Peterson et al., 2020; Scanlon et al., 2012).

The Northern High Plains aquifer region faces a multitude of challenges that threaten its long-term sustainability. For instance, the rapid expansion of irrigation in the region has led to overexploitation of groundwater pumping from the aquifer. As a result, water levels in the aquifer have declined drastically in many areas, resulting in increased pumping costs and reduced well yields. Although the efficiency of irrigation has increased over the past few decades, it still faces challenges in water loss due to evaporation and inefficient distribution.

The use of agrochemicals also poses significant threats to water quality in the NHP and its downstream region. The agrochemicals can leach into the soil and runoff from agricultural fields can carry these contaminants into nearby water bodies, contributing to water pollution and potentially leading to eutrophication and harmful algal blooms. Several studies have been conducted to investigate the impact of fertilizer, pesticides, and herbicide applications in the Mississippi River basin on eutrophication in the Gulf of Mexico.

Moreover, climate change-induced variations in precipitation patterns and increased temperatures further exacerbate water quantity and quality concerns. As water availability declines, agricultural activities and food production face growing uncertainties, impacting the regional economy and livelihoods of local communities. In the context of the Northern High Plains aquifer region, understanding the inherent linkages between food, energy, and water, is critical for sustainable food production and water resource management.

To address the challenges posed by water availability and water quality issues, and to improve water use efficiency in agriculture, various crop and water management strategies have been proposed in the Northern High Plains aquifer region. These include the selection of optimal crops that are drought resistant, optimal crop rotation practices that help maximize soil health and water use efficiency, optimal fertilizer application and timing, and implementing water-use regulations to incentivize farmers to adopt more efficient irrigation practices and encourage sustainable water resource management. Overall, the adoption of crop and water management strategies in the Northern High Plains aquifer region holds significant potential to ensure the sustainability of water resources and food production in the face of changing climate and land use change.

1.1.3.1 Climate and land use change impact on water cycle

Because of the warming climate, winter and spring precipitation is anticipated to increase while summer precipitation is likely to decrease in the future with high variability in climate extremes (Easterling et al., 2017). Several studies have investigated the impact of climate variability, land use change, and agricultural water use on hydrological processes (eg. aquifer-river interactions, streamflow, groundwater recharge, water budget) of the US High Plains aquifer. Rowe et al. (1994) examined the sensitivity of streamflow to changes in temperature and precipitation in the Little Blue River basin, in Nebraska. They found that in the semi-arid region where runoff is a small fraction of precipitation, streamflow is more sensitive to changes in precipitation than temperature changes. Ng et al., (2010) investigated the groundwater recharge characteristics in the US Southern High Plains where precipitation changes had a greater impact on groundwater recharge compared to temperature changes. They found that increased spring and winter precipitation resulted in increased recharge than in summer. Using observed groundwater level and streamflow data from USGS over the High Plains aquifer, Kustu et al., (2010) found that excessive groundwater withdrawal has significantly reduced the baseflow in most of the rivers in NHP with an increasing trend of low flow days. Meanwhile, Meixner et al., (2016) found that irrigation recharge is likely to increase in the areas of the NHP aquifer where surface water irrigation is used. This study stressed the need for a climate-food-energy-water integrated modeling approach to understand and project the basin-scale response to climate change.

These studies indicate significant changes in surface and subsurface hydrological processes in response to changing climate conditions, irrigation practices, and land use change, subsequently affecting the surface water and groundwater resources. Climate variability and land use change are most likely to alter the quantity and quality of surface water and groundwater systems in the future. Therefore, the evaluation of hydrological responses to complex land-atmosphere interactions associated with climate change and land use change is important for sustainable water resource management. Quantifying their effects necessitates the use and enhancement of hydrological models such as the Soil and Water Assessment Tool (SWAT) for improved assessment of hydrological processes that would help guide future water management strategies to adapt against changing climate and land use.

1.1.4 Hydrological model overview

Hydrological modeling is a commonly used approach to evaluate the environmental impacts of climate and land use change, and agricultural and water management practices. Some examples of available models include the SWAT, Topography based hydrological Model (TOPMODEL), Modular Finite Difference Model (MODFLOW), Groundwater and Surface-water FLOW model (GSFLOW), SWAT-MODFLOW, and PCRaster Global Water Balance coupled to MODFLOW (PCR-GLOBWB-MOD). SWAT has been widely used in several hydrological studies conducted to date in parts of the NHP region for small and large river basins (Daggupati et al., 2016; Strauch and Linard, 2009; Zeng and Cai, 2014).

The SWAT is a physically based, semi-distributed, and continuous-time hydrological model used to simulate the quality and quantity of surface and ground water and predict the environmental impact of land use, land management practices, and climate change in watersheds (Neitsch et al., 2011). The model was developed to assess water resources and predict the impacts of land use/cover changes, land management practices on soil erosion, sedimentation, and non-point source pollution on watersheds or large river basins.

Many studies have utilized the SWAT (Soil and Water Assessment Tool) model to assess the potential of biofuel feedstock production and its environmental benefits in geographically and climatically diverse regions and various land use types (Cibin et al., 2016; Gelfand et al., 2013a; Panagopoulos et al., 2017; Srinivasan et al., 2010). Most of these studies deal with the parametrization of plant growth parameters for Switchgrass/Miscanthus and its impact on soil properties, water quality, and hydrological processes. However, the application of SWAT for analyzing the impact of bioenergy feedstock production and the regional climate feedback in a semi-arid region, such as the NHP where groundwater has a significant contribution to streamflow is limited. Most of these studies were done in the energy deficit region where precipitation was sufficient to sustain the water demand of food crops as well as bioenergy crops. Therefore, additional research is needed to understand the effect of bioenergy crop production on ET, river-aquifer exchange, groundwater storage, and streamflow in a semi-arid region such as the NHP, where the streamflow is primarily driven by subsurface flow and only 9-10% of precipitation reaches the stream as runoff (Reidmiller et al., 2018).

SWAT has undergone major enhancements over the past few years, resulting in SWAT-MODFLOW (Bailey et al., 2016), SWAT-Carbon (SWAT-C) (Yang and Zhang, 2016), and SWAT+ (Bieger et al., 2017). These enhancements are aimed at improving skills in modeling watershed systems to provide a more flexible representation of interactions and processes within a watershed, such as river-aquifer interactions, soil carbon storage, and freeze/thaw cycles in soil. Despite these major improvements, there still exist some well-documented limitations of SWAT. For example, the SWAT auto-irrigation routine can falsely trigger irrigation events even after the crop harvest (Chen et al., 2017; Marek et al., 2017), resulting in an overestimation of irrigation demand and surface runoff. Likewise, In the SWAT-MODFLOW groundwater irrigation sub-module, the irrigation well remains active throughout the simulation period. However, each year, new irrigation wells are drilled depending on the irrigation requirement or wells can become inactive due to maintenance requirements. The inability to account for such changes could overestimate/underestimate the well pumping rate which affects the model's ability to provide an accurate representation of groundwater dynamics and sub-surface processes. Additionally, SWAT still utilizes a simplified vegetation growth sub-model adapted from EPIC (Williams et al., 1989). This vegetation growth sub-model uses a single plant growth pattern for all plant types (forest, grass, and annual crops), which lacks the representation of complex plant phenology, such as the growth of different plant compartments (root, shoot, leaf, etc.), and carbon and nutrient dynamics between above and belowground pools (Luo et al., 2008). Hence, there is a need to improve the SWAT by modifying the equations related to these processes.

1.2 Research Objectives

The main objective of this research is to enhance the SWAT and evaluate the potential influence of regional climate feedback in the context of large-scale cultivation of bioenergy crops and irrigational water use under changing climate on the regional hydrological processes, particularly in vulnerable regions like the NHP, to help make informed decisions for FEW resources management and address sustainable issues. The specific objectives of this study are:

Objective 1: Enhance the SWAT model to improve the representation of irrigation practices and validate the model for the NHP using observed datasets

To do this, first, the irrigation sub-module in the SWAT and SWAT-MODFLOW was improved and the hydrological model was set up for the NHP region. The modified model was validated using observed and remotely sensed data to assess its performance as a predictive tool without calibration. The modified model was then used to examine the impact of historical irrigation on the hydrological processes and agricultural productivity in the NHP. The simulation results showed that the SWAT and SWAT-MODFLOW overestimated evapotranspiration in the absence of calibration. Therefore, to further improve the model performance multiple model calibration approaches were explored.

Objective 2: Evaluate the single and multivariate calibration methods using streamflow and remotely sensed data

To do this, we calibrated the SWAT using different combinations of streamflow and remotely sensed hydrologic variables such as ET and soil moisture. The results showed that adding remotely sensed ET and soil moisture to the traditionally used streamflow for model calibration does not necessarily improve the model performance.

Objective 3: Evaluate the hydrologic responses of the NHP to land use change and regional climate feedback associated with large-scale bioenergy crop cultivation in the U.S.

To do this, first, the SWAT model for the NHP was calibrated and validated using observed streamflow, including instream total nitrogen, using the regionalization approach. The validated model was then run using multiple climate feedback scenarios to assess the differences in local direct impact from the cultivation of Miscanthus on marginal land and local indirect effect at the basin scale from changes in temperature and precipitation because of the climate feedback from the complex land-atmosphere interactions. The examination of the vegetation growth sub-model in SWAT revealed that there are limitations in the simulation of biomass production and biomass allocation to shoots and roots that could affect the representation of soil organic carbon and nutrient cycling.

Objective 4: Enhance the SWAT model for improved representation of biomass production and biomass allocation of perennial grasses

To do this, we integrated the grassland sub-model from DAYCENT into the SWAT vegetation growth sub-model for perennial grasses. The modified model was calibrated and validated for Switchgrass using observed biomass yield. The modified model performance is further evaluated for LAI and root/shoot based on expected ranges from published observational studies.

Objective 5: Develop an objective data-driven approach to screen near-natural streamgages to facilitate environmental impact assessment associated with climate and land use change, and hydrologic model optimization

The findings from the previous endeavors to achieve Objectives 1,2 and 3 indicated the need for streamflow data from near-natural streamgages that are representative of climatic conditions and watershed properties to help improve model optimization, trend analysis, and environmental impact assessment. For this, we developed an objective data-driven but simple screening method to identify streamgages minimally influenced by human activities.

1.3 Outline of Dissertation

The dissertation contains 7 chapters. Chapter 1 provides an overview of (a) hydrological changes in response to climate and land use change, water management practices, and bioenergy crop production, (b) the need for an enhanced hydrological model to examine the basin scale response to land use change and associated climate feedback, and (c) research objectives. Chapter 2 describes the enhancement of the groundwater irrigation scheme in SWAT-MODFLOW to improve the representation of water balance components, streamflow, and irrigation practices to examine the impact of historical irrigation on crop productivity, river-aquifer interactions, and hydrologic processes in the Northern High Plains Aquifer region. Chapter 3 explores the SWAT model calibration strategies using combinations of streamflow and remotely sensed based dataset and their impact on model performance in simulating streamflow, evapotranspiration, and soil moisture to identify the suitable calibration strategy for our study region. In Chapter 4, we examine the influence of land use change on marginal lands for bioenergy crop production and the corresponding climate feedback on the hydrologic processes in the NHP. In Chapter 5, to enhance the simulation of biomass crop production and allocation to different plant components with an aim to improve the representation of soil organic carbon, I modified and enhanced the grass growth sub-model in the SWAT model. The findings from Chapters 2, 3, and 4, indicated the need for a standard streamflow dataset for model optimization and environmental impact assessment. Chapter 6, describes the objective data-driven method based on correlation analysis to develop the near-natural streamflow dataset. Chapter 7 provides an overview of the key findings of this research work and the scope for future studies.

[1]

Chapter 2: Agricultural Irrigation Effects on Hydrological Processes in the United States Northern High Plains Aquifer Simulated by the Coupled SWAT-MODFLOW System

Materials presented in this chapter have been published in the journal Water as Dangol et al. (2022)

2.1 Introduction

Irrigation is important for proper crop growth and consistent food supply (Carruthers et al., 1997). Globally, 70% of freshwater is used for irrigation (FAO, 2011; Rost et al., 2008) and nearly 18% of the world's agricultural land is irrigated, which produces about 40% of global agricultural products (Garces-Restrepo et al., 2007). Especially in semi-arid regions, agricultural productivity relies heavily on groundwater resources for irrigation (Colaizzi et al., 2009). For instance, the U.S. High Plains aquifer, one of the world's largest aquifers (Aldaya et al., 2010), accounts for about 88% of total freshwater withdrawn for irrigation (Maupin and Barber, 2005) in the country. The continuous use of nonrenewable groundwater has already and may further threaten the environment and agricultural production (Scanlon et al., 2012). For example, excessive groundwater removal relative to natural recharge can lower the water levels of an aquifer and regional streams through coupled surface–groundwater dynamics (Barlow and Leake, 2012; Wen and Chen, 2006).

Dangol, S.; Zhang, X.; Liang, X.-Z.; Miralles-Wilhelm, F. Agricultural Irrigation Effects on Hydrological Processes in the United States Northern High Plains Aquifer Simulated by the Coupled SWAT-MODFLOW System. Water 2022, 14, 1938. https://doi.org/10.3390/w14121938.

Groundwater depletion levels in the U.S. Northern High Plains (NHP) aquifer vary across the region due to varying water demand for irrigation and recharge dynamics (Scanlon et al., 2012). For instance, the groundwater storage level in the Sandy Hills region in the NHP has remained relatively stable due to a higher recharge flux (Haacker et al., 2016; Scanlon et al., 2012; Smidt et al., 2016). The streamflow in the NHP decreased annually between 23 and 73%, and in the dry season (July–August) between 21 and 77%, from 1940 to 1980, primarily because of the decline in the groundwater level caused by increased groundwater pumping (Kustu et al., 2010). Furthermore, from 1996 to 2015 there was an 11% increase in irrigated acres on the NHP (Smidt et al., 2016). As a consequence of the increased irrigation, declining streamflow and groundwater levels, most river basins of Nebraska have been classified as fully appropriated, i.e., existing water uses and rights are equal to available water supplies, or over appropriated, i.e., existing water uses and rights exceed available water supplies (NDNR, 2016). Over the past century, the NHP has experienced several short-term and prolonged severe droughts resulting in considerable agricultural losses (Hua et al., 2019; J. Zhang et al., 2018), and such events are likely to increase in the future (Bathke et al., 2014). This could lead to severe water stress in the region. As such, there is an urgent need to improve understanding of hydrological processes and adapt future water management strategies in the NHP to recurring drought and improved water conservation.

Hydrological modeling is a commonly used approach to evaluate the effect of agricultural practices on surface and groundwater resources (Gao and Li, 2014). Multiple hydrological modeling studies conducted to date in parts of the NHP have been based on SWAT or MODFLOW for small and large river basins (Daggupati et al., 2016; Peterson et al., 2016; Rossman et al., 2018; Strauch and Linard, 2009; Zeng and Cai, 2014). In general, most SWAT modeling studies have been focused on evaluating and analyzing best management practices, water quality, water and sediment transport, irrigation, bio-energy crops, climate change and land use change (Daggupati et al., 2016; Srinivasan et al., 2010; Zeng and Cai, 2014). Meanwhile, MODFLOW based studies in the region primarily examined groundwater dynamics, e.g., river-aquifer interactions, groundwater level changes, groundwater irrigation and climate change (Chen and Chen, 2004; Hrozencik et al., 2017; Peterson et al., 2016; Rossman et al., 2018). Recently, these two models were coupled into SWAT-MODFLOW by Bailey et al. (Bailey et al., 2016). The coupled model improved the skills in simulating watershed systems where both surface water and groundwater processes (as well as their interactions) play a significant role on overall water budget (Molina-Navarro et al., 2019; Rumph Frederiksen and Molina-Navarro, 2021). The improvement can be attributed to a more realistic representation of physically based surface and subsurface processes, such as runoff, soil water storage, evapotranspiration, and aquifer recharge/discharge. Some other examples of coupled surface–groundwater models include ParFLOW (Kollet and Maxwell, 2006), PCR-GLOBWB-MOD (Sutanudjaja et al., 2011), and GSFLOW (Markstrom et al., 2008). These models are grid based and fully distributed (ParFLOW and PCR-GLOBWB-MOD) or semi-distributed (GSFLOW) with high data requirement and computation costs. Among them, SWAT-MODFLOW has a distinct advantage in its capability to simulate crop growth, agricultural management, land management practices, water and sediment transport, and its ability to use the existing SWAT and MODFLOW models of varying spatial extents.

SWAT-MODFLOW has been continuously enhanced over the last two decades (Bailey et al., 2016; Kim et al., 2008; Sophocleous et al., 1999). It links surface and groundwater flow processes to provide an improved understanding of complicated hydrological processes in large agricultural basins. SWAT-MODFLOW can assess the hydrological and agronomic responses of a fully integrated river–aquifer system to land use change (Jin et al., 2021), climate change (Chunn et al., 2019; Liu et al., 2020) and agricultural management practices (Aliyari et al., 2019; Wei and Bailey, 2019), which greatly benefits water resource management. SWAT-MODFLOW has been applied in watersheds of different spatial scales, ranging from 357 km2 in the Uggerby River Catchment, Denmark (Liu et al., 2019), to 72,000 km^2 in the South Platte River Basin (Aliyari et al., 2019). In this study, we used the version of SWAT-MODFLOW developed by Bailey et al. (Bailey et al., 2016).

When modeling the hydrology in a semi-arid region such as the NHP with intensive agricultural activities, a careful selection of the irrigation method is needed. Varying irrigation methods can produce different results because of differences in irrigation volume, timing, frequency, and recharge. Aliyari et al. (Aliyari et al., 2019) updated the SWAT auto-irrigation subroutines and MODFLOW Well package to link MOFDLOW pumping wells and SWAT HRUs for groundwater irrigation in SWAT-MODFLOW, and successfully implemented it in the South Platte river basin in the United States. In SWAT-MODFLOW, the groundwater irrigation volume can be prescribed by two methods: the MODFLOW Well package and the SWAT auto-irrigation routines (Bailey and Park, 2019). The first method allows the user to specify the pumping rate of each well in the MODFLOW grid cell, and provides a reasonable estimate of groundwater irrigation volume. This will provide irrigation water to the associated SWAT HRU. However, application of this approach is difficult in an intensively irrigated large agricultural basin in the absence of measured pumping rates.

The second method calculates the groundwater irrigation volume for the HRU using the auto-irrigation routines of SWAT. The irrigation volumes are converted to the pumping rate and fed to the associated pumping well in the MODFLOW grid cells. This method is commonly used in the case of inadequate irrigation scheduling data. It also accommodates the effects of spatiotemporal variability in climate, soil moisture, and plant growth conditions. However, this method could overestimate the irrigation amount because irrigation is performed even after crop harvesting (Chen et al., 2017). It can also underestimate the pumping rate because the number of pumping wells in the model domain remains constant throughout the simulation period, whereas, in practice, the number of active pumping wells can vary. This study tries to overcome these limitations by modifying the groundwater irrigation routine to better simulate irrigation practices. There is currently no study assessing the benefits of two groundwater irrigation methods in SWAT-MODFLOW. Hence, a careful evaluation of the two approaches is needed to seek an accurate representation of irrigation practices and water balance components.

In this study, we aimed to examine and make multiple changes to the SWAT-MODFLOW framework to enhance the representation of irrigation and hydrological processes in the NHP and understand the role of irrigation practices in affecting watershed hydrology in the 347,058 km^2 extent of the NHP. Specifically, we aimed to: (1) design a SWAT-MODFLOW model in the NHP and improve its capability of simulating irrigation processes; (2) evaluate the performance of the two irrigation options (SWAT auto-irrigation based on plant water stress and MODFLOW-based prescription of irrigation well-pumping rates) for simulating the groundwater demand and regional water budget; and (3) understand the effects of irrigation on various hydrological processes, such as groundwater recharge, evapotranspiration, and streamflow. This modeling exercise helps to represent the hydrology in an agriculturally intensive large watershed and generates knowledge regarding the role of irrigation in influencing hydrological processes. Such efforts hold promise to better support sustainable agricultural water management in large irrigation systems in the face of imminent climate change and potential groundwater shortages.

2.2 Materials and Methods

2.2.1 Study Area

The NHP aquifer (Figure 2.1a), located in the Midwest U.S.A., spans Nebraska, Colorado, Kansas, Wyoming, and North Dakota, covering an area of about 347,058 km^2 (Peterson et al., 2016). The NHP is comprised of multiple watersheds where intensive agricultural activities are carried out. The dominant land cover category in the NHP is range and pasture land (57.72%), followed by agriculture (33.47%), urban (3.38%), forest (3.01%), wetlands (1.42%), water and barren land (1%).

The region is dominated by convective storms in summer (April–September), which overlaps with the crop growing season (Scanlon et al., 2012). The annual precipitation (Figure A.1) shows a strong east–west gradient, decreasing from 900 mm in the east to 350 mm in the west. The estimated crop water use ranges from 584 to 711 mm for corn, and 508 to 635 mm for soybean, with higher crop water use in eastern Nebraska (Klocke et al., 1990). This difference in crop water demand and precipitation results in different irrigation needs. For example, according to (NDNR, 2016), the net corn irrigation requirement ranges from ~355 mm in the west to ~152 mm in the east of Nebraska for the entire growing season (May to September) for high yields. To meet these varied irrigation needs, both surface water and groundwater are used in the NHP (Peterson et al., 2016; Scanlon et al., 2012). Historically, most of the irrigation water was taken from the rivers and reservoirs in the region, but since 1940, irrigated areas using groundwater rapidly expanded (Peterson et al., 2016). By 2000, almost 97% of the total groundwater withdrawals in the High Plains were used for irrigation (Maupin and Barber, 2005) and nearly 84% of irrigation water was from groundwater in Nebraska (Hutson et al., 2004). In 2015, groundwater accounted for about 77% of the total water supply and about 84% of irrigation water in NHP; thus, irrigation used about 95% of the total groundwater withdrawals (Dieter et al., 2018).

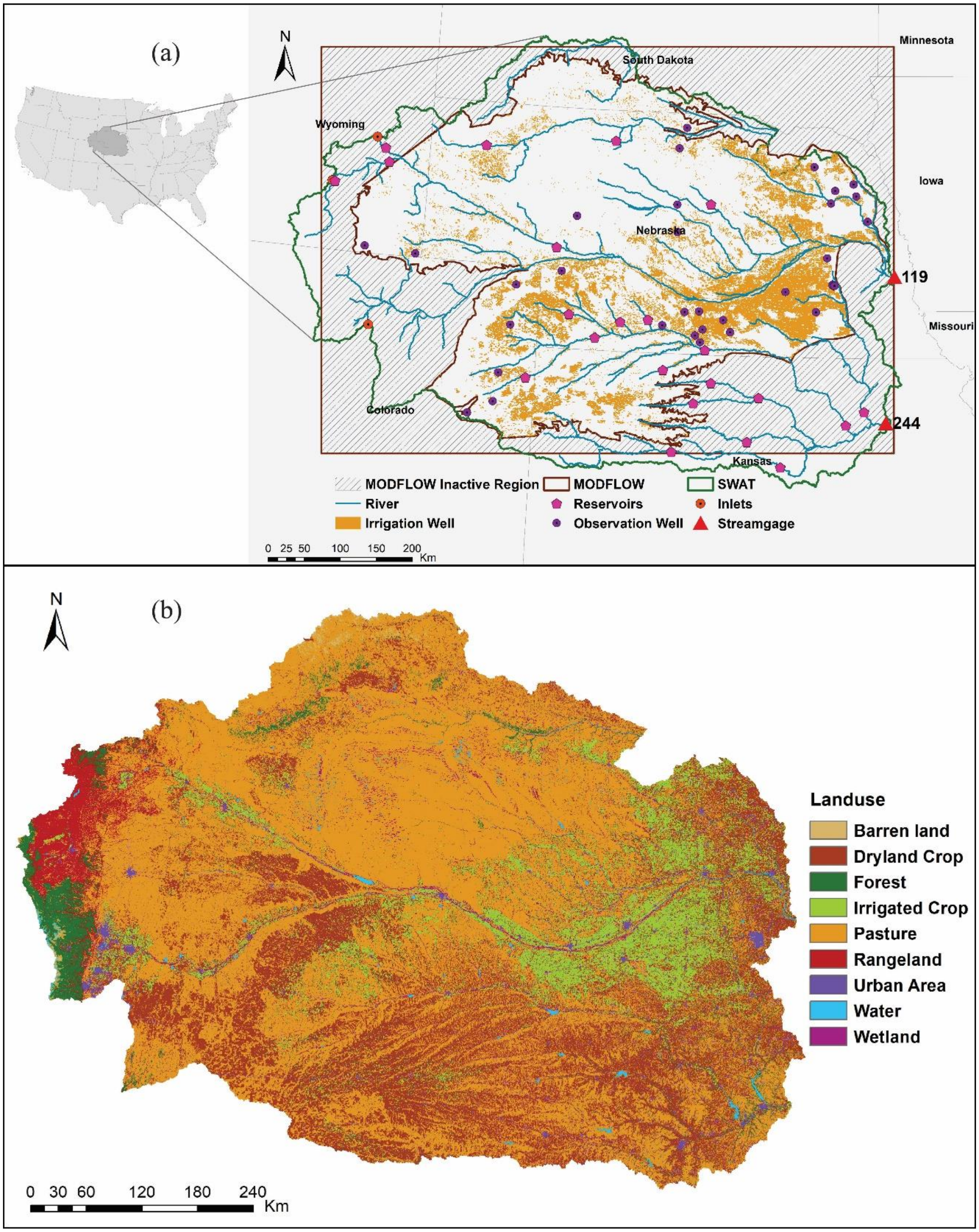

Figure 2.1. Modeling domains for SWAT and MODFLOW (a), and land use map (b), for the U.S. Northern High Plains.

2.2.2 SWAT Setup

SWAT is a physically-based model that simulates the hydrological processes by dividing the watershed into sub-basins which are further divided into fundamental units called hydrological response units (HRU) based on a unique combination of land use, soil type and slope (Neitsch et al., 2011). SWAT is capable of simulating reservoirs, wetlands, and a wide range of agricultural and water management practices (Douglas-Mankin et al., 2010; Garg et al., 2012).

Multiple geospatial datasets were used to configure the SWAT model setup (Table 1.1). Land use data was obtained from the Cropland Data Layer (CDL) 2008 (USDA NASS Cropland Data Layer, 2008) which contains detailed crop-specific information. Different cropland types were reclassified into corn, soybean and other small grains. The resulting digital map was then combined with Moderate Resolution Imaging Spectroradiometer (MODIS) irrigated land layers 2007 (Pervez and Brown, 2010a) to generate a land use map with cropland separated into irrigated and dry cropland (Figure 2.1b). Soil properties were derived from the State Soil Geographic (STATSGO) dataset. Soil properties from STATSGO were used in order to keep the number of HRUs manageable and reduce the computation time of the model simulation. Two slope classes 0–5% and >5% were used for defining HRUs. The unique combinations of land use, soil type, and slopes resulted in a total of 51,035 HRUs for the entire basin. Crop management operations (planting, harvesting, and fertilizer application) were included for corn, soybean and winter wheat, based on existing literature (Ferguson et al., 2006; Van Liew et al., 2012; Woznicki and Nejadhashemi, 2012).

Table 2.1. SWAT model input summary.

Data	Resolution	Source
Precipitation, Temperature, Relative Humidity, Wind Speed, Solar Radiation	0.3° × 0.3°	NARR (Mesinger et al., 2006a)
Digital Elevation Model (DEM)	90 m × 90 m	Shuttle Radar Topography Mission (SRTM) (Jarvis et al., 2008a)
Land Use	30 m × 30 m	(USDA NASS Cropland Data Layer, 2008)
MODIS Irrigated Land	250 m × 250 m	(Pervez and Brown, 2010b)
Soil Property	1:250,000	STATSGO (USDA-NRCS, 1994a)
Reservoir	22 large reservoirs	USBR, USACE (United States Bureau of Reclamation, 2019; US Army Corps of Engineers, 2013)

We used climate forcing data from the North American Regional Reanalysis (NARR) database to drive the SWAT simulations. NARR climate forcing data have assimilated multiple sources of observations (Mesinger et al., 2006a), including satellite observations, and have shown to provide good simulation of streamflow when used as climate forcing in hydrological models (Essou et al., 2016). The 22 large reservoirs that were identified to lie within the stream network (Figure 2.1a) in the SWAT domain were incorporated into the model. A detailed description of reservoir parameters and operations is provided in the Supplementary Information (Table A.1).

A large portion of the watershed is dominated by depressions, especially the Sand Hills in northern and northeastern Nebraska. The pothole module simulates depressions at the HRU-level and can reasonably represent the spatial distribution of seepage to MODFLOW grids. Therefore, the pothole module was applied to HRU classified as wetlands. Most of the lakes and wetlands in the Sand Hills are shallow and have a mean depth of ~800 mm (Rossman et al., 2018). Hence, the maximum pothole water depth in SWAT (POT_VOLX) was set to 800 mm which allows water to pond on the surface up to the depth of 800 mm before runoff takes place.

2.2.3 MODFLOW Setup

We used an existing MODFLOW model configured for the NHP by (Peterson et al., 2016) in our SWAT-MODFLOW setup. The groundwater model consists of 565 × 795 grid cells, with a resolution of 1 × 1 km2, and a single layer. Originally, the model setup used the Streamflow Routing package to simulate the discharge in rivers, but in the SWAT-MODFLOW setup, it was replaced by the River package (Harbaugh, 2005). This enabled the calculation of groundwater–surface water exchanges between the aquifer and rivers. The boundary conditions, including general head boundary, constant head, drain, well, and horizontal flow barrier packages (Figure 2.2) based on Peterson (Peterson et al., 2016) were also enabled in the present study. As most of the irrigation scheduling in the NHP takes place in the growing season, the groundwater irrigation was assumed to take place from May to September in the well package. The domain of the watershed delineated for SWAT was larger than the MODFLOW model boundary and the number of sub-basins in the southern section of the SWAT domain lay in the no-flow boundary or outside the MODFLOW boundary (Figure 2.1a). The original capability of each model was maintained in the non-overlapping region (Bailey et al., 2016).

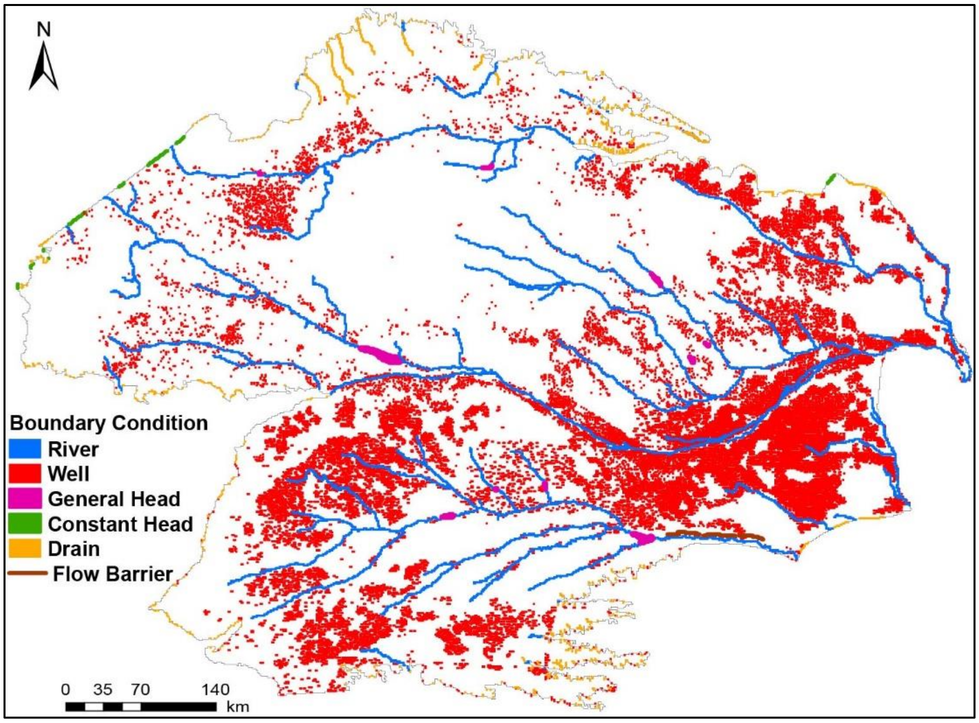

Figure 2.2. Boundary conditions of the MODFLOW model domain.

2.2.4 SWAT and MODFLOW Coupling

2.2.4.1 Irrigation Scheme

The groundwater irrigation operation can be simulated in SWAT-MODFLOW through two methods: First, the well pumping rate and locations defined in the MODFLOW well package were based on Peterson et al. (Peterson et al., 2016); it was used to dictate the groundwater irrigation amount in the SWAT auto-irrigation module. This setup is henceforth called Well-Irr. Second the groundwater irrigation amount determined by the SWAT auto-irrigation module was used to determine the pumping rates for irrigation wells in the MODFLOW grid cells. This setup is henceforth called

Auto-Irr. A plant water stress, defined as the ratio of actual to the potential plant transpiration, was used to trigger the irrigation in SWAT.

The SWAT auto-irrigation module requires an irrigation source (surface water or groundwater) as input. The irrigated cropland, corn, soybean and winter wheat, HRUs close to the irrigation wells were assigned groundwater as the irrigation source; the remaining HRUs were assigned river as the irrigation source. Additional details on irrigation source assignment to the cropland HRUs is provided in the Supplementary Information (Section 2.1). The coupling between the SWAT HRU and the MODFLOW grid was achieved following the manual coupling procedures described in detail by Bailey and Park (Bailey and Park, 2019). The SWAT HRUs were first disaggregated into individual polygons with specific geographic locations (DHRUs), and then intersected with the MODFLOW grid cells to determine the spatial relationship between HRUs, DHRUs, and MDFLOW grid cells. The mapping scheme in SWAT-MODFLOW passed SWAT variables (recharge, ET, and stream stage) to the corresponding MODFLOW grid. Additionally, the MODFLOW river grid cells were intersected with the SWAT sub-basins for the river–aquifer water exchange.

2.2.4.2 SWAT-MODFLOW Modifications

SWAT-MODFLOW was modified to improve simulations of water management practices for intensively irrigated watersheds (Aliyari et al., 2019; Wei and Bailey, 2019). In particular, the irrigation modules were modified to: (a) link MOFDLOW pumping wells and SWAT HRUs for groundwater irrigation, (b) include the canal irrigation, and (c) groundwater evapotranspiration. These changes improved model ability to produce more realistic effects of groundwater irrigation on streamflow and groundwater level than SWAT.

The SWAT-MODFLOW model developed by (Bailey et al., 2016) was modified and used in this study. Generally, each year, new irrigation wells are drilled depending on the irrigation requirement but limited by the groundwater regulations of the Natural Resource Districts in the region. Conversely, some wells become inactive or are taken out of service because of high operation cost or general modernization leading to replacement by a new well. The records of active irrigation wells and their locations can be obtained from the Nebraska Department of Natural Resources Groundwater Wells Database (Nebraska Department of Natural Resources., 2020). However, in the case of the SWAT auto-irrigation derived groundwater pumping rate, the irrigation well that is associated with the SWAT HRUs remains active throughout the simulation period. Therefore, the coupled irrigation function in SWAT-MODFLOW was modified to account for the annual changes in the number of irrigation wells during the growing season. In doing so, each irrigation well mapped to a SWAT HRU was activated or deactivated for a simulation year based on the irrigation well activation information in the MODFLOW Well package (Harbaugh, 2005). The SWAT auto-irrigation routine can falsely trigger irrigation events even after the crop harvest (Chen et al., 2017; Marek et al., 2017). Hence, the SWAT auto-irrigation function was modified to allow irrigation only when the MODFLOW wells were active during the growing season of that year.

The coupled model deactivated the SWAT groundwater module and replaced it with MODFLOW in the overlapping areas. Hence, the SWAT groundwater module was turned off even in the regions overlapping with inactive MODFLOW grid cells, where MODFLOW did not simulate the groundwater flow process. Therefore, when the SWAT domain overlaid the MODFLOW inactive grid cells (Figure 2.1a), the seepage and the subsurface flow were not considered in the SWAT-MODFLOW simulation. Additional modification of the coupled SWAT-MODFLOW model was performed in this work to keep the SWAT groundwater module active for the overlapping region with inactive MODFLOW grid cells.

2.2.4.3 River–Aquifer Interaction

In SWAT-MODFLOW, the interaction between surface water and aquifers was simulated using the MODFLOW River package. However, the MODFLOW model designed for the NHP (Peterson et al., 2016) used the Stream Flow Routing (SFR) package to simulate rivers. Hence, the SFR package was replaced by the River package in this study. The river network generated by SWAT was used to identify the MODFLOW river grid cells which varied spatially from the original MODFLOW SFR grids. The riverbed hydraulic conductivity had a significant impact on quantifying and understanding the stream–aquifer interactions (Chen, 2004; Cheng et al., 2011) that determine the baseflow and the effect of groundwater irrigation on streamflow. The riverbed hydraulic conductivity estimated by (Peterson et al., 2016) for the major rivers of the NHP that ranged from 0.03 to 3.00 m/d were linearly interpolated to the river grid cells. These values lay within the lower range of riverbed vertical hydraulic conductivity estimated by previous studies (Chen, 2004; Song et al., 2010) for the major rivers within the NHP. The river bed thickness values for river segments from (Peterson et al., 2016) were used in the MODFLOW River package.

2.2.4.4 System Parameter Adjustment

The calibration of integrated groundwater surface water models such as SWAT-MODFLOW is complex and computationally expensive (Chunn et al., 2019; Liu et al., 2019). Hence, only SWAT model parameters for crop and irrigation volume were optimized. SWAT model parameter adjustment was conducted in two parts. First, the fractional potential heat units for planting and harvest dates for corn, soybean, and winter wheat were adjusted until the model-simulated planting and harvest dates were within the beginning (planting) and end dates (harvesting) as provided on the document (Usual Planting and Harvest Dates) published by USDA (USDA-NASS, 2010).

Second, the model parameter for irrigation, plant water stress threshold, was then manually adjusted to reduce the bias in simulated annual groundwater irrigation volume in the NHP. For this purpose, the plant water stress that triggers irrigation was varied between 0.95 and 0.5 to obtain the lowest percent bias between the simulated and USGS estimated annual groundwater irrigation volume.

2.2.4.5 Experiment Design

To determine the appropriate irrigation management method between the Auto-Irr and Well-Irr setups, the SWAT-MODFLOW model was run from 1979 to 2008 with a 3-year warm-up period. The model performance for simulating streamflow, evapotranspiration, groundwater level, and annual groundwater irrigation volume was evaluated in the above-mentioned two scenarios. In addition, the Auto-Irr and Well-Irr performances for simulating monthly streamflow were compared with the SWAT model simulation results. The same SWAT parameters were used for the consistent surface water hydrological parameterization in all three setups.

Finally, the SWAT-MODFLOW setup that provided better model performance was used to evaluate the impact of irrigation on hydrological processes and agricultural productivity.

2.2.4.6 Evaluation Metrics

The model performance on crop yield, monthly streamflow, evapotranspiration, groundwater level, and annual groundwater irrigation volume simulated by the above-mentioned three model setups, was evaluated. The statistical metrics: coefficient of determination (R^2), Nash-Sutcliffe efficiency (NSE), root mean square error normalized against the observed mean value or normalized root mean square error (NRMSE), and percent bias (PBIAS), were used to evaluate model performance. R^2 measured if the variation in observed data was explained by the model. Its value ranged from 0 to 1, with values closer to 1 indicating good agreement; model performance was considered acceptable if $R^2 > 0.5$ (Moriasi et al., 2007). The NSE measured agreement between observed and simulated data. Its value ranged from negative infinity to 1, with values closer to 1 indicating good agreement. Following (Motovilov et al., 1999), the model performance for streamflow was considered to be satisfactory if NSE was between 0.36 and 0.75, and considered good if NSE was greater than 0.75. The NRMSE provided the (%) relative measure of simulated and observed values where the lower value indicated better performance. The model performance was often considered good when NRMSE < ±20%. PBIAS measured the tendency of simulated values to be greater or lower than observed values. PBIAS of 0% was the optimal value, with positive value indicating underestimation and negative value indicating overestimation by the model. Following (Daggupati et al., 2016), PBIAS of ±15% was considered good and PBIAS of ±25% was considered satisfactory.

The corn, soybean, and winter wheat yield simulated by the model were compared with county-level USDA National Agricultural Statistical Survey (NASS) data (USDA, 2016). County-level NASS data was aggregated to each sub-basin using an area-weighted average. NASS-reported crop yield in bushels per acre was converted to kg per hectare, as reported in SWAT output, following the method described in (Srinivasan et al., 2010). To further evaluate the effect of irrigation on the corn and soybean yield in the region, the spatial distribution of crop water productivity (CWP), defined as the ratio of crop yield to actual evapotranspiration (Jiang et al., 2015) at the sub-basin scale, was estimated. The CWP represented the water use efficiency of the crop, presented here in units of kg/m^3.

The model-simulated groundwater irrigation volume values were compared with the county-level USGS estimates. We aggregated the USGS county-level 5-year averaged groundwater irrigation volume data (US Geological Survey, 2016) to represent the overall groundwater irrigation volume in the NHP aquifer. The observed groundwater level values were obtained from the network of 39 USGS observation wells in the study region (Figure 2.1a). The mean of observed data was used if multiple observation wells were located within a 1 km^2 MODFLOW grid cell. A total of 2029 monthly groundwater level measurements were available for the period of 1982–2008.

In a semi-arid region, evapotranspiration (ET) plays an important role in the hydrological cycle. The Moderate Resolution Imaging Spectroradiometer (MODIS) based monthly ET dataset from 2000–2008 was utilized as the benchmark for model evaluation at the sub-basin scale. For this, the 8-day total 500 m gridded ET data from MODIS (MOD16A2) (Running et al., 2019) was spatially aggregated into monthly ET values for each of the 203 SWAT sub-basins that overlay the NHP aquifer.

In this study, R^2 and NSE were used as model performance indicators for streamflow, R^2 and NRMSE for groundwater level, R^2 for evapotranspiration, and PBIAS for crop yield. In the case of groundwater irrigation volume, the model performance was evaluated qualitatively due to limited observations.

2.3 Results

2.3.1 Model Performance

2.3.1.1 Annual Groundwater Irrigation

Figure 2.3 shows the annual groundwater irrigation volume for the NHP simulated by the SWAT-MODFLOW model with the two irrigation schemes described in Section 2.4.1. Both Well-Irr and Auto-Irr overestimated the annual groundwater irrigation volume. The Auto-Irr achieved much lower bias than the Well-Irr method (−30% vs. 86%). The model results generally indicated a gradual upward trend in the groundwater irrigation volume from 1995.

The annual groundwater irrigation volume estimated by Auto-Irr was closer to the USGS estimates compared with the Well-Irr setup. The use of the auto-irrigation module allowed for the irrigation demand to be based on climatic conditions, resulting in high irrigation demand during drought years. The years with peak irrigation volume simulated by the Auto-Irr corresponded well with the observed drought years in the NHP: 1989, 2002, and 2006. In the Well-Irr setup, the irrigation frequency and intensity were based on the MODFLOW Well package and stress period. Such detailed information was not available for each irrigation well over the simulation period, leading to less sensitivity of Well-Irr estimated irrigation volume to climate conditions. The normal water requirement for corn and soybean is 762 and 531 mm/year in Nebraska (Yonts et al., 2008), 642 and 580 mm/year in eastern Colorado (Schneekloth and Andales, 2009), 624 and 518 mm/year in Kansas (Rogers et al., 2015). The average annual precipitation in the NHP fell to 395, 354, and 517 mm in 1989, 2002, and 2006, respectively, well below the normal water requirement for corn and soybean in the region. The water deficit during these years increased groundwater irrigation substantially (Figure 2.3).

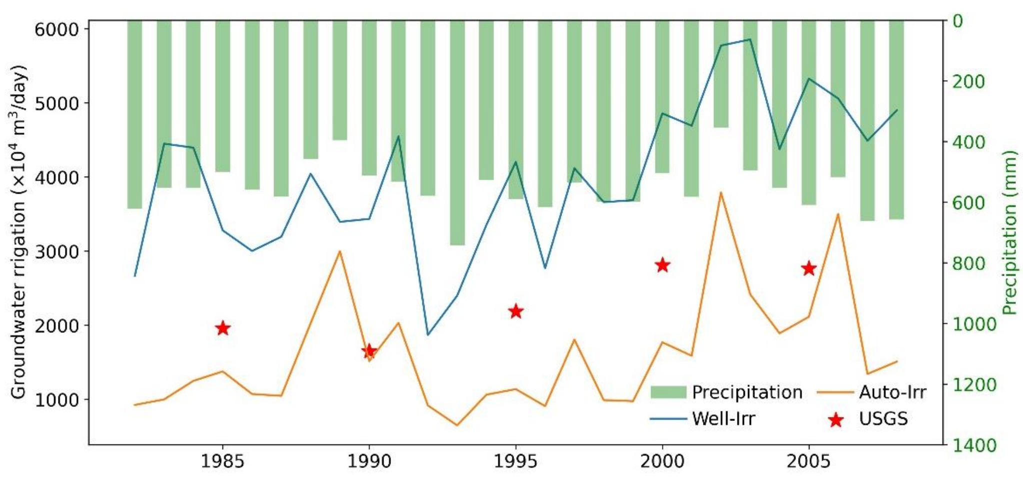

Figure 2.3. Reported and simulated total annual groundwater irrigation volume in the U.S. Northern High Plains aquifer.

2.3.1.2 Groundwater Level

The monthly mean groundwater level simulated by the Auto-Irr and Well-Irr setups were compared with the observed monthly groundwater level from USGS as shown in Figure 2.4. The R^2 for Auto-Irr and Well-Irr were found to be 0.998 and 0.997, respectively. This suggests that both irrigation settings were able to capture the dynamics of groundwater level variations. The NRMSE values also showed small differences between the two coupled model setups (13.55% (good) for Well-Irr, and 12.47% (good) for Auto-Irr). High hydraulic conductivity and specific yield across the NHP likely stabilized the saturated thickness of the aquifer despite large differences in groundwater withdrawals. However, for both setups, SWAT-MODFLOW underestimated the groundwater level compared with the observed values. The tendency of the model to simulate higher irrigation volumes (Figure 2.3) was a possible reason for the model underestimation of the groundwater level. The mean bias error (MBE) and mean absolute error (MAE) for Auto-Irr were −25.5 m and 25.6 m, respectively. The corresponding values for the Well-Irr were −27.8 m and 27.8 m. In general, these errors were <3% of the mean measured groundwater levels. The model biases may have arisen from multiple reasons. For example, the mean elevation of the model grid cell of 1 km^2 was different from the elevation of the USGS observation well, which was a single location in the cell. Errors may also have resulted from uncertainty in specifying model parameters, and pumping rates.

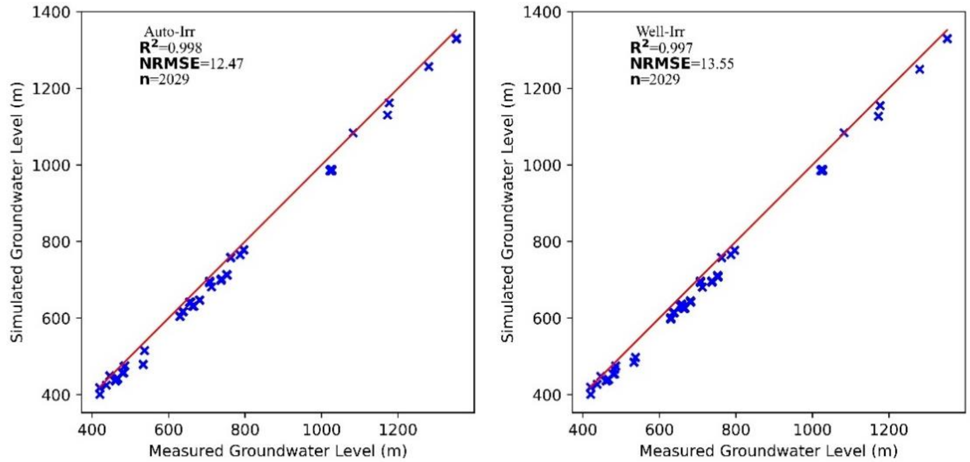

Figure 2.4. Comparison of observed and simulated mean monthly groundwater level of Auto-Irr and Well-Irr for the period of 1982–2008.

2.3.1.3 Streamflow

The Auto-Irr, Well-Irr, and SWAT simulated streamflow were evaluated against the observed mean monthly streamflow data obtained from USGS gauges at the outlet corresponding to sub-basins 119 (northern) and 244 (southern) (Figure 2.1a). The model performance for three model setups is summarized in Table 2. More details about the time series of monthly mean simulated and observed streamflow at the outlet of sub-basins 119 and 244 are shown in Figure A.2. For outlet 119, the R^2 values were 0.66, 0.63, and 0.62 for SWAT, Auto-Irr and Well-Irr, respectively. All were greater than 0.5, suggesting that all model setups could capture the streamflow variation satisfactorily for the northern section of the NHP. The NSE values increased from 0.13 for the SWAT, to 0.55 and 0.51 for Auto-Irr and Well-Irr, respectively, in SWAT-MODFLOW. For outlet 244, SWAT outperformed SWAT-MODFLOW with Auto-Irr and Well-Irr setups in terms of both R^2 and NSE. Auto-Irr slightly outperformed Well-Irr with an NSE of 0.53 vs. 0.51. Overall, at both locations, the SWAT-MODFLOW Auto-Irr (NSE = 0.53 and R^2 = 0.6) simulation performed better than Well-Irr.

Table 2.2. Statistical parameters for SWAT and SWAT-MODFLOW simulated (uncalibrated) stream discharge for 1982–2008.

Sub-basin	Model Type	Irrigation Type	R^2	NSE
120	SWAT	Auto Irrigation	0.66	0.13
	SWAT-MODFLOW	Auto Irrigation	0.63	0.55
	SWAT-MODFLOW	MODFLOW Well	0.62	0.51
244	SWAT	Auto Irrigation	0.76	0.75
	SWAT-MODFLOW	Auto Irrigation	0.68	0.53
	SWAT-MODFLOW	MODFLOW Well	0.68	0.51

We further used flow duration curves (FDC) to better understand the model's capability to simulate the streamflow regime. Figure 2.5 displays the streamflow regime (i.e., high flow to low flow conditions at outlets 119 and 244). Although the R^2 and NSE values from the SWAT alone simulation at outlet 244 were greater than other coupled simulation results, it failed to capture the low flow regime at this site. The FDC analysis indicated that SWAT significantly underestimated the low flow regime at these two sites. The simplified representation of an aquifer in SWAT may have resulted in the rapid depletion of the aquifer water level when the aquifer was used as an irrigation source (Chen et al., 2018). This could have reduced the baseflow and hence resulted in the underestimation of low flow regimes. Meanwhile, the low flow regime simulated by the coupled SWAT-MODFLOW setups were closer to the observed conditions when compared with SWAT. However, both SWAT-MODFLOW setups underestimated the high to mid-range flow regime for outlet 119. In the case of outlet 244, both SWAT-MODFLOW setups underestimated the entire flow regime. Among the coupled simulations, the largest underestimation of the low flow regime was found for Well-Irr. Overall, the performance of Auto-Irr for simulating stream discharge was the best among the coupled model setups. The SWAT-MODFLOW improved the R^2 and NSE of streamflow in the northern section (i.e., sub-basin 119) of the NHP, demonstrating the positive influence of including a spatially variable groundwater system. In general, these results showed that SWAT-MODFLOW could simulate stream discharge at a large-scale watershed such as the NHP within the acceptable ranges based on model performance evaluation criteria.

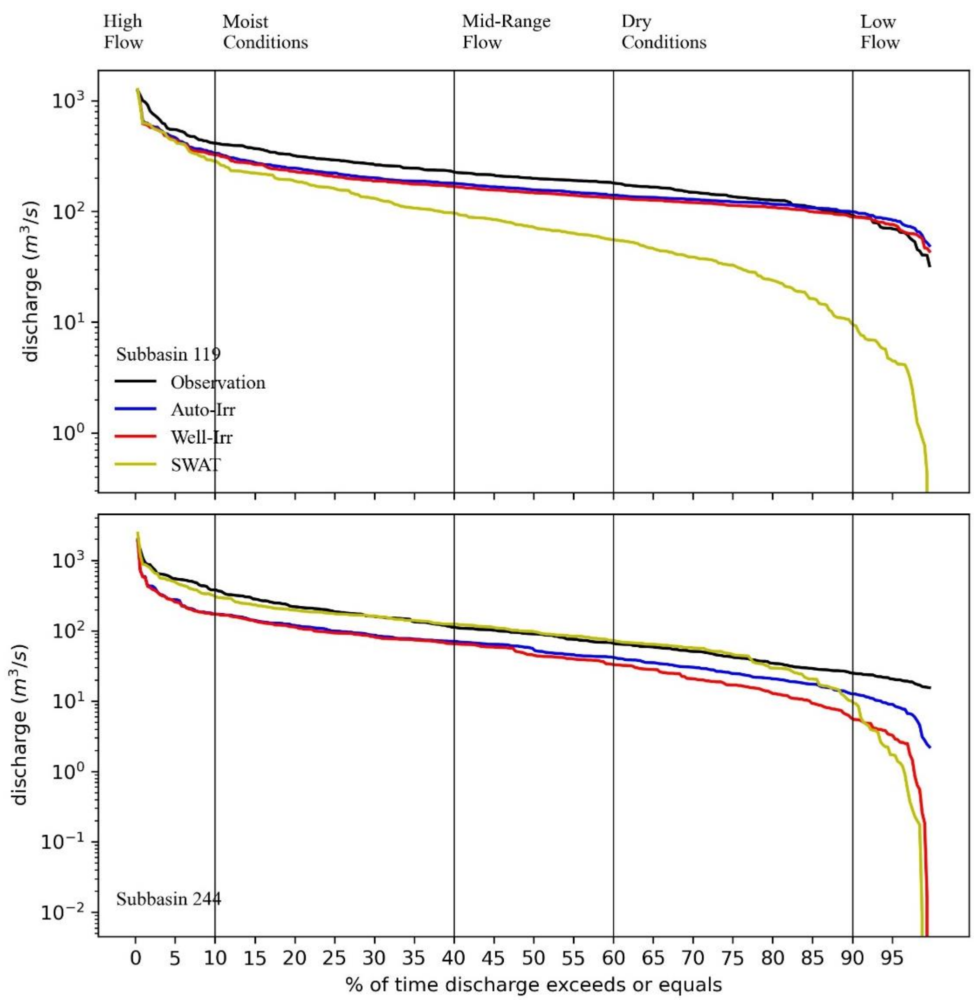

Figure 2.5. Simulated and observed flow duration curve at the outlets of U.S. Northern High Plains from 1982–2008.

2.3.1.4 Subbasin Evapotranspiration

Figures 1.6a and A.3 show the Auto-Irr, Well-Irr and SWAT simulated mean annual ET for all the sub-basins in the NHP. The simulated monthly and annual ET in three model setups were similar. The model setup had negligible effects on ET. The simulated ET from Auto-Irr and MODIS ET (Figures A.3 and A.4) shows the spatial resemblance over the NHP with a west to east gradient, generally lower ET in western and northcentral sub-basins, and higher ET in the eastern sub-basins of the NHP (Figures 1.6a and A.4). The west–east gradient could be attributed to the west–east gradient in annual rainfall and irrigation distribution in the NHP. The average annual ET for the entire basin was found to be 512 mm and 376 mm for Auto-Irr and MODIS, respectively. The model estimated mean annual ET values for the NHP were 38% more than MODIS. The sub-basins with high ET in the east and south of the NHP coincided with the irrigated croplands which suggests that additional moisture from irrigation during the growing season facilitated the crop growth that could have contributed to higher ET in these regions.

The R^2 of mean monthly ET at the sub-basin scale (Figure 2.6b) predicted by the Auto-Irr ranged from 0.01 to 0.80. The model simulated monthly ET with a mean R^2 of 0.54 and more than 70% of sub-basins had an R^2 greater than 0.5. Overall, the model performance indicated that the Auto-Irr with default SWAT parameters could provide reasonable estimates of monthly variation in ET at the sub-basin level.

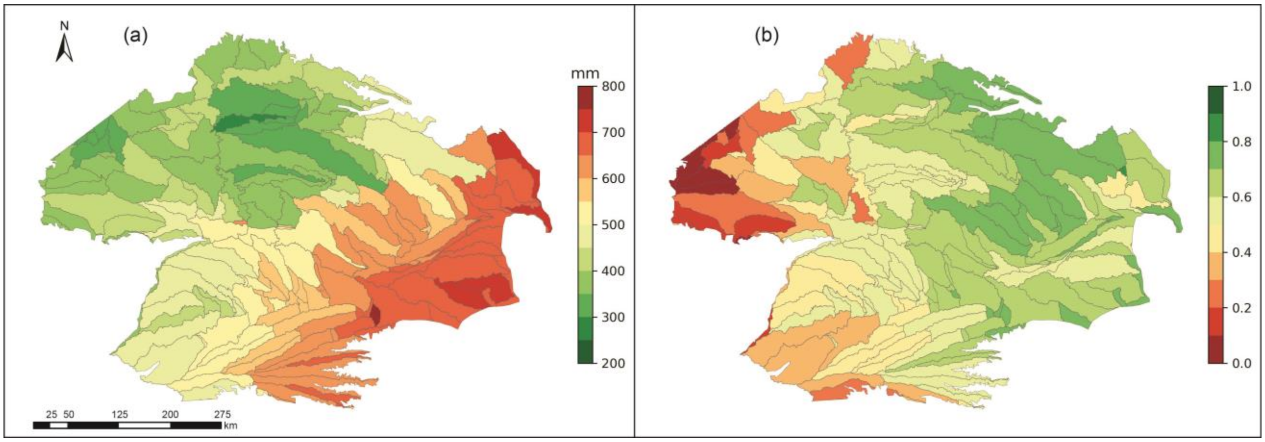

Figure 2.6. Sub-basin level (**a**) mean annual evapotranspiration simulated by Auto-Irr, and (**b**) R^2 between Auto-Irr simulated and MODIS evapotranspiration on a monthly scale from 2000–2008.

2.3.1.5 Crop Yield

The NASS corn yield ranged from 5464 to 7820 kg/ha with an average of 6771 kg/ha, and the soybean yield ranged from 1389 to 2157 kg/ha with an average of 1774 kg/ha. The simulated corn yield shown in Figure 2.7 ranged from 3840 to 7927, and 3837 to 7925 kg/ha with an average of 6080 and 6078 kg/ha for Auto-Irr and Well-Irr, respectively. The simulated soybean yield ranged from 802 to 2533 kg/ha and 802 to 2532 kg/ha with an average of 1719 and 1717 kg/ha for Auto-Irr and Well-Irr, respectively. The small difference in simulated corn and soybean yield by Auto-Irr and Well-Irr showed that the crop yield was less sensitive to the choice of the irrigation scheme. The overall PBIAS values for corn and soybean were 10.21 and 3.13% for Auto-Irr, and 10.23 and 3.21% for Well-Irr. This indicates the good performance of the coupled model setups in simulating the corn and soybean yields.

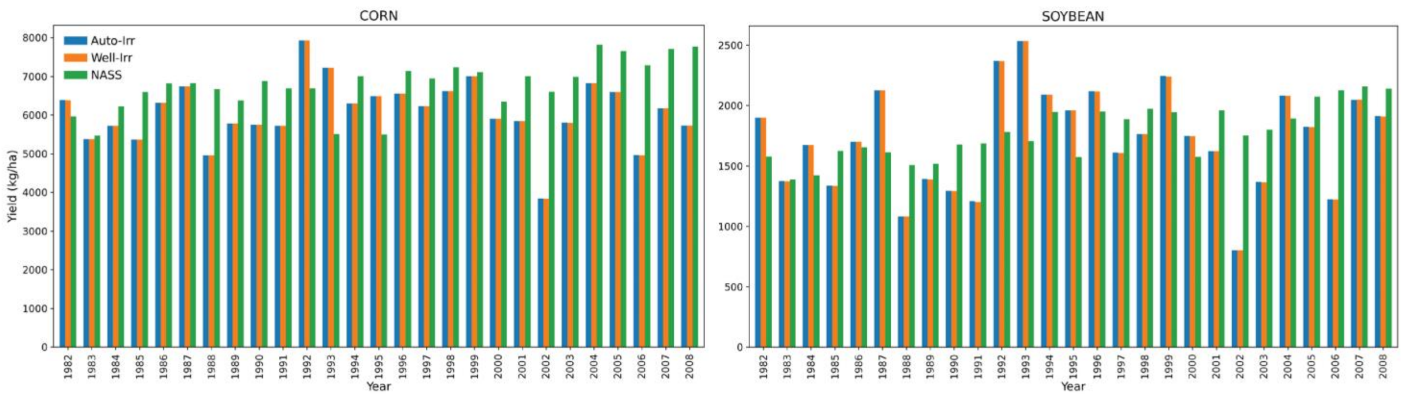

Figure 2.7. Comparison between Auto-Irr simulated and NASS corn and soybean yield in the NHP.

Given that the monthly stream discharge, groundwater level, annual groundwater pumping volume and corn and soybean yield simulated by the Auto-Irr were comparable with the observed values, and that the performance statistics indicated that the model could provide a reasonable characterization of the regional hydrological processes, Auto-Irr was used to assess the impact of water management practices in the NHP.

2.3.2 Irrigation Impacts on Groundwater Recharge

Groundwater recharge can be spatially variable depending on the vegetation, soil type, and climate. First, groundwater recharge over the NHP was examined under the current land and water management practices and then compared with a "no-irrigation" scenario to understand the overall impact of irrigation on groundwater recharge.

The spatial distribution of the long-term (1982–2008) mean annual recharge rate is displayed in Figure 2.8a. The mean annual recharge averaged across the NHP aquifer was 48.01 mm yr^{-1}, close to the value of 48 mm yr^{-1} obtained by (Szilagyi et al., 2005), a regional recharge study for Nebraska based on a simple water balance method. It was spatially variable with significant recharge around the north-central NHP (Sand Hills) and along the Platte and Elkhorn rivers. The recharge rate reached as high as 500 mm yr^{-1} in the Sand Hills and less than 0.5 mm yr^{-1} over the southern NHP and west of Sand Hills where precipitation is minimal and where the aquifer consists of clay soils. The elevated recharge rates in the northern part relative to the south of the NHP were associated with the soil properties which follow a gradient of high permeability in the north, to low permeability in the south (Smidt et al., 2016). The highly permeable sandy soils in Sand Hills reduce evapotranspiration and promote infiltration (Wang et al., 2009). The combination of low evapotranspiration and high infiltration rates over Sand Hills could explain the higher groundwater recharge rate. The spatial pattern of recharge was consistent with previously published studies (Smidt et al., 2016; Szilagyi et al., 2005; Zhang et al., 2016). A study by Zhang et al. (Zhang et al., 2016) used the Soil Water Balance (SWB) model to estimate the mean annual recharge for the period of 1950–2010 in the NHP that ranged from 0 to 499 mm yr^{-1}, matching closely with the 0–500 mm yr^{-1} range estimated in this study.

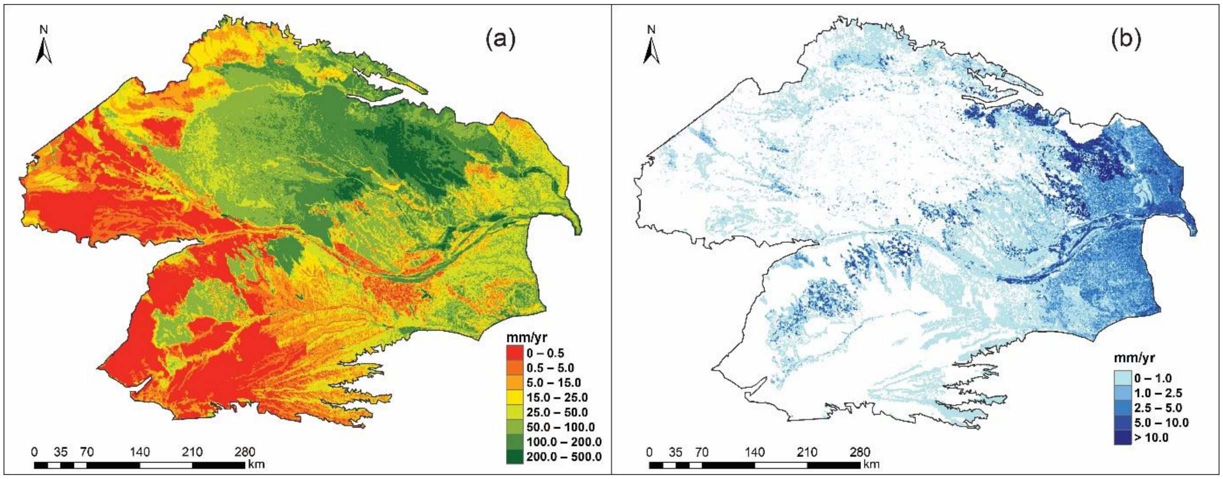

Figure 2.8. Auto-Irr estimated long-term (1982–2008) average (**a**) mean annual recharge, and (**b**) difference in annual recharge between irrigation and no-irrigation scenarios.

The spatial distribution of the difference in precipitation and ET (P-ET) in Figure 2.9a illustrates negative P-ET terms in the western and southern sub-basins. These sub-basins mostly corresponded with the areas of high irrigation demand dominated by irrigated crops (Figure 2.9b–d), low precipitation (Figure A.1), and low permeability of soils, which contributed to negligible recharge ~0 mm yr^{-1} (Figure 2.8a) despite additional water from irrigation in the region. Meanwhile, we found that in the eastern part of the NHP which receives high precipitation, despite high irrigation demand, mean annual precipitation exceeded the mean annual ET, resulting in a relatively higher recharge rate in the eastern NHP than in the western and southern parts (Figure 2.8a). Our result was supported by the similar findings of Crosbie et al. (Crosbie et al., 2013), which identified the high recharge rate in eastern Nebraska which was linked with the irrigation and coarse-textured soils.

Upon comparing the Auto-Irr and "no irrigation" scenarios from Figure 2.8b, we found that the regions with increased recharge overlapped the areas with irrigation wells. In irrigated areas, irrigation resulted in an overall increase in annual recharge that could exceed 10 mm yr^{-1}. The high recharge rates (>5 mm yr^{-1}) as a result of irrigation were found along the Platte and Elkhorn rivers. The groundwater recharge change due to irrigation was relatively small (~3.6%) in the study region. The previous studies that evaluated the effect of irrigation on groundwater recharge within our study region reported similar results. A study by Zhang et al. (Zhang et al., 2016) also found the negligible impact of irrigation on groundwater recharge in the NHP.

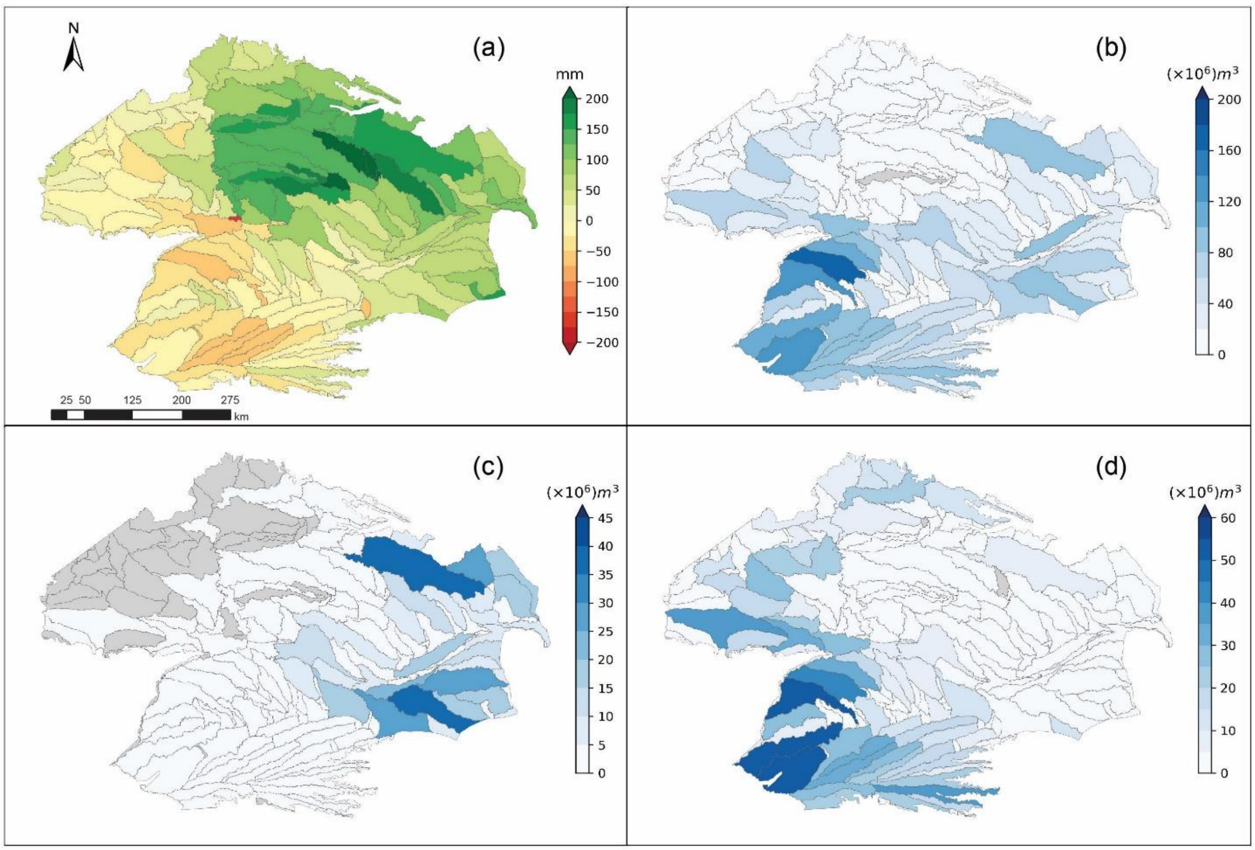

Figure 2.9. Simulated mean annual (**a**) difference in precipitation and evapotranspiration, (**b**) corn irrigation volume, (**c**) soybean irrigation volume, and (**d**) winter wheat irrigation volume, at the subbasin level from 1982–2008.

2.3.3 Irrigation Impacts on Surface-Groundwater Exchange

A comparison of the change in surface and groundwater exchange indicated that intensive irrigation could have a significant influence on the river discharge. In the absence of irrigation, on average there was an increase in groundwater discharge to all of the major rivers (Figure 2.10). Comparing the long-term annual average surface–groundwater exchange rates between irrigated and non-irrigated scenarios (Table 1.3) shows that irrigation practices decreased the groundwater discharge by 1.60 to 9.66 m3/s. The greatest decrease of 9.66 m3/s was found in the Platte River, followed by the Loup, Elkhorn, South Platte, Republican, Niobara, and North Platte rivers. These results indicated the significant effect of intensive irrigation on surface-groundwater exchange in the NHP, in good agreement with the Kustu et al. [13] finding that stream discharge was highly sensitive to irrigation pumping.

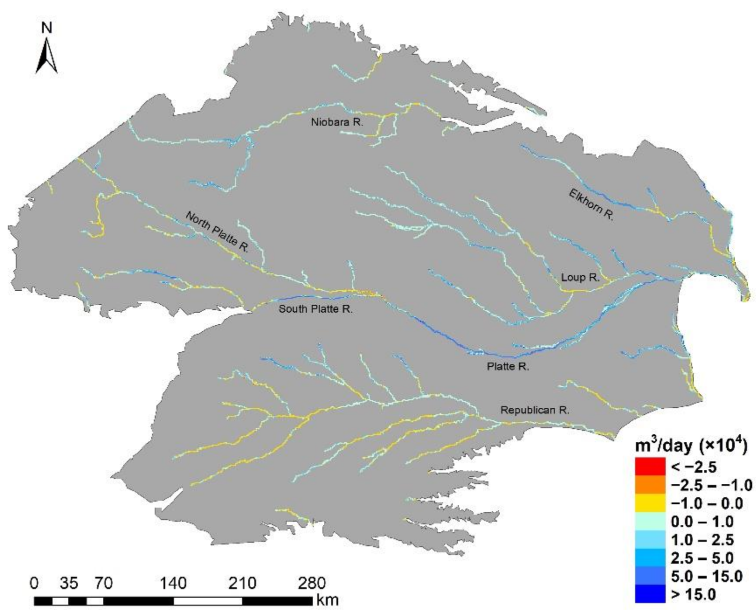

Figure 2.10. Auto-Irr estimated differences in the long-term (1982–2008) mean annual surface–groundwater exchange between irrigated and non-irrigated scenarios.

Table 2.3. Long-term (1982–2008) mean annual surface–groundwater exchange in major rivers of the NHP, where negative values indicate groundwater discharge.

Rivers	Irrigation (m^3/s)	No-Irrigation (m^3/s)	Difference (m^3/s)
North Platte River	−20.88	−22.48	1.60
South Platte River	3.72	0.63	3.09
Platte River	−18.97	−28.63	9.66
Loup River	−64.05	−69.99	5.94
Republican River	−16.26	−19.09	2.83
Elkhorn River	−10.65	−14.77	4.12
Niobara River	−24.31	−26.67	2.35

2.3.4 Hydrological Responses to Irrigation

A comparison of the effects of irrigation on the watershed scale water budget components (streamflow, groundwater recharge, and evapotranspiration) relative to the no-irrigation scenario over 1982–2008 for sub-basins overlaying the NHP aquifer is shown in Figure 2.11. The intensive irrigation in the region resulted in the largest impact on surface runoff (particularly during the growing season) and altered other water budget components. On the annual scale, as a result of irrigation, surface runoff increased 21.3%, groundwater infiltration increased 1.5%, soil water content increased 2.5% and ET increased 4.0%, compared with the no-irrigation scenario. It can be inferred that additional water from irrigation slightly increased soil water content and infiltration, resulting in more groundwater recharge and evapotranspiration, as well as higher surface runoff. The significant increase in seasonal surface runoff (up to 67% in July) demonstrates the potential impacts on the aquatic ecological system in the NHP caused by intensive irrigation.

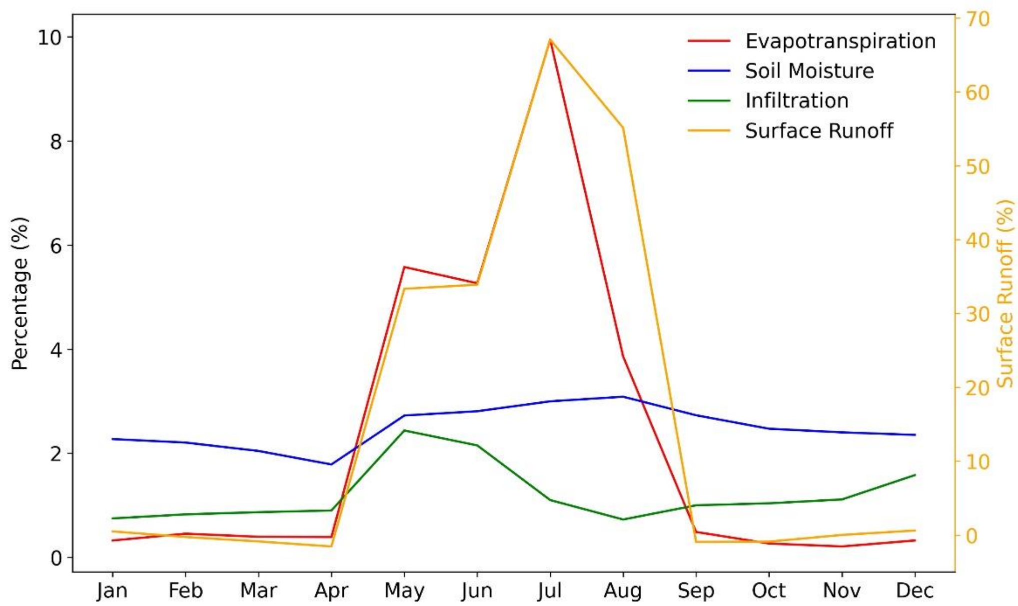

Figure 2.11. Long-term (1982–2008) seasonal hydrological processes analysis of U.S. Northern High Plains for irrigation scenario relative to no-irrigation scenario.

2.3.5 Irrigation Impacts on Crop Water Productivity

Figure 2.12 shows the changes in the average CWP (1982–2008) of corn and soybean, respectively, for the irrigation and no-irrigation scenarios. In the absence of irrigation, the CWP (corn and soybean) showed an upward west–east gradient, with lower values in the west and higher values in the east, which correlated with the precipitation distribution in the region (Figure A.1). This illustrates that the drier climate in the western sub-basins limited the crop yield. The simulated CWP for corn and soybean ranged from 0.39–1.8, and 0.01–0.39 kg/m^3, respectively. With irrigation, the average CWP of corn and soybean increased by 27.2 and 23.8%, respectively, at the sub-basin level. Correspondingly, the simulated irrigated CWP for corn and soybean ranged from 0.39–1.9, and 0.01–0.44 kg/m^3, respectively. Note that, the CWP increase in the eastern sub-basins under the irrigation scenario was minimal or closer to the no-irrigation scenario. The minimal CWP increase in the east of the NHP was not a surprise as the water deficit under no-irrigation was minimal. Meanwhile, in the western and central sub-basins where the water deficit was large, we observed pronounced increases in CWP, which suggested that the additional water from irrigation significantly increased the crop yield in those dry regions.

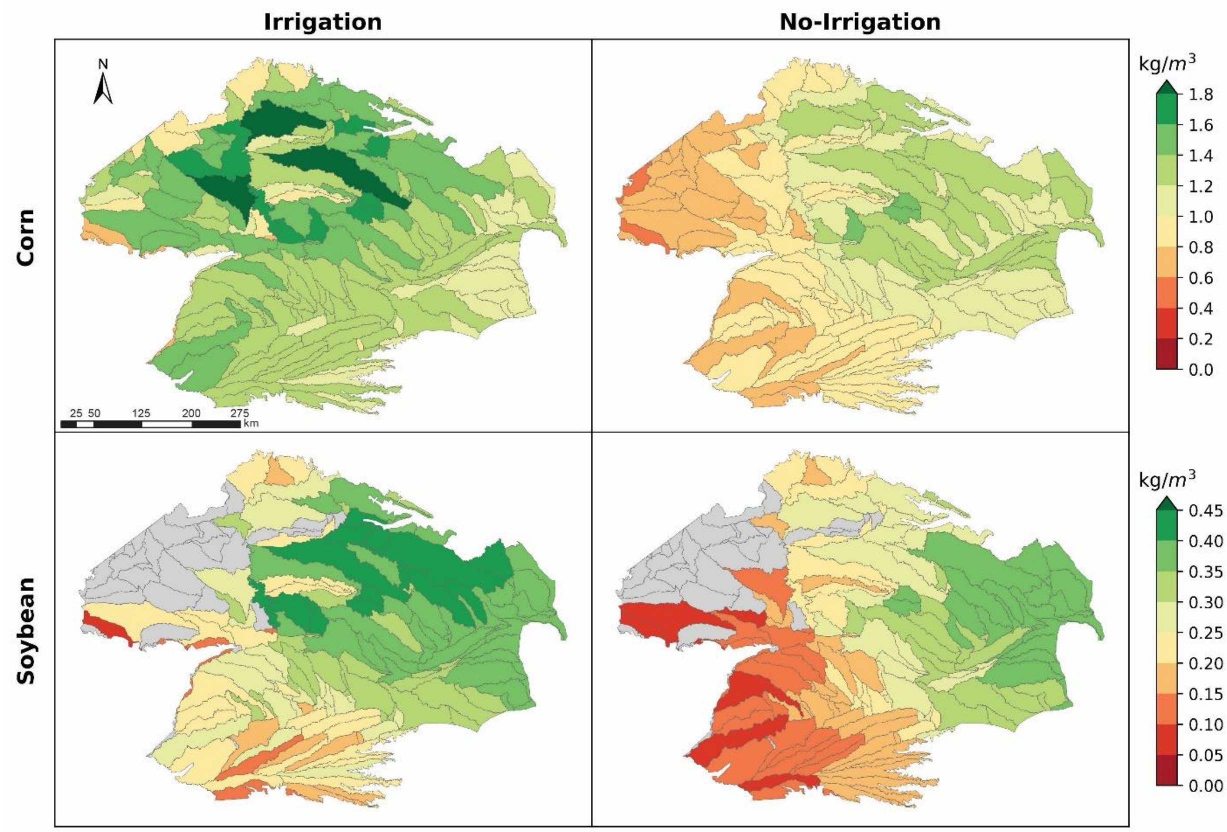

Figure 2.12. Simulated average annual values of crop water productivity for corn and soybean in the irrigation and no-irrigation scenarios. Gray shades represent regions without corn or soybean production.

2.4 Discussions

Caution should be used when interpreting the results from this study, which are subject to multiple caveats. For example, our model configuration assumes constant land use and land cover throughout the simulation period that presents difficulty in an accurate estimation of the irrigation demand and recharge rates. Additionally, the canal seepage was not simulated, which adds to the uncertainty in the modeled recharge rates. Therefore, further studies to allow dynamic land-use change and better representation of canal irrigation systems are needed.

Note that in our model evaluation and application, we did not apply automatic parameter calibration algorithms to adjust numerous parameters within the model. We made this choice for two reasons. First, the SWAT model was originally developed to operate in large-scale ungauged watersheds with minimal calibration efforts (Arnold et al., 1998), and Zhang et al. (Zhang et al., 2013b) and Arnold et al. (Arnold et al., 2015) noted that parameter calibration in many cases could not guarantee high fidelity of modeling results. Second, automatic optimization algorithms often require a large amount of resources and long times to identify globally optimal parameter solutions for complex hydrologic models such as SWAT (Zhang et al., 2009b), which is currently not affordable, as running SWAT-MODFLOW once for the NHP takes multiple days. As such, to ensure an objective comparison between different models, we used default model parameters or derived parameters from literature instead of intensively calibrating numerous parameters of SWAT-MODFLOW. In the future, further modifications of SWAT-MODFLOW are needed to assess the applicability of parallel processing for drastically reducing the computational resources needed to run the coupled model, thereby allowing for numerous model runs and understanding uncertainties associated with parameters and input data.

2.5 Summary and Conclusions

In this study, we conducted modification and evaluation of the SWAT-MODFLOW model's irrigation modules for improved representation of irrigation practices and the exchange of water fluxes in the U.S. Northern High Plains (NHP) aquifer. We found that SWAT-MODFLOW with irrigation based on auto-irrigation scheduling, triggered by plant water stress (Auto-Irr), attained better performance than SWAT-MODFLOW with prescribed irrigation based on well pumping rates in MODFLOW (Well-Irr) in terms of groundwater level, streamflow, and ET, and was capable of explicitly representing groundwater level change as compared with the original SWAT model. Therefore, Auto-Irr was used to quantify and understand hydrologic and agronomic impacts of the intensive irrigation practices in the NHP.

The results showed that the groundwater recharge rate and groundwater level changes in the NHP were spatially variable and were all substantially impacted by irrigation practices. A comparison of Auto-Irr results with "no-irrigation" scenarios showed that intensive irrigation in the region had a significant impact on the groundwater levels and crop water productivity, but only exerted a modest effect on groundwater recharge, except in the region with dense irrigation wells.

The irrigation-caused changes in groundwater systems also translated into alterations in other hydrological processes, including streamflow, evapotranspiration (ET), soil moisture, and groundwater recharge. In general, the impact of irrigation slightly altered soil moisture, and groundwater recharge, but significantly modified ET and streamflow regimes in the NHP, particularly during the growing season. For example, on the annual scale, as a result of irrigation, ET and surface runoff increased by 4.0% and 21.3%, respectively. During July, irrigation practices increased ET by 9.9% and surface runoff by 67.1%. Such large changes in surface runoff resulting from irrigation are expected to have significant impacts on aquatic ecosystems, which deserves further research in the future. Irrigation in the NHP also significantly increased corn and soybean yields and their crop water productivity (CPW). With irrigation, the average CWP of corn and soybean increased by 27.2 and 23.8%.

Overall, historical irrigation in the NHP greatly benefited crop productivity and caused pronounced modifications to the groundwater systems and other hydrological processes. Particularly, the decline in groundwater level raises concerns for future sustainable irrigation in the face of a warming climate; and significant alterations in streamflow during the growing season indicate that future design of sustainable irrigation practices should consider downstream aquatic ecosystems impacts. We anticipate that the exercises conducted here help to increase the understanding of the hydrological and agronomic impacts of historical irrigation and provide support for future efforts to enhance agroecosystem sustainability in the NHP and other regions facing water shortage challenges.

[2]

Chapter 3: Multivariate Calibration of the SWAT Model using Remotely Sensed Datasets

Materials presented in this chapter have been published in the journal Remote Sensing as Dangol et al. (2023)

3.1 Introduction

The conventional approach to calibrating hydrologic models often involves using streamflow data from hydrologic gauges to obtain the optimum values of model parameters for improved model performance (Herman et al., 2018; Parajuli et al., 2018). However, relying solely on streamflow data to constrain hydrologic model performances can result in the poor simulation of other hydrologic components such as evapotranspiration and soil moisture. In addition, streamflow data may not be readily available for a study region and time of interest due to the high cost and the discontinuity of hydrologic gauge operation. Due to these limitations, when a hydrologic model is calibrated against streamflow data available at the watershed outlet, the simulated hydrologic processes (e.g., streamflow, soil moisture, and ET) within the watershed can be subject to large uncertainties (Qi et al., 2020b; Zhang et al., 2013a).

Remotely sensed data can provide crucial information about the dynamics of the water budget (Paul et al., 2021; Senay et al., 2016; Sheffield et al., 2018; Yang et al., 2014). As such, the hydrologic calibration process can benefit from the inclusion

---

Dangol, S., Zhang, X., Liang, X.-Z., Anderson, M., Crow, W., Lee, S., Moglen, G.E., McCarty, G.W. Multivariate Calibration of the SWAT Model Using Remotely Sensed Datasets. Remote Sens. 2023, 15, 2417. https://doi.org/10.3390/rs15092417 of remotely sensed soil moisture (Li et al., 2018) and ET (Lee et al., 2022, 2021) data, in addition to traditionally used streamflow measurements, to capture the spatiotemporal distribution of the water budget components (Bastiaanssen et al., 1998; Immerzeel and Droogers, 2008; Parajuli et al., 2018), particularly in arid/semi-arid watersheds with regulated water resources systems, where evapotranspiration (ET) and soil moisture content play an important role in determining groundwater recharge and irrigation water requirements (Sheffield et al., 2018; Wu et al., 2015).

Among the numerous agrohydrologic models, the Soil and Water Assessment Tool (SWAT) (Arnold et al., 1998) is a representative model that has been widely used for watershed management and water quality studies in agricultural watersheds. To improve the reliability of the SWAT simulations in both gauged and ungauged watersheds, satellite-based data products that represent land surface dynamics (such as leaf area index) and water budget components (such as ET and soil moisture) have proven to be useful (Choudhary and Athira, 2021; Kundu et al., 2017; Myers et al., 2021; Rajib et al., 2020, 2016; Shah et al., 2021). Many studies have used remotely sensed data, and ET (Herman et al., 2018; Lee et al., 2022; Parajuli et al., 2018; Rajib et al., 2018; G. Zhang et al., 2020) or soil moisture (Choudhary and Athira, 2021; Kundu et al., 2017; Rajib et al., 2016) in particular, in conjunction with streamflow data to constrain the complex land–vegetation–atmosphere interaction in hydrologic models. These efforts aid in model parameter estimation and help improve model performance in capturing the spatial and temporal distribution of the water budget components cycle.

For example, Parajuli et al. (2018) used Moderate Resolution Imaging Spectroradiometer (MODIS) ET to evaluate if calibration using remotely sensed ET in combination with streamflow improves the streamflow simulation. Their findings suggested that multivariable calibration using remotely sensed data improved ET estimation, but the improvement in streamflow estimation was negligible. Rajib et al. (2018) found that multivariable calibration of streamflow and MODIS ET allows for the optimization of model biophysical parameters that improve the representation of vegetation dynamics and effectively reproduced both water and energy balance components. Lee et al. (2022) used Atmosphere–Land Exchange Inverse (ALEXI) ET in conjunction with streamflow and crop yield for multivariable calibration and demonstrated that the use of multiple constraints during model calibration helps reduce the model predictive uncertainty by minimizing the number of acceptable parameter sets.

Similar findings have been reported when the hydrologic models were calibrated using streamflow and soil moisture. For instance, Choudhary and Athira (2021) used streamflow and soil moisture together to calibrate the SWAT model. They found that calibration with streamflow data alone resulted in poor simulation of soil moisture and significantly different ET simulation compared to the calibration with streamflow and soil moisture together. They showed that constraining the simulated soil moisture slightly improved the baseflow simulation but the trade-off between surface runoff and soil moisture did not significantly improve the overall streamflow simulation. Rajib et al. (2016) found that calibration with streamflow data alone resulted in considerable uncertainty in soil moisture simulation, while inclusion of root zone soil moisture improved soil moisture simulation, reduced model uncertainty range, and significantly improved streamflow simulation.

Nevertheless, many issues exist with multivariable calibration and constraining the SWAT model with remotely sensed data. First, although the remotely sensed ET datasets are validated with measured data, their accuracy is subject to uncertainties in inputs (to algorithms deriving remotely sensed ET), temporal and spatial scaling, and coverage (Karimi and Bastiaanssen, 2015; Pan et al., 2020; Velpuri et al., 2013) that may cause hydrologic models to produce less accurate results for other components of the hydrologic cycle (e.g., soil moisture, baseflow, and groundwater discharge). With the continuous advancement in satellite technology and consistent global monitoring, multiple remotely sensed data products for evapotranspiration and soil moisture are becoming widely available (Dembélé et al., 2020; López et al., 2017). Notably, remotely sensed ET products differ from each other in terms of the algorithms used to derive the ET values and their capability to provide accurate estimates of ET in a region of interest. Second, a multivariable calibration approach can lead to complications due to trade-offs among model responses (Sirisena et al., 2020; Yapo et al., 1998). For example, the model parametrization can cause the predicted variable, e.g., streamflow, to be closer to the measured values at the cost of other components of the hydrologic processes such as ET, soil moisture, and groundwater discharge.

In addition, the structure or configuration of a hydrologic model can influence the model’s performance, calibrated parameter values, and response to different inputs (Zhang et al., 2011b, 2009a). Another strategy increasingly adopted in the SWAT modeling community to improve model performance consists of model modification to replace simplified empirical algorithms with physically based modules/algorithms that better represent physical processes such as plant growth (Strauch and Volk, 2013), soil organic carbon, nitrogen cycling (Yang and Zhang, 2016; Zhang et al., 2013b), and soil moisture content and temperature (Qi et al., 2016). For example, Qi et al. (2020b) and Wang et al. (2020) showed that modification of the SWAT model's biogeochemical and energy balance algorithms can influence the SWAT model-simulated hydrologic budgets and their responses to climate change.

Given the above knowledge gaps identified based on the literature review, we aim to provide insights into the following scientific questions: (1) Does the use of different remotely sensed ET and soil moisture products in addition to streamflow data help improve the performance of a calibrated hydrologic model? (2) Does the choice of different remotely sensed ET products for model calibration influence model performance? (3) Do variations in model structure influence model performance under multivariate calibration? The remote sensing datasets and hydrologic model are both open-access to the community. The results from this study are expected to help the hydrologic modeling community to better understand the strengths and caveats of using remotely sensed datasets, thereby designing more robust strategies for improving hydrologic modeling.

3.2 Materials and Methods

3.2.1 Study Area

The 6909 km^2 Little Blue River Watershed (LBRW), located in the Midwest of the USA, spans Nebraska and Kansas (Figure 3.1). The LBRW is an intensively irrigated agricultural watershed, with agricultural land (69.5%) as the dominant land cover category, followed by pastureland (28.8%) and forest (1.6%). The LBRW is part of the large High Plains Aquifer, where most of the agricultural irrigation is from groundwater. From 1985 to 2015, the annual irrigation water use in the watershed increased from 105×10^6 to 141×10^6 m^3 (Dieter et al., 2018). The watershed receives about 815 mm of rainfall annually with almost 65% of annual rainfall occurring in May–September (Dangol et al., 2022). The basin is primarily composed of silt loam and silt clay loam soils that have a large water-holding capacity and are relatively impermeable; hence, the groundwater recharge is a small fraction of the annual precipitation (Alley and Emery, 1986). The intensive use of groundwater for irrigation has significantly affected the water quantity in the study area. Moreover, agricultural activities have aggravated the water quality issues in the watershed (Barnes and Kalita, 2001; Helgesen, 1996). The hydrologic processes in the LRBW are complex, with substantial surface water and groundwater interaction (Helgesen, 1996), which is influenced by factors such as surface runoff, infiltration, and evapotranspiration. Given these conditions, water conservation is of utmost importance in the LBRW.

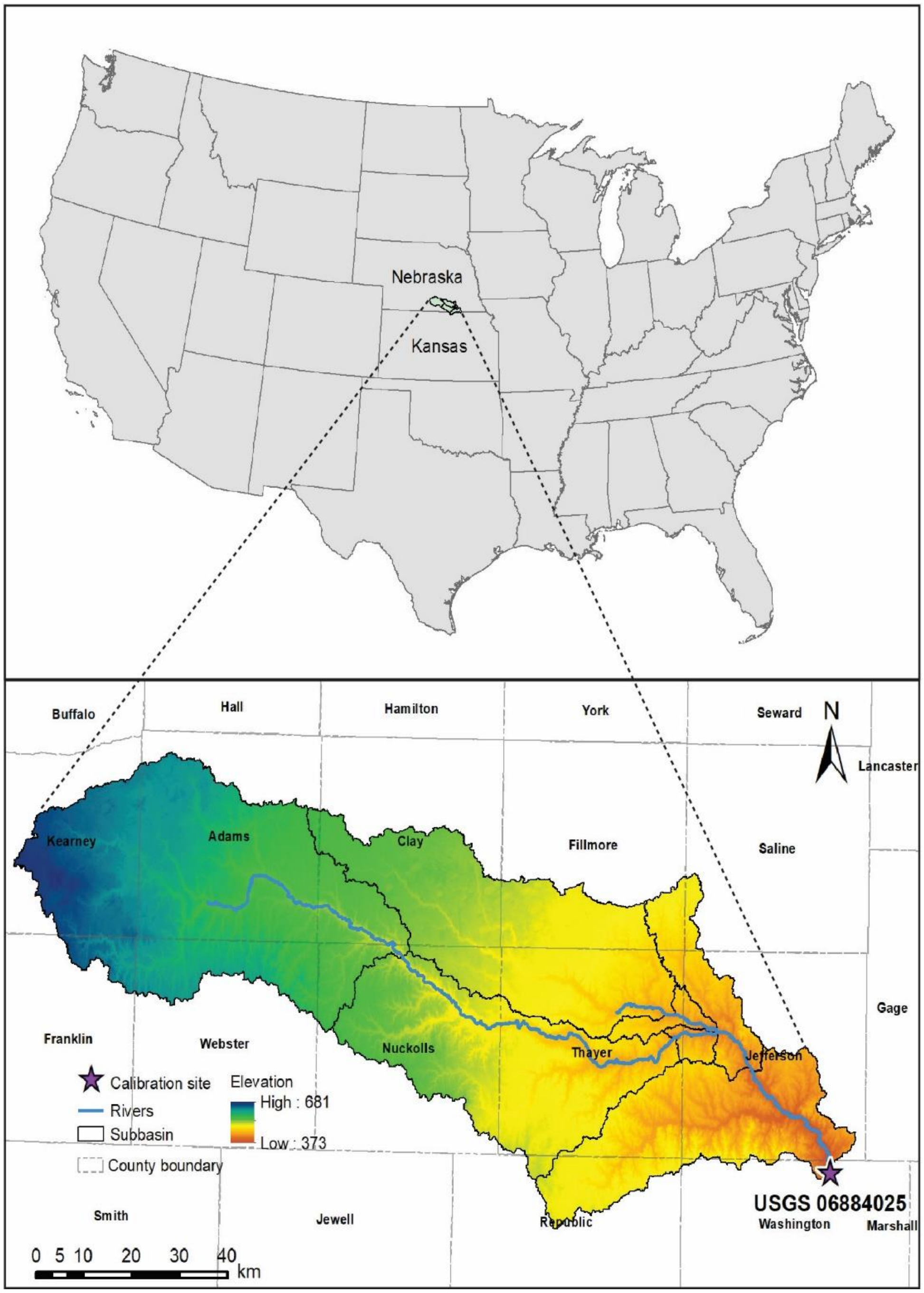

Figure 3.1. Location and elevation map for the 6909 km^2 Little Blue River Watershed.

3.2.2 Hydrologic Models

3.2.2.1 SWAT Model Description

The SWAT model is a physically based model that simulates hydrologic processes by dividing the watershed into subbasins which are further divided into hydrologic response units (HRU). The HRU represents a unique combination of homogenous land use, soil class, and slope (Neitsch et al., 2011). The surface runoff is simulated using the Natural Resources Conservation Service (NRCS) curve number method, and the flow of water within the soil profile is simulated using a simple tipping bucket approach (Neitsch et al., 2011). This simplified soil moisture model has been widely tested in several studies (Li et al., 2010; Uniyal et al., 2017). SWAT simulates the land phase of the hydrologic cycle based on the water balance equation (Neitsch et al., 2011):

$$SW_t = SW_o + \sum_{i=1}^{t}(R_{day} - Q_{surf} - E_a - W_{seep} - Q_{gw}), \tag{1}$$

where SW_t is the soil water content (mm); SW_o is the initial soil water content (mm); Q_{surf} is the surface runoff (mm); R_{day} is the precipitation (mm); E_a is the evapotranspiration (mm); W_{seep} is the percolation (mm) from the soil profile; Q_{gw} is the return flow (mm); and *t* is the time (days).

Evapotranspiration was calculated in SWAT using the Penman–Monteith method. The Penman–Monteith method (Monteith, 1965) uses solar radiation, air temperature, relative humidity, and wind speed to estimate the ET.

3.2.2.2 SWAT-C

To understand the extent to which changes in model structure/configuration can influence multivariate calibration results, we compared the SWAT-Carbon (SWAT-C) model with the SWAT model. SWAT-C employs the CENTURY (Parton et al., 1994)-

based soil organic matter and residue, which are modeled using five different pools (Liang et al., 2022; Yang and Zhang, 2016; Zhang, 2018; Zhang et al., 2013b). SWAT-C incorporates more detailed biochemical properties and environmental factors to simulate the soil organic matter residue dynamics considering both C and N cycling (Zhang et al., 2013b). In addition, the energy balance algorithms in SWAT-C are based on physically based equations, instead of empirical equations that link air temperature with soil temperature (Qi et al., 2021). These changes have resulted in substantial changes in hydrologic modeling as compared with the standard SWAT2012 (Qi et al., 2020b; Wang et al., 2021, 2020). SWAT-C has been successfully evaluated at the field scale (Yang and Zhang, 2016; Zhang et al., 2013b) and watershed scale (Qi et al., 2020b) in the US Midwest. Therefore, here we use both SWAT and SWAT-C to examine the responses of hydrologic modeling to the different strategies of using remotely sensed ET and soil moisture products.

3.2.3 Model Setup

The SWAT model for LBRW was configured using multiple geospatial datasets (Table 3.1 and Figure 3.2). The land use information from the Cropland Data Layer (CDL) 2008 (USDA NASS Cropland Data Layer, 2008) was overlaid with the MODIS irrigated land layer 2007 (Pervez and Brown, 2010a) to generate a land use map with cropland separated into irrigated and dry cropland. Soil data were derived from the State Soil Geographic (STATSGO) dataset. The thresholds of 5% for land use and 10% for soil class were used during the HRU generation. Here, the threshold is applied sequentially to land use and soil class. The land use covering less than 5% of the subbasin is removed and its area is redistributed among the remaining land use in the subbasin. Next, if the area of soil class within a land use is less than 10%, it is removed and redistributed to remaining soil class in that land use (Her et al., 2015). The SWAT model created using this threshold approach had 244 HRUs. This approach facilitated the removal of minor land uses and soil class in each subbasin and thereby obtained more computational efficiency without affecting the model performance. The crop management operations, planting, and harvesting, were based on USDA-NASS (USDA-NASS, 2010), and fertilizer application was based on Woznicki and Nejadhashemi, (2012), Ferguson et al. (2006), and Van Liew et al. (2012) for corn, soybean, and winter wheat, respectively. The irrigation operation was set up based on Dangol et al. (Dangol et al., 2022). The SWAT auto-irrigation module was used, with plant water stress based irrigation scheduling to trigger irrigation, which was shown to reasonably capture regional agricultural irrigation amount in the Northern High Plains aquifer. Meteorological data (precipitation, minimum and maximum temperature, relative humidity, wind speed, solar radiation) used to drive the SWAT model were obtained from the North American Regional Reanalysis (NARR) database (Mesinger et al., 2006b).

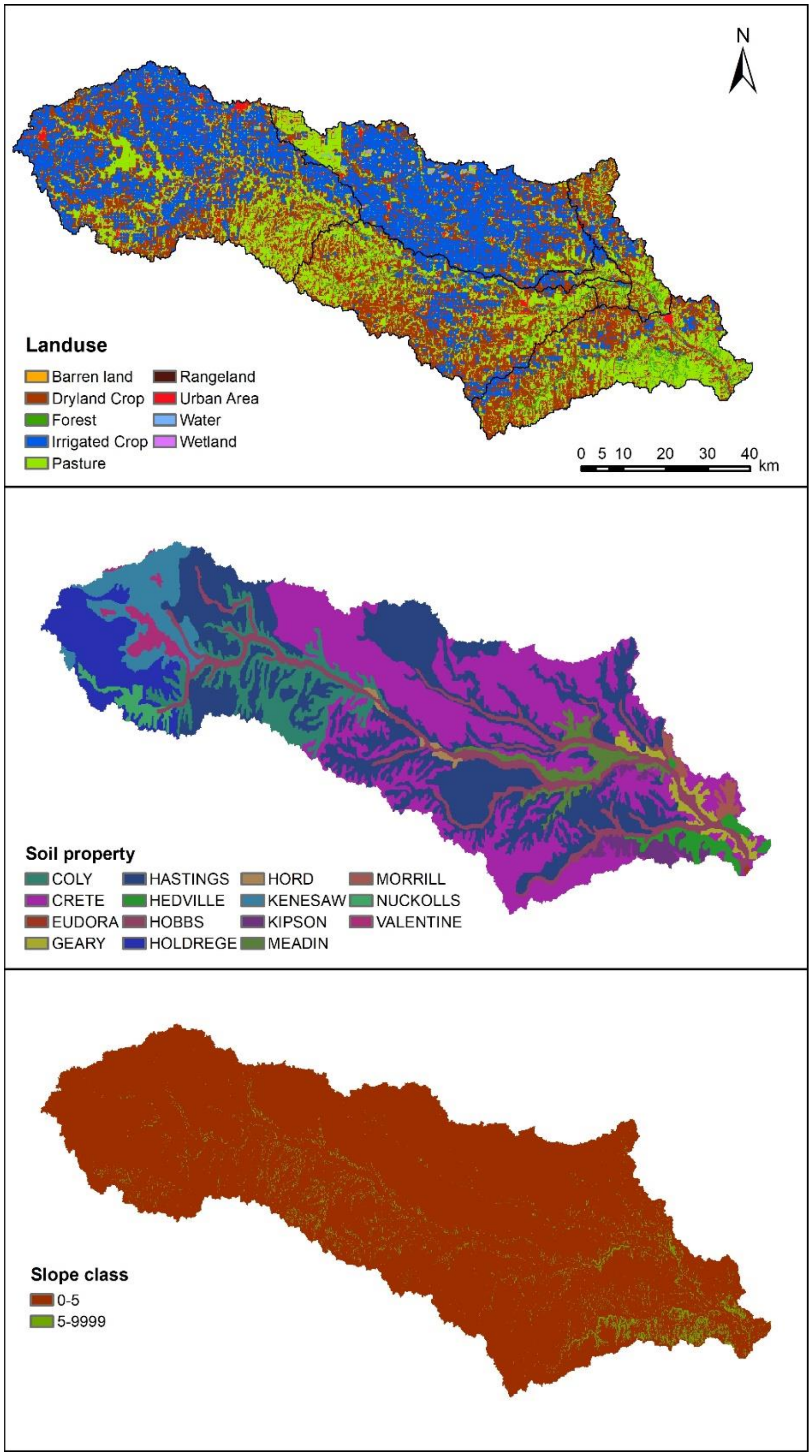

Figure 3.2. Land use, soil property, and slope class map for Little Blue River Watershed.

Table 3.1. Geospatial and climate data used to set up SWAT model.

Data	Resolution	Source
Weather	0.3° × 0.3°	NARR (Mesinger et al., 2006b)
Digital Elevation Model (DEM)	90 m × 90 m	Shuttle Radar Topography Mission (SRTM) (Jarvis et al., 2008b)
Land Use	30 m × 30 m	USDA NASS Cropland Data Layer (2008)
MODIS Irrigated Land	250 m × 250 m	Pervez and Brown (2010a)
Soil Property	1:250,000	STATSGO (USDA-NRCS, 1994b)

3.2.4 Remotely Sensed Evapotranspiration and Soil Moisture Content Data Products

To evaluate the impact of remotely sensed ET and soil moisture products on the model performance following the multivariable calibration, two ET datasets, MODIS and ALEXI, and a recently developed soil moisture dataset, Soil MERGE (SMERGE), were considered (Table 3.2).

Table 3.2. SWAT calibration input summary.

Data	Resolution	Source
MODIS Evapotranspiration	500 m × 500 m	Running et al. (2019)
ALEXI Evapotranspiration	4 km × 4 km	Anderson (1997)
SMERGE 40 cm volumetric soil moisture content	0.125° × 0.125°	Crow and Tobin (2018)

A brief description of these three remotely sensed datasets is provided as follows.

3.2.4.1 MODIS Evapotranspiration

The MODIS ET is an open-source global dataset widely used in hydrologic modeling because of its good spatiotemporal resolution, well-documented assessment, and validation over North America (Lin et al., 2018; Mu et al., 2013, 2011). The MODIS ET algorithm is based on the Penman–Monteith equation (Monteith, 1965), which considers surface energy partitioning processes and atmospheric drivers of ET. In this study, the monthly ET values were derived for each of the seven subbasins in watershed by spatially aggregating the 8-day total 500 m gridded ET data from MODIS (MOD16A2) for the period of 2001 to 2016. All MODIS pixels within each subbasin were averaged to produce ET average values.

3.2.4.2 ALEXI Evapotranspiration

The ALEXI model (Anderson, 1997) utilizes the two-source land surface algorithm to partition ET into canopy transpiration and soil evaporation components, to compute daily fluxes of ET at the 4 km resolution. The ALEXI ET products have been evaluated and validated against observed data using a Landsat/MODIS-based downscaling algorithm called DisALEXI (Norman et al., 2003) over a wide range of climatic conditions in North America (Anderson et al., 2011; Yang et al., 2018). In this study, daily 4-km gridded ALEXI ET was spatially aggregated into monthly values for each of the seven subbasins for the period of 2001 to 2016.

3.2.4.3 SMERGE Volumetric Soil Moisture Content

As discussed earlier, the multivariable calibration approach that targets streamflow and ET does not necessarily improve the estimation of other hydrologic processes such as soil moisture content. Soil moisture content has a significant impact on irrigation requirements and crop productivity. However, most multivariable calibration studies with streamflow and ET as target variables do not report the impact on soil moisture content. In this study, we used the SMERGE volumetric soil moisture dataset (0–40 cm) (Crow and Tobin, 2018; Tobin et al., 2017) to understand the effect of multivariable calibration on the simulation of the soil moisture content. The SMERGE daily soil moisture data are developed by combining the North American Land Data Assimilation System land surface model output with surface satellite retrievals from the European Space Agency Climate Change Initiative. The SMERGE dataset has been validated against the in situ measurements in the conterminous United States (Tobin et al., 2019). The SMERGE volumetric soil moisture content (m^3/m^3) is converted into depth units (mm) by multiplying it with soil moisture depth (400 mm) for comparison with the soil moisture estimates from the SWAT model.

3.2.5 Model Calibration and Evaluation

The SWAT model was run from 1998 to 2016 with three years of warm-up period (1998–2000) (Zhang et al., 2008) calibrated at a monthly time step for the period of 2001–2008, and validated for the period of 2009–2016. The model calibration was performed in two steps (Feng et al., 2018): first, the fractional potential heat units for planting and harvest dates for corn and soybean were adjusted to ensure the model-simulated planting and harvest dates aligned with the dates provided by USDA (USDA-NASS, 2010); second, the model was calibrated against different combinations of streamflow and the remotely sensed dataset (ET and soil moisture) simultaneously. Streamflow data for model calibration were obtained for USGS streamgage station 06884025 (Figure 3.1).

Model sensitivity analysis and calibration were performed using the Sequential Uncertainty Fitting algorithm version 2 (SUFI-2) procedure in SWAT-CUP (Moriasi et al., 2007) (Figure 3.3). Model parameters based on the existing literature were selected for sensitivity analysis. Using global sensitivity in SUFI-2, the most sensitive parameters (*p*-value < 0.1) were selected and adjusted during the calibration process for each calibration setup (Table 3.3). The multivariable calibration approach that has been shown to improve the ET calibration while maintaining the streamflow calibration (Herman et al., 2018) was selected for this study. A total of nine simulations were run using different combinations of observed MODIS ET, ALEXI ET, SMERGE soil moisture, and streamflow data for multivariable calibration including simulations for streamflow only, ET only, and soil moisture only calibration (Table 3.3).

Table 3.3. Calibrated SWAT model parameters under different calibration setups.

Parameters	**Unit**	**Benchmark (Streamflow Only)**	**MODIS Only**	**ALEXI Only**	**SMERGE Only**	**Streamflow + MODIS**	**Streamflow + ALEXI**	**Streamflow + SMERGE**	**Streamflow + SMERGE + MODIS**	**Streamflow + SMERGE + ALEXI**
r_CN2	*	−0.004 (−17.49)	0.188 (47.71)	−0.122 (−35.42)	−0.149 (−56.73)	0.0035 (−14.06)	−0.004 (−18.57)	−0.008 (−19.50)	−0.0003 (−16.35)	−0.025 (−20.44)
v_EPCO	*	0.946 (1.68)	0.904 (−3.01)	0.813 (2.26)	0.982 (3.38)	0.773 (1.50)	0.862 (1.72)	0.929 (1.78)	0.816 (1.62)	0.982 (−1.81)
a_GWQMN	mm	−250.75 (−1.58)	−486.25 (1.66)	329.25 (−1.74)	–	373.25 (−1.54)	−58.75 (−1.60)	−210.75 (−1.55)	399.75 (−1.51)	−434.5 (−1.57)
r_SOL_AWC	mmH_2O/mm soil	0.137 (−0.81)	−0.047 (−10.82)	0.067 (4.71)	0.282 (60.84)	−0.174 (−2.02)	–	0.129 (1.88)	0.088 (0.93)	0.233 (2.03)
v_FFCB	*	0.441 (0.88)	–	–	–	0.128 (0.80)	0.505 (0.91)	0.243 (0.85)	0.571 (0.77)	0.282 (0.88)
v_SURLAG	days	8.122 (−0.81)	–	–	–	3.863 (0.68)	6.483 (0.67)	–	–	–
v_REVAPMN	mm	100.133 (−0.81)	0.135 (−2.43)	59.384 (3.40)	247.38 (−3.09)	236.63 (−1.14)	–	218.13 (−0.92)	366.38 (−1.25)	174.256 (−0.71)
r_SOL_BD	Mg/m^3	−0.290 (−0.92)	0.058 (5.56)	–	0.217 (−3.98)	–	0.105 (−0.92)	−0.004 (−1.07)	–	0.249 (−1.06)
v_ESCO	*	–	0.973 (29.75)	0.931 (2.04)	–	0.948 (2.86)	–	–	0.989 (2.77)	–
v_GW_REVAP	*	0.023 (−0.90)	0.163 (5.24)	0.022 (−4.63)	0.143 (2.56)	–	0.037 (−1.11)	0.029 (−0.77)	–	0.021 (−0.97)
v_SLSOIL	m	–	29.21 (−2.14)	–	–	–	–	–	–	–

Note: r, v, and a represent the relative, replacement, and absolute changes in model parameters, respectively. "–" indicates that the parameter is not sensitive for model configuration and is not included in the model calibration; "*" indicates unitless parameters. The numbers inside the bracket represent the t-stat. The benchmark setup uses streamflow only. The other calibration setups used streamflow plus one or two more remote sensing products.

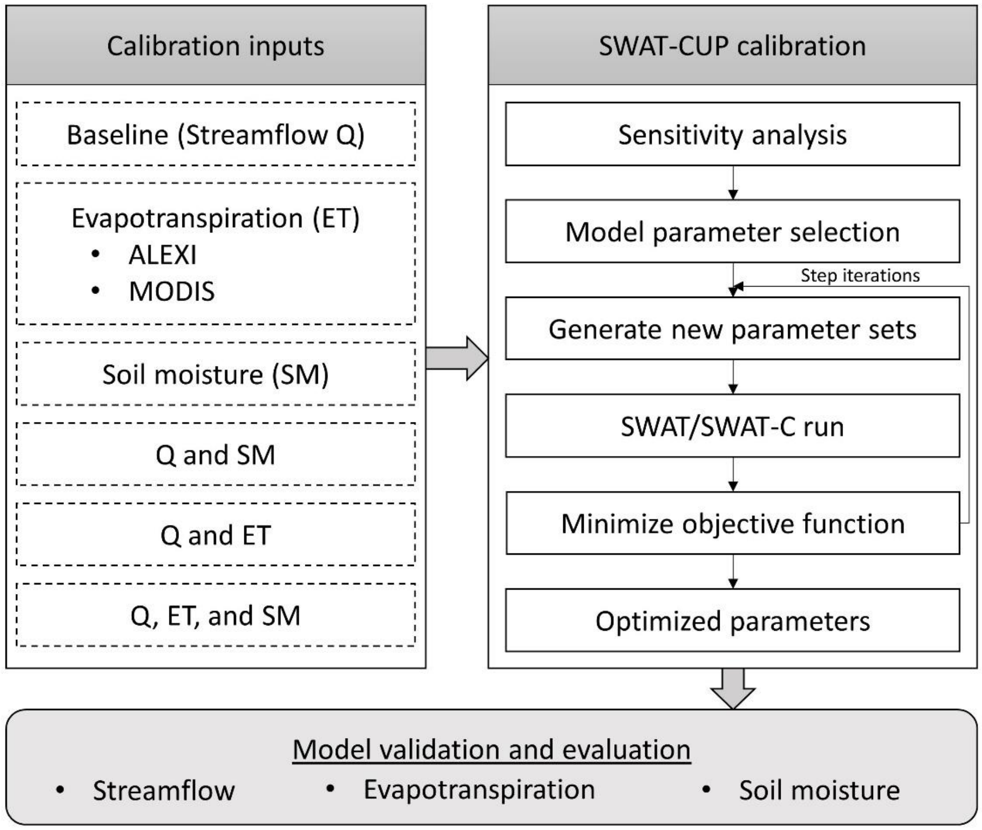

Figure 3.3. Flowchart showing the multivariable calibration and validation approach. Each set of variables used for multivariable calibration are shown in calibration inputs.

The Kling–Gupta Efficiency criterion (KGE) (Gupta et al., 2009) is used as the objective function for the multivariable calibration with equal weights assigned to each variable. For multivariable calibration, the aggregated value (KGE') of KGE is calculated as follows:

$$KGE' = w_Q \times KGE_Q + \sum_{j=1}^{n} w_{ET,j} \times KGE_{ET_j} + \sum_{j=1}^{n} w_{SM,j} \times KGE_{SM_j} \quad (1)$$

$$w_Q + \sum_{j=1}^{n} w_{ET,j} + \sum_{j=1}^{n} w_{SM,j} = 1 \quad (2)$$

$$w_Q = \sum_{j=1}^{n} w_{ET,j} = \sum_{j=1}^{n} w_{SM,j} \quad (3)$$

Where, subscript Q, ET, and SM indicate streamflow, evapotranspiration, and soil moisture; w_Q is the weight assigned to the objective variable of streamflow; $w_{ET,j}$

and $w_{SM,j}$ are the weights assigned to the objective variable of ET and soil moisture for subbasin j, where equal weights are assigned to each subbasin. This approach accounts for the spatial heterogeneity of ET and soil moisture in the watershed. The KGE for each variable is calculated as follows:

$$KGE = 1 - \sqrt{(r - 1)^2 - \left(\frac{\sigma_s}{\sigma_o} - 1\right)^2 - \left(\frac{\mu_s}{\mu_o} - 1\right)^2} \quad (2)$$

where r is the Pearson correlation coefficient; σ and μ are the standard deviation and mean of the variables, respectively; and the subscripts s and o indicate simulation and observation, respectively. KGE takes into account the variability, bias, and correlation between the observed and simulated values. KGE values range from −∞ to 1, with values closer to 1 indicating better model performance.

In addition, Nash–Sutcliffe efficiency (NSE) (Nash and Sutcliffe, 1970) and percent bias (PBIAS) are used to further assess the performance of streamflow and ET modeling results. The NSE and PBIAS are calculated as follows:

$$NSE = 1 - \frac{\sqrt{\sum_n^N (Q_0^n - Q_s^n)^2}}{\sqrt{\sum_n^N (Q_0^n - \overline{Q_o})^2}} \quad (3)$$

$$PBIAS = \frac{\sum_n^N (Q_0^n - Q_s^n)}{\sum_n^N Q_0^n} \times 100, \quad (4)$$

where Q_0^n and Q_s^n are the *n*th observed and simulated value, respectively; $\overline{Q_o}$ is the mean of observations; and N is the total number of time steps. The NSE represents the match between observed and simulated value. The NSE ranges from −∞ to 1, with 1 indicating perfect agreement. PBIAS represents the bias of the model. Positive values of PBIAS indicate underestimation and negative value indicate overestimation by the model. According to Moriasi et al. (2007), the model performance is considered to be satisfactory if NSE ≥ 0.5 and PBIAS is within ±25%.

3.3 Results

3.3.1 Sensitive Parameters Resulting from Different Multivariable Calibration Setups

The sensitive parameters and the calibrated values for each of the six calibration approaches are listed in Table 3.3. Sensitivity analysis reveals that eight out of the eleven parameters, in general, are important to all multivariable calibration approaches. SOL_AWC is an important soil property that determines the field capacity of the soil. A higher value of SOL_AWC increases the water-holding capacity of soil resulting in reduced surface runoff, lateral flow, and percolation. GWQMN determines the shallow aquifer discharge to the stream. Lower values of GWQMN increase the baseflow. EPCO controls plant water uptake from soil by modifying the depth distribution of uptake in the soil profile. Higher values of EPCO (when SMERGE is used) allow more of the plant water demand to be met from lower soil layers, increasing the evapotranspiration and reducing the surface runoff, groundwater recharge, and lateral flow. Overall, multivariable calibration tends to increase baseflow and reduce surface runoff, lateral flow, and percolation in SWAT, and to improve the streamflow, ET, and soil moisture simulation.

3.3.2 Impact of Multi-Variable Model Evaluation on Model Calbiration and Performance

The conventional SWAT model calibration approach that utilizes streamflow to optimize model parameters is considered here as the single-variable or benchmark calibration scenario. Figure 3.4 shows the SWAT-simulated monthly streamflow and ET for calibration and validation periods when calibrated with different combinations of streamflow, soil moisture, and ET datasets. Model calibration and validation using combinations of multiple calibration variables were also conducted, and their results are summarized in Table 3.4. In the following, we present the results from the use of different variables for model calibration.

Benchmark calibration (i.e., streamflow only) resulted in satisfactory performance of streamflow and ET for SWAT in the calibration period (Table 3.4). The PBIAS values for streamflow were within ±10% in the calibration period but deteriorated significantly to 43.3% in the validation period. This shows that model parameter adjustment for streamflow simulation during calibration did not successfully optimize the model performance for SWAT for the validation period. The NSE and KGE values for ET were > 0.8 for SWAT in calibration and validation periods. SWAT-simulated soil moisture produced KGE > 0.5 but did not meet the performance criteria for the NSE value (<0.5) in both calibration and validation periods.

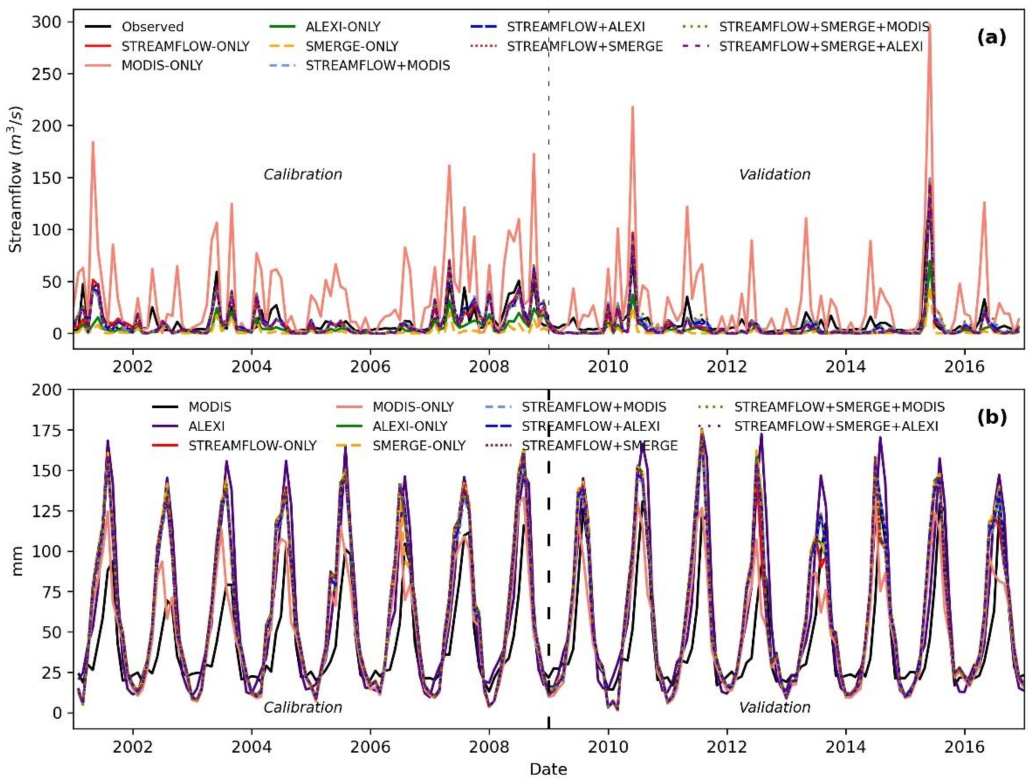

Figure 3.4. Comparison of observed and simulated monthly streamflow (**a**) and evapotranspiration (**b**) in the Little Blue River Watershed.

Table 3.4. Model calibration (Cal) and validation (Val) results for setups with different combinations of streamflow, ET, and soil moisture.

Calibration Setups	**Performance Metrics**	**NSE**		**KGE**		**PBIAS**	
		Cal	**Val**	**Cal**	**Val**	**Cal**	**Val**
Benchmark (Streamflow only)	Streamflow	0.56	0.72	0.78	0.55	4.48	43.31
	ALEXI ET	0.85	0.79	0.88	0.83	0.25	3.03
	Soil moisture	0.05	−0.28	0.69	0.65	7.02	10.96
	Average	**0.49**	**0.41**	**0.78**	**0.68**	**3.92**	**19.10**
ALEXI ET only	Streamflow	0.19	0.44	0.17	0.13	56.07	69.31
	ALEXI ET	0.86	0.81	0.88	0.85	−0.30	1.86
	Soil moisture	0.19	0.22	0.71	0.66	−3.90	−1.37
	Average	**0.41**	**0.49**	**0.59**	**0.55**	**17.29**	**23.27**
SMERGE only	Streamflow	−0.22	0.20	−0.13	−0.11	81.47	86.48
	ALEXI ET	0.85	0.81	0.89	0.86	0.21	1.34
	Soil moisture	0.44	0.37	0.74	0.73	1.71	5.12
	Average	**0.36**	**0.46**	**0.50**	**0.49**	**27.80**	**30.98**
Streamflow + ALEXI ET	Streamflow	0.53	0.75	0.77	0.63	2.82	35.52
	ALEXI ET	0.86	0.81	0.87	0.83	3.57	4.38

	Soil moisture	0.00	0.03	0.63	0.59	−6.71	−5.40
	Average	**0.46**	**0.53**	**0.76**	**0.68**	**−0.11**	**11.50**
Streamflow + SMERGE	Streamflow	0.52	0.72	0.78	0.56	5.22	42.12
	ALEXI ET	0.86	0.80	0.88	0.83	1.48	3.71
	Soil moisture	−0.01	0.12	0.69	0.66	−7.11	−4.48
	Average	**0.46**	**0.55**	**0.78**	**0.68**	**−0.14**	**13.78**
Streamflow + ALEXI ET + SMERGE	Streamflow	0.53	0.71	0.77	0.53	2.32	44.97
	ALEXI ET	0.86	0.80	0.89	0.83	0.49	3.15
	Soil moisture	0.22	0.24	0.71	0.67	−2.91	0.14
	Average	**0.54**	**0.58**	**0.79**	**0.68**	**−0.03**	**16.09**

Note: Benchmark setup represents model calibration with streamflow only. Other setups include streamflow and additional one or two calibration variables. The aggregate performance metrics are the average of the metrics for streamflow, ALEXI ET, MODIS ET, and soil moisture.

ALEXI ET-only calibration resulted in a modest improvement in ET, while the performance of soil moisture improved significantly at the expense of the performance of streamflow when compared to benchmark simulation in the calibration and validation periods. The NSE value for soil moisture increased from 0.05 to 0.19 and −0.28 to 0.22 during the calibration and validation periods, respectively. However, the model performance for streamflow deteriorated and did not meet the performance criteria for NSE (<0.5) and KGE (<0.5) values in both calibration and validation periods.

Soil moisture-only calibration significantly improved the performance of soil moisture, while the performance of streamflow worsened compared to the benchmark and ALEXI ET only setups in both calibration and validation periods. The performance of ET was similar to that obtained for benchmark simulation in the calibration period with modest improvement in the validation period.

When calibrated with streamflow and ET simultaneously, in general, the SWAT performance metrics for streamflow show negligible differences compared to the benchmark simulation for the calibration period, suggesting that streamflow simulations were not significantly affected by the consideration of the ALEXI ET dataset during calibration. It is worth noting that compared to the benchmark, including ET improved SWAT for simulating soil moisture from −0.28 to 0.03 in terms of NSE, but deteriorated KGE from 0.65 to 0.59 during the validation period. In addition, adding ET helped reduce model bias in simulating streamflow for the validation period (e.g., PBIAS decreased from 43.3% to 35.5%).

When calibrated with streamflow and soil moisture simultaneously, simulated streamflow and soil moisture also show similar results to those obtained for the benchmark simulations for SWAT. Constraining the model with soil moisture in addition to streamflow did not result in improved model performance for streamflow and soil moisture during calibration. However, during the validation period, the NSE value (i.e., 0.12) for SWAT-simulated soil moisture exhibited improvement compared to the benchmark simulation (−0.28). In addition, constraining the model with streamflow and soil moisture did not result in any noticeable improvement in ET simulation for SWAT. Adding soil moisture in the target function did not help reduce the model-simulated bias of streamflow in the validation period.

Simultaneously using streamflow, ET, and soil moisture data for model calibration did not result in significant improvement in the model performance in simulating streamflow, ET, and soil moisture. SWAT did not meet performance criteria for soil moisture in terms of NSE (<0.5) during calibration and validation. Including all three variables helped to attain the highest NSE (0.22) for soil moisture during the calibration, which translated to an NSE of 0.24 during the validation period.

Although adding ET or soil moisture as target variables can improve model performance regarding a specific variable, we found that adding additional target variables (i.e., ET and soil moisture) did not help achieve much improvement to overall model performance as indicated by the average performance metrics when compared with the benchmark simulation. However, using ET or soil moisture data only as the target calibration variable could result in a substantial decrease in model performance. For example, the ALEXI ET-only and SMERGE soil moisture-only calibration setups led to considerably lower KGE values (≤ 0.55) as compared to other calibration setups that include streamflow (≥ 0.68). This finding highlights the potential challenge in calibrating hydrologic models for ungauged basins where measured streamflow is not available.

It is also worth noting that all model setups were able to provide satisfactory model performance for both streamflow (except for ALEXI ET only and SMERGE only) and ET reasonably well (NSE > 0.5) (Table 3.4) during calibration and validation periods. However, for soil moisture simulation, none of the calibration setups resulted in satisfactory model performance (in terms of NSE). This finding could be attributed to the challenge of simulating soil moisture dynamics and the potentially large uncertainties associated with remotely sensed soil moisture products.

3.3.3 Effects of Choice of ET Products on Model-Simulated ET

In addition to ALEXI ET, the MODIS ET products have also been widely used. Figure 3.4b shows the dramatic difference between the ET estimates from ALEXI and MODIS over the LBRW; MODIS ET estimates were much lower than those of ALEXI.

Not surprisingly, the sensitive parameters and their calibrated values are considerably different when using MODSI vs. ALEXI ET. For example, the calibrated a_GWQMN values were 373.25 and −58.75 for the streamflow + MODIS and streamflow + ALEXI setups, respectively. The large difference between MODIS ET and ALEXI ET results in a substantial difference in streamflow estimates when calibrated using ALEXI ET only (Table 3.4) and MODIS ET only (Table 3.5), as seen in Figure 3.4a. SWAT failed to meet the streamflow performance criteria in terms of NSE (<0.5), KGE (<0.5), and |PBIAS| > 50% in both calibration and validation periods when calibrated with ET only. The MODIS ET-only setup considerably overestimated (PBIAS<−180%) the streamflow, while the ALEXI ET-only setup underestimated (PBIAS > 50%) the streamflow during calibration and validation periods.

Compared to the multivariable model calibration using ALEXI ET (Table 3.4), the multivariable calibration using MODIS ET achieved comparable calibration and validation results for streamflow (Table 3.5). However, the performance of SWAT in simulating ET substantially decreased when MODIS ET was used. For example, the NSE values for the multivariable calibration setups that include MODIS ET were less than 0 for the calibration period and less than 0.5 for the validation period. There were also large biases in model-simulated ET for the calibration setups with MODIS ET, with absolute PBIAS values larger than 30% in calibration and greater than 20% during validation. This result clearly shows that the choice of remotely sensed ET can have significant impacts on the calibration of SWAT. Therefore, it is critical to evaluate the quality of remotely sensed ET data before their use in model calibration. In addition, this finding highlights the importance of using multivariable calibration to constrain hydrologic model performance when the quality of a remote sensing product is unknown. The overall model performance (averaged performance metrics (Table 3.5)), in general, increased when more variables are used. For example, the average KGE values increased from −0.10, 0.61, and 0.67 for MODIS-only, Streamflow + MODIS ET, and Streamflow + MODIS ET + SMERGE setups, respectively. The multivariable approach helps minimize the impacts of errors in a single remote sensing product on the overall model performance.

Table 3.5. Model calibration (Cal) and validation (Val) results for setups with MODIS ET as a calibration variable.

Calibration Setups	**Performance Metrics**	**NSE**		**KGE**		**PBIAS**	
		Cal	**Val**	**Cal**	**Val**	**Cal**	**Val**
MODIS ET only	Streamflow	−7.60	−3.37	−1.92	−1.46	−213.13	−182.22
	MODIS ET	0.33	0.51	0.62	0.74	−14.45	−2.11
	Soil moisture	0.05	−0.11	0.52	0.43	5.11	6.05
	Average	**−2.41**	**−0.99**	**−0.26**	**−0.10**	**−74.16**	**−59.43**
Streamflow + MODIS ET	Streamflow	0.52	0.75	0.77	0.71	2.39	25.96
	MODIS ET	−0.16	0.38	0.30	0.60	−37.20	−24.08
	Soil moisture	0.05	−0.10	0.58	0.52	5.77	6.91
	Average	**0.14**	**0.34**	**0.55**	**0.61**	**−9.68**	**2.93**
Streamflow + MODIS ET + SMERGE	Streamflow	0.49	0.73	0.75	0.78	3.51	15.97
	MODIS ET	−0.13	0.41	0.30	0.62	−35.46	−22.09
	Soil moisture	−0.05	0.00	0.68	0.62	−7.67	−6.49
	Average	**0.10**	**0.38**	**0.58**	**0.67**	**−13.21**	**−4.20**

3.3.4 Variations in Hydrologic Pathways under Different Calibration Schemes

The seasonal values of key hydrologic pathways at the watershed level (Figure 3.5) were analyzed to evaluate the overall impact of multivariable calibration on the SWAT simulations. Although the performance metrics of SWAT-simulated streamflow are similar for the multivariable calibration setups (Tables 4 and 5), the results clearly show that the difference in calibration setup meaningfully affected the surface runoff, percolation, lateral flow, and groundwater discharge. The simulated surface runoff among different multivariable calibration setups shows little variance, whereas single variable calibration setups show considerable variability. Spatial distribution of surface runoff for different calibration setups is shown in Figure 6. Surface runoff, in general, is low in the western and southern region and high over the north-central portion of the watershed.

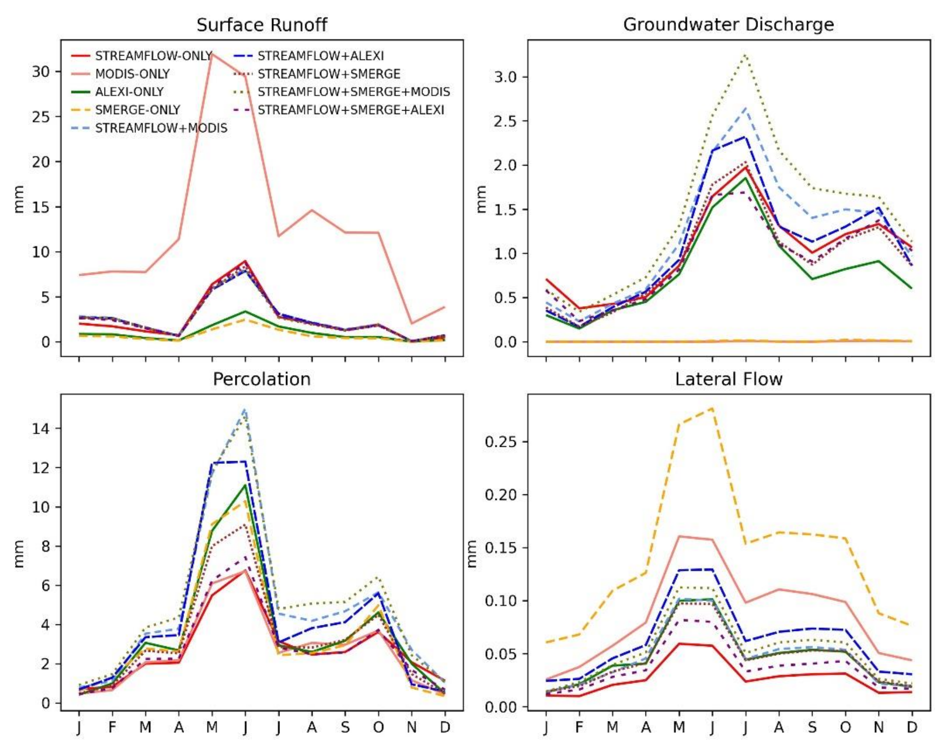

Figure 3.5. SWAT-simulated watershed scale surface runoff, groundwater discharge, percolation, and lateral flow.

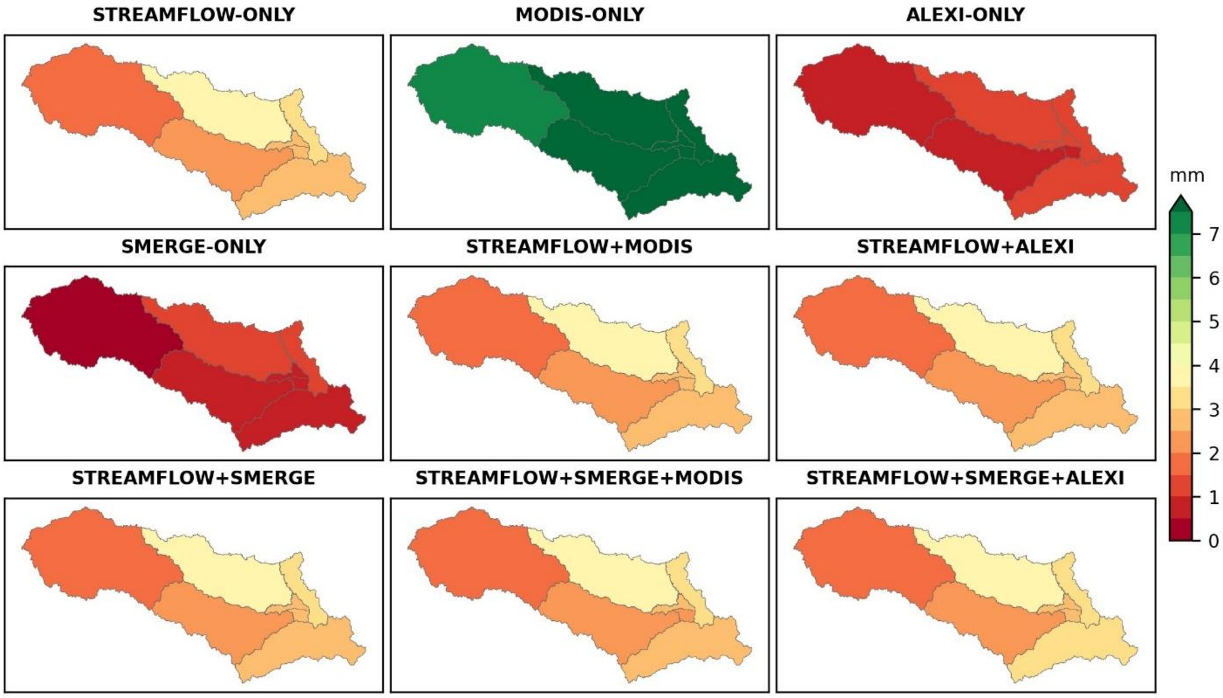

Figure 3.6. Spatial distribution of SWAT-simulated subbasin level mean monthly surface runoff under different calibration setups.

The monthly distribution of SWAT-simulated percolation/groundwater discharge is spread out with varying magnitude. In general, the downstream subbasins are the main contributors to the groundwater discharge, as shown in Figure 3.7. The SMERGE-only and the MODIS-only setup stands out among the calibration setups as the simulated groundwater discharge to streams is negligible throughout the year. Both MODIS-only and SMERGE-only setups have high GW_REVAP values, i.e., 0.163 and 0.143, respectively, compared to other calibration setups (Table 3.3). The GW_REVAP controls the water movement from the shallow aquifer to overlying unsaturated soil layers. The high value of GW_REVAP reduces the water level in the shallow aquifer resulting in a corresponding decrease in groundwater discharge. In addition, the MODIS-only setup simulated considerably higher surface runoff and lateral flow. On the other hand, the SMERGE-only setup simulated much lower surface runoff and high lateral flow with increased water holding capacity of soil layers (Table 3.3). This results in negligible/no groundwater discharge in the MODIS only and SMERGE only setups.

Among the multivariable calibration setups, the streamflow + ALEXI + SMERGE simulated the lowest percolation and groundwater discharge, while the streamflow + MODIS estimated the highest. In addition, the simulated lateral flow, although of negligible magnitude compared with surface runoff and groundwater discharge, showed variation by a factor of two. These differences in simulated hydrologic pathways can have implications for assessing water management effects on groundwater resources in arid and semi-arid regions.

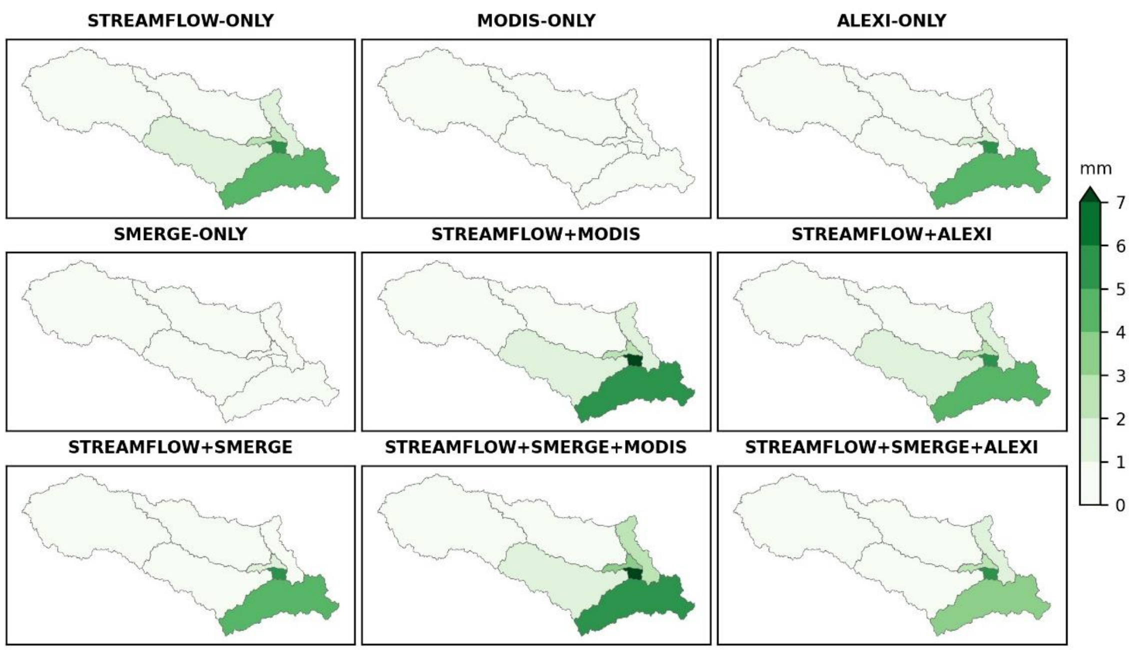

Figure 3.7. Spatial distribution of SWAT-simulated subbasin level mean monthly groundwater discharge under different calibration setups.

3.3.5 Influence of Model Structure on Multivariate Model Calibration

We also calibrated the SWAT-C model for the benchmark and three multivariate calibration scenarios (Table 3.6). In general, the overall performance of

SWAT-C, as indicated by the averaged performance metrics, is comparable to that of SWAT for the calibration period (Table 3.4). For example, the averaged KGE values for SWAT-C range between 0.79 and 0.80 for the calibration periods, which are close to the corresponding range of 0.76–0.79 for SWAT. However, there are substantial differences in terms of the validation results. For the validation period, the averaged KGE values, ranging between 0.77–0.78, are generally consistent with the calibration results for SWAT-C; in comparison, the averaged KGE values for SWAT decreased to 0.68 for the benchmark and three multivariate calibration setups. Furthermore, the averaged PBIAS values for SWAT-C were within ±10% for both calibration and validation periods under the four calibration setups (Table 3.6). In contrast, SWAT attained larger average PBIAS values, particularly for the validation period, ranging from 11–19% (Table 3.4).

Table 3.6. Model calibration (Cal) and validation (Val) results for SWAT-C under setups with different combinations of streamflow, ET, and soil moisture.

Calibration Setups	**Performance Metrics**	**NSE**		**KGE**		**PBIAS**	
		Cal	**Val**	**Cal**	**Val**	**Cal**	**Val**
Benchmark (Streamflow only)	Streamflow	0.63	0.72	0.80	0.79	−2.02	18.59
	ALEXI ET	0.84	0.81	0.87	0.83	1.86	7.13
	Soil moisture	0.08	0.11	0.71	0.73	0.41	0.82
	Average	**0.52**	**0.55**	**0.79**	**0.78**	**0.08**	**8.85**
Streamflow + ALEXI ET	Streamflow	0.64	0.71	0.81	0.76	5.45	17.68
	ALEXI ET	0.84	0.81	0.88	0.83	2.28	7.39
	Soil moisture	0.08	0.11	0.71	0.72	−0.43	−0.22
	Average	**0.52**	**0.54**	**0.80**	**0.77**	**2.43**	**8.28**
Streamflow + SMERGE	Streamflow	0.62	0.69	0.80	0.77	7.59	5.49
	ALEXI ET	0.86	0.82	0.87	0.84	2.61	7.61
	Soil moisture	−0.03	−0.05	0.73	0.71	6.25	6.20
	Average	**0.48**	**0.49**	**0.80**	**0.77**	**5.48**	**6.43**
Streamflow + ALEXI ET + SMERGE	Streamflow	0.63	0.69	0.80	0.77	8.31	5.48
	ALEXI ET	0.85	0.82	0.87	0.84	2.74	7.63
	Soil moisture	−0.04	−0.05	0.73	0.72	6.26	6.27
	Average	**0.48**	**0.49**	**0.80**	**0.78**	**5.77**	**6.46**

The performance of SWAT and SWAT-C also differed substantially from each other for individual target variables. For the benchmark calibration, PBIAS values for streamflow were within ±10% in the calibration period but deteriorated to 43.3% for SWAT and to 18.6% for SWAT-C in the validation period. For the three multivariate calibration setups, SWAT-C also achieved much smaller PBIAS as compared with SWAT for streamflow in the validation period (35–45% for SWAT vs. 5–18% for SWAT-C). Despite the large difference between SWAT and SWAT-C in simulating streamflow, their performances in simulating ALEXI ET and soil moisture were similar (Tables 3 and 5). Both models achieved high correlation and small bias in simulating ALEXI ET but performed poorly in simulating soil moisture.

In addition, we also found that, like SWAT, adding additional target variables did not much improve the performance of SWAT-C as compared to the benchmark calibration that only used streamflow. For example, the average KGE values for SWAT-C ranged between 0.77–0.78 for the validation period under the four calibration setups.

3.4 Discussion

The use of different combinations of target calibration variables can have pronounced impacts on the sensitive parameters. Although eight out of the eleven parameters (Table 3.3) are commonly sensitive parameters for different calibration setups, there are noticeable differences between the number and values of sensitive parameters. In general, the calibration setups that included streamflow achieved comparable overall model performance (Table 3.4), indicating that the calibrated parameter sets were equally good for representing hydrologic processes in the LBRW.

Such equifinality in calibrated parameter sets has been broadly discussed in the previous literature (Beven and Freer, 2001). Even though the use of remotely sensed ET and soil moisture helps constrain the model parameters, further information regarding their validity for simulating hydrologic processes, such as runoff, percolation, and groundwater discharge (Figure 3.5), is required to identify robust models. Without data to evaluate the calibrated SWAT models, the calibrated parameter sets can be used to derive ensemble estimation of the hydrologic processes of interest.

When streamflow is not included in a calibration setup (e.g., ALEXI ET only and SMERGE soil moisture only), the model calibration resulted in poorer model performance compared to those calibration setups with streamflow considered as a target variable (Table 3.4). This finding shows that using streamflow for hydrologic model calibration is critical. The quality of remotely sensed ET and soil moisture products deserve further examination and improvement to ensure robust model calibration, particularly for ungauged basins.

When multiple remotely sensed products are available, it is critical to evaluate their quality and choose the one that is best suited for model calibration. In our study, we noticed a substantial difference between ALEXI ET and MODIS ET over the LBRW, though both of them have been widely used in hydrologic model calibration. Specifically, we found that the MODIS ET values were substantially lower than ALEXI ET. This is consistent with the findings reported by Zhang et al. (B. Zhang et al., 2020) and Miralles et al., (Miralles et al., 2016), where the MODIS algorithm was found to systematically underestimate ET in semi-arid regions, while ALEXI tended to overestimate ET in semi-arid region.

The use of MODIS ET for multivariate model calibration substantially decreased the model performance compared to using ALEXI ET (Tables 3 and 5). In particular, when MODIS ET was the only target variable, streamflow was overestimated by ca. 200%, which is much higher than the ca. 60% overestimation for the ALEXI ET-only calibration setup. This is likely because MODIS ET underestimated ET and led to more runoff generation (Figure 3.5). Previous studies showed that MODIS ET could be subject to a relative error of 25% at the global scale (Faisol et al., 2020), with potentially even greater errors at the regional scale. These findings highlight the importance of assessing the quality of remotely sensed products before including them in model calibration. When data quality information is not available, it is recommended to use multiple target variables to calibrate hydrologic models to minimize the potential negative impacts of errors in one target variable on the overall performance of the model. As shown in Table 3.5, the use of streamflow and SMERGE soil moisture could help achieve better model calibration results than using MODIS ET only.

Notably, the SWAT model could not satisfactorily capture the magnitude and dynamics of soil moisture derived from SMERGE products. There are two possible reasons. First, the SWAT model's bucket-based soil moisture simulation algorithm has been shown to slightly underperform compared to physically based soil water routing approaches (Qi et al., 2018). Further improvements to the SWAT soil moisture algorithms to increase its performance hold promise. Second, the quality of the

SMERGE soil moisture products may not warrant its direct use for calibrating hydrologic models. The previous assessment showed a noticeable discrepancy between SMERGE and other remote sensing-based soil moisture products and field observations (Tobin et al., 2019). In addition, it is worth noting that the ET and soil moisture products are derived from remote sensing observations and models. Taking those remote sensing products as observations risks assuming model outputs as ground truth.

The use of different ET datasets in multivariable calibration substantially altered the model hydrologic responses (surface runoff, percolation, lateral flow, and groundwater discharge) (Figure 3.5). These uncertainties might be reduced by using the blended ET dataset obtained from the data fusion of multiple remotely sensed ET products that compensate for their deficiencies (Sun et al., 2017), instead of using a single ET product. Finally, model calibration results are dependent on the structure of the model. The multivariate calibration results using SWAT-C shared multiple findings with SWAT, such as the use of remotely sensed ET and soil moisture products. These data do not provide much improvement compared with using streamflow only, and result in poor performance for simulating soil moisture. However, multivariate calibration of SWAT-C also showed different results, particularly in terms of the model performance in the validation period. In general, SWAT-C performance was comparable to SWAT during the calibration period, but much better in the validation period as indicated by the much smaller bias in simulated streamflow. This result shows that the use of multiple target variables in model calibration helps constrain model performance regarding multiple hydrologic processes, but it could not address uncertainties from the model structure. Therefore, multiple structures of the SWAT model or even multiple models should be examined or combined to achieve robust hydrologic modeling.

The findings of this study share both similarities and differences with other studies that showed improvements in model calibration using remote sensing ET products, such as those conducted by Lee et al. (Lee et al., 2022, 2021). They found that using ET products improved the model performance for ET, whereas we did not find substantial differences in model performance when including ET products in model calibration. The assessment studies by Lee et al. (Lee et al., 2022, 2021) were concentrated on the energy-limited watershed situated in the eastern United States. In contrast, our research focuses on a water-limited watershed, which poses different challenges due to varying climate, land cover, soil properties, and management practices. Therefore, multivariable calibration with ET may not necessarily improve model performance for watersheds with varying characteristics. Despite these differences, our research shares some common findings, such as that calibration with remotely sensed data alone resulted in the degradation of model performance for streamflow.

3.5 Conclusions

The use of measured variables in addition to streamflow is critical for robust hydrologic model calibration. In this study, we evaluated the impact of using different combinations of remotely sensed datasets in the multivariable calibration of SWAT for simulating streamflow, ET, and soil moisture. We found that using remotely sensed data in conjunction with streamflow for model calibration may not necessarily improve the simulation of streamflow, ET, and soil moisture. For example, the use of MODIS ET products can cause deterioration in model performance compared to the benchmark calibration scheme (i.e., streamflow only), while the use of ALEXI ET helps to achieve comparable or even better model performance.

It is worth noting that SWAT can capture well the variability in ET and streamflow but generally fails to reproduce the dynamics of soil moisture derived from the SMERGE dataset. This could be explained by two reasons: (1) the SWAT model's soil moisture algorithms have been widely discussed as an oversimplified bucket model and cannot adequately represent soil moisture dynamics; and (2) the SMERGE dataset was derived by combining remote sensing-observed surface soil moisture and model simulations, which may be subject to large uncertainties and is not suitable for direct use in model calibration.

Overall, the choice of using remote sensing-based hydrologic variables for model calibration can have substantial influence on model-simulated hydrologic processes, such as surface runoff and groundwater discharge. Although this study showed the potential of using remote sensing-based hydrologic variables to improve the calibration of SWAT for robust representation of hydrologic processes, careful assessment of the quality of the remote sensing datasets is critical for ensuring reliable model performance. The relatively poor performance of SWAT in simulating soil moisture points to the need for future efforts to identify better strategies to improve the use of remotely sensed soil moisture datasets for calibrating hydrologic models. In addition, the difference in model structure can impact the performance of multivariate model calibration, indicating the need for careful model structure assessment to ensure robust model calibration for hydrologic modeling.

Chapter 4: Water quantity and quality implications of land use change-induced climate feedbacks in the U.S. Northern High Plains

4.1 Introduction

Land use change and climate variability can substantially affect the hydrological processes (IPCC, 2022; Scanlon et al., 2007). Land use change can alter land-atmosphere interactions through biophysical processes such as differences in leaf area index (LAI), albedo, and evapotranspiration. The extent and nature of these changes depend on a combination of factors, including crop type, land and water management practices, and the extent of land use change (Duveiller et al., 2020).

Future climate change mitigation scenarios often include large-scale bioenergy crop production over cropland and marginal land as a promising alternative to fossil fuels (Creutzig et al., 2015). For example, scenarios of converting cropland (e.g., corn, maize, soybean, sorghum) or marginal land (e.g., grassland) or a combination of both to bioenergy crops have been extensively studied (Dolan et al., 2020b; Gelfand et al., 2013b; He et al., 2022; Qin et al., 2012). Depending on the choice of bioenergy feedstocks, type of land use expansion or conversion, management practices (e.g., use of tillage, fertilizer, and irrigation), and climatic conditions, those studies showed that such a conversion could provide environmental benefits such as reduced surface runoff and soil erosion, improved water quality, and increased soil organic carbon. On the other hand, converting cropland marginal land to bioenergy crops could lead to a reduction in downstream water availability through increased evapotranspiration and reduced groundwater recharge (Gheewala et al., 2011; Guo et al., 2018b; Schilling et al., 2008b; Wu et al., 2012b). Therefore, concerns have been raised about the environmental impacts of large-scale land use change for bioenergy crop production, particularly under a warming climate (Gelfand et al., 2013b; He et al., 2022; Liebig et al., 2008; McLaughlin and Walsh, 1998; Schmer et al., 2011). From a water quality perspective, Song et al. (2016) found that bioenergy crop cultivation reduces nitrogen leaching relative to row crops and herbaceous plants when grown without applying N fertilizer. They also reported the varied response of soil water content depending on the location and land use change for bioenergy crop production.

Most of the earlier studies are mainly focused on examining the local effect of bioenergy production on watershed processes. It is worth noting that regional precipitation and temperature could be pronouncedly altered due to biophysical feedback of growing bioenergy crops on a large scale (He et al., 2022). The use of marginal lands for bioenergy crop production could reduce albedo, increase evapotranspiration, and reduce temperature locally, which could also have a rippling effect on the region. For instance, He et al. (2022) found that large-scale production of miscanthus primarily in the eastern US increased precipitation by up to 15% during the growing season in the U.S. Midwest. Such climate feedback could provide benefits in vegetation growth, including improved biomass production from the reduced temperature and water stress on crops, especially in these water-limited regions. Similarly, a recent global-scale study by Li et al. (2023) also showed the non-local impact of bioenergy related land use change, such as precipitation increases in arid and semi-arid regions. They found that the increased precipitation and reduced runoff from bioenergy crop production offset the enhanced evapotranspiration and limit the impact on soil water content. However, increased precipitation and reduced temperature could also lead to an increase in surface runoff and streamflow resulting in reduced water quality (Prathumratana et al., 2008). In general, far less is known about the hydrologic response to large-scale bioenergy crop production and the accompanying climate feedback in the warming climate.

This study aims to evaluate the hydrological responses to the conversion of cropland and marginal land to bioenergy crops by considering both local land use change and the feedback of large scale bioenergy crop production to the local climate in the Northern High Plains in the U.S. Because of complex climate-land-vegetation-water system interactions, and the teleconnected nature of climate feedback from large-scale bioenergy crop production, hydrological models are needed to assess the system-level watershed response to climate-crop feedback scenarios that consider both climate drivers and crop and water management. We applied the Climate-Weather Research and Forecasting (CWRF) to simulate future climate scenarios with and without considering the feedback of bioenergy crops to the local and regional climate in the eastern U.S. Next, we used the Soil and Water Assessment Tool (SWAT) (Arnold et al., 1998) model to quantify the differences between hydrological processes under the climate scenarios and assess the role of the feedbacks of bioenergy crops to the climate in influencing hydrological processes in the Northern High Plains. Specifically, we evaluate (1) crop yield, (2) watershed scale water budget components (surface runoff, evapotranspiration, soil moisture, and groundwater recharge, and (3) streamflow and instream total nitrogen under diverse climate scenarios Our research helps demonstrate the importance of considering biophysical feedbacks of large scale bioenergy production to local climate and subsequent implications for water quantity and quality at the watershed scale. These results are anticipated to expand the knowledge base regarding the sustainability of bioenergy production, thereby supporting future science-informed bioenergy policies and watershed protection planning.

4.2 Materials and Methods

4.2.1 Study area

This study is focused on the Northern High Plains (NHP) (Figure 4.1) aquifer region that spans Nebraska, Colorado, Kansas, Wyoming, and North Dakota in the U.S. Midwest (Peterson et al., 2016). The NHP comprises multiple watersheds with a total area of about 347,058 km^2. The region is dominated by convective storms in summer (April–September) with a strong east–west gradient, decreasing from 900 mm in the east to 350 mm in the west. This period overlaps with the crop-growing season in this region (Scanlon et al., 2012). The dominant land cover in the NHP consists of range and pasture land (57.72%), followed by agriculture (33.47%), urban (3.38%), forest (3.01%), wetlands (1.42%), and water and barren land (1%). The NHP region undergoes intensive agricultural practices, including large-scale irrigation and the use of fertilizers and pesticides. The NHP is recognized as a major contributor of nitrogen which contributes about 25–50% of instream total nitrogen transported to the Gulf of Mexico (Alexander et al., 2008). Hence, future land use and climate change are of considerable socio-economic concern in this region.

4.2.2 Climate data and Climate-crop feedback scenarios

In this study, we used climate data from a set of climate-crop feedback scenarios developed using the Climate-Weather Research and Forecasting (CWRF) model (Liang et al., 2012). The climate-crop feedback scenarios were simulated using the CWRF model, driven by two Global Climate Model (GCM) participating in the Coupled Model Intercomparison Project Phase 6 (CMIP6) (Eyring et al., 2016) under the historical forcing (1969-2014) and future high greenhouse gas emission scenario (2015-2060): Shared Socioeconomic Pathway (SSP) 5-Representative Concentration Pathway (RCP) 8.5 (SSP585). We used an aggressive emission scenario of SSP585 to help understand the upper limits of hydrological responses to climate-crop feedback and land use change. Because of the large uncertainty in the future climate projections by GCMs, substantial variations may arise in the representation of climate-crop feedback processes, which could either amplify or attenuate the hydrological processes. We used two CMIP6 models: Max Planck Institute Earth System Model (MPI-ESM1.2) and Community Earth System Model (CESM), representing the two extremes of the equilibrium climate sensitivity (ECS). The ECS represents the global mean temperature response to a doubling of atmospheric CO_2 concentration among the GCMs (IPCC, 2014). Within the CMIP6 models, MPI-ESM1.2 has an ECS of about 3°C (Mauritsen et al., 2019), among the low sensitivity models. The CESM has an ECS of about 5.3 °C (Danabasoglu et al., 2020) and is categorized as a high sensitivity model.

4.2.2.1 CWRF model overview

CWRF is a regional climate model with the full functionality of the Weather Research and Forecasting (WRF) model and a large repository of physics schemes

(Liang et al., 2012). CWRF can realistically simulate observed precipitation and temperature patterns for CONUS (Liang et al., 2012). CWRF utilizes the Conjunctive Surface-Subsurface Process (CSSP) to realistically simulate land-atmosphere interactions and terrestrial hydrological processes (Choi et al., 2013, 2007; Dai et al., 2004, 2003; Gan et al., 2015; Ji et al., 2017; Liang et al., 2012, 2005; Xu et al., 2014; Yuan and Liang, 2011). It incorporates vertical and lateral water movement, including surface flow routing for the prediction of streamflow (Choi et al., 2013). CWRF has incorporated an ensemble cumulus parameterization based on Grell and Dvénéyi (2002) with major improvements detailed in Qiao and Liang (2017, 2016, 2015). The ensemble cumulus parameterization has demonstrated reliable performance over the ocean (Qiao and Liang, 2016), land (Qiao and Liang, 2017), and in other climate regimes (Jiang et al., 2021; Li et al., 2021; Liang et al., 2019), as well as for extreme precipitation (Qiao and Liang, 2015; Sun and Liang, 2020). Bioenergy crop production is simulated by the crop growth model (BioCro) (Miguez et al., 2012), and maize production is simulated by the DSSAT model (Jones et al., 2003). These models were coupled with the CWRF model to simulate the land, crop, and climate interactions. The details of CWRF simulations for climate feedback scenarios can be obtained from Chao et al. (2023) (in preparation). This study conducted historical simulations from October 1, 1969, to January 1, 2014, as well as future simulations from October 1, 2015, to January 1, 2061, spanning a 45-year period. The research focused on a North American 30-kilometer grid, which includes the entire contiguous United States, as previously documented by Liang et al. in 2012. For both historical and future runs, all CWRF simulations were driven by lateral boundary conditions derived from the two latest CMIP6 models: MPI-ESM1.2 and CESM model, to gauge the model uncertainties.

4.2.2.2 Scenarios

To understand how the representation of vegetation coverage and its corresponding climate-crop feedback affects the regional climate and subsequently the hydrological processes, we used CWRF to simulate two scenarios for each GCM: one control run where feedback from vegetation growth is not considered, and one sensitivity scenario with the climate-crop feedback due to maize, miscanthus, and energycane (miscan_ecane_mz) cultivated in the U.S. for the present condition and projected future scenario under SSP585. The control run serves as the reference for assessing changes in hydrological processes resulting from regional climate changes due to climate-crop feedback and land use change. These changes in regional climate, as a response to climate-crop feedback, arise from complex interactions between the atmosphere and land surface processes, which are partially determined by the extent of vegetation coverage and its phenology.

To further investigate the impact of the extent of vegetation coverage, specifically maize, miscanthus, and energycane, and their phenology on regional climate resulting from differences in climate-crop feedback, we utilized three additional scenarios that include climate-crop feedback from various combination of vegetations: (a) maize only (mz), (c) miscanthus only (miscan), and (c) miscanthus and maize (miscan_mz). In total, we simulated 10 scenarios, combining 5 climate-crop feedback scenarios from two GCMs, as listed in Table B.1. Since the CWRF simulations can not incorporate the detailed crop and water management practices that substantially impact agro-hydrological processes in the NHP, we used SWAT model to understand the influence of changes in regional climate, due to climate-crop feedback, on the hydrological processes in the NHP. We used daily outputs of precipitation and maximum and minimum temperature from each scenario as climate input for the SWAT model.

4.2.3 SWAT model setup

We used a previously established SWAT modeling tool for NHP (Dangol et al., 2022), which divides the NHP into 277 subbasins (Figure 4.1a). A 90 m digital elevation model (DEM) from the Shuttle Radar Topographic Map was used for watershed configuration delineation. A land use map was created by combing the Cropland Data Layer (CDL) for 2007 with the 2008 MODIS irrigation map being used to differentiate irrigated and rainfed crop land. The State Soil Geographic (STATSGO) soil map provides soil properties, such as texture (i.e., sand, silt, and clay), hydraulic conductivity, and soil organic matter. By overlaying the land use and soil maps, we derived a total of 51,323 hydrologic response units (HRUs), which are the homogenous areas formed by the unique combinations of land use, soil type, and slope which each subbasin. Crop and water management practices such as fertilizer application and irrigation sources (surface water and groundwater) were also included. The detailed model setup information can be obtained from Dangol et al. (2022).

In the unmanaged grassland ecosystem, the atmospheric deposition of nitrogen tends to increase biomass production in nitrogen-limited watersheds (Fernández-Martínez et al., 2017; Sullivan and Gao, 2016). Hence, the wet and dry atmospheric deposition rates reported by the National Atmospheric Deposition Program (NADP)

(NADP, 2022) were used as a source of nitrogen input. The historical daily weather data from 1997 to 2015 were obtained from the North American Regional Reanalysis (NARR) dataset (Mesinger et al., 2006b), including precipitation, maximum air temperature, minimum air temperature, relative humidity, wind speed, and incoming solar radiation. The SWAT is run using NARR for model calibration and validation.

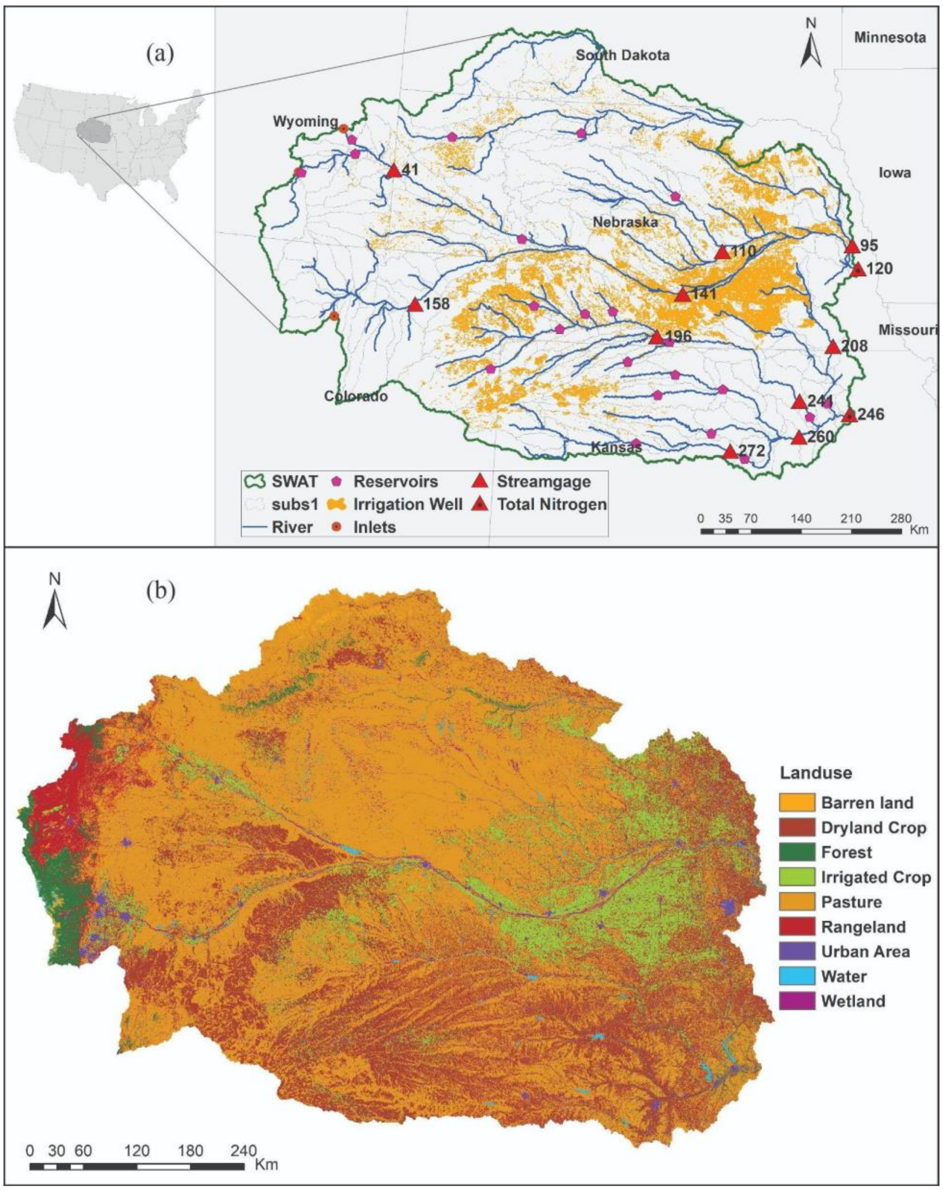

Figure 4.1. Study area with (a) SWAT domain and (b) land use information.

4.2.4 Model calibration and evaluation

The calibration of the SWAT model for large watersheds is computationally expensive (Chun et al., 2018; Feng et al., 2018). To reduce the computational cost for model calibration, a regionalization approach was implemented for the calibration of streamflow and instream total nitrogen. SWAT model calibration was done in two parts following the approach described in previous studies (Dangol et al., 2023; Feng et al., 2018). First, a coarser SWAT model was developed using the thresholds of 5% for land cover and 10% for soil class during HRU delineation, resulting in 5,129 HRUs. The threshold approach was used to remove minor land uses and soil types in each sub-basin to reduce the computation cost without significantly deteriorating model performance.

The fractional potential heat units for planting and harvest dates for corn and soybean were adjusted to match the planting and harvest dates documented by USDA (USDA-NASS, 2010). The coarse SWAT was calibrated for monthly streamflow at multiple outlets as shown in Figure 4.1. The streamflow in upstream subbasins was calibrated at first followed by downstream subbasins. The model parameters were selected based on the existing literature and sensitivity analysis (Table B.2). We used the Sequential Uncertainty Fitting algorithm version 2 (SUFI-2) procedure in SWAT Calibration and Uncertainty Programs (SWAT-CUP) for sensitivity analysis and calibration (Abbaspour et al., 2015). Using global sensitivity in SUFI-2, the most sensitive parameters to streamflow (p-value < 0.1) were selected (Table B.3). The Kling–Gupta Efficiency criterion (KGE) (Gupta et al., 2009) is used as the objective function to calibrate the SWAT from 2001 to 2007. The KGE is calculated as,

$$KGE = 1 - \sqrt{(r-1)^2 - \left(\frac{\sigma_s}{\sigma_o} - 1\right)^2 - \left(\frac{\mu_s}{\mu_o} - 1\right)^2} \qquad (1)$$

Where, r is the Pearson correlation coefficient, and are the standard deviation and mean of the variables respectively, and the subscripts r and o indicate the simulation and observation respectively. The KGE value ranges from -∞ to 1, with values closer to 1 indicating good model performance.

After streamflow calibration, the model parameters (Table B.4) sensitive to monthly instream total nitrogen were identified and calibrated following the same procedure as discussed above for streamflow. The most sensitive parameters for instream total nitrogen are listed in Table B.5. The model was calibrated for total instream nitrogen at the two outlets of the Republican (Subbasin 246) and Platte River (Subbasin 120) basins simultaneously. In the final step, the model parameters optimized for the coarse model are transferred to the fine-resolution model (HRUs generated without soil, land use, and slope threshold). This regionalization approach assumes that the model parameters remain unchanged between the coarse and fine models. This method is computationally inexpensive and widely used to adjust model parameters of large watersheds (Daggupati et al., 2016; Feng et al., 2018). We then validated the model performance for monthly streamflow and instream total nitrogen for the period of 2008-2015. In addition, we also evaluated the model performance using other metrics, including Nash-Sutcliffe efficiency (NSE) (Nash and Sutcliffe, 1970), coefficient of determination (R^2), and percent bias (PBIAS).

The outlets where the model was calibrated for streamflow and instream total nitrogen are shown in Figure 4.1. Daily streamflow data were obtained from the United States Geological Survey (USGS) (https://waterdata.usgs.gov/nwis/sw). Daily instream total nitrogen data for the outlets were obtained from the SPARROW dataset (Saad et al., 2011). Generally, water quality data is measured a few times in a month. Hence, monthly instream total nitrogen was estimated using LOADEST (Runkel et al., 2004) based on daily data from the SPARROW dataset, which is widely used in the hydrological community.

4.2.5 Marginal landuse allocation

Pastureland, rangeland, and barren land are the major marginal land use categories in this study. SWAT simulates the terrestrial hydrological and biogeochemical processes at the HRU scale. The fractional area, calculated as the ratio of the HRU area to the corresponding subbasin area, is assigned to each HRU in the model. The fractional area determines the contribution of the HRU (i.e. specific land use and soil type) to the watershed. We used USDA STATSGO soil classification to identify low-productivity land, which is considered here as marginal land for bioenergy crop production. The procedure used to identify marginal land from pasture, rangeland, and barren land is described below:

1. The fraction of marginal land available in each subbasin is calculated from the CWRF gridded land use map (Figure B.1), which was based on (Cai et al., 2011).
2. For each subbasin, the least productive HRUs among pasture, rangeland, and barren land are identified from the soil productivity index (SPI) for each soil class by Schaetzl et al. (2012). The HRUs with SPI>=11 are classified as productive land, and their land use classification remains unchanged. These

HRUs with the largest slope among the least productive soil are selected as marginal lands. The total fractional area of selected HRUs may not exactly match the marginal land fraction of the subbasin. Therefore we selected HRUs such that the total fractional area does not exceed ±5% of the fraction of marginal land allocated to that subbasin.

3. The selected HRUs are then used for bioenergy crop production.

We identified 11.2% of the NHP land cover as marginal lands based on the marginal land classification scheme described above. Figure B.2 shows the distribution of marginal lands in the NHP. In general, marginal land areas are concentrated in the Republican River basin.

The plant growth parameters for simulating miscanthus production are adopted from the study by Cibin et al., (2016). These optimized miscanthus growth parameters have been shown to provide a reasonable estimate of biomass yield and LAI (Trybula et al., 2015). Note that we did not apply irrigation to Miscanthus. Following the crop management practices for Miscanthus in the Great Lakes Bioenergy Research Center (GLBRC) farm sites (Martinez-Feria and Basso, 2020), 56 kg N ha^{-1} of nitrogen fertilizer is applied once each year in the early growing season. Miscanthus is harvested annually in mid-October, except for the first three years, which are taken as the establishment period. The validated SWAT is run for 82 years from 1979 to 2060. The changes in crop and biomass yields, water balance components, streamflow, and total instream nitrogen in the NHP are evaluated against the control run. We used 1985-2014 as the present and 2031-2060 as the future conditions. This helps understand the overall impact of bioenergy-driven land use change and climate-crop feedback on the hydrological processes in the NHP.

4.3 Results

4.3.1 Model calibration and evaluation

4.3.1.1 Streamflow

Table B.3 shows the calibrated parameter values for streamflow at ten locations in the NHP. The simulated and measured monthly streamflow generally match well during both calibration and validation period as shown in Figure B.3. In general, SWAT performs satisfactorily at all calibration stations (with KGE >0.3 during calibration and validation), except for subbasin 110 (KGE <0 during both calibration and validation) (Figure B.3). Overall, the KGE values are greater than 0.50, indicating that SWAT can reasonably simulate streamflow at multiple stations within the NHP. During calibration, the model performance is good with a KGE of 0.62 and 0.79, NSE of 0.24 and 0.58, PBIAS of 6.84 and 2.29%, and R^2 of 0.53 and 0.66, at the outlets of Platte (Subasin 120) and Republican (Subbasin 246) river basins, respectively (Figure 4.2). During validation, the model performance remains good, with a KGE of 0.68 and 0.61, NSE of 0.62 and 0.51, PBIAS of 21.58% and 26.55%, and R^2 of 0.72 and 0.59 at Subbasin 120 and 246, respectively. In the validation period, SWAT tends to underestimate the streamflow, likely due to the model's tendency to simulate reduced low flow in groundwater dominated watersheds such as the NHP (Dangol et al., 2022).

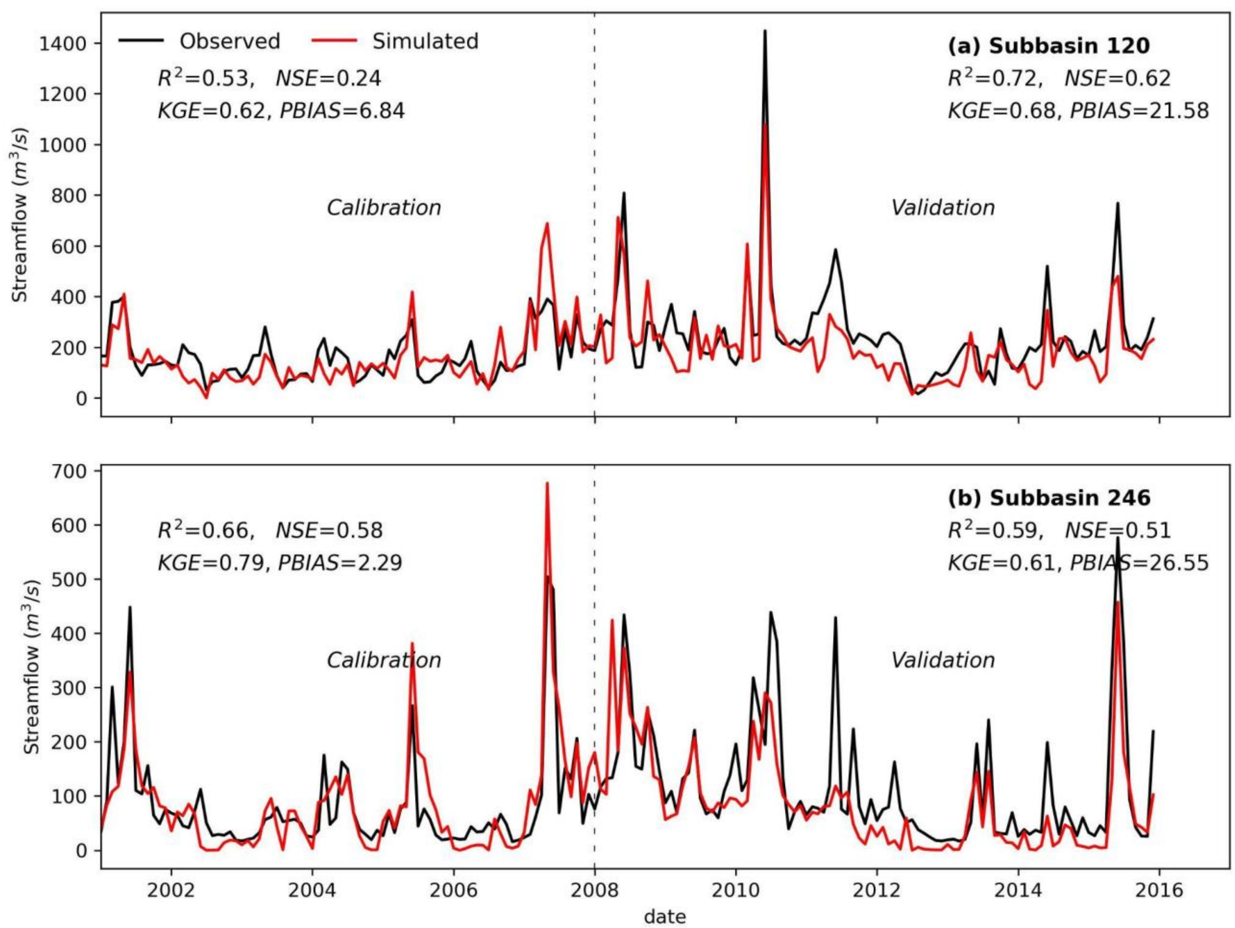

Figure 4.2. Comparison of observed and simulated streamflow during calibration and validation at the outlet of (a) Platte and (b) Republican river basin.

4.3.1.2 Instream total nitrogen

We also calibrate the model for monthly instream total nitrogen at the outlets of the Platte and Republican River basins. The calibrated parameter values for total nitrogen at two locations are listed in Table B.5. Figure 4.3 shows the model performance for monthly instream total nitrogen during calibration and validation. Overall, SWAT captures the dynamics of total nitrogen with R^2 of 0.19 and 0.56 during calibration, and R^2 of 0.79 and 0.31 during validation at the outlets of the Platte and Republican River basins, respectively. SWAT achieves KGE>0.40 and PBIAS < ±25% during both calibration and validation at the two outlets. In general, the model can reasonably estimate monthly instream total nitrogen. Notably, the model has mixed performance in terms of NSE during calibration and validation. This highlights the inherent difficulties in simulating accurate values of instream total nitrogen due to uncertainties in crop and water management practices, such as timing and frequency of fertilizer and irrigation application.

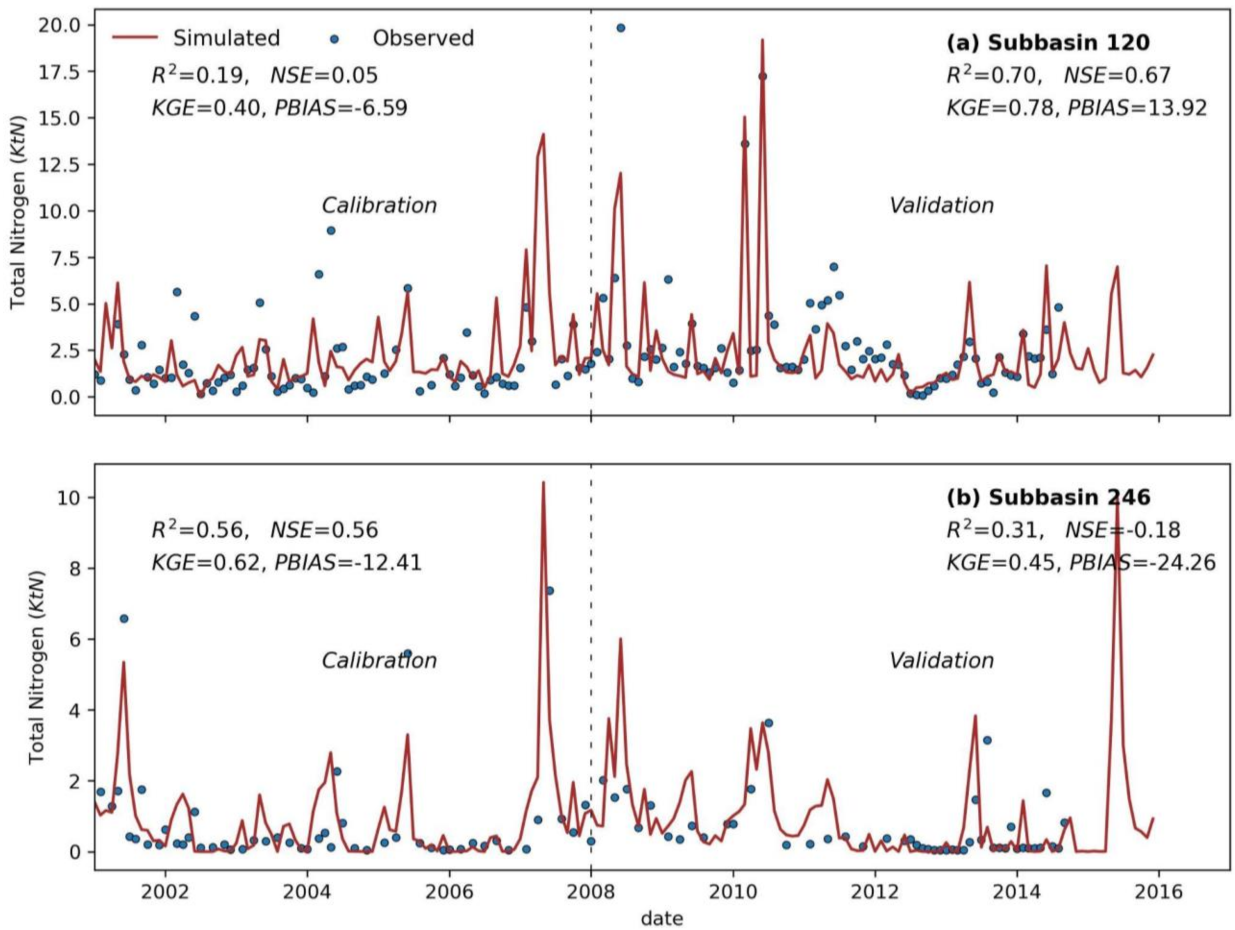

Figure 4.3. Comparison of observed and simulated instream total nitrogen during calibration and validation at the outlet of (a) Platte and (b) Republican river basin.

4.3.2 Changes in precipitation and temperature

Figure 4.4 shows the monthly precipitation and temperature changes for the 'miscan_ecane_mz' scenario in the present condition and future scenario under SSP585. In general, there is a consistent precipitation increase, with a peak increase in

July in both the present and future conditions. Precipitation further increases in the future compared to the present condition. On average, precipitation increases modestly by 2% and 6% in the present and future conditions, respectively, during summer. The seasonal patterns of the changes in monthly temperature are similar in both the present and future conditions (Figure 4.4b). There is a substantial decrease in average temperature from late spring to late fall months, with the peak decrease occurring in August. The temperature decrease is more pronounced in the future condition compared to the present condition. On average the temperature decreases by 0.27 and 0.30 °C in the present and future conditions, respectively. This is consistent with the results reported by He et al. (2022), which found a temperature decrease of about 0.5–1.0 °C in the U.S. Midwest because of the cooling effect from higher evapotranspiration and albedo resulting from the cultivation of bioenergy crops on marginal lands. While our results fall in a lower range compared to their findings, these differences can be attributed to the difference in the driving forces of the climate model.

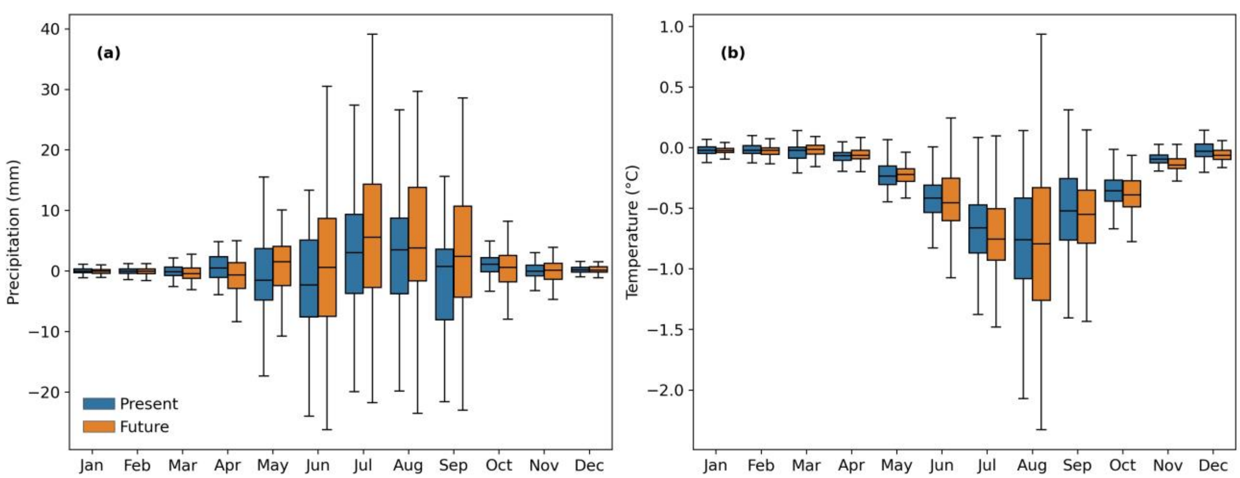

Figure 4.4. Seasonal changes in monthly (a) precipitation and (b) average temperature for miscan_ecane_mz scenario relative to control run in the present condition and future scenario under SSP585. Here miscan_ecane_mz represent the CWRF climate data with climate-crop feedbacks from miscanthus, energycane, and maize. The control run does not consider climate-crop feedbacks.

4.3.3 Impacts on water balance components

4.3.3.1 Impacts on HRU scale

Figure 4.5 shows the seasonal hydrological impacts for the HRUs where miscanthus is cultivated. In the early growing season, the early emergence of miscanthus and high LAI reduce surface runoff and increase ET (Figures 4.5a-b), as reported in previous studies (Cibin et al., 2016; Holder et al., 2019; Vanloocke et al., 2010). On average, annual surface runoff decreases by 24.6%, while ET increases by 4.7% in the present condition. Interestingly, ET decreases in late fall when precipitation shows negligible change (Figure 4.4a), which can be attributed to the substantial decline in soil water content during summer months (Figure 4.5c). The canopy shading effect, which shades the soil column below the leaves, also contributes partially to the reduction of ET (Hickman et al., 2010; Vanloocke et al., 2010) during this period. Soil moisture content decreases throughout the year by 12.2% annually, subsequently reducing percolation by 15.6% in the present condition (Figure 4.5d). Notably, surface runoff increases in future condition because of the precipitation increase from climate-crop feedback. In future condition, despite the increased cooling effect from climate-crop feedback (Figure 4.4b), the warmer temperature further increases ET by 12.6% (Figure 4.5b). The increase in ET results in a substantially reduction in soil moisture content and percolation by 39.5 and 47.2%, respectively.

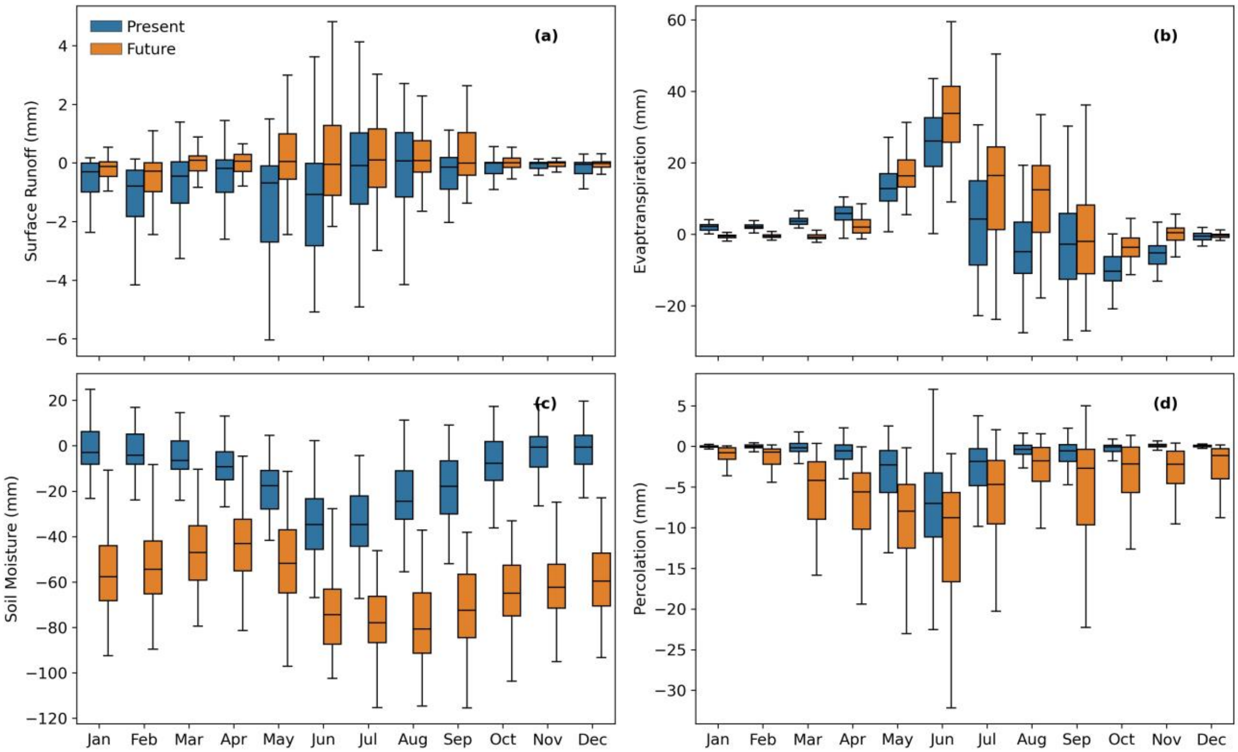

Figure 4.5. Seasonal changes in (a) surface runoff, (b) evapotranspiration, (c) soil moisture, and (d) percolation in HRUs used for miscanthus cultivation for miscan_ecane_mz climate-crop feedback scenario in the present condition and future scenario under SSP585.

4.3.3.2 Impacts on watershed scale

The impact on surface runoff, evapotranspiration, soil moisture, and percolation shows similar seasonal patterns in the present and future conditions (Figure 4.6). In general, surface runoff increases by 4% and 13% during the growing season in response to increased precipitation in the present and future conditions, respectively. ET increases modestly by 0.7% and 3% in both present and future conditions during the growing season. Although, temperature decreases during the growing season, high water demand by miscanthus subsequently increases ET and reduces soil moisture content. Soil moisture decreases modestly by 0.7% in the present condition and further declines by 3.7% in the future condition. On average, percolation (groundwater recharge) does not change much in the present condition (ca 0.1%) during the growing season but increases by 2.7% in the future condition. Furthermore, we found that the hydrological responses vary between the Republican and Platte River basins. For example, ET increases during early summer, and soil moisture content substantially reduces in the Republican river basin compared to the Platte river basin (Figure B.4). This difference arises due to the differences in the extent of marginal land conversion for miscanthus cultivation between the Platte (4%) and Republican (20%) river basins.

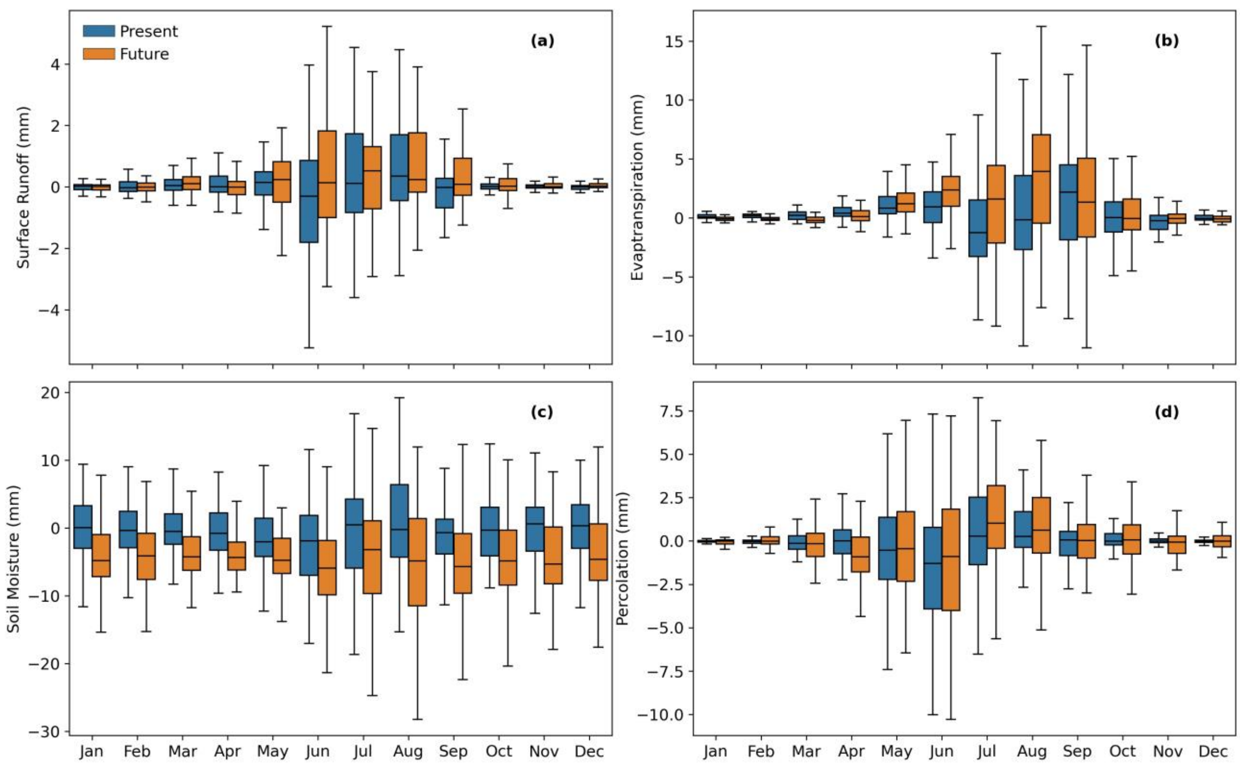

Figure 4.6. Seasonal changes in a) surface runoff, (b) evapotranspiration, (c) soil moisture, and (d) percolation at watershed level in response to miscan_ecane_mz climate-crop feedback scenario in the present condition and future scenario under SSP585.

4.3.4 Impacts on streamflow and water quality

Precipitation increase generally enhances streamflow and nitrogen loading in rivers (Hoque et al., 2014; Nangia et al., 2010). In our study area, increased precipitation leads to higher streamflow and nitrogen loading in the Platte and Republican river basins (Figure 4.7). However, the seasonal pattern of these changes differs between the two river basins under present and future conditions.

In the Platte river basin, streamflow increases during the growing season, aligning with the seasonal pattern of increased precipitation. However, in the Republican river basin, streamflow increases from June to November because of reduced surface runoff in early summer and increased water yield in mid-fall. Notably, streamflow in the Platter river basin increased from 2% under present condition to 13% under future condition during the growing season. In the Republican river basin, the streamflow increase of 22% (June to November) under the present condition reduces to 15% under future condition. Also, streamflow decreases during late winter and spring in the Republican river basin under future condition due to substantially low soil moisture content (Figure 4.5c) resulting in reduced subsurface flow.

The increased streamflow, caused by increased surface runoff and groundwater discharge, leads to higher nitrogen loading. The seasonal patterns of nitrogen loading are similar to those of streamflow in both river basins. In the Platte river basin, despite a small relative change in streamflow during late winter and spring under the present condition, nitrogen loading increases substantially (Figure 4.7c). This increase can be attributed to the rise in surface runoff, leading to an increase in nitrogen loading. In contrast, the negligible change in nitrogen loading under future condition can be attributed to reduced soil moisture content and subsurface flow. In the Republican river basin, large scale miscanthus cultivation reduces nitrogen uptake from the soil, resulting in higher soil nitrogen content and subsequently higher nitrogen loading compared to the Platter river basin. The increase in nitrogen loading in the late fall is due to increased groundwater discharge resulting from miscanthus harvest operations.

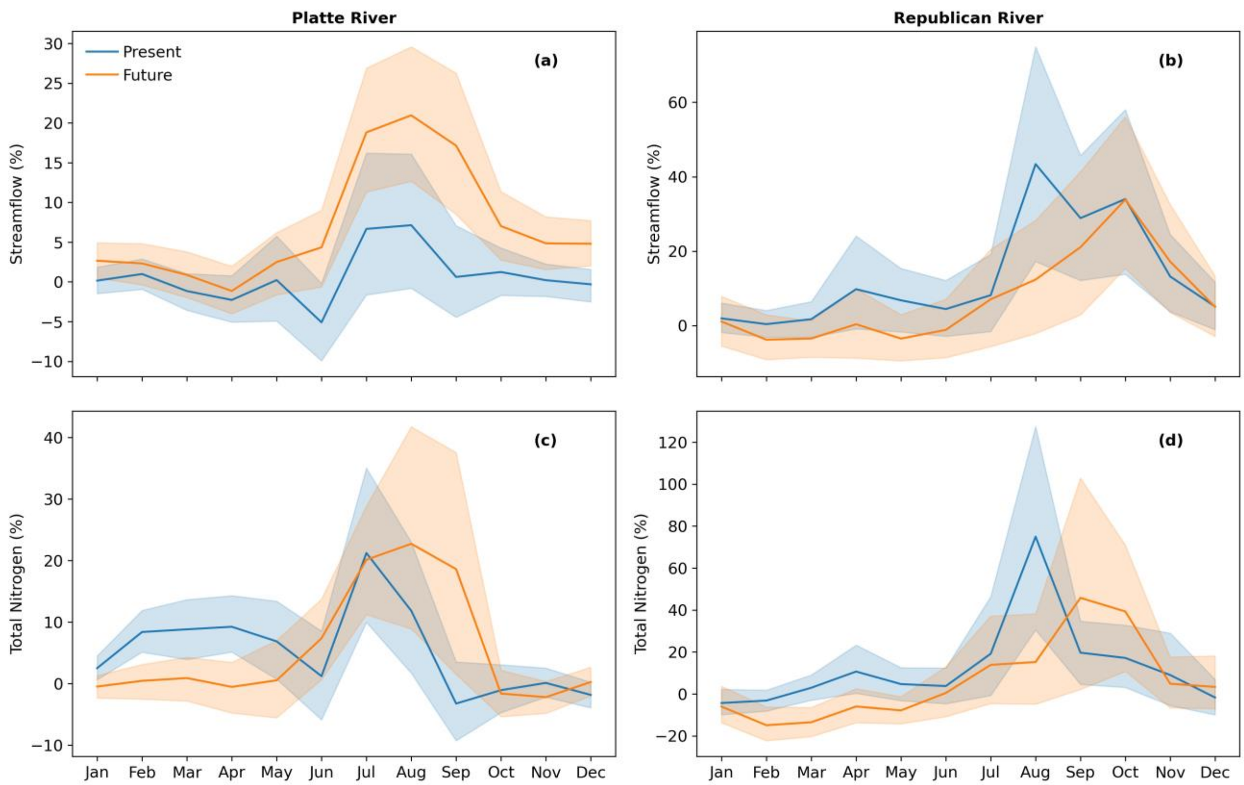

Figure 4.7. Seasonal changes in (a-b) streamflow and (c-d) instream total nitrogen at the outlet of the Platte and Republican River basins during the present condition and future scenario under SSP585. The shading represents the 95% confidence interval.

4.3.5 Response to climate-crop feedback scenarios

4.3.5.1 Precipitation and temperature

Figure 4.8 shows substantial variability in annual precipitation under different climate-crop feedback scenarios. Among these scenarios, 'miscan_ecane_mz' exhibits the largest increase in summer precipitation by 2% and 6% in the present condition and future scenario under SSP585, respectively (Table B.1). In general, there is a consistent regional increase in precipitation for both present and future conditions when the climate-crop feedback from bioenergy crop production is included. In contrast, the 'mz' scenario results in a modest precipitation decrease of less than 1% in the present and future conditions.

The seasonal patterns of mean temperature changes are similar across the climate-crop feedback scenarios in both present and future conditions (Figure 4.8). The temperature decrease is more pronounced in the future condition compared to the present condition across all scenarios. Among the scenarios, 'mz' exhibits negligible temperature changes (Figure 4.8b and Table B.1). On the other hand, 'miscan_eacne_mz' scenario shows the largest temperature decrease, followed by 'miscan_ecane' and 'miscan' in the present and future conditions, respectively. Overall, the feedback strength increases with the addition of feedback from energycane and maize, followed by energycane with miscanthus (Figure 4.8b and Table B.1).

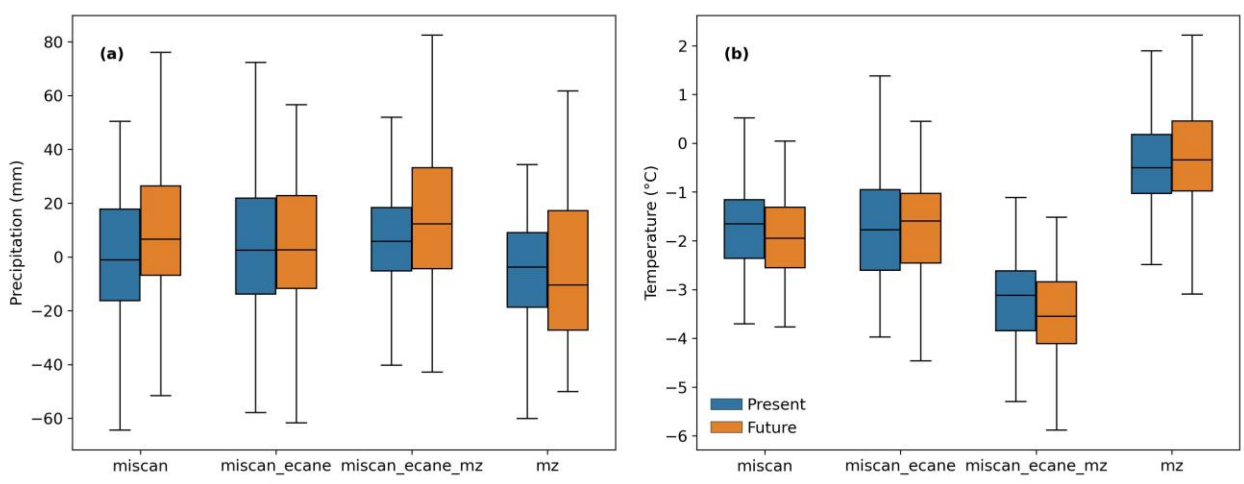

Figure 4.8. Comparison of changes in annual (a) total precipitation and (b) average temperature across the climate-crop feedback scenarios in the present condition and future scenario under SSP585.

4.3.5.2 Water budget components

The relative changes in annual surface runoff, evapotranspiration, soil moisture, and percolation at the watershed scale show consistent patterns in both present and future conditions across the climate-crop feedback scenarios (Figure 4.9). Surface runoff decreases modestly for ‘mz’, ‘miscan’, and ‘miscan_ecane’ scenarios by <3% in the present condition. In contrast, the ‘miscan_ecane_mz’ scenario results in a modest increase of 1.8%. In the future condition, surface runoff increases for all scenarios, ranging from 0.5% to 7.6%. The changes in ET remain negligible (within ±1%) across all scenarios in the present condition. However, scenarios involving climate-crop feedback from the bioenergy crops show a modest increase in ET (<2%) in the future condition. The decline in soil moisture content reduces when climate-crop feedback from energycane and maize is introduced in combination with miscanthus (Figure 4.9c). Among the scenarios incorporating feedback from bioenergy crops, ‘miscan’ exhibits the largest decrease in soil moisture content, while ‘miscan_ecane_mz’ exhibits the smallest decrease in both present and future conditions. A similar pattern is found for percolation across the feedback scenarios. These results show that the changes in water budget components, resulting from the changes in precipitation and temperature, are highly sensitive to plant phenology within the context of climate-crop feedback scenarios.

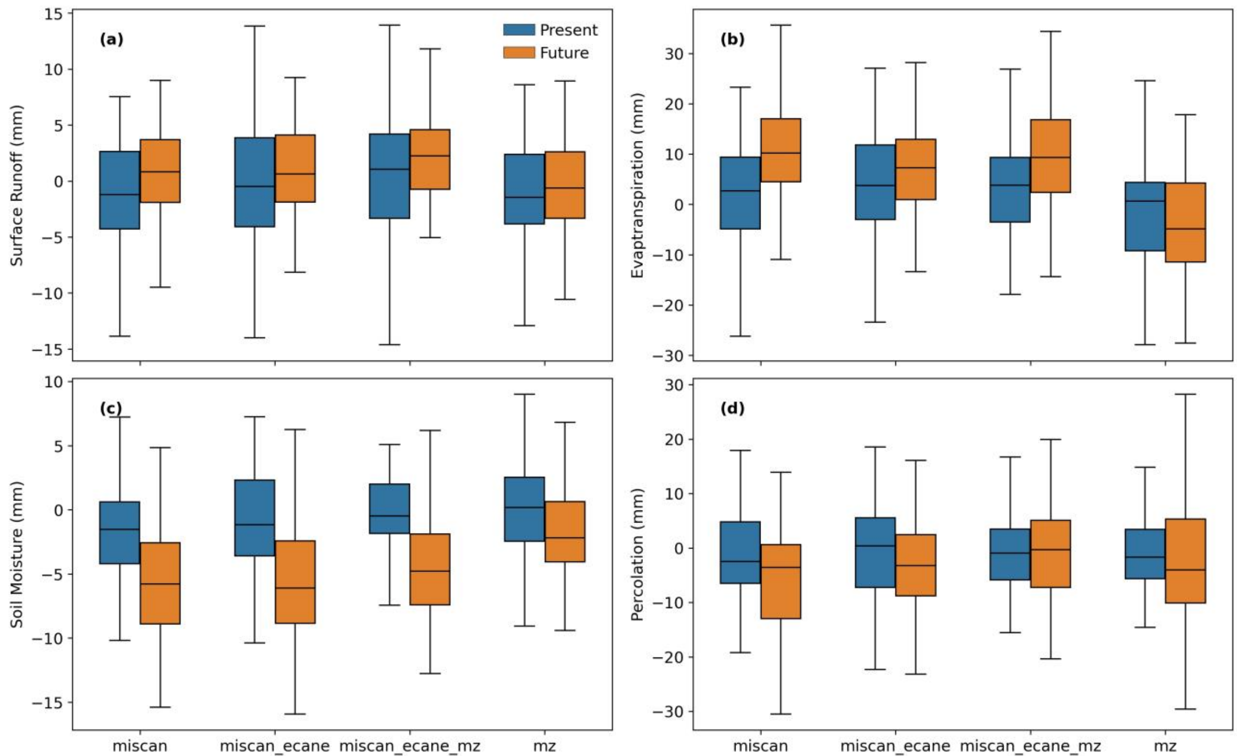

Figure 4.9. Comparison of changes in annual (a) surface runoff, (b) evapotranspiration, (c) soil moisture, and (d) percolation at watershed scale in response to the climate-crop feedback scenarios in present condition and future scenario under SSP585.

4.3.5.3 Streamflow and instream total nitrogen

The changes in annual average streamflow and instream total nitrogen in the Platte river basin show similar trends with varying magnitude across climate-crop feedback scenarios (Figures 4.10a and 4.10c). In contrast, the response of the Republican river basin displays a mixed response depending on the climate-crop feedback scenarios (Figures 4.10b and 4.10d). In the Platte river basin, both streamflow and nitrogen loading increase in the future condition compared to the present condition across all scenarios. The Republican river basin exhibits a similar response for the 'mz' scenario only. Meanwhile, the remaining three scenarios show a decline in streamflow and nitrogen loading in the future condition compared to the present condition. The reduced annual average streamflow and nitrogen loading in the Republican river basin can be explained by a decline in subsurface flow resulting from decreased soil moisture and percolation in the future condition compared to the present condition. Among the four climate-crop feedback scenarios, 'miscan_ecane_mz' simulates the largest increase in streamflow and nitrogen loading in the Platte river basin by 5.5% and 2.3%, respectively, in the future condition. Meanwhile, 'miscan_ecane_mz' simulates negligible changes in streamflow and an 8.6% decrease in nitrogen loading in the Republican river basin during this period.

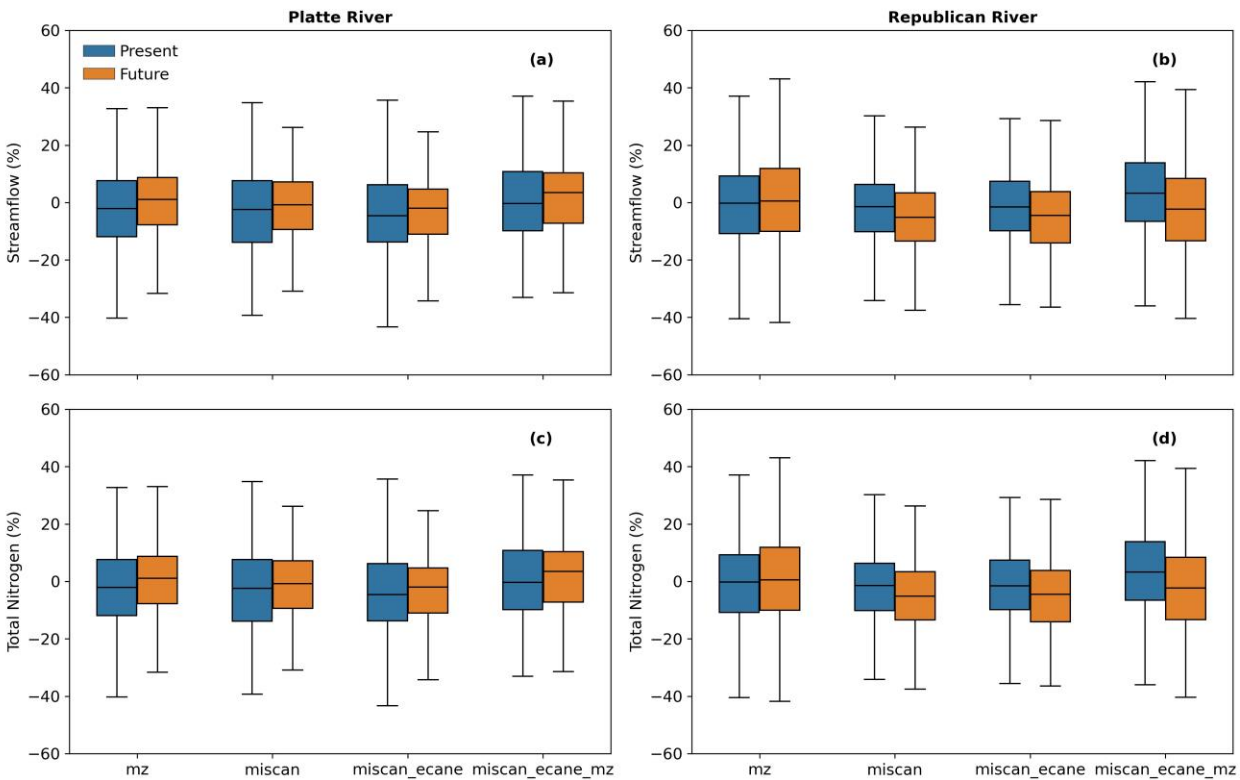

Figure 4.10. Comparison of changes in annual (a-b) streamflow and (c-d) instream total nitrogen at the outlet of the Platte and Republican River basins in response to the climate-crop feedback scenarios in present condition and future scenario under SSP585.

4.3.6 Impacts on crop yield

We also examined how precipitation and temperature changes and subsequent differences in water budget components affect crop yields. We assess the effects of climate-crop feedback on maize and soybean yields by using percentage changes relative to the control scenario. In all climate-crop feedback scenarios, reduced temperature and increased precipitation during the growing season improve maize and soybean yields in both present and future conditions (Figure 4.11). Under the present condition, the greatest increase in maize and soybean yields occurred in the scenario of 'miscan_ecane_mz', followed by 'miscan_ecane'. This yield increase corresponds well in magnitude with the temperature decrease in both scenarios. On average, maize and soybean yields increase by 0.9% to 3.5% and 1.6% to 6.1%, respectively, under the present condition. Similarly, in the future condition, maize and soybean yields increase, with the largest increase in 'miscan_ecane_mz'. On average, maize and soybean yields increase by 0.2% to 4.5% and 1.2% to 11.0%, respectively.

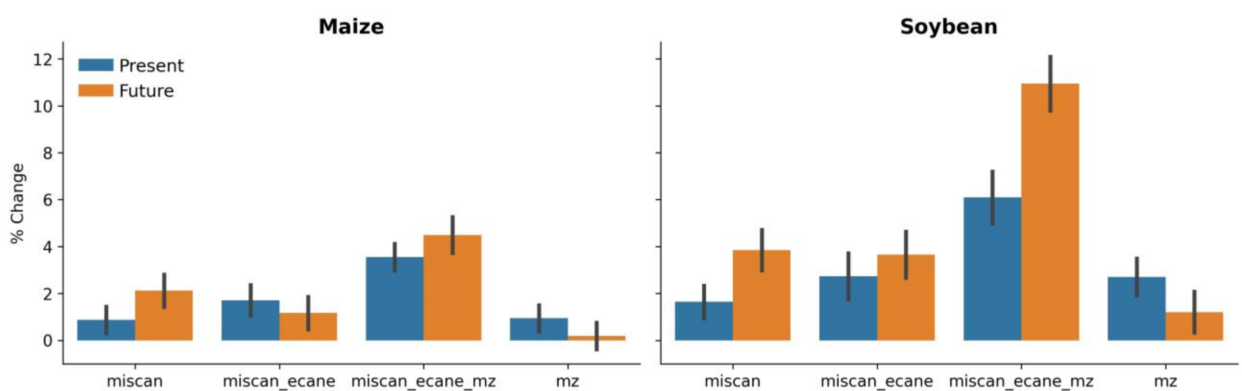

Figure 4.11. Comparison of changes in corn and soybean yield across the climate feedback scenarios. The error bar represents the standard error.

4.4 Discussion

Our results show that miscanthus cultivation on marginal land increases ET and reduces surface runoff, soil moisture, and percolation, despite cooler and wetter conditions in the NHP due to climate-crop feedback. These results are consistent with earlier studies (Feng et al., 2015; McIsaac et al., 2010; T. L. Ng et al., 2010; Schilling et al., 2008b), which have shown that miscanthus, with deep rooting system and large LAI, has higher ET leading to reduced soil water content and percolation. On a watershed scale, the cooler and wetter conditions in the NHP substantially increase surface runoff, modestly increase ET, and reduce soil moisture content. The study by Vanloocke et al. (2010) also indicated minimal impacts on ET from land use change of <10% for miscanthus production in the U.S. Midwest. However, they assumed a uniform distribution of miscanthus over the Midwest and neglected the influence of crop-atmosphere interaction on regional climate. In contrast, our study concentrated miscanthus production in the Republican river basin and considered the climate-crop feedback. The land use change of 11.2% in the NHP for miscanthus production is close to the threshold of 10% used by Vanloocke et al. (2010), and the results for ET are also consistent.

Precipitation increase from climate-crop feedback enhances streamflow and nitrogen loading in the Platte and Republican river basins. Our results differ from similar studies assessing the impact of land use change scenarios that do not account for changes in precipitation and temperature from climate-crop feedback. For example, a study by Vanloocke et al. (2017) found that a 15% conversion of maize for miscanthus production decreases streamflow by 3–6% in the Upper Missouri river basin and reduces nitrogen loading by 5–15%. However, in our study area, miscanthus cultivation on a large scale in the Republican river basin reduces surface runoff and soil moisture content, subsequently reducing streamflow and nitrogen loading from late winter to early summer months. Moreover, differences in the extent of land use change from marginal land to miscanthus between the Platte and Republican river basins resulted in substantially different seasonal patterns of streamflow and nitrogen loading. These results highlight the importance of accounting for precipitation and temperature changes from climate-crop feedback, which can substantially influence the impact of land use change.

In an intensively irrigated agricultural watershed such as the NHP, changes in precipitation, temperature, and water budget components can impact agricultural productivity (Lu et al., 2020). Overall, cooler and wetter conditions during the growing season reduce temperature and water stress on crops, resulting in improved crop yields. Both maize and soybean yields improved in the present and future conditions. Similar results were also reported by Brown et al. (2000) and Lobell and Asner (2003).

The analysis of various climate-crop feedback scenarios impact on climate and watershed hydrological processes shows consistent results, indicating increased precipitation and reduced temperature during the growing season in the present and future conditions. However, this study accounts for the climate-crop feedback from maize, miscanthus, and energycane only and does not account for feedback from other vegetation, such as a forest. Changes in precipitation and temperature and their impact on hydrology and water quality could be different with the inclusion of additional feedback from other vegetation. Likewise, the findings of this study are specific to the NHP and may be different for other regions.

4.5 Conclusion

In this study, we used SWAT to simulate how precipitation and temperature changes due to climate-crop feedback from large-scale cultivation of bioenergy crops in U.S. marginal land affect terrestrial hydrology, water quality, and crop productivity in the NHP watershed. We also examined the seasonal patterns of streamflow and nitrogen loading in the Platte and Republican river basins within the NHP to show how different land use scenarios affect basin responses to these changes. Moreover, we conducted a sensitivity analysis to assess the impacts of different combinations of climate-crop feedback among cultivating three crops (miscanthus, energycane, and maize) under the present and future conditions simulated by two GCMs.

Cultivating miscanthus on marginal land provides local benefits, such as reduced surface runoff to prevent soil erosion, but also increases local ET to reduce soil moisture and percolation. However, at the basin scale, increased precipitation during the growing season leads to a substantial increase in surface runoff. The ET increase at the HRU level due to miscanthus cultivation is offset by cooler temperatures from climate-crop feedback across the NHP, leading to a modest ET increase at the basin scale. Under the land use scenario involving miscanthus, energycane, and maize (miscan_ecane_mz), alongside a temperature decrease of 0.27°C, a 2% increase in precipitation leads to a 4% increase in surface runoff and a 0.7% increase in ET at the watershed level, compared to the control scenario in the present condition. In future condition, climate-crop feedback further decreases temperature by 0.3 °C and increases precipitation by 6%, increasing surface runoff and ET by 13% and 3%, respectively. The precipitation increase contributes to higher streamflow and nitrogen loading in the NHP. However, the extent of marginal land use for miscanthus cultivation results in different seasonal patterns of streamflow and nitrogen loading between the Platte and Republican river basins. The Republican river basin, with a larger fraction of land use for miscanthus cultivation, exhibits increased streamflow and nitrogen loading from mid-summer to mid-fall, while the Platter river basin exhibits increased streamflow and nitrogen loading during the summer. Interestingly, in the future condition, large scale miscanthus cultivation in the Republican river basin reduces annual nitrogen loading by 8.6%, while it increases by 2.3% in the Platter river basin.

The sensitivity analysis with different combinations of climate-crop feedback of maize, miscanthus, and energycane shows results similar to those obtained from the miscan_ecane_mz. Among the scenarios involving climate-crop feedback from the bioenergy crops, the feedback strength increases with the addition of feedback from energycane and maize, followed by energycane with miscanthus. Meanwhile, maize only scenario exhibits negligible changes in hydrological processes and nitrogen loading in rivers. Notably, we found that the cooler and wetter conditions in the NHP generally improve maize and soybean yields. We expect that the results from this study will help policy-makers consider the effects of climate-crop feedback in a comprehensive assessment of climate policies involving land use change for bioenergy crop production.

[3]

Chapter 5: Advancing the SWAT model to simulate perennial bioenergy crops: A case study on switchgrass growth

Materials presented in this chapter has been published in the journal Environmental Modelling and Software as Dangol et al. (2023)

5.1 Introduction

The transition from fossil fuel to carbon-neutral or carbon-negative energy sources, such as bioenergy, has been incentivized through policies such as the Renewable Fuel Standard (RFS) established by the U.S. Energy Independence and Security Act (EISA) 2007 (Schnepf and Yacobucci, 2013; U.S. EPA, 2022). The wide use of grain crops for bioenergy production in the U.S. has raised serious concerns regarding the competition between food and fuel and detrimental environmental impacts (Lark et al., 2022; Searchinger et al., 2008; Zhang et al., 2010). Perennial grasses have been recognized as a potential resource to fulfill future EISA mandated cellulosic biofuel production, minimize conflicts with food production, reduce negative impacts on the environment, and mitigate regional climate change (Gelfand et al., 2013b; LeDuc et al., 2017; National Research Council, 2009). In addition to bioenergy production, perennial grasses like switchgrass and miscanthus can serve as a means to sequestrate carbon (Clifton-Brown et al., 2007; Qin et al., 2012). The extensive root biomass and absence of tillage promote carbon sequestration in soil (Agostini et al.,

---

Dangol, S., Zhang, X., Liang, X.-Z., & Blanc-Betes, E. (2023). Advancing the SWAT model to simulate perennial bioenergy crops: A case study on switchgrass growth. Environmental Modelling & Software, 105834. https://doi.org/10.1016/j.envsoft.2023.105834.

2015; Anderson-Teixeira et al., 2009; Rasse et al., 2005). Although field experiments offer valuable insights to understand and quantify the environmental impacts of biofuel feedstock production, scaling up the results to regional, national, or global scales, requires modeling approaches. Therefore various models have been developed and applied to represent the vegetation growth processes of perennial grasses like switchgrass, miscanthus, and energycane (Cibin et al., 2016; Gopalakrishnan et al., 2012; He et al., 2022; Kiniry et al., 2008; Lee et al., 2012; Miguez et al., 2012). Existing models such as Daily CENTURY (DAYCENT), Soil and Water Assessment Tool (SWAT), DeNitrification-DeComposition (DNDC), Environmental Policy Integrated Climate (EPIC), Decision Support System for Agrotechnology Transfer (DSSAT), Agricultural Land Management Alternatives with Numerical Assessment Criteria (ALMANAC), and BioCro have been tested and applied to estimate productivity and environmental consequences associated with cultivation of perennial grasses (Cibin et al., 2016; Davis et al., 2010; Kantola et al., 2022; Lee et al., 2012; Nocentini et al., 2015; Proulx et al., 2022; Sharara et al., 2020; Sinistore et al., 2015; Trybula et al., 2015). Given that most of those models operate at the field and regional scales, SWAT stands out with its unique capabilities to provide a thorough evaluation of the impacts on water budget and water quality at the watershed scale. However, the poor representation of the perennial crops limits its ability to reproduce biogeochemical processes, with potential implications on estimates of evapotranspiration fluxes, runoff, and discharge.

The SWAT plant growth sub-model and parameters have been extensively tested for food/feed crops like corn, soybean, wheat, barley, etc. (Gassman et al., 2010;

Luo et al., 2008; Zhang et al., 2013b), while few studies (Cibin et al., 2016; Nelson et al., 2006; T. L. Ng et al., 2010; Trybula et al., 2015) have evaluated its suitability to simulate perennial bioenergy crops. Switchgrass shows great potential as a bioenergy crop with relatively high productivity and different cultivars already available in the market for optimum allocation across climatic zones (Clifton-Brown et al., 2019; Larnaudie et al., 2022; Mehmood et al., 2017). Nonetheless, despite previous attempts, the lack of explicit representation of shoot and root growth is a major drawback of the SWAT (Zhang et al., 2011a). Field observations have shown that root growth, in general, is influenced by temperature, moisture, and nutrient availability and exhibits large sensitivities to climatic conditions (Sainju et al., 2017).

In earlier studies involving switchgrass, plant growth parameters were parameterized for a lowland cultivar, Alamo, adapted to grow in wetter conditions (Trybula et al., 2015). For example, Srinivasan et al. (2010) adapted crop growth parameters for Alamo Switchgrass in large-scale bioenergy simulations to assess the environmental impacts of land use change. Trybula et al. (2015) then parameterized the SWAT crop growth parameters for an upland switchgrass cultivar adapted to grow in drier conditions, based on experimental field data, and improved the model representation of plant growth for perennials. Previous studies also parameterized switchgrass (both lowland and upland cultivars) in the EPIC model to evaluate the environmental impacts of cultivating switchgrass for bioenergy production (Egbendewe-Mondzozo et al., 2013, 2011). Note that SWAT employs a simplified vegetation growth sub-model adapted from EPIC (Williams et al., 1989). Therefore, the above studies, in general, used a single plant growth pattern for all plant types (forest, grass, and annual crops), which lacks representation of complex plant phenology, for example, growth of different plant compartments (root, shoot, leaf, etc.), carbon and nutrient dynamics between above and belowground pools (Luo et al., 2008). As such, further improvements of the SWAT vegetation growth sub-model are needed to more reliably characterize the behavior of perennial grass growth and provide assessment of hydrologic, nutrient, and carbon cycle responses to bioenergy feedstock production.

This study aims to enhance the SWAT plant growth sub-model to improve simulation of biomass production of perennial grass. We integrated the grass growth sub-model from DAYCENT into SWAT and referred to the new model as the SWAT–GRASS hereafter. The DAYCENT grass sub-model can simulate crop development, biomass production, and carbon and nutrient allocation to shoot and root as influenced by various elements such as climate, nutrient, and water availability (Parton et al., 1998). The model has been used to simulate biomass production of perennial grasses like switchgrass and miscanthus on the field and regional scale (Chen et al., 2021; Davis et al., 2010; Hudiburg et al., 2016, 2015). We evaluated the SWAT–GRASS model against the observed switchgrass biomass yield at multiple farm sites in Wisconsin, Michigan, and Illinois. The sites considered here represent both low and high productivity land areas that help assess the potential for sustainable bioenergy feedstock production. The improved representation of vegetation growth provides new features into the SWAT model for studying the watershed scale impact of growing perennial bioenergy crops on soil organic matter, nutrient uptake, and water quality. The outcomes of this study will also be helpful in model development and application for different types of perennial grasses to generate more realistic information for understanding the sustainability issues related to bioenergy feedstock production.

5.2 Materials and methods

5.2.1 SWAT plant growth sub-model

The SWAT model utilizes a simplified plant growth sub-model based on the EPIC model for all plant types (annual crops, grass, and forest) to simulate plant growth based on accumulated heat units (Williams et al., 1989). The growth sub-model first simulates the potential plant biomass production under ideal conditions based on the radiation use efficiency coefficient and the intercepted photosynthetically active solar radiation. Then, it calculates the actual growth of the plant taking into account the influence of temperature, water, nitrogen, phosphorus, and aeration stress factors (Neitsch et al., 2011) as described in Appendix C.

The SWAT model determines the seasonal partitioning of plant biomass to root by a static root-shoot ratio (*RSR*) at the specific plant growth stage (Eq. C.1). Such simplified assumptions of plant root fraction could result in substantial differences in biomass yield of perennials and overall impact on hydrologic processes, water quality, and soil organic carbon. For example, the default values of root fraction at the planting (*rsr1*) and maturity (*rsr2*) are 0.2 and 0.4 respectively. Based on this assumption, about 60% of plant biomass would be available as yield at the early growing season and about 80% when harvested at the end of the growing season. This method does not consider the explicit allocation of accumulated biomass into shoot and root, nor the impact of climate conditions on root development. In addition, the simple *RSR* approach does not consider the fact that perennial grasses such as switchgrass and miscanthus translocate nutrients to root during the late growing season, which the plant remobilizes during the next growing season (Ashworth et al., 2017; Massey et al., 2020). Such nutrient cycling during different phases of plant growth reduces the plant nutrient stress, resulting in high biomass production even in low-productivity soil. Furthermore, the plant biomass death during senescence and subsequent return to soil is not well simulated in SWAT. For perennials, a fraction of biomass (generally 10%) dies off and is added to soil organic matter during dormancy in SWAT. However, SWAT does not account for the root and shoot biomass death separately during the growing season, which affects the soil organic matter dynamics.

5.2.2 DAYCENT grass growth sub-model

DAYCENT is a biogeochemical model that simulates the dynamics of carbon, nitrogen, phosphorous, and sulfur for grassland, agricultural land, forest, and savannas (Del Grosso et al., 2008; Parton et al., 1998). The model has separate plant production sub-models for grass/crop, forest, and savanna to predict biomass growth. Its grass growth sub-model, detailed in Metherell et al. (1993), accounts for the dynamic nature of biomass allocation to shoot and root based on plant growth stage, climatic conditions, and nutrient availability. DAYCENT also simulates shoot and root death and accounts for nutrient translocation within the plant. For instance, if water or nutrients are limited, the plant response would be to allocate more resources to roots (Davis et al., 2010; Kantola et al., 2022). In this study, we incorporated DAYCENT's grass sub-model (see details in Appendix D) into SWAT to create the SWAT–GRASS$_D$ model.

5.2.3 Modifications to potential biomass production

DAYCENT uses a simplified approach to estimate the leaf area index as leaf area ratio (LAR) multiplied by total aboveground biomass. By default, LAR is set to a constant value of 0.01 for all crops/grasses. However, LAR has been found to vary spatially (Y. Zhang et al., 2018). The SWAT requires LAI to compute rainfall interception by the plant canopy and potential evapotranspiration (Neitsch et al., 2011), which subsequently affects plant water use. The use of a LAR coefficient for LAI development in DAYCENT could reduce the performance of the integrated model in simulating plant water use and biomass production (Y. Zhang et al., 2018). Thus, the calculation of potential biomass production was further modified to incorporate the influence of seasonally varying leaf area on solar radiation intercepted by the perennial grasses. For this, an additional scaling factor, *laiprod*, used in the DAYCENT forest sub-model, is introduced in Eq. (D.1). The new equation is as follows:

$$tgprod = shwave \times T_{stress} \times SM_{stress} \times Sdlng \times CO2cpr \times biof \times laiprod \qquad (1)$$

where, *tgprod* (*g C/m²*) is the potential biomass production on a given day, *shwave* is downwelling solar radiation (*Lg/day*), SM_{stress} is the soil moisture effect, T_{stress} is the temperature effect, *Sdlng* is the constraint on biomass production representing the seedling growth, *CO2cpr* is the effect of CO_2 concentration on biomass production, *scenfrac* represents the loss of biomass due to senescence, and *biof* is the effect of physical obstruction by standing dead biomass.

$$laiprod = 1 - exp(-k_l \times LAI) \qquad (2)$$

where, k_l is light extinction coefficient, and *LAI* is leaf area index calculated by SWAT as:

$$LAI_i = LAI_{i-1} + \Delta LAI_i \quad (3)$$

$$\Delta LAI_i = \left(fr_{LAImx,i} - fr_{LAImx,i-1}\right) \times LAI_{mx} \times \left(1 - exp\left(5 \times (LAI_{i-1} - LAI_{mx})\right)\right) \quad (4)$$

where, ΔLAI_i is increment of leaf area index on day i, $fr_{LAImx,i}$ and $fr_{LAImx,i-1}$ are fraction of maximum leaf area index on day i and i-1, LAI_i and LAI_{i-1} are leaf area indices on day i and i-1, and LAI_{mx} is the maximum leaf area index for the plant.

The introduction of the scale factor *laiprod* was accompanied by the substitution of soil moisture stress (SM_{stress}) in Eq. (D.1) with SWAT estimated plant water stress ($Stress_w$). $Stress_w$ is proportional to the ratio of actual plant water uptake to potential evapotranspiration (Eq. (C.4)), which is considered to be a good measure of water stress impact on biomass production (Y. Zhang et al., 2018). The newly integrated SWAT–GRASS model with these modifications is referred to as SWAT–$GRASS_M$.

5.2.4 Field experimental sites

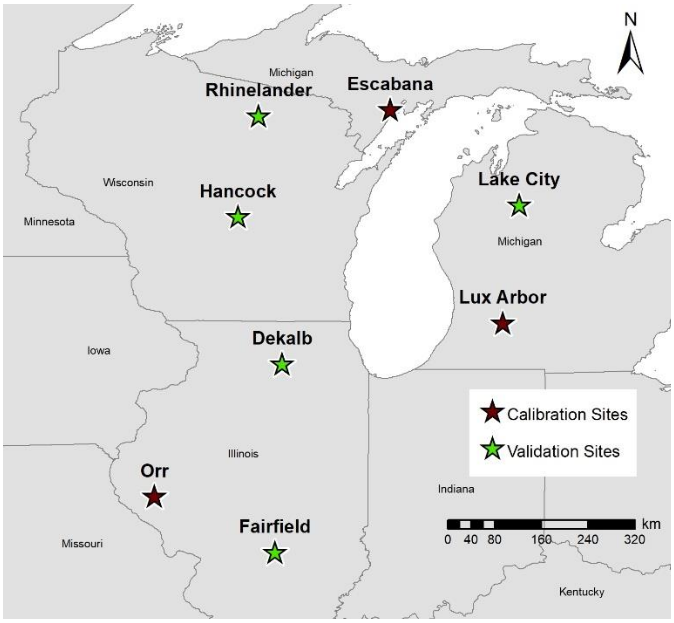

Figure 5.1. Location of GLBRC and AR field sites.

The SWAT and two versions of SWAT–GRASS models were evaluated at five Great Lakes Bioenergy Research Center (GLBRC) field sites in Michigan and Wisconsin (Escaban, Hancock, Rhinelander, Luxarbor, and Lakecity) and three field sites across Illinois (Fairfield, Orr, and Dekalb; selected from Arundale et al., (2014)) (referred to as AR sites) (Figure 5.1). For these sites, biomass yield data for the Cave-in-Rock cultivar were available. The average annual precipitation and temperature range between 766 and 1044 mm and 6 and 13 °C, respectively, across all eight field sites (Table 5.1 and Figure E.1). In general, switchgrass biomass yield was higher in sites with warmer temperatures and higher precipitation (Hartman et al., 2012; Li et al., 2022).

Table 5.1. Field sites used to calibrate and validate SWAT and SWAT–GRASS plant growth parameters for switchgrass.

Data source	Location	Latitude, Longitude	Soil taxonomic class	Data record length	Annual Precipitation (mm)	Annual Average Temperature (°C)
GLBRC	Rhinelander, Wisconsin	45.66, -89.21	Sandy loam	2014-2021	808	5.8
	Hancock, Wisconsin	44.11, -89.53	Sand	2014-2021	838	8.0
	*Escabana, Michigan	45.76, -87.18	Fine sandy loam	2014-2021	766	6.5
	Lake City, Michigan	44.29, -85.19	Sand	2014-2021	852	7.8
	*Lux Arbor, Michigan	42.47, -85.45	loam	2014-2021	933	9.5
Arundale et al. (2014)	Fairfield, Illinois	38.95, -88.96	Silt loam	2006-2009	1044	13.3
	Dekalb, Illinois	41.85, -88.85	Silt loam	2006-2011	935	10.2
	*Orr, Illinois	39.81, -90.82	Silt loam	2006-2011	973	12.5

Note: * indicates the sites that were used for model calibration. The three sites selected here represent the two ends of the gradient from the cooler, drier, and low productivity areas Escabana and Lux Arbor sites to the warmer, wetter, and high productivity Orr site.

5.2.5 Model setup

The SWAT and SWAT-GRASS models were setup for watersheds (within which the field sites were located) using the geospatial inputs listed in Table 5.2. In SWAT, Hydrologic Response Units (HRUs) are generated by the unique combination of land use, soil, and slope within a watershed. Here, we use the HRUs collocated with the switchgrass field sites and further assign detailed management operations. The field-level management operations were scheduled by date, consisting of planting, fertilizer application, and harvesting, as detailed by Arundale et al. (2014) for the AR sites and by Martinez-Feria and Basso (2020) for the GLBRC sites (Table 5.1). Switchgrass was planted between May and June and harvested every subsequent year between October and November. The fertilizer application rates were based on Arundale et al., (2014) and Martinez-Feria and Basso (2020). For additional information on experimental design, see GLBRC data catalog at https://data.sustainability.glbrc.org/datatables and Arundale et al. (2014). The harvesting efficiency (*HARVEFF*) of 0.8 was used based on settings from Ng et al. (2010). The upland switchgrass plant growth parameters for SWAT were adopted from the study by Cibin et al. (2016). For SWAT–GRASS, upland switchgrass growth parameters were adopted from Davis et al. (2010). The switchgrass growth parameters used in SWAT and SWAT–GRASS are provided in Tables E.1 and E.2, respectively.

In the natural grassland ecosystem, the primary source of nitrogen is wet and dry atmospheric deposition (Del Grosso et al., 2008). The atmospheric deposition of nitrogen tends to increase biomass production in nitrogen-limited watersheds (Fernández-Martínez et al., 2017; Sullivan and Gao, 2016). Given the relevance of atmospheric nitrogen deposition on biomass production of grass, the wet and dry atmospheric deposition rates reported by National Atmospheric Deposition Program (NADP) (NADP, 2022) were used. The total annual wet and dry nitrogen atmospheric deposition was computed for each site. The SWAT weather data inputs were obtained from North American Land Data Assimilation System (NLDAS-2) dataset (Xia et al., 2009). The model simulations for GLBRC sites and AR sites were conducted from 2013 to 2021 and from 2005 to 2009/2011, respectively.

Table 5.2. Geospatial inputs used for SWAT setup

Data	Resolution	Source
Meteorology data	0.125° × 0.125°	NLDAS-2 (Xia et al., 2009)
Digital Elevation Model (DEM)	90m × 90m	Shuttle Radar Topography Mission (SRTM) (Jarvis et al., 2008b)
Land Use	30m × 30m	USDA NASS Cropland Data Layer (2008)
Soil Property	1:24,000	Soil Survey Geographic database(SSURGO) (USDA-NRCS, 1994b)

5.2.6 Model calibration and validation

We simultaneously calibrate the three models at multiple sites to ensure parameter generality for testing sites. This approach helps in the generalization of switchgrass growth parameters for application across large areas (Zhang et al., 2008). The field-level biomass yield data from GLBRC field sites (Martinez-Feria and Basso, 2020) and Arundale et al., (2014) (Table 5.1) were used to optimize and evaluate the SWAT and SWAT–GRASS for simulating upland switchgrass biomass yield. The observed biomass yields from three field sites (Escabana, Orr, and Luxarbor) were used to calibrate the models. By including these sites, we aimed to ensure that the optimized model parameters would account for the variability in temperature, precipitation, and soil productivity. Sensitivity analysis and calibration of plant growth parameters were carried out using the Sequential Uncertainty Fitting algorithm version 2 (SU-FI-2) procedure in SWAT-CUP (Abbaspour et al., 2015). The Kling–Gupta efficiency criterion (*KGE*) (Gupta et al., 2009) was used as the objective function for model calibration. *KGE* ranges from -∞ to 1, with a higher value of *KGE* indicating better model performance. We further evaluated the model performance for simulated yield using percent bias (*PBIAS*), correlation coefficient (R), and root mean square error (*RMSE*) (Moriasi et al., 2007).

The SWAT plant growth parameters selected for sensitivity analysis were based on prior studies (Cibin et al., 2016; T. L. Ng et al., 2010; Trybula et al., 2015) and are listed in Table E.3. The SWAT–GRASS plant growth parameters selected for the sensitivity analysis were based on previous studies (Chamberlain et al., 2011; Davis et al., 2010; Lee et al., 2012) and are listed in Table E.4. The sensitivity analysis, as described above for SWAT, was implemented for SWAT–GRASS as well.

To establish confidence in the SWAT–GRASS model and the optimized switchgrass growth parameters, we validated the model simulated yield with independent biomass yield datasets for the remaining five field sites (Hancock, Rhinelander, Lake City, Fairfield, and Dekalb) from the GLBRC and AR sites that span across a range of climatic conditions in different geographical regions (Illinois, Michigan, and Wisconsin) (Figure 5.1). We assessed the model prediction uncertainty by estimating the P-factor and R-factor using SUFI-2. The P-factor quantifies the percentage of observed data that falls within the 95% prediction uncertainty (95PPU) band, ranging from 0 to 1. The R-factor is the ratio between the width of the 95PPU band and the standard deviation of the observed data, with values ranging from 0 to infinity. The P-factor close to 1 and the R-factor close to 0 indicates low prediction uncertainty.

5.3 Results and discussion

5.3.1 Sensitivity analysis

Tables E.3 and E.4 list the SWAT and SWAT–GRASS plant growth parameters used for sensitivity analysis. Using global sensitivity in SUFI-2, the most sensitive parameters were identified and adjusted through the calibration process with final optimal values shown in Tables 3 and 4. The SWAT model was found to be sensitive to *BIO_E*, *T_OPT*, *T_BASE*, *RSR2C*, *LAIMX2*, and nutrient fraction parameters for nitrogen at three stages of plant growth (i.e., *PLTNFR1*, *PLTNFR2*, and *PLTNFR3*) (Figure E.2), which is consistent with the sensitivity analysis results from Trybula et al. (2015). *PLTNFR2* was one of the most sensitive parameters followed by *PLTNFR1*, which indicates that plant nitrogen cycling had a major impact on SWAT-simulated switchgrass yield. *PLTNFRs* control the amount of nitrogen in plant biomass that subsequently determines the plant nitrogen demand and plant nutrient stress during plant growth. *BIO_E* (radiation use efficiency) determines the daily biomass production. *LAIMX2* determines the LAI development and affects plant water demand and photosynthetically active radiation. *T_OPT* and *T_BASE* affect plant temperature stress and the timing of plant maturity. It is worth noting that the adjustment of *T_OPT* and *T_BASE* to ca. 20.8 and 9.7 °C from their default values of 25 and 10 °C, respectively, intensified the crop growth within a narrower temperature range, specifically between *T_BASE* to 2×*T_OPT-T_BASE*. This adjustment resulted in higher sensitivity of biomass production to temperature stress.

Table 5.3. Calibrated SWAT plant growth parameters for Switchgrass biomass yield.

ID	Parameters	Description	Range used	Fitted value
1	*r_T_OPT*	The optimal temperature for plant growth (°C)	±20%	-17%
2	*r_T_BASE*	Base temperature for plant growth (°C)	±20%	-3%
3	*r_BIO_E*	Radiation use efficiency (biomass/energy ratio)	±40%	33%
4	*r_PLTNFR1*	Plant nitrogen fraction at emergence	±50%	17%
5	*r_PLTNFR2*	Plant nitrogen fraction at 50% maturity	±50%	26%
6	*r_PLTNFR3*	Plant nitrogen fraction at maturity	±50%	47%
7	*v_LAIMX2*	Fraction of the leaf area index corresponding to the 2nd. point on the optimal leaf area development curve	0.8 to 0.95	0.921
8	*v_RSR2C*	Root fraction at the end of the growing season	0.35 to 0.60	0.398

Note: Here r and v represent the relative change and replacement of model parameters by adjusted value.

Both SWAT–GRASS$_D$ and SWAT–GRASS$_M$ were found to be sensitive to *T_OPT, T_BASE, ppdf(2), ppdf(3), ppdf(4), prdx, riint, cfrtcn(2), crptf(1), clsgres, pltmrf,* and *fallrt* (Figures E.3 and E.4). The parameters *pramn(1,2)* and *pramx(1,2)* regulate the C:N ratio of aboveground and belowground biomass. *T_OPT* and *T_BASE* in conjunction with *ppdf(2), ppdf(3),* and *ppdf(4)* determine the plant's response to changes in atmospheric temperature and control the timing of plant maturity. *prdx* is the maximum potential monthly biomass production rate that affects daily biomass production. *cfrtcn(2)* affects the biomass allocation to roots under nitrogen stress. *crptf(1)* determines the nitrogen translocation from the shoot to the root during the late growing season. *clsgres* regulates the late-season growth of the plant. *pltmrf* is the planting month reduction factor that scales the plant growing from seedlings. *fallrt* regulates the rate at which standing dead biomass is transferred to surface litter. For

SWAT–GRASS$_D$, the most sensitive parameter was *fallrt*, followed by *T_BASE, DLAI, prdx, T_OPT, crprtf(1), ppdf(2),* and *pltmrf* (Figure E.3). Similarly, for SWAT–GRASS$_M$, the most sensitive parameter was *prdx*, followed by *fallrt, DLAI, T_BASE, T_OPT, ppdf(2),* and *FRGRW1* (Figure E.4).

Table 5.4. Calibrated SWAT–GRASS plant growth parameters for switchgrass biomass yield.

ID	Parameters	Description	Range used	Fitted Values	
				SWAT–GRASS D	SWAT–GRASS M
1	*r_T_OPT*	optimal temperature for plant growth (°C)	±40%	-14%	7%
2	*r_T_BASE*	base temperature for plant growth (°C)	±40%	23%	24%
3	*v_DLAI*	Fraction of growing season when leaf area starts declining	0.8 to 1.2	1.045	1.014
4	*v_LAIMX1*	Fraction of the max. leaf area index corresponding to the 1st. point on the optimal leaf area development curve	0.05 to 0.10	–	0.100
5	*r_FRGRW1*	Fraction of the plant growing season corresponding to the 1st. Point on the optimal leaf area development curve	±20%	–	5%
6	*r_FRGRW2*	Fraction of the plant growing season corresponding to the 2nd. point on the optimal leaf area development curve	±20%	–	0.7%
7	*r_ppdf(2)*	maximum temperature for plant growth (°C)	±30%	11%	-0.8%
8	*r_ppdf(3)*	left curve shape parameter that controls temperature effect on plant growth	±30%	12%	13%
9	*r_ppdf(4)*	right curve shape parameter that controls temperature effect on plant growth	±30%	21%	-5%
10	*v_prdx*	potential aboveground monthly biomass production (g C/m^2)	0.5 to 4.0	2.809	2.161
11	*v_riint*	Root impact intercept that controls the impact of root biomass on nutrient availability	0.4 to 1.0	0.487	0.834
12	*v_cfrtcn(1)*	maximum fraction of carbon allocated to roots under maximum nutrient stress	0.5 to 0.7	0.502	0.630
13	*v_cfrtcn(2)*	minimum fraction of carbon allocated to roots in the absence of nutrient stress	0.2 to 0.3	0.334	0.357
14	*v_cfrtcw(1)*	minimum fraction of carbon allocated to roots under maximum water stress	0.4 to 0.7	0.618	0.599

15	*v_cfrtcw(2)*	minimum fraction of carbon allocated to roots in the absence of water stress	0.2 to 0.3	0.355	0.308
16	*v_crprtf(1)*	fraction of N transferred to a vegetation storage pool at death	0.50 to 0.95	0.861	0.791
17	*v_pramn(1,1)*	minimum aboveground C:N ratio with zero biomass	15 to 25	–	17.097
18	*v_pramn(1,2)*	minimum aboveground C:N ratio with biomass equal to biomax	40 to 80	74.355	68.158
19	*r_pramx(1,2)*	maximum aboveground C:N ratio with biomass equal to biomax	±20%	–	13%
20	*v_prbmn(1,1)*	intercept for calculating the minimum C:N ratio for belowground biomass as a linear function of annual precipitation	40 to 60	42.239	49.864
21	*v_prbmn(1,2)*	slope for calculating the minimum C:N ratio for belowground biomass as a linear function of annual precipitation	0.0 to 1.0	–	0.113
22	*r_clsgres*	late season crop growth restriction factor	±20%	-10%	-2%
23	*r_biomax*	biomass level above which the minimum and maximum C:E ratios of new shoot increments equal pramn(:,2) and pramx(:,2) respectively (g biomass/m^2)	±30%	–	1.2%
24	*v_pltmrf*	plant mature root fraction	0.8 to 1.0	0.955	0.987
25	*v_fallrt*	fall rate (fraction of standing dead which falls each month)	0.005 to 0.15	0.009	0.096

Note: Here r and v represent the relative change and replacement of model parameters by adjusted value.

These results indicate that the parameters regulating the plant nitrogen cycle, such as plant nitrogen use efficiency and the impact of nitrogen stress on biomass production, are critical factors in determining biomass yield in SWAT. Meanwhile, parameters that regulate the plant growth response to temperature changes and plant growth processes during senescence were critical factors for biomass yield in SWAT–GRASS$_D$ and SWAT–GRASS$_M$. Overall, these findings provide insights into the key parameters that should be considered when predicting biomass production using SWAT, SWAT–GRASS$_D$, and SWAT–GRASS$_M$ models.

5.3.2 Model calibration and validation for biomass simulation

5.3.2.1 Calibration

SWAT, SWAT–GRASS$_D$, and SWAT–GRASS$_M$ were able to capture the variability in biomass yield with $R \geq 0.5$ (Figure 5.2). The *PBIAS* was found to be within ±25% and $KGE \geq 0.45$ for all three models (Figure 5.2), indicating low bias in model performance. These results demonstrate the ability of all three models to reasonably simulate biomass yield across the three calibration sites. Among the three models, SWAT achieved the least bias, while SWAT–GRASS$_M$ performed the best in terms of capturing the variability in observed biomass yield. SWAT–GRASS$_M$ exhibited improved accuracy in simulating the standard deviation of observed biomass yield across the calibration sites (2.4 Mg/ha vs. observed standard deviation of 2.9 Mg/ha), while SWAT (2.0 Mg/ha) and SWAT–GRASS$_D$ (2.1 Mg/ha) underestimated variability. SWAT–GRASS$_D$ performed the least in terms of *R*, *KGE*, and *RMSE*. With the modifications introduced in SWAT–GRASS$_M$, the SWAT–GRASS$_M$ shows considerable improvement in simulating biomass yield.

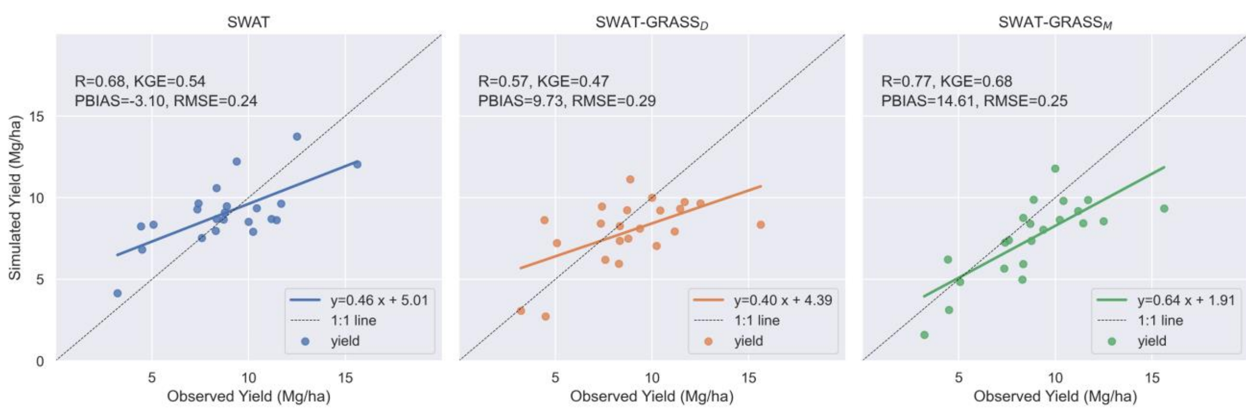

Figure 5.2. Scatter plots of SWAT, SWAT–GRASS$_D$, and SWAT–GRASS$_M$ simulated and observed annual dry weight biomass yield for all calibration sites.

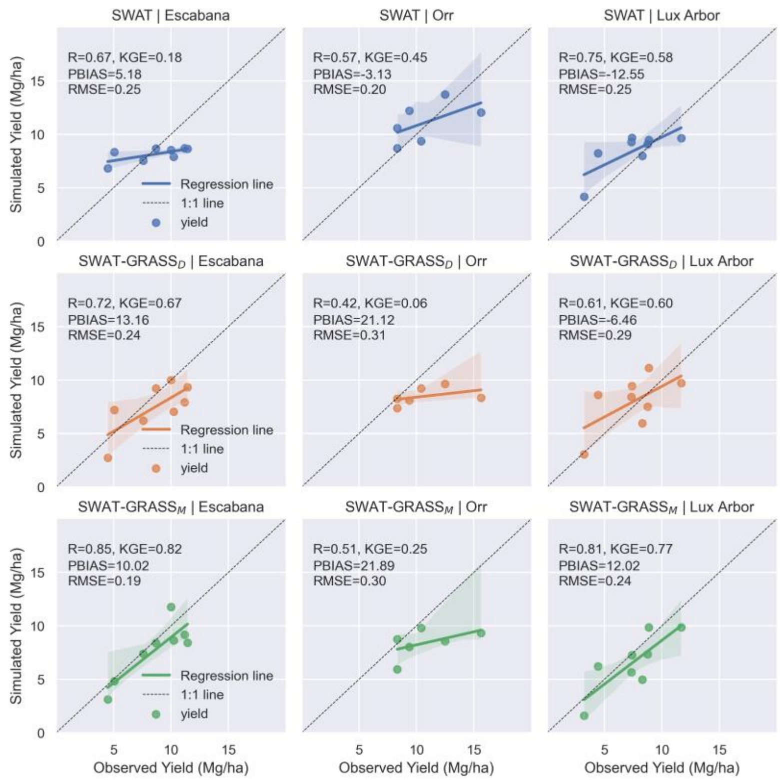

Figure 5.3. Scatter plots of SWAT, SWAT–GRASS$_D$, and SWAT–GRASS$_M$ simulated and observed annual dry weight biomass yield for individual calibration field sites.

At the individual site level, the performance metrics of the three models vary across the field sites (Figure 5.3). For example, both SWAT–GRASS$_D$ and SWAT–GRASS$_M$ outperformed SWAT in simulating biomass yield for Escabana in terms of *R* and *KGE*. Likewise, at Lux Arbor, SWAT–GRASS$_D$ performed modestly better in terms of *KGE*, while SWAT–GRASS$_M$ exhibited substantial improvement in terms of both *R* and *KGE* compared to SWAT. On the other hand, at Orr, SWAT–GRASS$_D$ performed poorly than SWAT in terms of *KGE*, *RMSE*, and *PBIAS*, and simulated biomass yield substantially worse than SWAT–GRASS$_M$, which still had lower *KGE* and *RMSE* than SWAT. In general, the calibration results show that none of the three models can consistently outperform the other two models in terms of all metrics and at all sites, indicating that each of these three models has their own strengths and weaknesses. This result also demonstrates that the plant growth processes are complex, and it is difficult to identify a single optimum algorithm.

5.3.2.2 Validation

Across the five validation sites, SWAT, SWAT–$GRASS_D$, and SWAT–$GRASS_M$ simulated average annual biomass yields of 8.9, 7.7, and 7.8 Mg/ha, respectively, compared to the observed value of 7.1 Mg/ha. SWAT performed satisfactorily with a *KGE* of 0.37 and a *PBIAS* of -25.77%. In comparison, SWAT–$GRASS_D$ achieved a higher *KGE* (0.46) and reduced *PBIAS* (-8.67%) and *RMSE* (0.45) compared to SWAT. SWAT–$GRASS_M$ modestly outperformed SWAT–$GRASS_D$, with a *R* of 0.55, *RMSE* of 0.44, and a *KGE* of 0.47 (Figure 5.4). We found that the model performance was substantially influenced by the underestimation of two instances of high yields (16 Mg/ha) observed at Fairfield in 2007 and 2008. Assuming these points as outliers, SWAT–$GRASS_M$ achieved a substantial improvement in the simulation of biomass yield compared to both SWAT and SWAT–$GRASS_D$ in terms of *R* (0.58 vs 0.42 and 0.51), *RMSE* (0.42 vs 0.53 and 0.44), and *KGE* (0.54 vs 0.28 and 0.48), respectively.

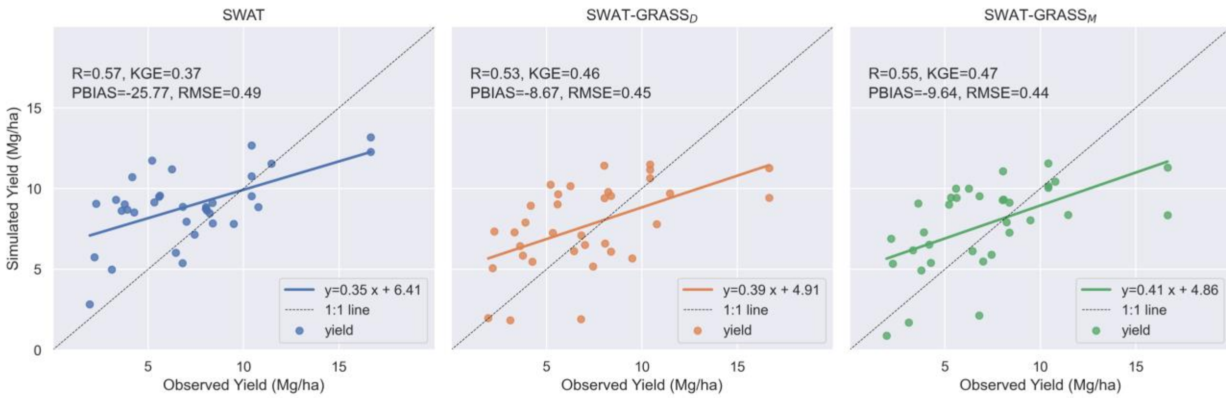

Figure 5.4. SWAT, SWAT–GRASS$_D$, and SWAT–GRASS$_M$ simulated annual dry weight biomass yield for all validation sites.

Figure 5.5 compares the observed and simulated biomass yield at each validation field site and demonstrates that model performance varied considerably across validation field sites (Hancock, Rhinelander, Lake City, Fairfield, and Dekalb) and between the models during validation. The observed mean dry weight biomass yield varies considerably across the field sites, ranging from 3.6 to 13.8 Mg/ha. In general, the three models simulated mean biomass yield well at Rhinelander, Lake City, and Fairfield, but showed large bias at Hancock and Dekalb (Table E.5). The varied performance of the models across different sites could be caused by the accuracy of observed yield data and other input data, such as soil properties and management practices.

Across the five validation sites, SWAT–GRASS$_M$ provided comparable or improved performance when compared to SWAT and SWAT–GRASS$_D$ in terms of *R* and *KGE*, across the validation sites (Figure 5.5). For most sites, both SWAT–GRASS$_D$ and SWAT–GRASS$_M$ demonstrate good performance as indicated by *R* and *KGE* values, except for Fairfield and Hancock. It is also worth noting that SWAT–GRASS$_M$ achieved comparable *PBIAS* compared with SWAT and SWAT–GRASS$_D$ at

Rhinelander and Fairfield, and lower *PBIAS* at Hancock, Lake City, and Dekalb. Meanwhile, SWAT achieved lower *RMSE* at Lake City and Fairfield compared with SWAT–GRASS$_D$ and SWAT-GRASS$_M$. Similar to the calibration results, although none of the three models can outperform the other two in terms of all metrics and at all sites, SWAT–GRASS$_M$ provided the best overall performance.

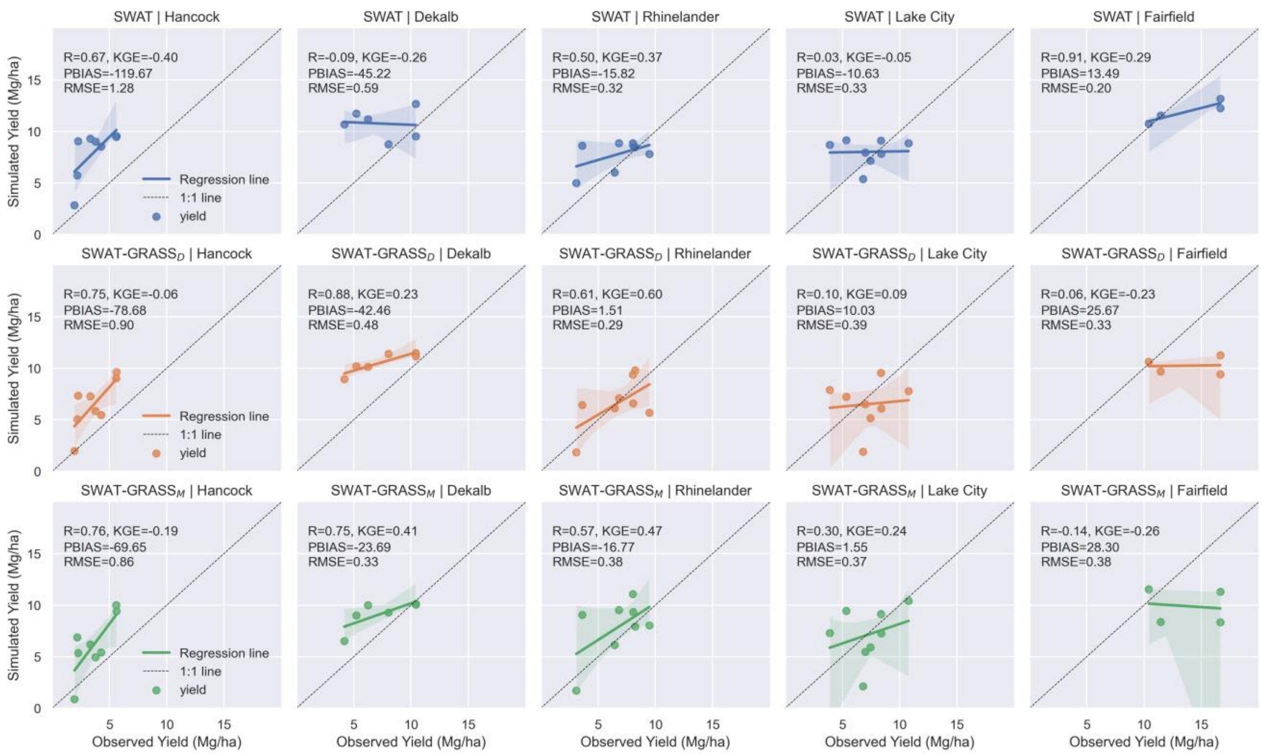

Figure 5.5. SWAT, SWAT–GRASS$_D$, and SWAT–GRASS$_M$ simulated annual dry weight biomass yield for individual validation field sites.

5.3.2.3 Uncertainty analysis

We calculated the P-factor and R-factor for biomass yield at the eight field sites using the final calibrated parameter ranges. The values of P-factor and R-factor are listed in Table E.6. The P-factor ranged from 0.13 to 0.63, 0.38 to 0.67, and 0.38 to 0.83 for SWAT, SWAT–GRASS$_D$, and SWAT–GRASS$_M$, respectively. The R-factor ranged from 0.62 to 1.11, 0.97 to 2.18, and 1.73 to 3.10 for SWAT, SWAT–GRASS$_D$, and SWAT–GRASS$_M$, respectively. In general, SWAT–GRASS$_M$ and SWAT–GRASS$_D$ obtained P-factor values closer to 1 (or the fraction of observations covered in the 95% confidence interval) than SWAT. Notably, the changes made in SWAT–GRASS$_M$ helped it obtain slightly greater P-factor and R-factor values than SWAT–GRASS$_D$. These results indicate that the modification of crop growth made the model to better represent the uncertainties associated with switchgrass yield prediction.

5.3.3 Assessment of model simulated Leaf Area Index

LAI is an important plant parameter for all three models for simulating plant growth. As measured LAI data for the field sites were not available, we used regression-estimated LAI to qualitatively assess the model ability to accurately represent LAI dynamics. We compared the seasonal development of LAI simulated by SWAT, SWAT–GRASS$_D$, and SWAT–GRASS$_M$ against the regression-estimated seasonal LAI for upland switchgrass by Madakadze et al., (1998), hereafter referred to as CTRL (Figure 5.6). The regression model is based on LAI data measured until the late summer months. Therefore, to ensure consistency, we qualitatively evaluate the simulated LAI values only up to August.

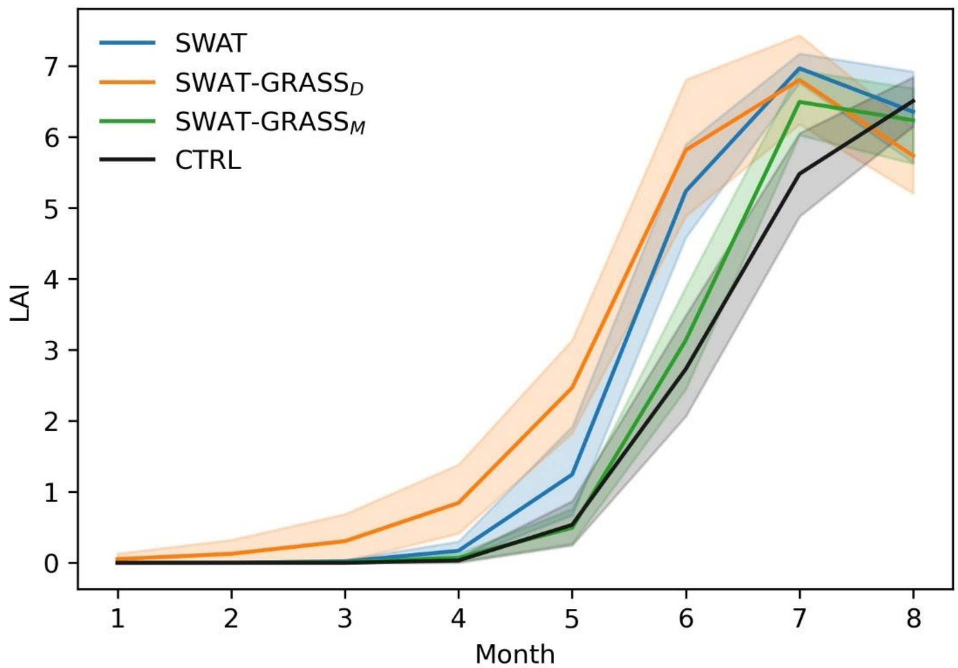

Figure 5.6. Comparison of SWAT, SWAT–GRASS$_D$, and SWAT–GRASS$_M$ simulated LAI with regression model fitted LAI (Madakadze et al., 1998), where shading represents 95% confidence limits.

SWAT and SWAT–GRASS$_D$ exhibited earlier and more rapid LAI development than the CTRL data, while SWAT–GRASS$_M$ simulates lower and gradual LAI development from mid-spring months that matches well with CTRL. The broad temperature ranges for SWAT–GRASS$_D$ within which biomass production can take place, allow for plant growth in early spring that contribute to early LAI development. In contrast, the relatively high T_BASE and narrow temperature range for plant growth (*T_BASE* = 12.4, *ppdf(2)* = 49.6, and *ppdf(4)* = 2.39) in SWAT–GRASS$_M$ limited plant growth in cooler early spring months. All three models simulate a rapid increase in LAI during the early summer months before reaching its peak value in July, in alignment with the CTRL data. Also, all three models simulate a gradual decline from July to August. Among the three models, SWAT–GRASS$_M$ overall better represented the seasonal dynamics of LAI, specifically in spring and early summer. This is likely a reason explaining the overall better performance of SWAT–GRASS$_M$.

5.3.4 Assessment of model simulated root to shoot ratio

Figure 5.7 compares the simulated *RSR* across all sites for October. As described in Appendix A, SWAT calculates *RSR* as a function of potential heat unit (PHU), which resulted in a nearly constant *RSR* (0.66-0.67) at harvest. In contrast, SWAT–GRASS$_D$ and SWAT–GRASS$_M$ simulated *RSR* with much higher variability, ranging from 0.55 to 0.90 and 0.62 to 1.05, respectively. The high *RSR* variability in SWAT–GRASS$_D$ and SWAT–GRASS$_M$ results from the impacts of temperature, water, and nutrient on the biomass allocation between root and shoot, which differed among the sites. In general, SWAT–GRASS$_D$ and SWAT–GRASS$_M$ allocate a high proportion of biomass to roots in warmer and wetter locations (i.e., AR sites). Specifically, the *RSR* value is high for Fairfield, Orr, and Dekalb, which receive high annual precipitation (>934 mm).

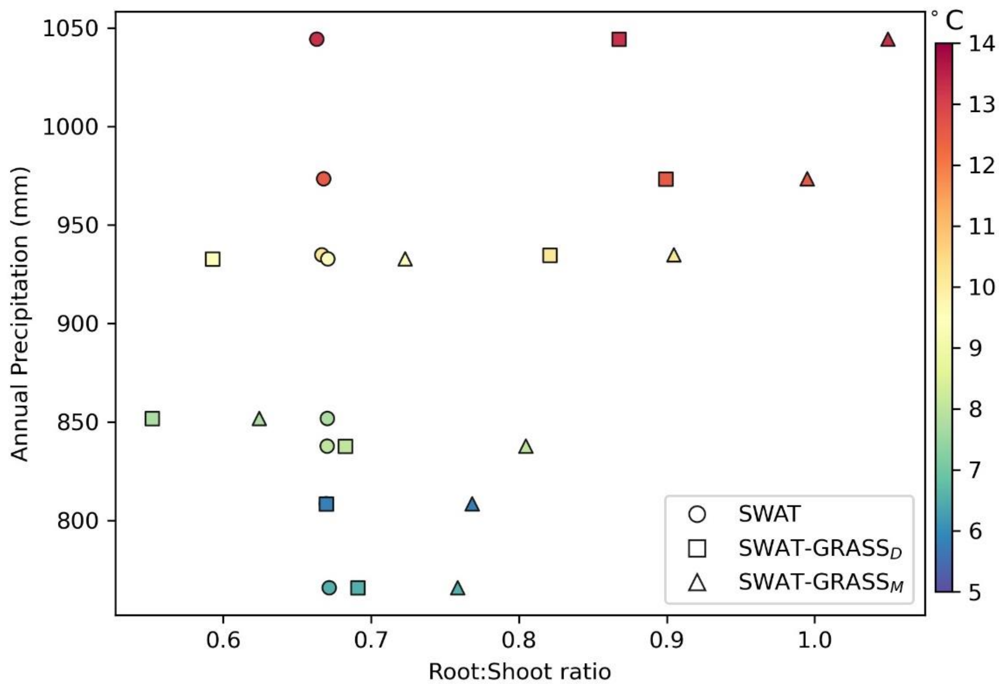

Figure 5.7. Comparison of SWAT, SWAT–GRASS$_D$, and SWAT–GRASS$_M$ simulated site averaged mean root-to-shoot ratio (*RSR*) for October. The color gradient represents the average annual temperature for each site.

The *RSR* values fall well within the broad range of values (0.19–3.07) reported in previous observation-based studies (Frank et al., 2004; Jung and Lal, 2011; Sainju et al., 2017; Wayman et al., 2014; Zan et al., 2001). The *RSR* simulated with the three models in this study is somewhat similar to the *RSR* reported by Wayman et al. (2014), 0.88–0.95, in Nebraska and Pennsylvania where mean annual precipitation ranged between 700 and 1120 mm, and by Zan et al., (2001), which reported *RSR* in the lower range of 0.4–0.7 in Quebec, Canada, with a mean air temperature of 6.5°C and an annual precipitation of 1062 mm. It is also worth noting that other studies reported contrary findings. For example, Jung and Lal, (2011), reported the *RSR* of 0.19–0.56 in Ohio which is smaller than the *RSR* estimated in this study. Sainju et al. (2017) reported high *RSR* in the range of 1.39–3.07 in Montana, which received low annual precipitation of 271–453 mm. These findings highlight that the variability of biomass allocation is not only influenced by climate conditions but also by nutrient and water management. Nonetheless, the observed RSR values are highly variable, therefore the constant RSR simulated by SWAT is not realistic. The observational data also corroborate that both SWAT–GRASS$_D$ and SWAT–GRASS$_M$ can represent the effects of climate on root and shoot development.

5.3.5. Assessment of model simulated hydrological process and nitrogen cycle

We evaluated the impact of the differences in biomass production and LAI development as simulated by SWAT, SWAT–GRASS$_D$, and SWAT–GRASS$_M$ on both hydrological processes and the nitrogen cycle. In general, the seasonal cycle of surface runoff, evapotranspiration, soil moisture content, and groundwater percolation simulated by SWAT, SWAT–GRASS$_D$, and SWAT–GRASS$_M$ were similar (Figure E.5), with small variations arising from the differences in biomass production and LAI development (Figure 5.6). In contrast, we found substantial differences in the seasonal plant nitrogen uptake and total soil nitrate content simulated by the models, particularly during the early growing season (Figure E.6). SWAT and SWAT–GRASS$_D$ simulated high plant nitrogen uptake during the early growing season (Figure E.6a) as reflected by the early LAI development (Figure 5.6). Meanwhile, SWAT–GRASS$_M$ exhibited lower nitrogen uptake during this period, leading to an increase in soil nitrate content (Figure E.6b).

5.3.5 Strengths, limitations, and future directions of the SWAT-GRASS model

This study integrated and modified the DAYCENT grass sub-model into SWAT to improve the representation of biomass production, biomass allocation, and nutrient content of perennial grasses, using switchgrass as an example. SWAT considers climate conditions and nutrient availability in biomass production but does not fully account for their influence on root and shoot biomass allocation. While SWAT can satisfactorily simulate the biomass yield, it fails to simulate the high variability observed in root biomass allocation under different climatic conditions. This limits SWAT's ability to provide a credible understanding of the complex interactions between climate conditions, bioenergy feedstock production, and soil biogeochemistry. The SWAT–GRASS$_D$, which incorporates the DAYCENT grass sub-model into SWAT, addresses this limitation but falls short in certain aspects. For example, SWAT–GRASS$_D$ does not explicitly account for the influence of canopy leaf area on the interception of incident solar radiation and biomass production, resulting in early plant growth and overestimation of biomass allocation and LAI in the early growing season. The introduction of an additional scaling factor that incorporates the influence of LAI dynamics in the SWAT–GRASS$_M$ provides an improved estimation of biomass yield and LAI development.

Although none of the three models examined here can consistently outperform the others in terms of all metrics, the results show that the overall performance of SWAT–GRASS$_M$ is comparable to or better than SWAT and SWAT–GRASS$_D$ in simulating switchgrass biomass yield, in terms of *R*, *KGE*, and *PBIAS* for most cases. The improved performance of SWAT–GRASS$_M$ in investigating the suitability of perennial grass such as switchgrass for biomass production, which in conjunction with other capabilities within SWAT (e.g., water quantity and quality) (Arnold et al., 1998; Neitsch et al., 2011) and SWAT-Carbon (e.g., soil organic carbon and riverine carbon fluxes) (Liang et al., 2022; Qi et al., 2020a; Zhang, 2018) makes it a powerful tool to study environmental impacts of using perennial grasses at the regional scale.

Note that, despite the more comprehensive algorithms in the two SWAT–GRASS models that can better represent the aboveground and belowground biomass development as influenced by climate, nutrients, and water, multiple aspects of the new models could be further improved, such as the representation of processes related to the interception of solar radiation, and the development of roots in the soil column. The current model assumes the root depth of the perennial plant to be equal to 3 m or to span the entire depth of the soil column for the entire growing period. The root depth and distribution could affect plant water and nutrient uptake, as well as the distribution of soil organic matter. In addition, unlike SWAT, the two SWAT–GRASS models do not consider the influence of vapor pressure deficit on radiation use efficiency and subsequently impact biomass production. Therefore, further work is deserved to improve these processes in SWAT–GRASS to better simulate plant growth and biomass production of perennial grass.

Additionally, several parameters used by the two SWAT-GRASS models, such as the fraction of nutrients allocated to the root during the late growing season, vary at different ages of perennial plants. The current modification assumes that these parameters remain static throughout the lifespan of the plant. This approach could result in uncertainties regarding the model's ability to simulate nutrient uptake from soil and nutrient allocation to different plant parts. Also, comprehensive data to evaluate the model capability of representing the development of LAI, aboveground biomass, and belowground biomass were rarely available. Therefore, more comprehensive model assessment awaits future research.

Collectively, the integration and modification of the new grass sub-model, which accounts for water, temperature, and nutrient stress on biomass production and allocation to plant shoot and roots, can provide reasonable (i.e. similar or better) simulation of biomass yield compared to SWAT. Particularly the SWAT–GRASS$_{M}$ holds promise in simulating LAI and root and shoot development under diverse climate and management conditions more realistically. These new capabilities make it a promising tool to support future studies that examine the potential of switchgrass and other perennial grasses for biomass production and their subsequent environmental impacts and benefits. We share the new model https://sites.google.com/view/swat-carbon to facilitate future efforts to apply and further enhance the model developed in this study.

5.4 Conclusion

We integrated and modified the DAYCENT grass growth module into the SWAT model to improve the simulation of biomass production for perennial grasses, using switchgrass as a test example. In addition to using the default algorithms in DAYCENT (SWAT–GRASS$_{D}$), we also revised the calculation of potential biomass production (SWAT–GRASS$_{M}$) to incorporate the effect of LAI dynamics. Overall, the model improvement includes four major aspects: (1) process-based biomass allocation to root and shoot that accounts for the influence of the nutrient and water stress, such that more biomass is allocated to the root with an increase in stress; (2) process-based algorithms for plant nutrient demand and uptake during the growing period, and nutrient translocation during senescence; (3) biomass loss as surface litter/residue to the soil during plant growth and senescence; (4) scaling of potential biomass production by LAI to represent the seasonal changes in the interception of solar radiation by the plant.

All three models (i.e., SWAT, SWAT–GRASS$_D$, and SWAT–GRASS$_M$) were evaluated at eight field sites (with diverse climatic conditions) in Wisconsin, Michigan, and Illinois for biomass yield simulation. Both SWAT–GRASS$_D$ and SWAT–GRASS$_M$ satisfactorily simulated observed yields, and their performance metrics were comparable to or better than those of SWAT at the evaluation sites. Particularly, SWAT–GRASS$_D$ and SWAT–GRASS$_M$ can explicitly simulate root and shoot growth as influenced by climate, nutrient, and water conditions, thereby providing more realistic estimation of the allocation of accumulated biomass and nutrients between aboveground and belowground biomass pools. This feature is critical for reliable estimates of the role of root in nutrient and carbon cycling. Notably, SWAT–GRASS$_M$ in general outperformed SWAT–GRASS$_D$ in terms of both biomass yield and seasonal LAI development. Overall, incorporating DAYCENT's grass module into SWAT added important capabilities to the model for credible assessment of agronomic and environmental impacts of growing perennial grasses for biomass production. The new integrated SWAT–GRASS$_M$ model is a public domain model to support future efforts in sustainable bioenergy production.

Chapter 6: An objective approach for selecting streamgages with near-natural flow

6.1 Introduction

Streamflow observation is a crucial variable in hydrology that provides an aggregate response of hydrological processes, including precipitation, evapotranspiration, and groundwater flow, within a watershed. Streamflow captures the spatial and temporal variation of hydrological processes, which is important for understanding the dynamics of a watershed. Therefore, the hydrological and land surface models that are widely used to study regional hydrology and simulate streamflow across diverse climatic conditions (Choi et al., 2013; Lawrence et al., 2019), are generally calibrated with observed streamflow. Calibrated hydrological models help improve the reliability of the representation of streamflow and water budget components such as evapotranspiration, surface runoff, and groundwater recharge. Additionally, streamflow is widely used to identify long-term trends and assess the impacts of climate variability and extreme events on hydrological processes (Lins and Slack, 2005; Zhang et al., 2001). Scientists and water resource managers are increasingly integrating streamgage data, along with complementary remotely sensed hydrological datasets, such as precipitation, evapotranspiration, and soil moisture. These studies seek to address questions about historical trends and hydrological responses to climate variability, land use change, and evolving water management practices (Coleman and Budikova, 2013; Dudley et al., 2020; Kisi, 2010; Ryberg et al., 2016; Yasarer et al., 2020).

Given the increased risks of floods and droughts, exacerbated by the high climate variability, and the intensification of the hydrologic cycle in the future (IPCC, 2023), the reliable assessment of the spatial-temporal variability of the hydroclimatic variables and their effect on water resource availability is essential for sustainable water resource management. Conventionally, near-natural streamflow data are used for model calibration and observational analysis for environmental impact assessments. However, most of the watersheds of interest are agricultural watersheds or those influenced by human activities. It is worth noting that most of the large-scale hydrologic models overlook the human impacts on streamflow. Furthermore, most of the streamflow data are affected by human activities, such as reservoir operation, diversion of water for irrigation, and irrigation runoff (Kustu et al., 2011) leading to potential inaccuracies in the observational analysis and model results if streamflow data from substantially regulated basins are used. This makes it imperative to select minimally influenced streamgages where the flow variations are primarily driven by climate factors such as precipitation. The selection of minimally influenced streamgages for observational analysis and model optimization and evaluation will improve the overall accuracy in the representation and understanding of hydrological processes. Also, these streamgages serve as the reference to identify human impacts.

There are few objective or semi-objective data-driven approaches for selecting near-natural streamgages with long-term records that account for basin properties. Two commonly used streamgage databases are Geospatial Attributes of Gages for Evaluating Streamflow (GAGES-II) (Falcone, 2011) and U.S. Geological Survey (USGS) Hydro-Climatic Data Network-2009 (HCDN-2009) (Lins, 2012). The

GAGES-II and HCDN-2009 (a subset of the GAGES-II) databases utilize multiple criteria to assess the extent of human influence on streamflow. These criteria include data availability (20 years of complete data from 1950 for GAGES-II), watershed characteristics, a hydrologic modification index based on GIS-derived variables (e.g., presence of dams, reservoir storage, road density, fragmentation of undeveloped land), visual inspections of stream gages and drainage basins using high-resolution satellite imagery and digital topographic imagery (Lins, 2012). The HCDN-2009 dataset is considered to include the streamgages that are minimally affected by anthropogenic influences (Lins, 2012; Newman et al., 2015), and is widely used to evaluate the effect of climate variability, land use change, and water withdrawal on streamflow (Addor et al., 2017; Dudley et al., 2020; Hodgkins et al., 2019; Zhou et al., 2021).

However, the GAGES-II and HCDN-2009 dataset has some notable drawbacks. For instance, both reference and non-reference streamgages have large variations in the hydrologic disturbance index. Hence, the hydrologic disturbance index may not accurately represent the extent of hydrologic alteration in the basin (McManamay et al., 2012). Additionally, it has sparse spatial coverage across the contiguous U.S. (CONUS) and many of these streamgages have relatively small drainage areas. Moreover, it is not completely free from anthropogenic influences (Falcone et al., 2010; Miller and Piechota, 2011). These gages cannot reflect current and future natural streamflow regimes because of human activities that may have occurred after 2009. Therefore, the streamgages in HCDN-2009 are more useful for studies at the watershed scale than the regional scale. Regional scale studies require good spatial coverage with highly heterogeneous watersheds. Moreover, the framework used for identifying reference streamgages is not applicable in other regions of the world due to the lack of data required to determine the anthropogenic modification index. Recent studies have presented alternative approaches to identify minimally influenced streamgages. For example, Zhou et al. (2021) used criteria such as length of the data record, reservoir capacity, runoff ratio, and drainage area, to identify near-natural streamgages and investigate the hydroclimatic influence of vegetation on streamflow. Sando and McCarthy, (2018) considered streamflow to be unregulated if the cumulative drainage area of all upstream dams were less than 20% of the streamgage drainage area. Marti and Rydberg, (2023) developed an objective approach to identify substantially regulated streams based on the dam disturbance metrics (Wieczorek et al., 2021). Similarly, Carlisle et al. (2016, 2009) used empirical statistical models, which required a large number of predictor variables, to identify natural streamflow condition. Although recent advancements in methodologies offer potential improvements for selecting minimally influenced streamgages, there is a lack of a simple data-driven objective approach in selecting streamgages with wide spatial coverage and representing the landscape relevant to the people experiencing the impact of climate variability (Dudley et al., 2020).

To address this issue, we developed and applied a selection algorithm to identify the acceptable reference streamgages that have minimal human disturbances. Since precipitation is the major water source for streamflow, the changes in streamflow should be highly sensitive to changes in precipitation unless human interventions, such as dam operations, alter natural flow. Although the mean precipitation has been used in the GAGES-II to characterize the watershed, one important and straightforward metric overlooked is the correlation between precipitation and streamflow. Assuming a watershed system is impacted only by natural water sources and sinks, the streamflow should be well correlated with precipitation. Using correlation analysis between precipitation and streamflow as a primary tool in the robust data-driven selection algorithm, we investigated if the precipitation-streamflow correlation can be used as an indicator to associate the hydrologic alteration in watersheds due to human activities. We examined the spatial and temporal pattern of precipitation-streamflow correlation and determined the threshold of correlation value based on which streamgages are classified into reference (minimally influenced) and non-reference streamgages. Finally, we utilized the streamflow data from the reference streamgages to assess the precipitation and streamflow trend and characterize the regional characteristics across the contiguous United States (CONUS).

6.2 Materials and Methods

6.2.1 Precipitation and streamflow

The daily precipitation data used in this study was obtained from the NOAA Global Historical Climatology Network Daily (GHCND) dataset (Menne et al., 2012). The GHCND has good temporal coverage from 1880 to the present. We identified GHCND stations with at least 40% available records during 1951-2020 in the CONUS. A total of 8,516 stations of daily precipitation data were selected based on these criteria. We constructed a 30×30 km^2 gridded daily precipitation dataset from the GHCND station data. The steps involved in constructing the gridded precipitation data are described as follows:

1. The climate station data were remapped to the 30×30 km^2 grid cells using the natural neighbor interpolation tool in ArcGIS. The advantage of natural neighbor interpolation is that it uses a Voronoi map to identify the region of influence of each climate station, which is used to calculate the weights of each climate station based on proportionate areas to each grid cell. The precipitation value for each grid cell was then calculated using area-weighted averages of neighboring climate stations.
2. To adjust for elevation differences between GHCND station locations and the grid cell, the Parameter-elevation Regressions on Independent Slopes Model (PRISM) (Daly et al., 1994) precipitation dataset was used. The topographic adjustment involved conservative mapping of PRISM data to the 30km grid. Then the monthly mean value from PRISM was divided by the gridded station data to get the ratio at each grid cell.
3. This monthly ratio was multiplied by the daily gridded value from Step 1 to get the final elevation-adjusted gridded daily precipitation data.

We obtained the daily streamflow observations for streamgages from the USGS. We selected streamgages with daily streamflow data from 1979 to 2020, which consists of 24,219 streamgages within the CONUS.

6.2.2 Watershed characteristics

We obtained several basin characteristics from the GAGES-II dataset, specifically, reservoir storage capacity (Ml/km^2) within the basin, base flow index (BFI), drainage area (km^2), basin elevation (m), watershed fragmentation (%), irrigated area (%), dam density (number of dams per 100 km^2), road density (km of roads per watershed area), impervious area (%), and developed area (%). These basin characteristics are used to identify the human disturbance within a watershed.

6.2.3 Streamgage selection criteria

We propose a simple four-step method, primarily based on a combination of machine learning clustering method and correlation analysis to identify minimally disturbed streamgages in the CONUS. From the pool of 24,219 streamgages, we identified the streamgages as reference (minimally disturbed) or non-reference streamgages based on the following steps:

1. **Length of data record**: Streamgages should have at least 75% of the daily streamflow data for the period of 1979-2020. Zhou et al., (2021) used similar thresholds to select streamgages. This criterion for the record length is essential to detect meaningful variations and trends in streamflow.
2. **K-means clustering**: K-means clustering is an unsupervised machine learning algorithm that partitions a dataset into distinct clusters with data points having similar properties (Hartigan and Wong, 1979). It has been widely used in the identification of hydro-climatologically similar watersheds for environmental assessment and model optimization (Farsadnia et al., 2014; Rateb et al., 2020). K-means clustering is simple, flexible, and can process large datasets quickly (Aytaç, 2020). This method offers a data-driven approach to group different watersheds based on their characteristics that reflect human disturbance. We applied K-mean clustering based on the basin characteristics that are

representative of the hydrologic disturbances. In particular, we included watershed fragmentation (%), irrigated area (%), dam density (number of dams per 100 km^2), road density (km of roads per watershed area), impervious area (%), and developed area (%) as a measure of hydrologic disturbance within the basin. These basin characteristics have been widely used in previous studies (Eng et al., 2019; Falcone, 2011; Lins, 2012) to classify watersheds into minimally disturbed and regulated streamgages. We grouped the streamgages into an optimal number of clusters, and we selected the cluster with minimum mean values of all hydrologic disturbance measures.

3. **Runoff ratio:** The runoff ratio represents the conversion rate of precipitation to total runoff within a basin. It is strongly influenced by climatic conditions (precipitation, temperature, etc.), basin characteristics (slope, elevation, soil, land cover, etc.), and human activities (Huo et al., 2021; Li et al., 2020; Merz and Blöschl, 2009). In the context of human activities, there is a potential for interbasin water transfer, i.e., the transfer of water into a basin through canals or pipelines. This can substantially increase the runoff ratio. Therefore, the runoff ratio has been used to identify watersheds impacted by interbasin water transfer (Newman et al., 2015). In this study, we established a threshold value for runoff ratio based on GAGES-II reference streamgages. The runoff ratio is calculated as the ratio of mean annual streamflow to basin averaged annual total precipitation. We calculated the threshold as the 95th percentile of the runoff ratio from these streamgages. We then excluded the basins with runoff ratio exceeding the threshold from further analysis.

4. **Correlation analysis**: In this study, we used correlation analysis between basin-averaged precipitation and streamflow to further screen for regulated streamgages. This analysis consists of two steps: (1) calculation of Spearman's rank correlation (*R*) at multiple time steps and lag period, and (2) determination of correlation threshold for the classification of streamgages. Due to distinct regional hydro-climatic regimes across the CONUS, streamflow with minimal influence from human activities should show a response to variation in precipitation at multiple timescales ranging from days to months. We performed the cross-correlation analysis between precipitation and streamflow at multiple timescales (ranging from 1 to 30 days at an increment of 5 days). We used basin-average precipitation since streamflow responds to precipitation events within the watershed (Cheung et al., 2008). To remove spurious correlation resulting from human activities (i.e., a maximum correlation was detected at longer lag periods for which physical interpretation was not possible), we removed the correlation values with the lag period exceeding the 75 percentile of the distribution of lag period for each timescale. Finally, we determined the correlation threshold by characterizing the frequency distribution of maximum correlation into two groups by applying the Gaussian mixture model algorithm. This method uses a probabilistic approach to group a given dataset into multiple Gaussian distribution that approximates the distribution of a given dataset (He, 2013; Luke et al., 2017). We separated the streamgages into two clusters representing the high and low correlation values. We used the median correlation value estimated from the low correlation cluster

as a threshold to classify the streamgages as reference or regulated. We classified the streamgages with maximum correlation value (p-value ≤ 0.05) exceeding the threshold as reference and remaining streamgages as regulated.

6.2.4 Trend analysis

We further examined the trend in precipitation and streamflow for selected reference streamgages within the CONUS using the non-parametric Mann-Kendall trend test (Kendall, 1948; Mann, 1945). The Mann-Kendall (MK) test is a widely employed method for detecting monotonic upward or downward trends in hydro-climatology. One of its advantages is that it does not require data to follow a particular distribution or have a complete record for the entire analysis period. However, when it comes to streamflow, the serial correlation poses a challenge, making the conventional MK test unsuitable. To address this, we utilized the pre-whitened MK test in this study to eliminate the influence of serial correlation.

The Mann-Kendall test determines whether to accept the null hypothesis (absence of monotonic trend) or accept the alternative hypothesis (presence of monotonic trend). The MK test is applied to the total annual basin-averaged precipitation and streamflow for the period of 1979 to 2020. In this study, the p-value of 0.05 is used to classify the significance of the trend. The magnitude of trends was calculated using Sen's (1968) slope (Theil, 1992). Previous studies analyzing the trends of hydroclimatic variables in CONUS have found that precipitation and streamflow exhibit different seasonal behavior (Dethier et al., 2020; Lins and Slack, 2005; Martino et al., 2013; Ryberg et al., 2016). Therefore, trend analysis for four climatological seasons was performed as well. Seasons are defined as spring (March, April, May), summer (June, July, August), fall (September, October, November), and winter (December, January, February).

6.3 Results

6.3.1 Cluster analysis

The optimal number of clusters is three based on the silhouette score (Figure F.1). The three clusters have distinct frequency distributions for watershed fragmentation, urban area, road density, and irrigated area (Figure F.2). Cluster 1, Cluster 2, and Cluster 3 account for about 59.5%, 35.5%, and 5% of streamgages, respectively. Cluster 1 has the minimum mean values for the disturbance measures. For example, the median basin developed area, impervious area, basin fragmentation, and dam density are 2.5%, 0.3%, 14.3%, and 0.46, respectively. The developed area and impervious area within watersheds categorized into Cluster 1 generally remain well below 10% and 5%, respectively, aligning with the criteria provided by Hodgkins et al. (2019) for identifying the least disturbed watersheds. This indicates that Cluster 1 represents the streamgages with lower human disturbance on the streamflow. The streamgages in Cluster 2 and Cluster 3 have high human disturbances and are categorized as regulated.

6.3.2 Runoff ratio

The threshold runoff ratio calculated from the streamgages, categorized as the GAGES-II reference streamgages, is 1.04. This is close to the water limit line (runoff ratio =1). Most of the basins lie well below the water limit line with large variability in runoff ratio indicating the influence of heterogeneous climatic conditions and basin characteristics (Figure 6.1). The streamgages below the runoff ratio threshold have a median runoff ratio of 0.33, while the excluded streamgages have a median runoff ratio of 1.37. In this study, the runoff is calculated from the observed streamflow, hence it includes both direct runoff and baseflow. Therefore, the runoff ratio of some selected streamgages could exceed 1.0 where baseflow has a dominant contribution to the streamflow. Nevertheless, a high runoff ratio of excluded streamgages (>1.04) indicates a substantial anthropogenic effect on streamflow due to activities such as return flow from irrigation, substantial reservoir operation, and urban settings. The urban setting and water management practices can affect the contribution of baseflow and surface runoff to streamflow by changing the soil permeability and flow pathways (Nunes et al., 2011).

We find high variability in runoff ratio among the water resource divisions with the median runoff ratio varying between 0.05 and 0.53. In the dry central US, the runoff ratio is low for most basins with a median runoff ratio of 0.13, while in wet eastern and western coastal regions runoff ratio is high with a median value of 0.39 and 0.38, respectively. The large variability across the region indicates that hydro-climatic condition is an important control of the runoff ratio.

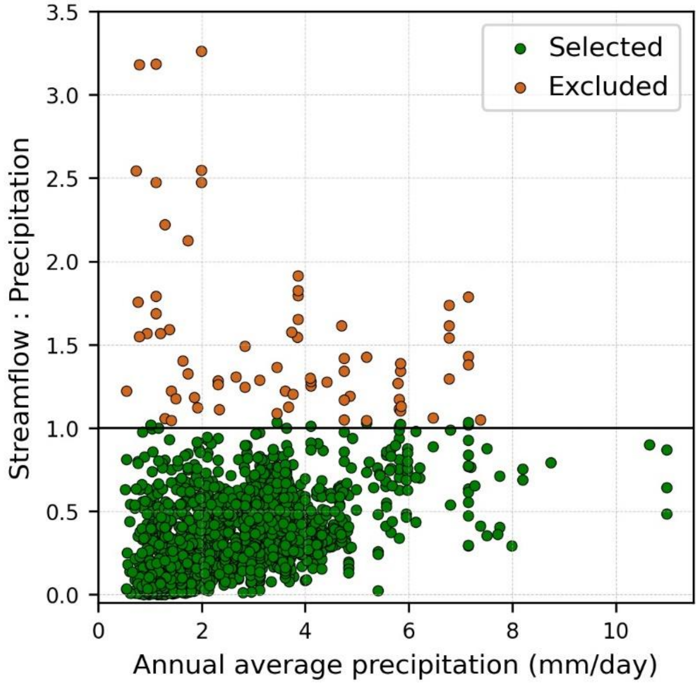

Figure 6.1. Distribution of runoff ratio (ratio of streamflow to precipitation) and basin average precipitation corresponding to streamgages selected from cluster analysis. The horizontal black line indicates the water limit.

6.3.3 Correlation analysis

From a pool of 24,219 streamgages, 2,101 are selected for correlation analysis consisting of 506 (24%) streamgages classified as reference gages in GAGES-II. Cluster analysis helps screen streamgages whose streamflow is influenced by human disturbance to some extent. Notably, numerous streamgages located downstream of the Upper Mississippi, Missouri, and Great Lakes region are excluded from the correlation analysis (Figure F.3b). These areas are recognized for their extensive agricultural activities and water management operations, which substantially influence the streamflow. However, the distribution of maximum correlation calculated for the streamgages screened after cluster analysis and examining the runoff ratio shows the presence of streamgages with a weak correlation between precipitation and streamflow (Figure 6.2). This indicates that watershed classification based on human disturbance measures alone is not sufficient to determine the reference condition of streamgages.

The threshold correlation value estimated from the Gaussian mixture model is 0.32. Streamgages with a maximum correlation ≥0.32 are considered as reference and the remaining streamgages as non-reference (i.e., regulated). After the correlation analysis, 1,544 streamgages are categorized as reference streamgages, which provide broad spatial coverage across the CONUS (Figure F.3b). About 19% (n=97) of the 506 reference streamgages in GAGES-II, selected for correlation analysis, have $R<0.32$ and are classified as non-reference after correlation analysis. This indicates that local human disturbance has changed since the conception of the GAGES-II dataset in these basins. The regional distribution of reference streamgages identified in this study, including reference gages in GAGES-II, are provided in Table F.1. The drainage area of reference streamgages ranges from 2 to 49,264 km^2, with a median drainage area of 867 km^2. The basin elevation ranges from 7 to 3,245 m, with a median elevation of 570 m.

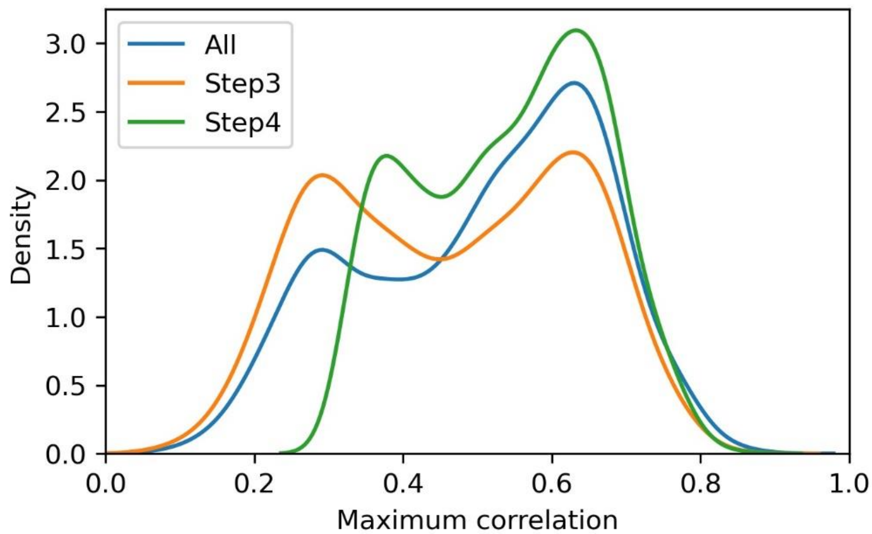

Figure 6.2. Comparison of the frequency distribution of maximum correlation for streamgages selected after steps 3 and 4 of the selection algorithm.

6.3.3.1 Relationship between watershed features and precipitation-streamflow correlation

We examined the relationship between basin characteristics, particularly mean basin elevation and baseflow index, and precipitation-streamflow correlation. We selected these two variables due to their strong relationship with climatic conditions and streamflow (Falcone et al., 2010; Lins, 2012). A comparison between two groups of basins, one selected for correlation analysis and the other excluded, shows that the excluded streamgages have no discernible relationship between R and basin elevation and baseflow index (Figures F.4a and F.4c). In contrast, the streamgages selected for the correlation analysis generally show an increase in R as both elevation and baseflow index decrease (Figures F.4b and F.4d).

6.3.3.2 Spatial and temporal distribution of correlation

We assessed the regional characteristics of the spatial and temporal relationships between precipitation and streamflow correlation at the water resource division scale, which represents regions with major river systems in the U.S. as defined by the 2-digit Hydrologic Unit Codes of the USGS (Figure F.3a). Figure 6.3 shows the spatial relationship between precipitation and streamflow correlation at multiple temporal scales and lag periods for streamgages selected for correlation analysis. In general, we found a significant correlation at the monthly scale (25 to 30 days) across all water resource divisions (Figure 6.3a). About 69.3%, 22.5%, and 5% of streamgages show maximum correlation at the timescale of 30, 25, and 1 day, respectively (Figure F.5). Notably, the R is high at smaller timescales (1D to 15D) for streamgages in California, the western Pacific Northwest, southeastern Missouri, Upper Mississippi, Ohio, and the western South Atlantic Gulf.

At a smaller time scale, multiple factors contribute to noises in precipitation-streamflow relationships resulting in low correlation values for most streamgages. For example, most of the precipitation in the Rocky Mountains occurs in the form of snow in winter which contributes to streamflow in a longer time scale (months to seasons). Likewise, in Florida, basins are dominated by sandy soils which promote infiltration. A large fraction of precipitation is transported to the river through subsurface processes (such as lateral flow and baseflow). As a result, it takes a long time to observe the response of streamflow to precipitation events. When a larger time step is used, most of the noises are smoothed out and hence correlation may increase, as indicated by the spatial distribution of correlation across the CONUS, particularly over the Rocky

Mountains (Figure 6.3). Hence, with the increase in temporal scale the number of streamgages showing significant correlation ($R \geq 0.3$) also increased.

The streamgages with the highest correlation are concentrated across a narrow corridor spanning from the Gulf Coast and Texas in the South to the Ohio Valley, and the northeastern Mid-Atlantic region with a temporal scale of 20D to 30D. Notably, the highest correlation with the temporal scale ranging from 1D to 30D is found along the western coastal region, which is characterized by highly variable spatial and temporal precipitation patterns, topography, and climatic conditions. The heterogeneity in the temporal scale of the correlation between precipitation and streamflow at different lag periods suggests that in addition to climatic conditions other than precipitation, factors such as temperature and watershed characteristics also play a substantial role in determining the streamflow response to changes in precipitation.

Figure 6.4 shows a boxplot of the maximum lagged correlation by water resource divisions in the CONUS, which illustrates the regional differences in the distribution of correlation. In general, streamgages with significantly high correlation ($R \geq 0.5$) are concentrated in the Lower Mississippi, the South Atlantic Gulf, the Tennessee, Ohio, and the Mid-Atlantic. Meanwhile, streamgages with low correlation ($R < 0.5$) are concentrated in the Upper Colorado, eastern parts of the Pacific Northwest and California, and western parts of the Upper Mississippi. The snowmelt runoff is the major contributor to streamflow in these regions during the spring months. The delayed response of streamflow to precipitation events in these regions contributes to the low correlation values.

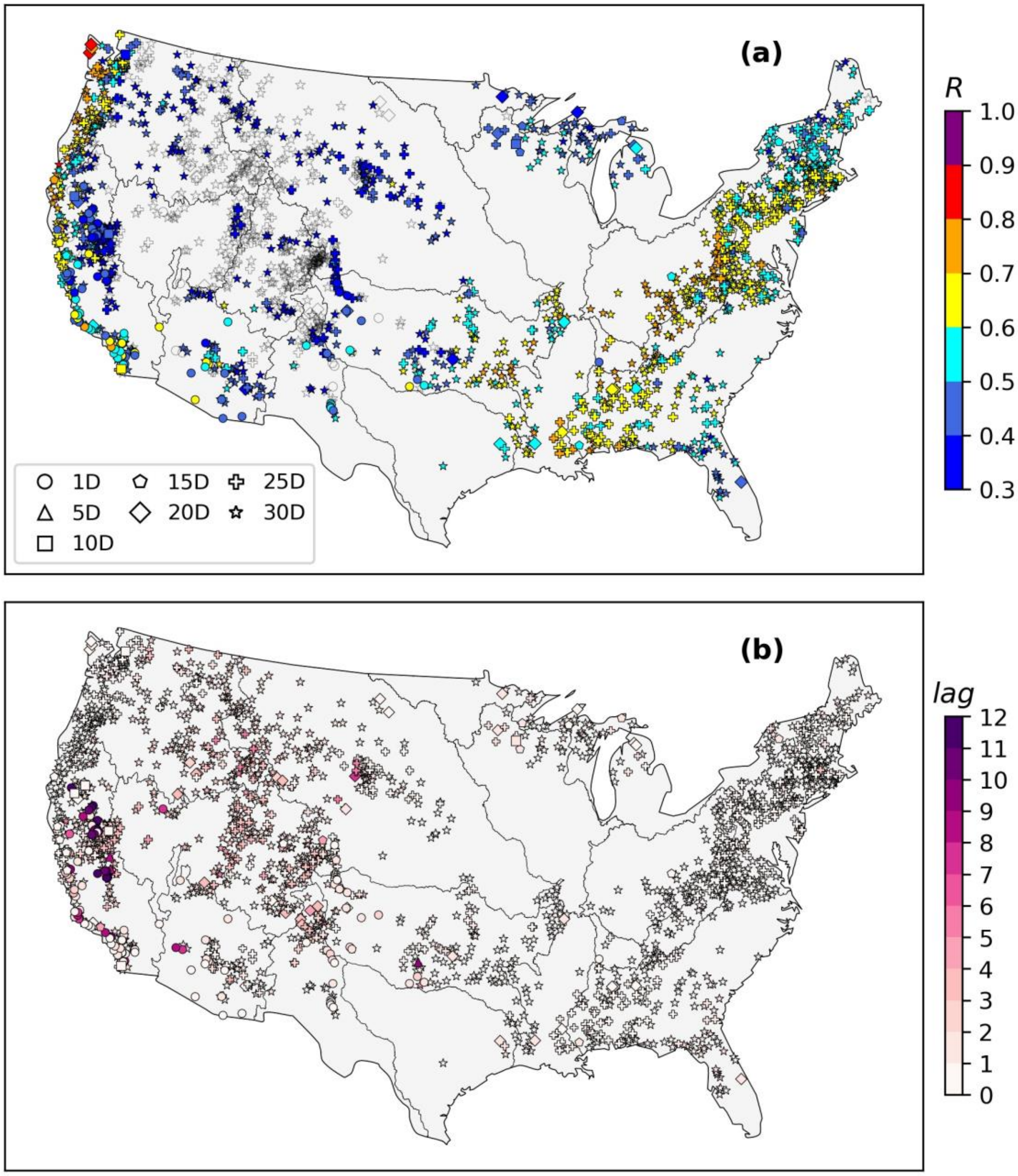

Figure 6.3. Maximum lag-correlation between basin-averaged precipitation and streamflow at multiple time windows (1D-30D) from 1979 to 2020 (a) and lag period corresponding to the maximum correlation. The streamgages with a data record length of 75% are shown here. The marker type indicates the temporal scale at which the maximum correlation was calculated.

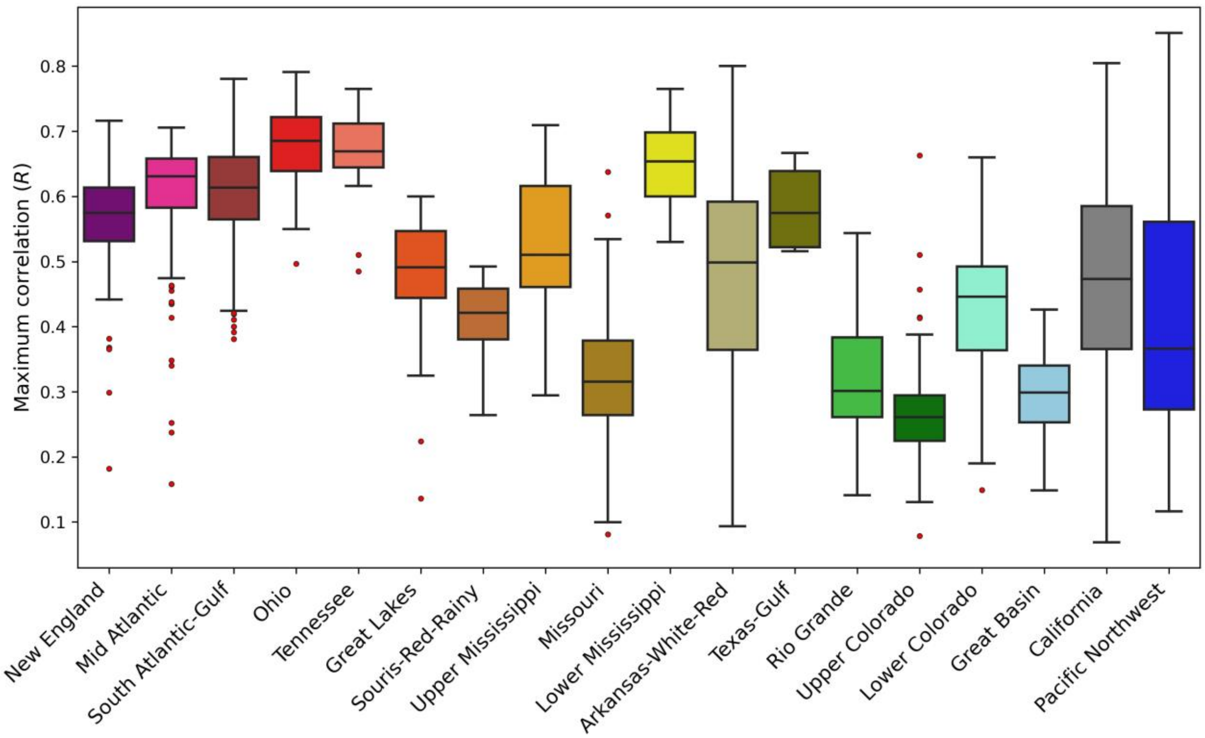

Figure 6.4. Distribution of correlation for each water resource division in CONUS.6.3.4 Trend analysis

6.3.4 Trend analysis

6.3.4.1 Annual precipitation and streamflow

The spatial distribution of annual precipitation and streamflow trends shows two distinct regions with opposite trends (Figure 6.5). In the Upper Colorado, the Lower Colorado, and the northern parts of Rio Grande decreasing trends in precipitation are observed. In contrast, across most of the central and eastern U.S., there is an increase in precipitation trends (Figure 6.5a), consistent with the findings reported by Bishop et al. (2019).

The spatial distribution of streamflow trends is similar to precipitation trends for most streamgages (Figure 6.5b). For example, regions with positive streamflow trends, such as Ohio, New England, Mid-Atlantic, and northern parts of Upper Mississippi, are coherent with the corresponding precipitation trends in those regions. Similar trends in annual streamflow are also reported by Zheng et al. (2021). The spatial coherence in the precipitation and streamflow trends indicates the presence of common climatological factors acting in these areas, resulting in a uniform response. Additionally, these regions correspond with the streamgages showing the largest correlation between precipitation and streamflow and experiencing the largest increase in total annual precipitation.

In contrast, the Souris Red Rainy, the Great Lakes, the Arkansas-White-Red, the South Atlantic Gulf, southern parts of the Mid-Atlantic, and Tennessee experience increasing precipitation trends that do not result in increasing streamflow trends. Most of the streamgages in these regions show no trend, and in some cases even exhibit decreasing trends. This indicates that the streamflow trends in these regions are influenced by a combination of factors beyond just precipitation, including temperature, land use, and watershed properties. The hydrological influences from precipitation, temperature, and vegetation may have contributed to an absence of trend in streamflow within these regions (Stahl et al., 2010).

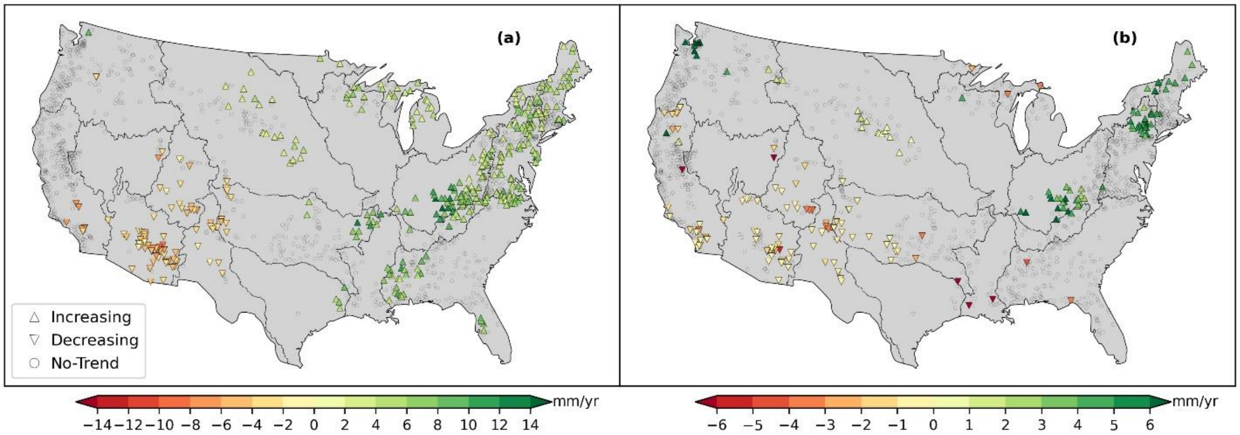

Figure 6.5. Spatial distribution of annual (a) precipitation and (b) streamflow trends for the period of 1979-2020.

6.3.4.2 Seasonal precipitation and streamflow

The precipitation trend in the CONUS varies distinctly across different regions and seasons (Figure 6.6). In spring, precipitation increased in the Great Lakes, Souris Red Rainy, Upper Mississippi, and Arkansas White Red. Meanwhile, precipitation decreased in Upper and Lower Colorado. In summer, precipitation increased in the eastern U.S., but no significant trend was observed in the Great Lakes region. Notably, in the fall, the central and eastern U.S. did not exhibit any significant trends. Meanwhile, summer and fall precipitation decreased significantly in California, Pacific Northwest, and Upper Colorado. In winter, the precipitation increased in the Northeast and Midwest regions while no trends were observed in the Western U.S. The spatial pattern of season precipitation trend is similar to the results reported by Ficklin et al. (2016) for most seasons, except for winter. Ficklin et al. (2016) found increased precipitation in the western U.S. and decreased precipitation in the south and southeastern coastal U.S., while we found no such trend. It is important to note that

Ficklin et al. (2016) used mean precipitation corresponding to 674 HCDN-2009 streamgages in their analysis, while our study utilized total precipitation. Likewise, Bishop et al. (2019) found an increasing trend in precipitation during fall in the southeast U.S. However, our findings indicate no trend in fall precipitation. Moreover, we observed the largest increase in precipitation in the southeast during summer, in the northeast during winter, and in the upper Midwest during spring.

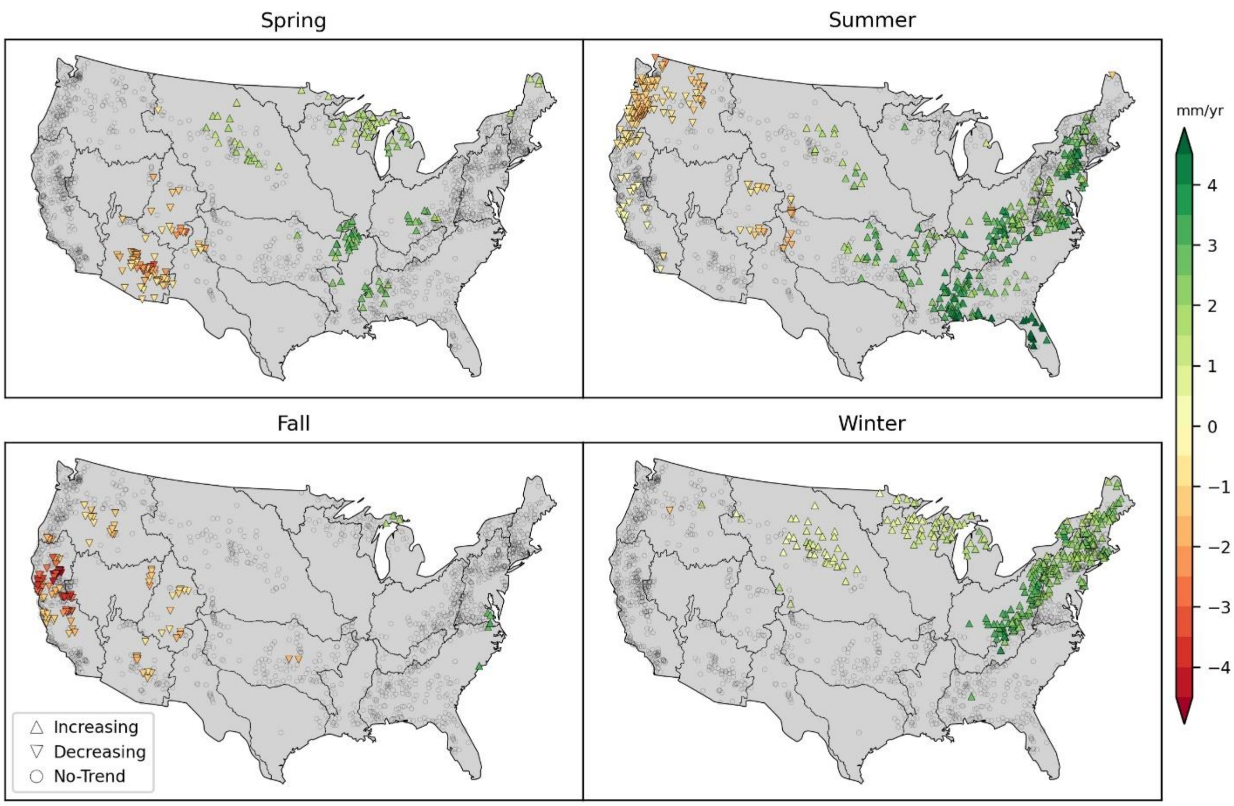

Figure 6.6. Spatial distribution of seasonal precipitation trend for the period of 1979-2020.

The seasonal streamflow trends exhibit less seasonal variability but with varying magnitudes as shown in Figure 6.7. In the western U.S., including Upper and Lower Colorado, California, and the southern parts of the Pacific Northwest, we observe decreasing trends in streamflow. Interestingly, even though no winter precipitation trend is evident in the Upper and Lower Colorado, these regions show decreasing streamflow trends. Notably, the slope of the trend in these regions is relatively small (±0.4mm/yr). The decoupling of precipitation and streamflow trends during the winter season likely suggests a delayed response of streamflow to fall precipitation, potentially influenced by baseflow dynamics on watershed hydrology during winter (Ficklin et al., 2016).

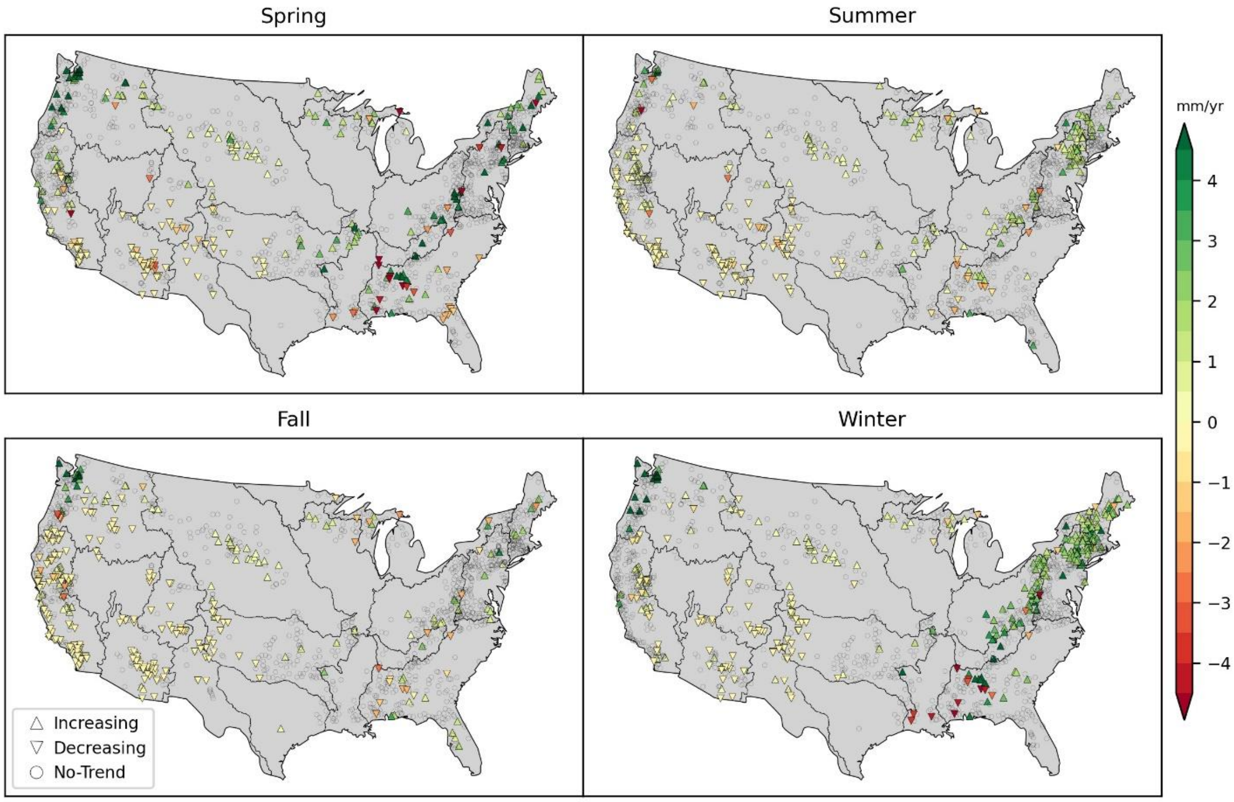

Figure 6.7. Spatial distribution of seasonal streamflow trend for the period of 1979-2020.

In the northcentral U.S., we identify consistent but weak increasing trends in streamflow for all seasons. In the eastern U.S., the seasonal streamflow trends present a mix of both increasing and decreasing patterns. Numerous streamgages in Ohio, Mid-Atlantic, and New England exhibit strong positive trends during winter. Interestingly, the mixed streamflow trends in the southeastern U.S. despite an increasing precipitation trend, suggest a disconnection between precipitation and streamflow trends. This is likely due to high evapotranspiration in these regions, leading to drier soils, thereby offsetting the impact of increased precipitation.

6.4 Discussion

While streamflow data are becoming widely accessible, insufficient information on topography, water use, land use, and the impact of human activities in the basins, constrain the rigorous quality checks necessary for identifying reference streamgages. Nonetheless, several studies have used commonly available basin characteristics, such as reservoir volume, fraction of urban area, an analysis of basin water balance components, and even visual inspection as a quality check procedure to categorize streamgages as reference or regulated. Despite these efforts, a simple and objective approach that utilizes easily accessible hydro-climate and basin properties datasets for identifying reference streamgages is lacking. In this study, we proposed a selection method primarily based on a clustering algorithm and correlation analysis between precipitation and streamflow at various temporal scales and lag periods, complemented by a systematic screening process using basin properties to identify streamgages with minimally disturbed streamflow.

We used K-means clustering to group watersheds based on their characteristics that reflect various aspects of human disturbance. While K-means provides a simple and fast approach, alternative advanced techniques, such as hierarchical clustering or random forests could provide more refined grouping, leading to more accurate identification of reference streamgages. The watershed characteristics representing the human disturbance used in our analysis were obtained from the GAGES-II dataset, which represents the watershed condition before 2009. To further enhance the accuracy of reference streamgage identification, the use of human disturbance measures derived from more recent remotely sensed datasets is needed.

The near-natural streamflow is an important consideration in water resource assessment and hydrologic modeling studies, as it provides a more accurate and representative response to hydroclimatic conditions of the basin. Most of the studies investigating the relationship between climate variability and streamflow have emphasized the importance of objective data-driven approaches for the selection of near-natural streamgages (Eng et al., 2019; McManamay et al., 2022). These studies have primarily used either HCDN-2009 or GAGES-II reference streamgages, which are further screened based on data record length. While this approach helps identify appropriate streamgages for further analysis, its applicability is limited to the U.S. due to the complexity involved in constructing these datasets. The selection process includes multiple screening stages, including the visual examination of topographic maps and expert judgments at the watershed level, which requires time-consuming analyses and resources. This makes it difficult to develop a similar dataset in other data sparse regions. In contrast, the selection method introduced in this study offers a simple and objective alternative that can be easily implemented in data-sparse regions. The reference streamgages identified in our study cover diverse basin characteristics and have a large sample size, which will help improve the generalization of environmental and anthropogenic impact assessment. These streamgages also serve as valuable calibration and validation points for hydrological models, thereby it could help enhance the accuracy and confidence in model projections.

We used the reference streamgages identified in this study to examine the spatial patterns of the precipitation and streamflow trends. The spatial patterns of precipitation and streamflow trends on annual and seasonal scales are similar to the findings of previously published studies (Hodgkins et al., 2019; Ryberg et al., 2016). However, our trend analysis revealed interesting anomalies in the southeastern U.S. and the Mid-Atlantic region. Despite an increasing annual precipitation trend, most streamgages showed no trend in annual streamflow, while some even exhibited a decreasing trend. Similar anomalies have also been reported in some streamgages in Europe by Stahl et al. (2010). These anomalies can be attributed to the high sandy soil content in basins across the southeastern U.S., allowing these basins to retain additional precipitation as basin storage, thereby resulting in no trend in streamflow. To better understand these anomalies, further investigation is needed by taking into consideration additional variables such as temperature, land use, and water balance components, which can substantially influence hydrological processes. For instance, land use change can impact runoff, evapotranspiration, and soil infiltration, subsequently affecting streamflow trends (Zeng et al., 2021).

6.5 Conclusion

In this study, we present a simple and objective method for identifying reference streamgages. We use K-means clustering to identify a group of basins with minimum human disturbance. We then apply the correlation analysis between basin-averaged precipitation and streamflow to further screen for regulated streamgages in two stages: (1) calculating Spearman’s rank correlation at multiple time steps and lag period, and (2) determining the correlation threshold using Gaussian mixture model algorithm to classify streamgages as reference or regulated. The selection method identifies 1,544 streamgages as reference streamgages, which provides broad spatial coverage across the CONUS. Notably, numerous streamgages located downstream of the Upper Mississippi, Missouri, and Great Lakes region are categorized as regulated streamgages.

We found regional differences in the spatial distribution of the correlation between precipitation and streamflow. The streamgages with the highest correlation are concentrated in the western coastal U.S. and across a narrow corridor spanning from the Gulf Coast and Texas in the South to Ohio Valley, and the northeastern Mid-Atlantic region. We also found a distinct relationship between the correlation and basin characteristics for the streamgages selected for correlation analysis. We found that generally correlation increases as both basin elevation and baseflow index decrease.

We further analyzed annual and seasonal precipitation and streamflow trends across the CONUS for reference streamgages. The northeast and southwest U.S. show consistent but opposite trends in annual precipitation and streamflow. Seasonal precipitation trends vary distinctly across different regions and seasons, while seasonal streamflow trends show less seasonal variability in the CONUS. In contrast, we found a mix of increasing and decreasing streamflow trends in the southeastern U.S. despite an increasing precipitation trend. This indicates a disconnection between precipitation and streamflow trends, likely due to high evapotranspiration in these regions that offset the impact of increased precipitation.

As the water resource management strategies for climate resilience will require periodic examination and evaluation of existing streamgages, the streamgage selection approach presented here can be valuable. It will assist water resource managers and the regional hydrologic modeling community in identifying and selecting appropriate streamgages to assess the impact of climate change and land use changes on hydrologic processes or to optimize hydrologic models for improved representation of water balance and land-atmosphere interactions.

Chapter 7: Future Work

In this study, the irrigation sub-model and plant growth sub-model of the SWAT model were enhanced to provide an improved representation of water management practices, and biomass production and allocation for perennial grasses. The SWAT project was configured for the U.S Northern High Plains (NHP) aquifer region run using the modified model, which has shown to provide reasonable simulation of hydrological processes and agricultural production in the region. I am working on enhancing the plant (grass and forest) sub-model in the Soil and Water Assessment Tool-Carbon (SWAT-Carbon) (Zhang et al., 2013b) to improve the estimation of biomass production and allocation, as well as nutrient and carbon cycling of perennial bioenergy grasses like Switchgrass and Miscanthus. I plan to apply the modified SWAT-Carbon on large watersheds such as NHP, and further assess the influence of climate feedback scenarios on the soil organic carbon and nutrient cycling in the NHP. I plan to expand this modification to model forest ecosystem and integrate it into SWAT-Carbon to improve the representation of hydrologic and carbon cycling for forest and incorporate rapidly growing remotely sensed datasets representing plant phenology and hydrologic processes, to improve model representation of biogeochemical variables. These model improvements will provide guidance for better watershed conservation practices to help improve water quality.

Furthermore, this study also presented a data-driven objective approach to screen near-natural streamgages. The annual and seasonal trend analysis of precipitation and streamflow associated with the selected streamgages shows results consistent with the published studies and reveals interesting anomalies in precipitation and streamflow trends in the southeastern U.S. that were otherwise ignored. I plan to expand this analysis to examine the streamflow response to historical and future changes in large scale regional circulation patterns such as Great Plains Low Level Jet. Additionally, I plan to utilize the streamflow data from the selected near-natural streamgages to evaluate their impact on hydrological model optimization and model performance. The results from these experiments will help to establish the newly developed screening method as a standard approach to identify near-natural streamgages that could be easily implemented in data scarce regions.

Appendix A. SWAT model results for the Northern High Plains Aquifer region

A.1 SWAT setup

A.1.1 Reservoir parameters and operation

Reservoir operations were simulated using the target release method with a specified minimum and maximum monthly discharge. The target release method represents the general rules of reservoir operation (water preservation and flood control) and simulates reservoir water release as a function of reservoir target storage. The reservoir target storage is set at the emergency spillway elevation for the non-flood season and at the primary spillway elevation for the flood season. The minimum and maximum monthly flow from each reservoir was estimated based on the discharge information obtained from US Army Corps of Engineers (USACE), US Bureau of Reclamation (USBR) and US Geological Survey (USGS) and converted to the SWAT input format. Reservoir parameters such as surface area and storage volume at the principal spillway and emergency spillway were obtained from the USACE and the USBR (USBR, 2019; USACE, 2013). The reservoirs simulated in the model and their corresponding parameters are listed in Table A1.

Table A.1. Reservoir summary

S.No	**Name**	**ESA[1] (ha)**	**EVOL[2] (10^4 m^3)**	**PSA[3] (ha)**	**PVOL[4] (10^4 m^3)**
1	Bonny reservoir	2038.07	15889.69	133.96	88.32
2	Box butte reservoir	832.87	5638.24	649.54	3830
3	Calamus reservoir	2127.10	16354.71	1181.72	6439.38
4	Cedar Buff reservoir	4366.71	46549.81	2779.88	847.28
5	Enders dam	973.30	9193.13	266.29	1228.42
6	Grayrocks reservoir	1462.46	13283.35	798.47	4663.73
7	Guernsey reservoir	964.00	5525.99	542.30	1945.81

8	Harlan county lake	9232.42	102230.82	5397.89	39445.09
9	Harry strunk	1409.57	6502.29.29	368.6868	1788.67
10	Kanopolis lake	5648.80	45549.70	3660.51	6102.52
11	Kirwin reservoir	4305.60	38801.33	2052.23	12264.74
12	Lake Mcconaughy	12308.14	216636.09	8903.40	177312.75
13	Merritt reservoir	1303.94	10640.12	1177.27	9203.24
14	Milford lake	13446.60	93333.61	6357.43	47959.68
15	Norton	2151.39	16696.02	882.65	4456.19
16	Red willow/Hugh butler	1085.00	10493.21	289.36	1100.39
17	Trenton/Swanson dam	3231.53	30389.49	792.40	2571.93
18	Turtle creek lake	21732.39	278419.26	4998.05	41333.91
19	Waconda lake	13631.11	89179.12	5100.03	23828.74
20	Webster reservoir	3431.05	32159.66	1403.09	9543.43
21	Wheatland reservoir 2	3278.07	18528.35	2792.43	13868.76
22	Wilson reservoir	13712.05	205620.50	3660.51	29915.34

[1]Emergency spillway area
[2]Emergency spillway volume
[3]Principal spillway area
[4]Principal spillway volume

A.2 SWAT-MODFLOW coupling

A.2.1 SWAT irrigation source assignment

To determine the appropriate irrigation source for cropland HRUs in SWAT, the grid based irrigation well locations from the Peterson et al. (2016) model were used to determine SWAT cropland HRUs irrigated with groundwater. Each MODFLOW well was mapped to the overlapping HRU (cropland) using ArcGIS. Then the irrigation source was assigned using the following framework: (i) if an irrigation well was mapped to the HRU classified as irrigated cropland, groundwater was assigned as the irrigation source (ii) if a HRU classified as irrigated cropland was not associated with any irrigation well, the river was assigned as the irrigation source, and (iii) if an irrigation well was mapped to the dry cropland, then the auto-irrigation function was used with groundwater as the irrigation source.

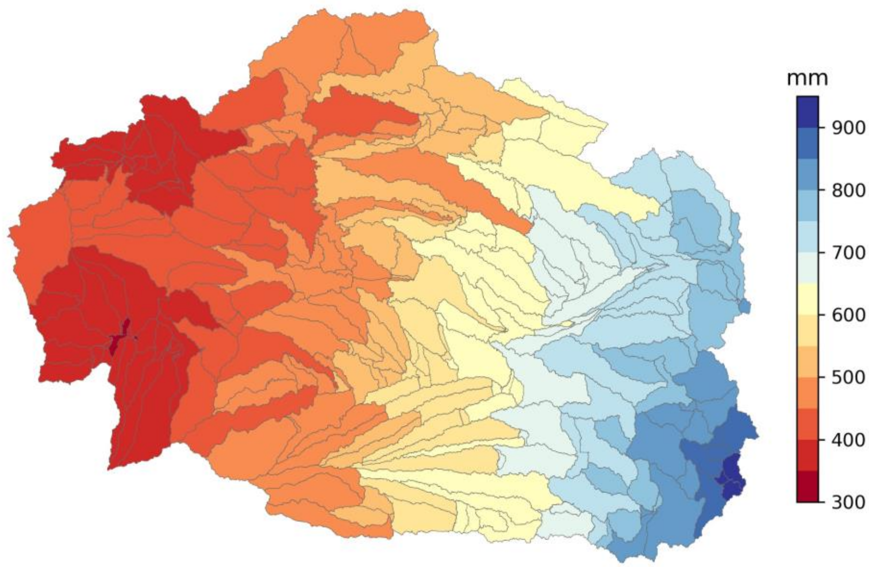

Figure A.1. North American Regional Reanalysis (NARR) based average annual precipitation (1982-2008) at the sub-basin scale for SWAT domain.

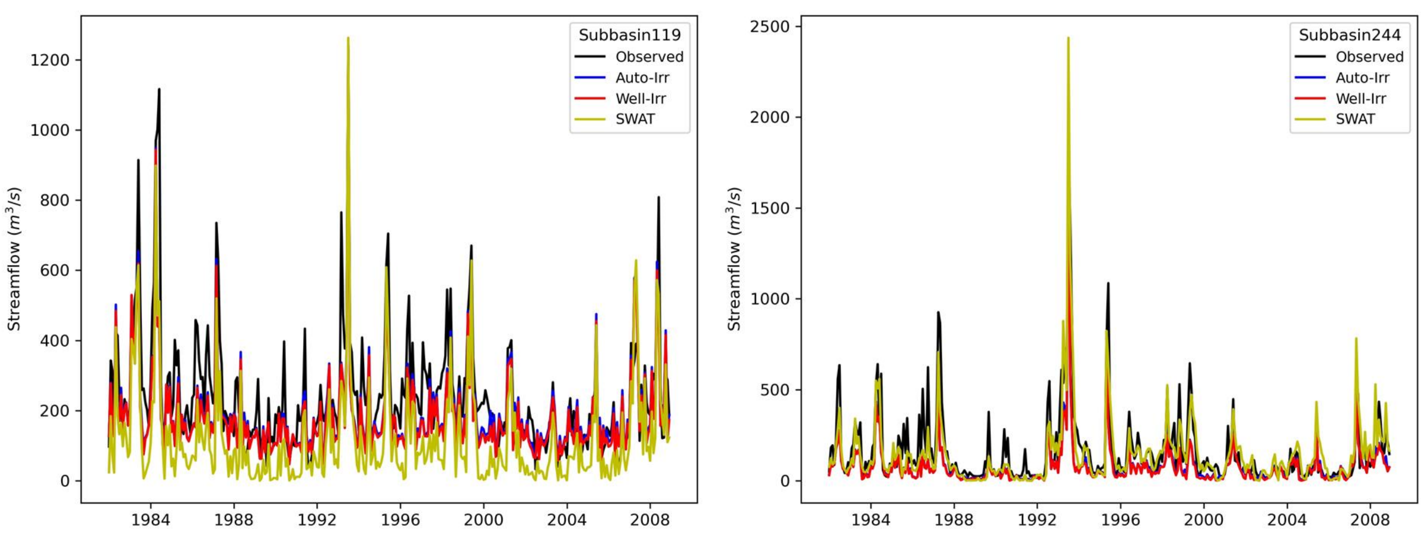

Figure A.2. Monthly mean streamflow at the outlet of watersheds in Northern High Plains.

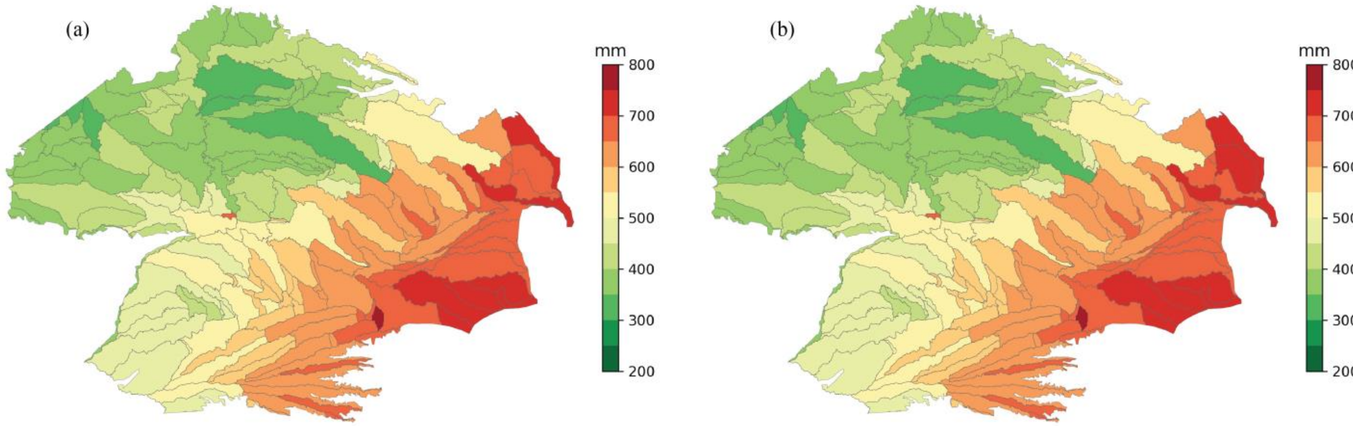

Figure A.3. Sub-basin level mean annual evapotranspiration simulated by (a) SWAT only and (b) Well-Irr, for 2000-2008.

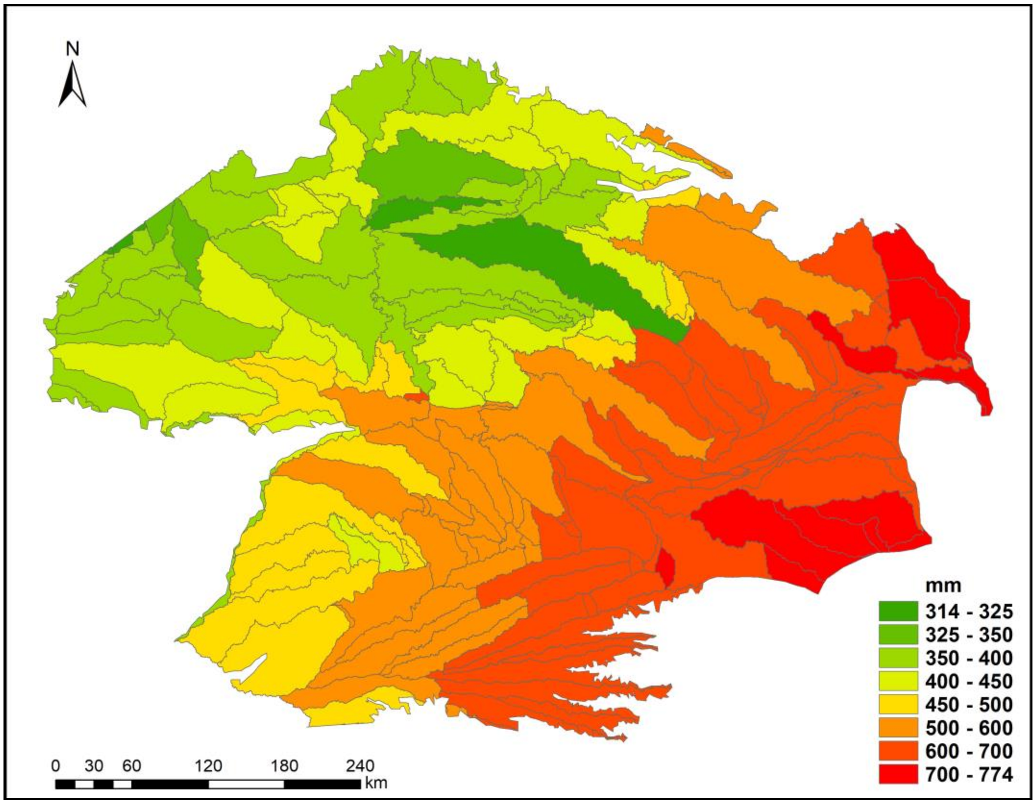

Figure A.4. Sub-basin level mean annual evapotranspiration estimated from Moderate Resolution Imaging Spectroradiometer (MODIS) from 2000-2008.

Appendix B. SWAT model result for land use and climate feedback scenarios

Table B.1. Changes in precipitation (growing season) and average annual temperature relative to the corresponding control scenarios.

Scenario	Present		Future	
	Precipitation (%)	Average temperature (°C)	Precipitation (%)	Average temperature (°C)
MPI-mz	-0.9	-0.04	0.2	-0.03
MPI-miscan	-0.7	-0.14	3.6	-0.14
MPI-miscan_ecane	-0.7	-0.14	6.6	-0.16
MPI-miscan_ecane_mz	2.4	-0.28	6.3	-0.30
CESM-mz	3.4	-0.05	4.2	-0.02
CESM-miscan	2.9	-0.14	13.6	-0.19
CESM-miscan_ecane	7.8	-0.15	7.5	-0.13
CESM-miscan_ecane_mz	2.5	-0.26	11.5	-0.29

Note: mz, miscan, miscan_ecane, and miscan_ecane_mz represents scenarios with climate-crop feedback from maize, miscanthus, miscanthus+energycane, and miscanthus+energycane+maize, respectively.

Table B.2. List of parameters selected for sensitivity analysis of monthly streamflow.

Parameters	**Description**	**File**	**Min**	**Max**
r_CN2	SCS runoff curve number	mgt	-0.2	0.2
v_EPCO	Plant uptake compensation factor	hru	0.75	1.00
v_ESCO	Soil evaporation compensation factor	hru	0.75	1.00
v_SLSOIL	Slope length for lateral subsurface flow (m)	hru	0	150
r_SLSUBBSN	Average slope length (m)	hru	-0.3	0.3
v_LAT_TTIME	Lateral flow travel time (days)	hru	0	180
r_CANMX	Maximum canopy storage (mm H_2O)	hru	-0.5	0.5
a_GWQMN	Threshold depth of water in the shallow aquifer required for return flow to occur (mm)	gw	-500	500
v_GW_REVAP	Groundwater "revap" coefficient	gw	0.02	0.2
v_REVAPMN	Threshold depth of water in the shallow aquifer for "revap" to occur (mm)	gw	0.01	500
v_GW_DELAY	Groundwater delay (days)	gw	30	450
v_ALPHA_BF	Baseflow alpha factor (days)	gw	0	1
r_SOL_AWC	Available water capacity of the soil layer (mm H_2O/mm soil)	sol	-0.3	0.3
r_SOL_BD	Moist bulk density (Mg/m^3)	sol	-0.3	0.3
r_SOL_K	Saturated hydraulic conductivity (mm/hr)	sol	-0.3	0.3

Table B.3. Calibrated parameter values for monthly streamflow at 10 locations.

Parameters	Description	Min value	Max value	Sub 41	Sub 95	Sub 110	Sub 120	Sub 141	Sub 158	Sub 196	Sub 208	Sub 246	Sub 260
r_CN2	SCS runoff curve number	-0.4	0.4	-0.385	-0.114	-0.049	0.049	0.129	-0.197	-0.098	0.009	0.001	-0.026
v_SLSOIL	Slope length for lateral subsurface flow	0	200	178.16	25.54	53.92	18.413	107.887	188.585	97.889	–	–	–
v_ESCO	Soil evaporation compensation factor	0.70	0.95	0.723	–	–	–	–	0.827	0.933	–	–	–
v_EPCO	Plant uptake compensation factor	0.70	0.97	0.954	–	0.736	0.776	0.926	0.898	0.751	0.957	0.808	–
v_LAT_TTIME	Lateral flow travel time	0	250	–	–	240.18	177.89	231.031	87.707	–	–	–	–
r_SOL_K	Saturated hydraulic conductivity	0.5	-0.5	-0.137	0.111	–	–	-0.002	-0.481	0.102	–	–	–
r_SOL_AWC	Available water capacity of the soil layer	-0.4	0.4	0.417	–	0.184	–	–	–	–	–	–	–
r_SOL_BD	Moist bulk density	-0.5	0.5	-0.489	0.253	–	–	0.299	-0.047	0.351	–	–	–
a_GWQMN	Threshold depth of water in the shallow aquifer required for return flow to occur (mm)	-650	650	–	–	–	–	–	623.268	–	-323.25	–	–
v_GW_DELAY	Groundwater delay (days)	30	450	–	–	–	–	–	230.098	–	–	–	–
v_GW_REVAP	Groundwater "revap" coefficient	0.02	0.2	–	0.022	–	0.123	0.083	0.181	–	–	–	–
v_ALPHA_BF	Baseflow alpha factor (days)	0	1	–	0.813	–	0.194	0.384	–	–	–	–	–
r_OFLOWMN	Minimum flow discharge from reservoir	-0.4	0.4	-0.365	–	–	–	–	–	–	–	–	–
r_OFLOWMX	Maximum flow discharge from reservoir	-0.4	0.4	-0.257	–	–	–	–	–	–	–	–	–

Note: r, v, and a represent the relative, replacement, and absolute changes in model parameters respectively. "–" indicates that the outlet is not sensitive to the parameter.

Table B.4. List of parameters selected for sensitivity analysis of monthly instream total nitrogen.

Parameters	**Description**	**File**	**Min**	**Max**
r_ANION_EXCL	Fraction of porosity from which anions are excluded	sol	-0.3	0.3
r_CDN	Denitrification exponential rate coefficient	bsn	-0.3	0.3
r_HLIFE_NGW	Half-life of nitrate in the shallow aquifer (days)	gw	0	100
r_SDNCO	Denitrification threshold water content	bsn	-0.3	0.3
v__SHALLST_N	Concentration of nitrate in groundwater contribution to streamflow from subbasin (mg N/l)	gw	0	1000
v_AI5	Rate of oxygen uptake per unit NH3-N oxidation (mg O_2/mg NH_3-N)	wwq	3	4
v_AI6	Rate of oxygen uptake per unit NO2-N oxidation (mg O_2/mg NO_2-N)	wwq	1	1.14
v_BC1	Rate constant for biological oxidation of NH4 to NO2 in the reach at 20 °C (1/day)	swq	0.1	1
v_BC2	Rate constant for biological oxidation of NO2 to NO3 in the reach at 20 °C (1/day)	swq	0.2	2
v_BC3	Rate constant for hydrolysis of organic N to NH4 in the reach at 20 °C (1/day)	swq	0.2	0.4

v_ERORGN	Organic N enrichment ratio for loading with sediment	hru	0	5
v_FISCO	Nitrogen fixation coefficient	bsn	0.3	0.6
v_K_N	Michaelis-Menton half-saturation constant for nitrogen (mg N/L)	wwq	0.01	0.3
v_N_UPDIS	Nitrogen uptake distribution parameter	bsn	5	35
v_NPERCO	Nitrogen percolation coefficient	bsn	0	1
v_RS3	Benthic source rate for NH4-N in the reach at 20 °C (1/day)	swq	0	1
v_RS4	Rate coefficient for organic N settling in the reach at 20 °C (1/day)	swq	0.001	0.1
v_RSDIN	Initial residue cover (kg/ha)	hru	0	100
v_SOL_NO3	Initial NO3 concentration in the soil layer (mg/kg)	chm	0	100
v_SOL_ORGN	Initial organic N concentration in the soil layer (mg/kg)	chm	0	100

Table B.5. Calibrated parameter values for monthly total instream nitrogen.

Parameters	Description	Fitted value
v_NPERCO	Nitrogen percolation coefficient	0.408
r_SDNCO	Denitrification threshold water content	-0.040
v_N_UPDIS	Nitrogen uptake distribution parameter	8.383
r_CDN	Denitrification exponential rate coefficient	-0.168
v_ERORGN	Organic N enrichment ratio	4.939
v_SOL_ORGN	Initial organic N concentration in the soil layer [mg/kg]	93.125
r_ANION_EXCL	Fraction of porosity from which anions are excluded	0.229
v_SOL_NO3	Initial NO3 concentration in the soil layer [mg/kg]	85.275
v_RS3	Benthic source rate for NH4-N in the reach at 20 °C [1/day]	0.601
v_RS4	Rate coefficient for organic N settling in the reach at 20 °C [1/day]	0.346
v_BC2	Rate constant for biological oxidation of NO2 to NO3 in the reach at 20 °C [1/day]	0.695
v_BC3	Rate constant for hydrolysis of organic N to NH4 in the reach at 20 °C [1/day]	0.284

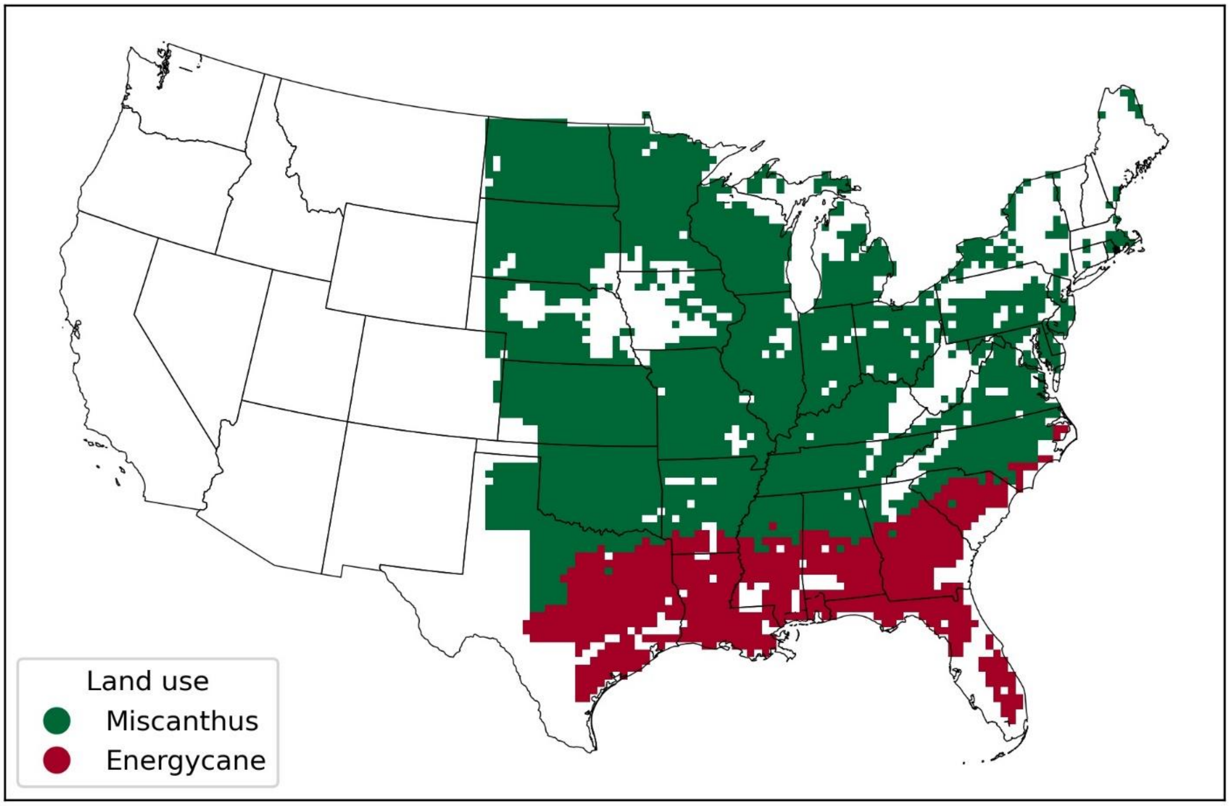

Figure B.1. Spatial distribution of miscanthus and energycane production. Grids with marginal land allocation of less than 1% are masked.

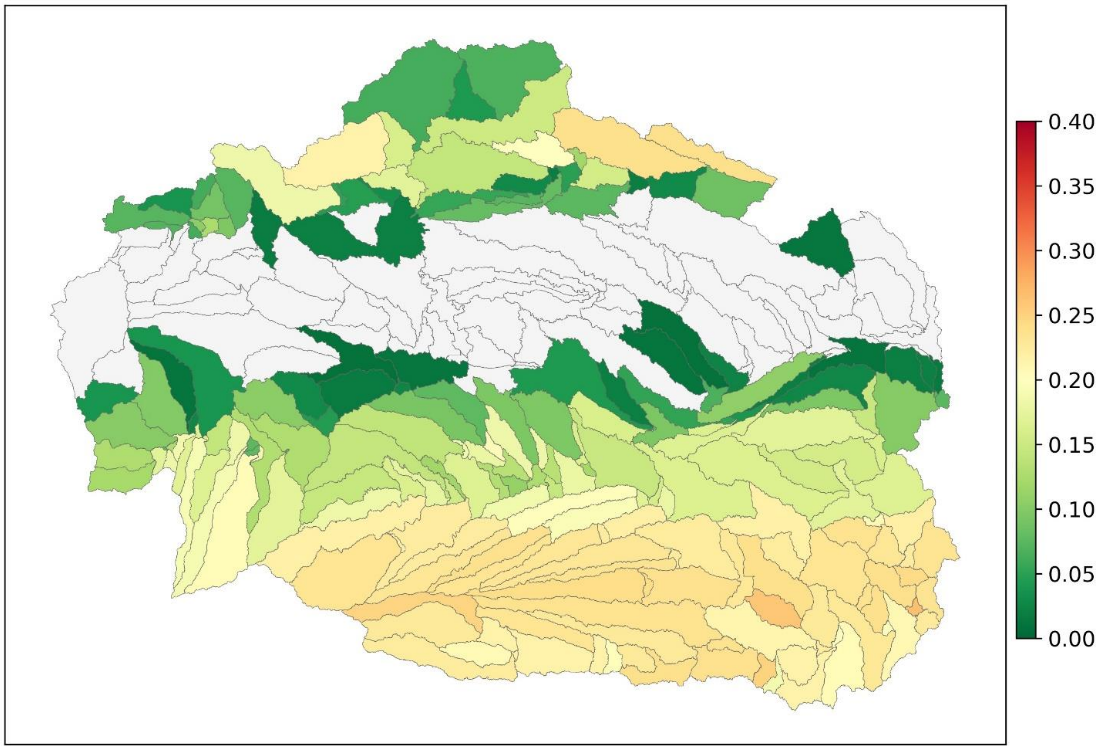

Figure B.2. Fractional marginal land use (MRLU) area for miscanthus production in each subbasin.

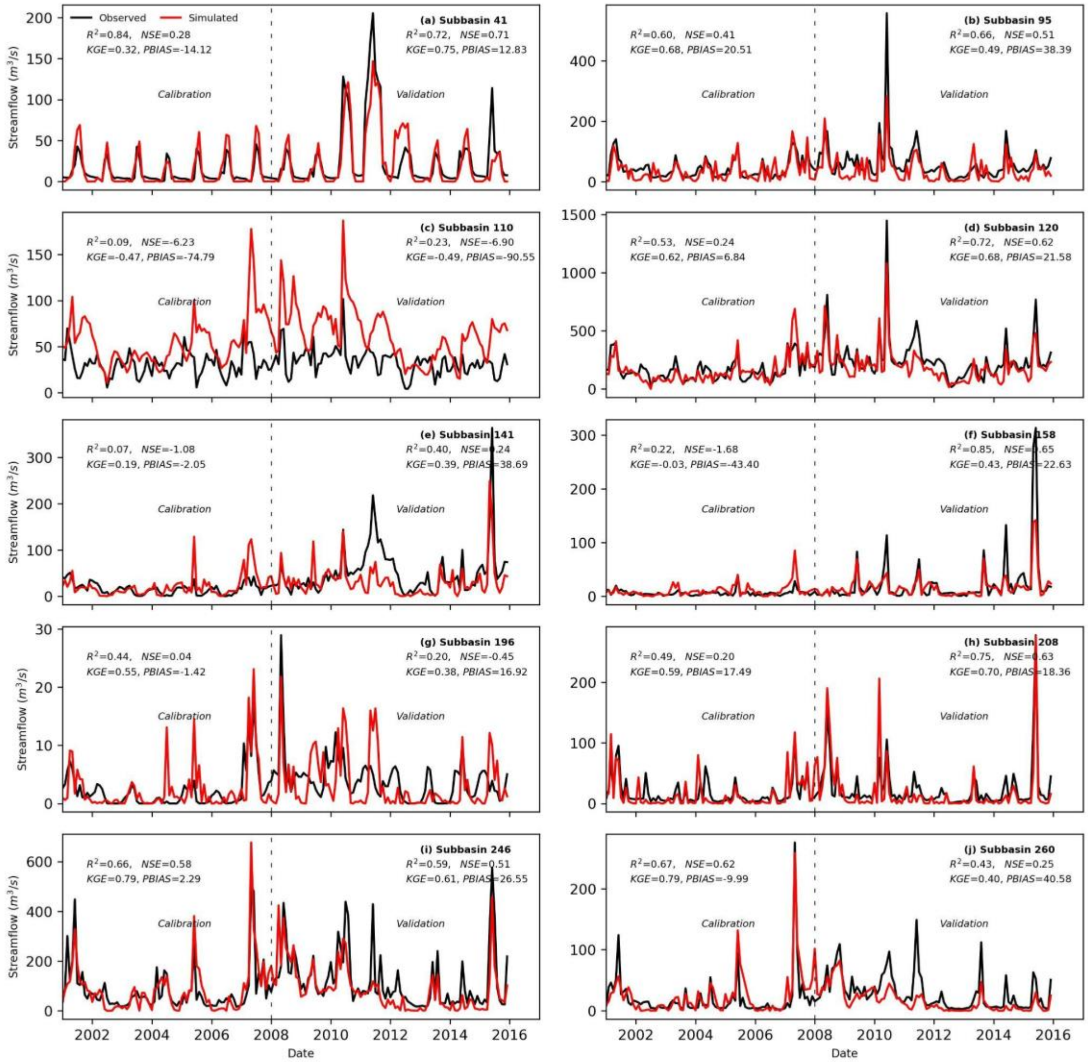

Figure B.3. Comparison of observed and simulated streamflow at outlets used for model calibration during the calibration and validation period.

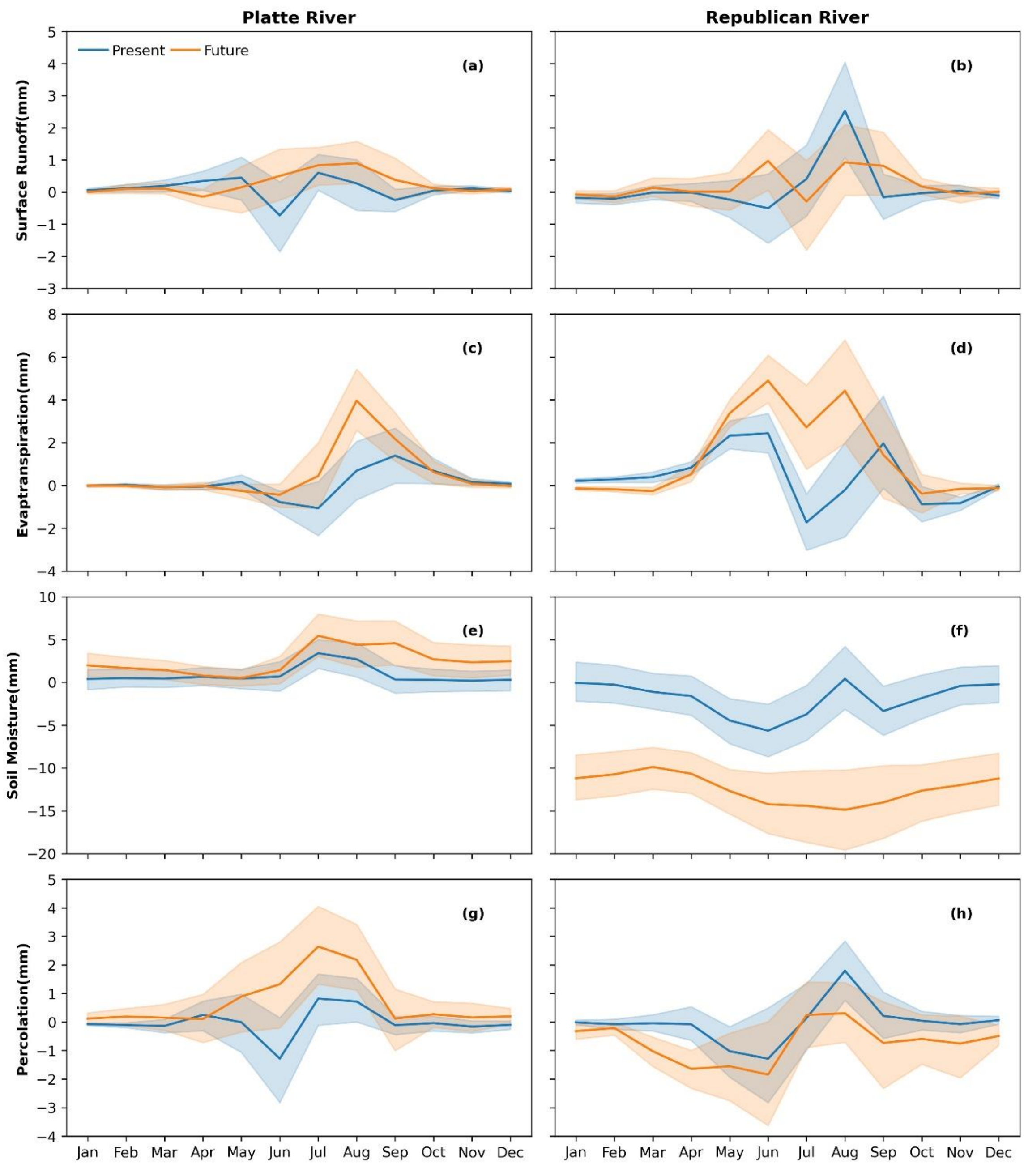

Figure B.4. Seasonal changes in the water balance component for the Platte and Republican River basins under miscan_ecane_mz scenario in the present and future conditions.

Appendix C. The SWAT model's grass growth processes

C.1 Biomass allocation

The SWAT vegetation growth sub-model simulates biomass production of the entire plant as a single entity and utilizes empirical relationships to partition above and belowground biomass using the parameter plant root fraction (*RF*). The temporal evolution of *RF* is calculated in SWAT as a function of potential heat unit accumulation (PHU) and user-defined plant-specific root fraction at the planting (*rsr1*) and maturity (*rsr2*) of the growing season of plant growth (Neitsch et al., 2011).

$$RF = rsr_1 - (rsr_1 - rsr_2) \times PHU \quad \text{(C.1)}$$

The plant root fraction is then used to calculate the aboveground biomass as

$$aboveground\ biomass = (1 - RF)\ \times\ total\ plant\ biomass \quad \text{(C.2)}$$

C.2 Plant growth constraints

SWAT incorporates multiple stress factors to limit plant biomass production. SWAT calculates temperature, water, nitrogen, and phosphorus stress at a scale of 0-1 (0 representing the maximum stress and 1 indicating no stress) (Neitsch et al., 2011). The most limiting factor among the four plant stress is then used to adjust the potential biomass production.

$$Stress_T =$$

$$\begin{cases} 1 & when\ T_{avg} \leq T_{base} \\ 1 - exp\left[\frac{-0.1054(T_{opt}-T_{avg})^2}{(T_{avg}-T_{base})^2}\right] & when\ T_{base} \leq T_{avg} \leq T_{opt} \\ 1 - exp\left[\frac{-0.1054(T_{opt}-T_{avg})^2}{(2T_{opt}-T_{avg}-T_{base})^2}\right] & when\ T_{opt} \leq T_{avg} \leq 2T_{opt} - T_{base} \end{cases} \quad \text{(C3)}$$

$$Stress_W = 1 - \frac{W_{actualup}}{E_t} \quad \text{(C.4)}$$

$$Stress_E = 1 - \frac{\varphi_E}{\varphi_E + exp(3.535 - 0.2597\varphi_E)} \quad \text{(C.5)}$$

$$\varphi_E = 200\left(\frac{bio_E}{bio_{E,opt}} - 0.5\right) \quad \text{(C.6)}$$

Where, T_{avg}(℃) is the average air temperature, T_{opt}(℃) is the optimum temperature for plant growth, T_{base}(℃) is the base temperature for plant growth, $W_{actualup}(mm\ H_2O/day)$ is the actual plant water uptake, $E_t(mm\ H_2O/day)$ is the maximum plant transpiration, φ_E is the scaling factor for nutrient E=N, P (nitrogen, N and phosphorous, P), $bio_E(kg\ E/ha)$ is the amount of nutrient E in plant biomass, $and\ bio_{E,opt}(kg\ E/ha)$ is the optimal amount of nutrient E in plant biomass, and $Stress_T$, $Stress_W$, and $Stress_{E=N,P}(unitless)$ are temperature, water, and nutrient stress respectively.

C.3 Plant nutrient demand

In the SWAT model, the daily nutrient uptake by plant is calculated as a function of the difference between plant actual nutrient content and plant optimal nutrient content, and soil nutrient availability. The plant-specific parameters for nutrient fraction parameters for each nutrient (nitrogen and phosphorous) which characterizes the optimal contents of nutrients in the plant at three growth stages (emergence, 50% maturity, and maturity). Nutrient fraction parameters for nitrogen *(PLTNFR*) and phosphorus (*PLTPFR*) are defined at the three growth stages and used to calculate the plant optimal nutrient content at different stages of plant growth. Furthermore, SWAT uses two plant-specific parameters, the fraction of nitrogen (*CPNYLD*) and phosphorus (*CPPYLD*) in aboveground biomass at harvest, to calculate the amount of nutrients removed during harvest operation that subsequently affects the nutrients added to soil from harvest residue.

Appendix D. The DAYCENT model's grass growth processes

D.1 Potential biomass production

Incoming solar radiation is provided as an input to the vegetation growth sub-model for estimating the potential biomass production. The potential plant biomass production is calculated as a function of a plant-specific maximum monthly biomass production and scaled by six terms (values between 0 and 1) that represent the effects of climatic conditions and plant phenology, respectively. DAYCENT uses the multiplication of stress factors under the assumption that the interactions of multiple stress factors limit plant biomass production (Del Grosso et al., 2008).

$$tgprod = shwave \times prdx \times T_{stress} \times SM_{stress} \times Sdlng \times CO2cpr \times scenfrac \times biof \qquad \text{(D.1)}$$

where, *tgprod* (*g C/m²*) is the potential biomass production on a given day, *shwave* is downwelling solar radiation (*Lg/day*), SM_{stress} is the soil moisture effect calculated as a function of relative soil water content fraction, T_{stress} is the temperature effect, *Sdlng* is the constraint on biomass production representing the seedling growth, *CO2cpr* is the effect of CO_2 concentration on biomass production, *scenfrac* represents the loss of biomass due to senescence, and *biof* is the effect of physical obstruction by standing dead biomass.

$T_{stress} =$

$$\begin{cases} exp\left(\frac{ppdf(3)}{ppdf(4)} \times \left(1 - frac^{ppdf(4)}\right)\right) \times \left(frac^{ppdf(3)}\right) & if\ frac > 0 \\ 0 & if\ frac \leq 0 \end{cases} \quad \text{(D.2)}$$

$$frac = \frac{ppdf(2) - Tavg}{ppdf(2) - ppdf(1)} \quad \text{(D.3)}$$

where, *Tavg* is the average air temperature (°C), *ppdf(1)* is the minimum temperature for plant growth (°C), *ppdf(2)* is the optimum temperature for plant growth (°C), *ppdf(3)* is the left shape coefficient of the function curve of temperature effect on growth, and *ppdf(4)* is the right shape coefficient of the function curve of temperature effect on growth

$$SM_{stress} = \begin{cases} \frac{1.0}{(1.0 + \exp(9.0 * (wscoeff(1) - cwstress)))} & \text{if PET} \geq 0.01 \\ 0.01 & \text{if PET} < 0.01 \end{cases} \quad \text{(D.4)}$$

where, *wscoeff(1)* is the relative water content required for 50% of maximum production and *cwstress* is the relative water content of the wettest soil layer.

$$cwstres = max\left(\frac{SWC_l - WP_l}{FC_l - WP_l}\right) \quad \text{(D.5)}$$

where, SWC_l, WP_l, *and* FC_l are, respectively, the soil water content, wilting point, and field capacity of soil layer *l*.

$$CO2cpr = 1 + \frac{(co2ipr - 1)}{log10(2.0)} l \times log10\left(\frac{co2}{330}\right) \quad \text{(D.6)}$$

where, *co2ipr* is the plant production ratio when atmospheric CO_2 concentration is doubled, *co2* is atmospheric CO_2 concentration (ppmv).

$$Sdlng = \begin{cases} MIN\left(1.0,\ pltmrf\ +\ aglivc \times \frac{(1-pltmrf)}{fulcan}\right) & when\ PHU < 0.25 \\ 1 & when\ PHU \geq 0.25 \end{cases} \quad (D.7)$$

where, *pltmrf* is the reduction factor to limit the seedling growth, *aglivc* is aboveground live carbon (*g C/m²*), and *fulcan* is aboveground live carbon full canopy cover (*g C/m²*)

$$biof = \begin{cases} bioprd + 0.75 \times (1 - bioprd) \times \frac{aglivc}{bioc} & if\ \frac{aglivc}{bioc} \leq 1 \\ bioprd + 0.75 \times (1 - bioprd) + 0.25 \times (1 - bioprd) \times \left(\frac{aglivc}{bioc} - 1\right) & if\ 1 < \frac{aglivc}{bioc} \leq 2 \\ biof = 1 & if\ \frac{aglivc}{bioc} > 2 \end{cases}$$

(D.8)

$$bioprd\ =\ 1 - \frac{bioc}{biok5 + bioc} \quad (D.9)$$

$$bioc = \begin{cases} stdcis + 0.1 \times sol_{rsd(surface)} & \\ 0.1 & if\ stdcis + 0.1 \times sol_{rsd(surface)} \leq 0 \\ pmxbio & if\ stdcis + 0.1 \times sol_{rsd(surface)} > pmxbio \end{cases}$$

(D.10)

where, *biok5* is (standing dead+10% surface litter) carbon at which production is reduced to half maximum due to physical obstruction by dead material (*g C/m²*), *pmxbio* is the maximum standing dead biomass +10% surface litter carbon for calculation of the potential negative effect of physical obstruction by standing dead and surface litter on biomass production (*g C/m²*), *stdcis* is standing dead carbon (*g C/m²*), sol_{rsd} (surface) is plant residue carbon in surface soil layer (*g C/m²*). For compatibility with SWAT, biomass production ceases when the accumulated potential heat unit exceeds 1 (i.e. plant maturity).

D.2 Actual biomass production and allocation

The plant-specific parameters are used to estimate the *RF* to allocate the potential biomass production to the different plant compartments (aboveground and belowground). The optimum *RF* is calculated as a function of four plant-specific parameters (*cfrtcn(1), cfrtcn(2), cfrtcw(1), cfrtcw(2)*), that represents the maximum and minimum fraction of carbon allocated to root under nutrient and water stress.

$$RF = (cfrtcw(1) + cfrtcw(2) + cfrtcn(1) + cfrtcn(2))/4.0 \qquad \text{(D.11)}$$

The calculated optimum *RF* is then used to partition the potential plant biomass into aboveground and belowground components. In addition, the optimum *RF* is used to compute the plant nutrient demand taking into account the impact of root biomass (*rtimp*) on the availability of nutrients from the soil.

The nutrient uptake by the aboveground and belowground biomass is dependent on the availability of nutrients and nutrient content of the plant which is further constrained between plant-specific upper and lower nutrient limits set for both plant compartments. To adjust for changes in nutrient content as the plant ages, the limits of the nutrient content of aboveground biomass are calculated as a function of aboveground biomass. Meanwhile, the limits of the nutrient content of belowground biomass are calculated as a function of annual precipitation. The most limiting nutrient is then used to scale the potential biomass production and calculate the actual biomass production and corresponding nutrient concentration and nutrient uptake. A linear relationship is then used to estimate the impact of water and nutrient limitations on the allocation of actual biomass between shoot and root. The water limitation is calculated as a function of soil moisture effect on potential production and plant-specific parameter *cftrcw*. The nutrient limitation is calculated as a function of nutrient stress and plant-specific parameter *cftrcn.* The most limiting factor between the water and nutrient limitation is used to determine the actual fraction of biomass allocated to the root. This approach incorporates the plant's response to water and nutrient stress such that more allocation of biomass to the root takes place when water and nutrient stress increases.

$$fracrc = max(h2oeff, ntreff(iel)) \tag{D.12}$$

$$h2oeff = (cftrcw(2) - cftrcw(1)) \times (SM_{stress} - 1) + cfrtcw(2) \tag{D.13}$$

$$ntreff(iel) = (cftrcn(2) - cftrcn(1)) \times \left(\frac{totale(iel)}{demand(iel)} - 1\right) + cfrtcn(2) \tag{D.14}$$

where, *iel* represents nutrients nitrogen and phosphorous, *totale(iel)* is the nutrient *iel* (nitrogen or phosphorous) available for biomass production, and *demand(iel)* is plant demand of nutrient *iel* for optimum biomass production. The potential aboveground and belowground biomass is then calculated as:

$$bgprod = tgprod * fracrc \tag{D.15}$$

$$agprod = tgprod - bgprod \tag{D.16}$$

where, *tgprod* is total plant biomass, *agprod* is aboveground biomass, and *bgprod* is belowground biomass. The belowground biomass is further categorized into juvenile and mature roots.

D.3 Shoot and root die-off

Unlike SWAT, the death of shoot and root is simulated in the growing season. The shoot and root death are determined by soil moisture, soil temperature, and plant-specific maximum senescence parameters. Root death takes place when the soil temperature is greater than 2°C. In senescence months (i.e., when PHU > Fraction of growing season when leaf area starts declining, DLAI) shoot death rate is set to a fixed plant-specific fraction *fsdeth(2)*. The dead shoot biomass (standing dead) is transferred to the surface soil layer (0-10cm) as the plant residue at the plant-specific fall rate (*fallrt*). Meanwhile, the dead root biomass is distributed to different soil layers based on the depth distribution of roots in the soil column following the approach used by SWAT during plant kill operations. During dormancy, SWAT assumes 10% of plant biomass is returned to the surface soil layer as plant residue, which is adopted in the new sub-model.

D.4 Plant nutrient storage

The DAYCENT grass sub-model simulates the nutrient flow for the nutrient storage pool in addition to the nutrient flow for each plant compartment. A fraction of nutrients from aboveground biomass which is converted to standing dead material is transferred to the nutrient storage pool during the growing season. In addition, a fraction of nutrient uptake by the plant from the soil during the late growing season is allocated to the nutrient storage pool. The nutrients accumulated in the storage pool are remobilized by the plant during the early growth phase such that plants use nutrients in the storage pool before utilizing soil nutrients for biomass production. Nutrient uptake from the internal plant storage pool by each plant compartment is calculated as

$$uptake_{above} = \begin{cases} uptake_{storage,iel} \times euf_{above} \times (1.0 - clsgres) & if\ PHU > 0.8 \\ uptake_{storage,iel} \times euf_{above} & if\ PHU \leq 0.8 \end{cases} \quad (D.17)$$

$$uptake_{below} = uptake_{storage,iel} \times euf_{below} \quad (D.18)$$

Nutrient flow into the internal plant storage pool is calculated as:

Step 1. Obtained from the conversion of aboveground live biomass to standing dead

$$storage(iel) = fdeth \times aglive(iel) \times crprtf(iel) \quad \text{(D.19)}$$

Step 2. Obtained from soil nutrient uptake during the late growing season

$$storage(iel) = uptake_{soil,iel} \times euf_{above} \times clsgres \qquad if\ PHU > 0.8$$

(D.20)

where, $uptake_{soil,iel}$ is the plant uptake of nutrient *iel* from soil (g E/m2), $uptake_{storage,iel}$ is plant uptake of nutrient *iel* from the internal storage pool (g E/m2), *fdeth* is the death rate of shoots to standing dead, *aglive(iel)* is the concentration of nutrient *iel* in the plant (g E/m2), *clsgres* is late growing season restriction factor (0-1), *crprtf(iel)* is the fraction of nutrient *iel* translocated from aboveground biomass at death, euf_{above} is the fraction of nutrient uptake from aboveground biomass, and euf_{below} is the fraction of nutrient uptake from belowground biomass.

Appendix E. SWAT-GRASS model performance

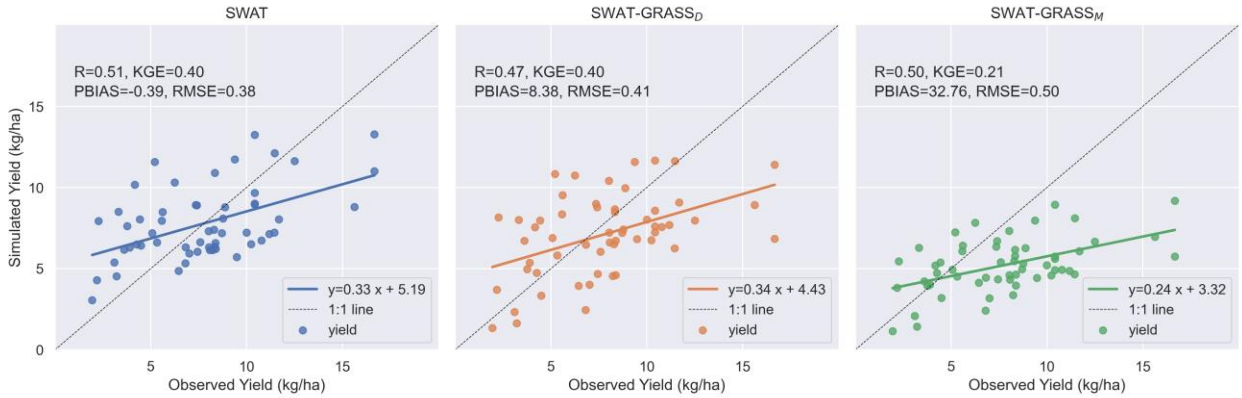

Figure E.1. Scatter plots of SWAT, SWAT-GRASSD, and SWAT-GRASSM simulated and observed annual switchgrass biomass yield for all field sites using default plant growth parameters.

Table E.1. Plant growth parameters of Switchgrass for SWAT based on Cibin et al. (2016).

S. No	Parameter	Description	Value
1	*T_OPT*	Optimal Temperature (°C)	25
2	*T_BASE*	Base Temperature (°C)	10
3	*BIO_E*	Radiation Use Efficiency (biomass/energy ratio)	17
4	*HVSTI*	Harvest Index	1
5	*HEFF*	Harvest Efficiency	0.75
6	*WSYF*	Lower Limit of Harvest Index due to stress ((kg/ha)/(kg/ha))	1
7	*BLAI*	Maximum Leaf Area Index (LAI)	8
8	*DLAI*	Fraction of growing season when growth declines	1
9	*RFR1C*	Root Fraction (emergence)	0.89
10	*RFR2C*	Root Fraction (maturity)	0.49
11	*ALAI_MIN*	Minimum LAI for plant during dormant period (m^2/m^2)	0
12	*EXT_COEFF*	Light extinction coefficient	0.5
13	*LAIMX1*	First point fraction of BLAI for optimum growth curve	0.1
14	*FRGRW1*	Fraction of growing season coinciding with LAIMX1	0.1
15	*LAIMX2*	Second point fraction of BLAI for optimum growth curve	0.85
16	*FRGRW2*	Fraction of growing season coinciding with LAIMX2	0.4
17	*PLTNFR(1)*	Plant nitrogen fraction at emergence (kg N/kg biomass)	0.0073
18	*PLTNFR(2)*	Plant nitrogen fraction at 50% maturity (kg N/kg biomass)	0.0068
19	*PLTNFR(3)*	Plant nitrogen fraction at maturity (kg N/kg biomass)	0.0053
20	*CNYLD*	Plant nitrogen fraction in harvested mass (kg N/kg yield)	0.0054
21	*PLTPFR(1)*	Plant phosphorus fraction at emergence (kg P/kg biomass)	0.0011

22	*PLTPFR(2)*	Plant phosphorus fraction at 50% maturity (kg P/kg biomass)	0.0014
23	*PLTPFR(3)*	Plant phosphorus fraction at maturity (kg P/kg biomass)	0.0012
24	*CPYLD*	Plant phosphorus fraction in harvested mass (kg P/kg yield)	0.0010
25	*CHTMX*	Max. Canopy Height (m)	2
26	*RDMX*	Max. Rooting Depth (m)	3
27	*USLE_C*	Min. Crop Factor for Water Erosion	0.003
28	*GSI*	Stomatal conductance (m/s)	0.005
29	*CN*	Curve Number	31[A], 59[B], 72[C], 79[D]
30	*OV_N*	Manning's roughness for overland flow	0.24

Table E.2. Plant growth parameters of Switchgrass for SWAT-GRASS based on Davis et al. (2010).

S. No	**Parameter**	**Description**	**Value**
1	prdx	Potential aboveground monthly biomass production (g C/m^2)	1.0
2	*T_OPT/ppdf(1)*	Optimum temperature for plant growth (°C)	25
3	*T_BASE*	Minimum temperature for plant growth (°C)	10
4	*ppdf(2)*	maximum temperature for plant growth (°C)	50
5	*ppdf(3)*	left curve shape parameter that controls temperature effect on plant growth	0.5
6	*ppdf(4)*	right curve shape parameter that controls temperature effect on plant growth	2.5
7	*cfrtcn(1)*	Maximum fraction of carbon allocated to roots under maximum nutrient stress	0.3
8	*cfrtcn(2)*	Minimum fraction of carbon allocated to roots under no nutrient stress	0.1
9	*cfrtcw(1)*	minimum fraction of C allocated to roots under maximum water stress	0.3
10	*cfrtcw(2)*	minimum fraction of C allocated to roots under no water stress	0.1
11	*crprtf(1)*	Fraction of N transferred to a vegetation storage pool from grass/crop to root at death	0.8
12	*crprtf(2)*	Fraction of P transferred to a vegetation storage pool from grass/crop to root at death	0.8
13	*snfxmx*	Symbiotic N fixation maximum for grass/crop (g N fixed per g C of new growth)	0.0
14	*pltmrf*	Planting month reduction factor to limit seedling growth	1.0
15	*clsgres*	Late season crop/grass growth restriction factor	1.0

16	*fulcan*	Value of aboveground live C at full canopy cover above which potential production is not reduced (g C/m^2)	1000.0
17	*pramn(1,1)*	Minimum aboveground C:N ratio with zero biomass	20
18	*pramn(1,2)*	Minimum aboveground C:N ratio with biomass equal to BIOMAX	60
19	*pramn(2,1)*	Minimum aboveground C:P ratio with zero biomass	390
20	*pramn(2,2)*	Minimum aboveground C:P ratio with biomass equal to BIOMAX	390
21	*pramx(1,1)*	Maximum aboveground C:P ratio with zero biomass	40
22	*pramx(1,2)*	Maximum aboveground C:P ratio with biomass equal to BIOMAX	220
23	*pramx(2,1)*	Maximum aboveground C:P ratio with zero biomass	440
24	*pramx(2,2)*	Maximum aboveground C:P ratio with biomass equal to BIOMAX	440
25	*prbmn(1,1)*	Intercept for calculating the minimum C:N ratio for belowground biomass as a linear function of annual precipitation	40
26	*prbmn(1,2)*	Slope for calculating the minimum C:N ratio for belowground biomass as a linear function of annual precipitation	0
27	*prbmn(2,1)*	Intercept for calculating the minimum C:P ratio for belowground biomass as a linear function of annual precipitation	390
28	*prbmn(2,2)*	Slope for calculating the minimum C:P ratio for belowground biomass as a linear function of annual precipitation	0
29	*prbmx(1,1)*	Intercept for calculating the maximum C:N ratio for belowground biomass as a linear function of annual precipitation	60
30	*prbmx(1,2)*	Slope for calculating the maximum C:N ratio for belowground biomass as a linear function of annual precipitation	0
31	*prbmx(2,1)*	Intercept for calculating the maximum C:P ratio for belowground biomass as a linear function of annual precipitation	420
32	*prbmx(2,2)*	Slope for calculating the maximum C:P ratio for belowground biomass as a linear function of annual precipitation	0
33	*riint*	root impact intercept used for calculating the impact of root biomass on nutrient availability	0.8
34	*rictrl*	root impact control term on nutrient availability	0.015
35	*favail(1)*	Fraction of N available per month to plants	0.15
36	*favail(3)*	Minimum fraction of P available per month to plants	0.20
37	*favail(4)*	Maximum fraction of P available per month to plants	0.40
38	*favail(5)*	Mineral N in surface layer corresponding to maximum fraction of P available	2.00

39	*npp2cs*	Multiplier used to estimate GPP as a function of NPP to estimate amount of carbon stored in carbohydrate storage pool	1.0
40	*co2ipr*	the calculated effect on production of doubling the atmospheric CO2	1.15
41	*biomax*	biomass level above which the minimum and maximum C/E ratios of new shoot increments equal pramn(:,2) and pramx(:,2) respectively	300
42	*mrtfrac*	Fraction of belowground root production that goes to mature root	0.05
43	*cmxturn*	Fall rate (fraction of standing dead which falls each month)	0.21
44	*cgresp(1)*	Maximum fraction of aboveground C that goes to growth respiration	0.23
45	*cgresp(2)*	Maximum fraction of juvenile root C that goes to growth respiration	0.23
46	*cgresp(3)*	Maximum fraction of mature root C that goes to growth respiration	0.23
47	*cmrspnpp(1)*	X1 value, based on predicted aboveground production, of line function that decreases maintenance respiration	0.0
48	*cmrspnpp(2)*	Y1 value, based on predicted aboveground production, of line function that decreases maintenance respiration	0.0
49	*cmrspnpp(3)*	X2 value, based on predicted aboveground production, of line function that decreases maintenance respiration	1.25
50	*cmrspnpp(4)*	Y2 value, based on predicted aboveground production, of line function that decreases maintenance respiration	1.0
51	*cmrspnpp(5)*	X2 value, based on predicted aboveground production, of line function that decreases maintenance respiration	4.0
52	*cmrspnpp(6)*	Y2 value, based on predicted aboveground production, of line function that decreases maintenance respiration	1.5
53	*ckmrspmx(1)*	maximum fraction of aboveground live C that goes to maintenance respiration for crops	0.1
54	*ckmrspmx(2)*	maximum fraction of belowground live C that goes to maintenance respiration of juvenile roots for crops	0.1
55	*ckmrspmx(3)*	maximum fraction of belowground live C that goes to maintenance respiration of mature roots for crops	0.03
56	*fsdeth(1)*	maximum shoot death rate at very dry soil conditions	0.10
57	*fsdeth(2)*	fraction of shoots which die during senescence	0.99
58	*fsdeth(3)*	fraction of shoots which die when aboveground live C is greater than fsdeth(4)	0.1
59	*fsdeth(4)*	level of aboveground C above which shading occurs and shoot senescence increases	300
60	*rdrj*	Maximum death rate of juvenile root at very dry soil condition	0.8
61	*rdrm*	Maximum death rate of mature root at very dry soil conditions	0.2

62	*fallrt*	Fall rate (fraction of standing dead which falls each month)	0.15
63	*pslsrb*	Slope term which controls the fraction of phosphorous that is labile	1.0
64	*sorpmx*	Maximum phosphorous sorption potential for soil	20
65	*biok5*	Level of aboveground standing dead + 10% of litter C at which production is reduced to half maximum due to physical obstruction by dead material (g/m2)	60

Table E.3. SWAT plant growth parameters selected for sensitivity analysis

Parameters	**Description**
T_OPT	Optimal Temperature for plant growth (℃)
T_BASE	Base Temperature for plant growth (℃)
BIO_E	Radiation Use Efficiency (biomass/energy ratio)
PLTNFR(1)	Plant nitrogen fraction at emergence
PLTNFR(2)	Plant nitrogen fraction at 50% maturity
PLTNFR(3)	Plant nitrogen fraction at maturity
CNYLD	Plant nitrogen fraction in harvested mass
DLAI	Fraction of growing season when growth declines
BIOEHI	Biomass energy ration corresponding to the second point on radiation use efficiency curve
BMDIEOFF	Fraction of aboveground biomass that dies off at dormancy
WSYF	Lower Limit of Harvest Index due to stress
RSR1C	Root to shoot ratio at the beginning of the growing season
RSR2C	Root to shoot ratio at the end of the growing season
EXT_COEF	Light extinction coefficient
FRGRW1	Fraction of the plant growing season corresponding to the 1st point on the optimal leaf area development curve
FRGRW2	Fraction of the plant growing season corresponding to the 2nd point on the optimal leaf area development curve
LAIMX1	Fraction of the maximum leaf area index corresponding to the 1st point on the optimal leaf area development curve
LAIMX2	Fraction of the maximum leaf area index corresponding to the 2nd point on the optimal leaf area development curve

Table E.4. SWAT-GRASS plant growth parameters selected for sensitivity analysis based on Cibin et al. (2016) and Davis et al. (2010).

Parameters	**Description**
T_OPT	Optimum temperature for plant growth (℃)
T_BASE	Minimum temperature for plant growth (℃)
riint	Root impact intercept used to control nutrient allocation
rictrl	Root impact control term used to control nutrient allocation
cfrtcn(1)	Maximum fraction of carbon allocated to roots under maximum nutrient

	stress
cfrtcn(2)	Minimum fraction of carbon allocated to roots under no nutrient stress
biomax	Biomass above which the minimum and maximum C:E ratios of new shoot increments equal pramn(:,2) and pramx(:,2) respectively (g/m^2)
prdx	Potential aboveground monthly biomass production ($g\ C/m^2$)
clsgres	Late season crop/grass growth restriction factor
crprtf(1)	Fraction of N transferred to a vegetation storage pool from grass/crop leaves at death
crprtf(2)	Fraction of P transferred to a vegetation storage pool from grass/crop leaves at death
pramn(1,1)	Minimum aboveground C/N ratio with zero biomass
pramn(1,2)	Minimum aboveground C:N ratio with biomass equal to BIOMAX
pramx(1,1)	Maximum aboveground C/N ratio with zero biomass
pramx(1,2)	Maximum aboveground C/N ratio with biomass equal to BIOMAX
prbmn(1,1)	Intercept for calculating the minimum C:N ratio for belowground biomass as a linear function of annual precipitation
prbmn(1,2)	Slope for calculating the minimum C:N ratio for belowground biomass as a linear function of annual precipitation
prbmx(1,1)	Intercept for calculating the maximum C:N ratio for belowground biomass as a linear function of annual precipitation
prbmx(1,2)	Slope for calculating the maximum C:N ratio for belowground biomass as a linear function of annual precipitation
fsdeth(1)	maximum shoot death rate at very dry soil conditions
ppdf(2)	maximum temperature for plant growth (°C)
ppdf(3)	left curve shape parameter that controls temperature effect on plant growth
ppdf(4)	right curve shape parameter that controls temperature effect on plant growth
cfrtcw(1)	minimum fraction of C allocated to roots under maximum water stress
cfrtcw(2)	minimum fraction of C allocated to roots under no water stress
fallrt	Fall rate (fraction of standing dead which falls each month)

Table E.5. Observed and simulated mean Switchgrass dry weight biomass yield (Mg/ha) at the GLBRC and AR field sites.

Model	**Escabana**	**Hancock**	**Rhinelander**	**Lux Arbor**	**Lake City**	**Fairfield**	**Orr**	**Dekalb**
Observed	8.59	3.62	6.72	7.50	7.25	13.80	10.76	7.41
SWAT	8.14	7.94	7.79	8.44	8.02	11.94	11.10	10.77
SWAT-GRASS$_D$	7.46	6.46	6.62	7.98	6.52	10.26	8.49	10.56
SWAT-GRASS$_M$	7.73	6.13	7.86	6.60	7.15	9.90	8.41	9.18

Table E.6. Summary of uncertainty analysis of each field site.

Site	Parameter	Model		
		SWAT	SWAT-GRASS$_D$	SWAT-GRASS$_M$
Escabana	P-factor	0.38	0.38	0.38
	R-factor	0.62	0.97	1.73
Hancock	P-factor	0.13	0.38	0.50
	R-factor	1.11	2.18	3.10
Rhinelander	P-factor	0.50	0.38	0.63
	R-factor	0.94	0.99	2.03
Lux Arbor	P-factor	0.50	0.50	0.75
	R-factor	0.61	1.46	1.90
Lake City	P-factor	0.63	0.38	0.50
	R-factor	0.94	1.02	2.26
Fairfield	P-factor	0.50	0.50	0.50
	R-factor	0.87	1.31	2.02
Orr	P-factor	0.50	0.67	0.67
	R-factor	0.85	1.39	2.43
Dekalb	P-factor	0.50	0.67	0.83
	R-factor	0.66	1.82	2.54

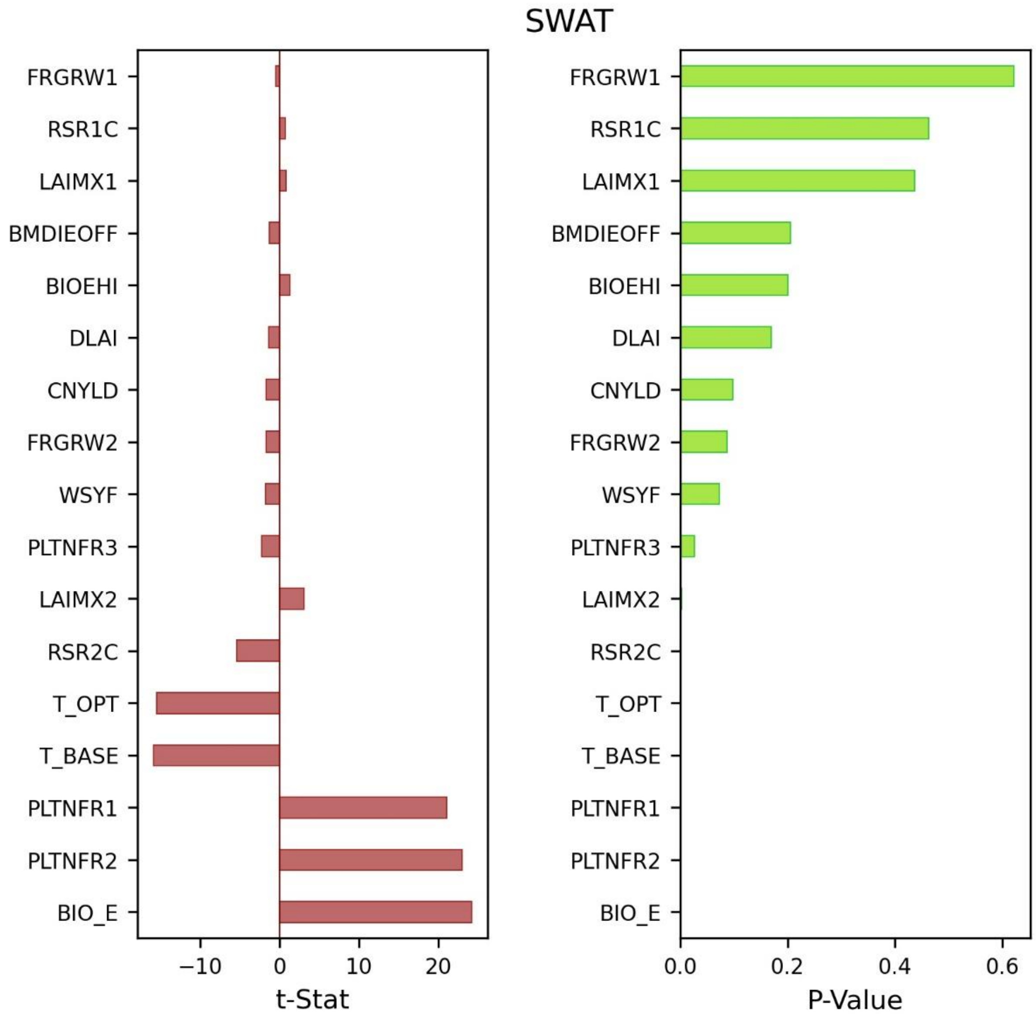

Figure E.2. Global sensitivity analysis of plant growth parameters for SWAT.

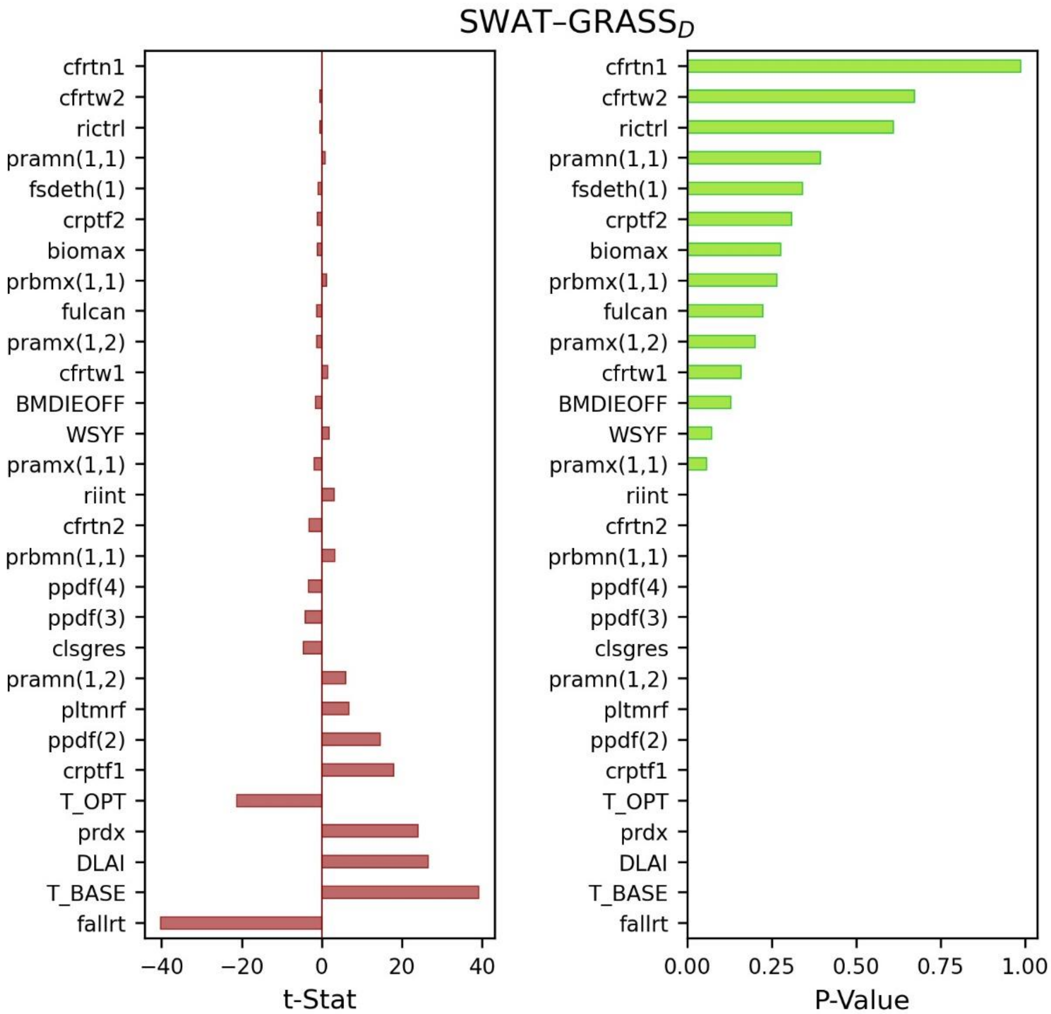

Figure E.3. Global sensitivity analysis of plant growth parameters for SWAT–GRASS$_D$.

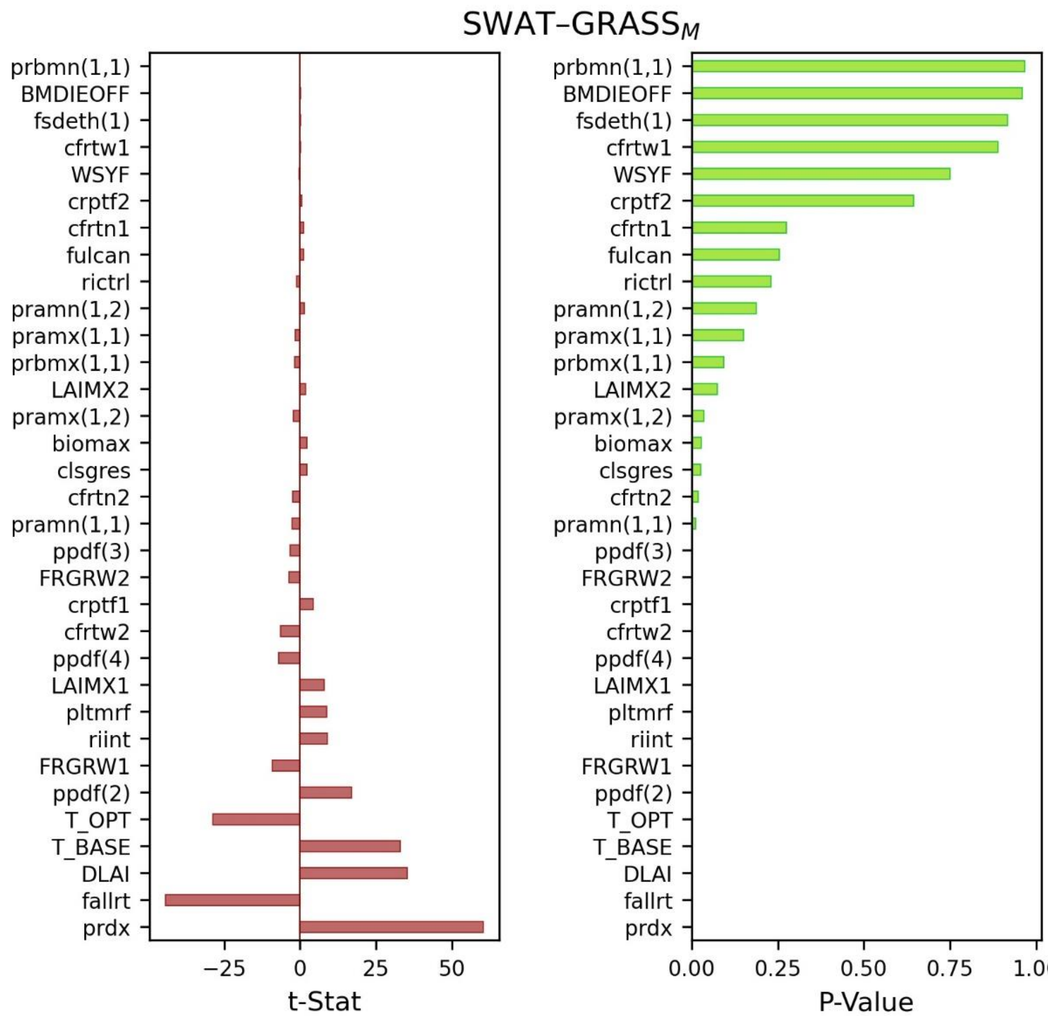

Figure E.4. Global sensitivity analysis of plant growth parameters for SWAT–GRASS$_M$.

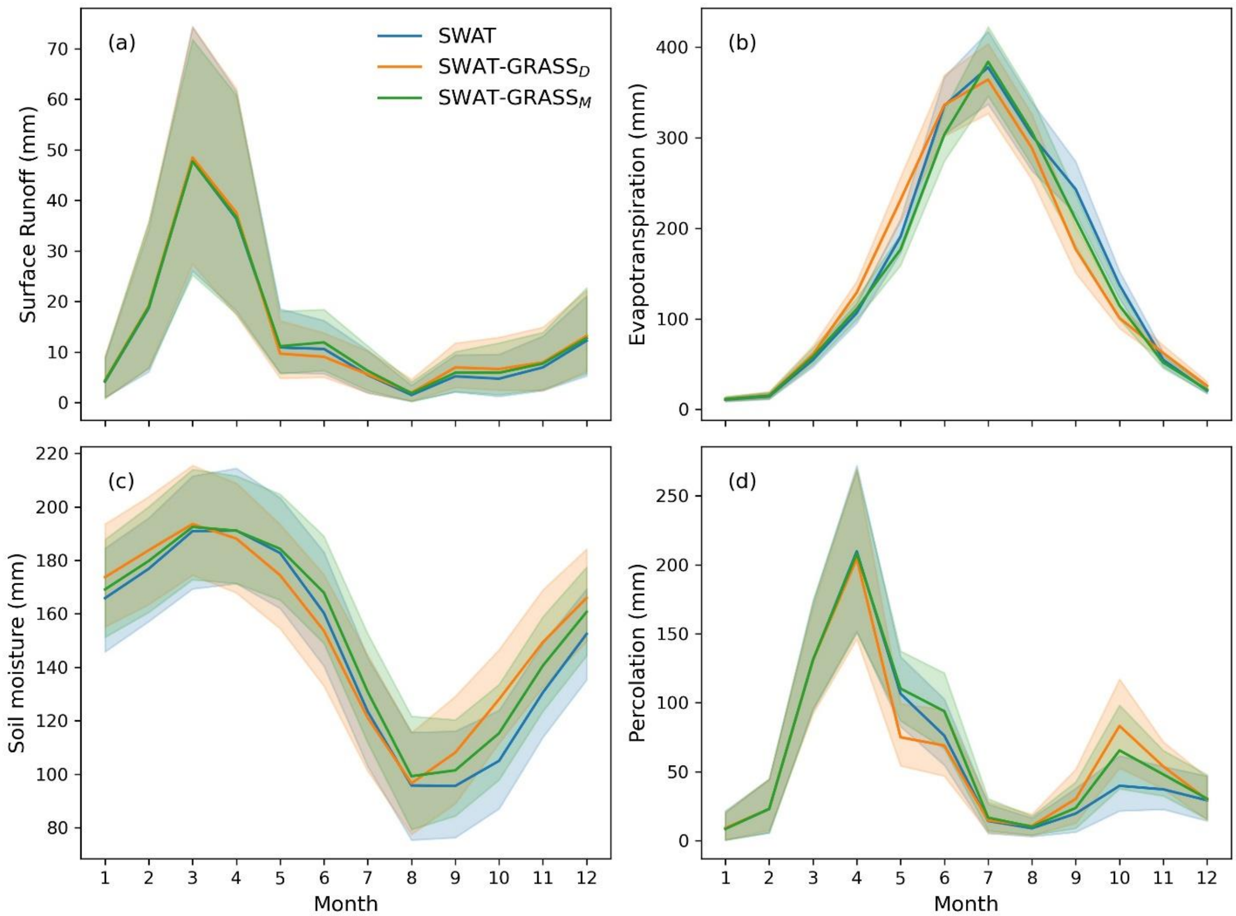

Figure E.5. Mean seasonal (a) surface runoff, (b) evapotranspiration, (c) soil moisture content, and (d) percolation simulated by SWAT, SWAT–GRASS$_D$, and SWAT–GRASS$_M$ at the switchgrass cultivated HRUs. The shading represents 95% confidence interval.

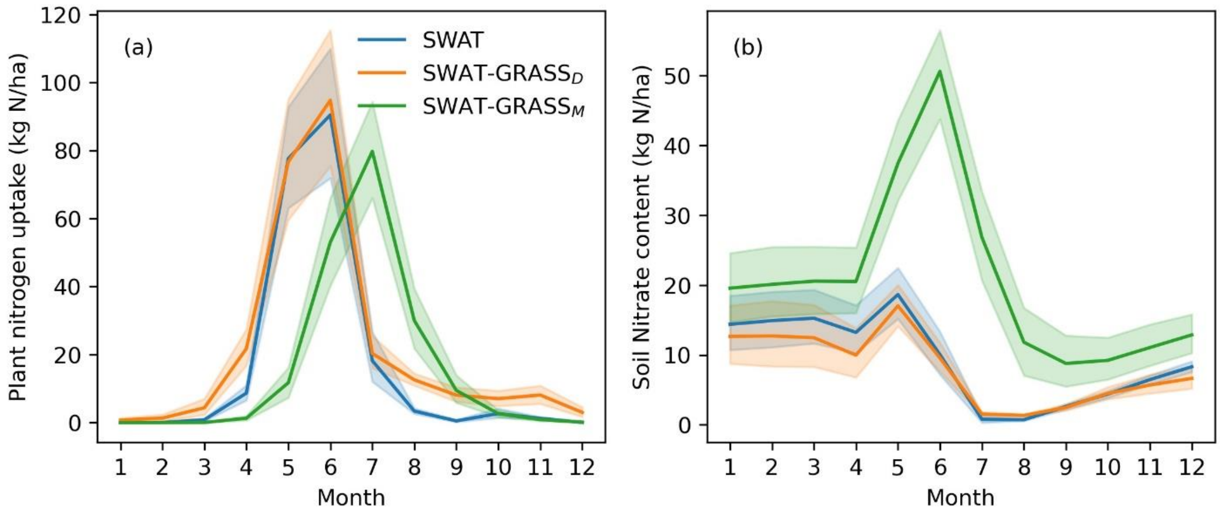

Figure E.6. Mean seasonal (a) plant nitrogen uptake and (b) total soil nitrate content simulated by SWAT, SWAT–GRASS$_D$, and SWAT–GRASS$_M$ for switchgrass. The shading represents 95% confidence interval.

Appendix F. Selected near-natural streamgages

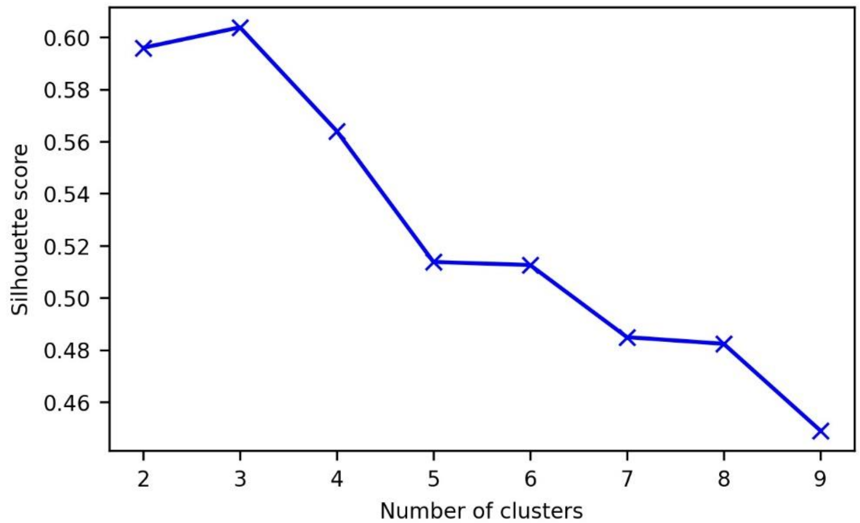

Figure F.1. Relationship between the number of clusters and silhouette score.

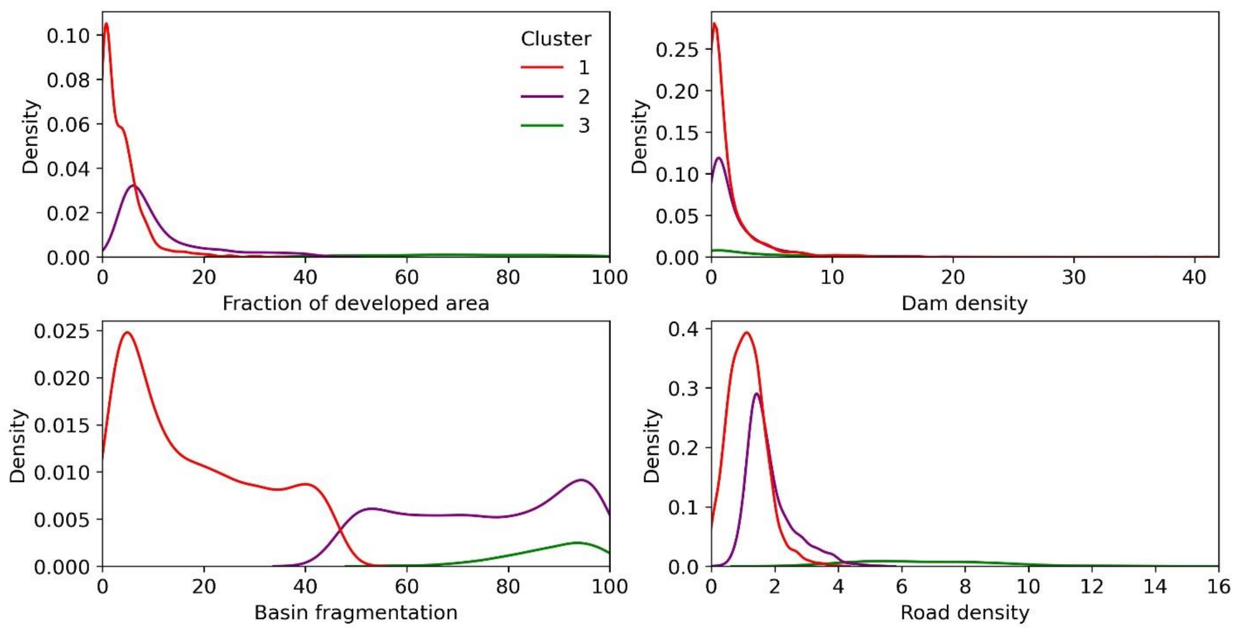

Figure F.2. Frequency distribution of basin characteristics representative of human disturbance within a basin.

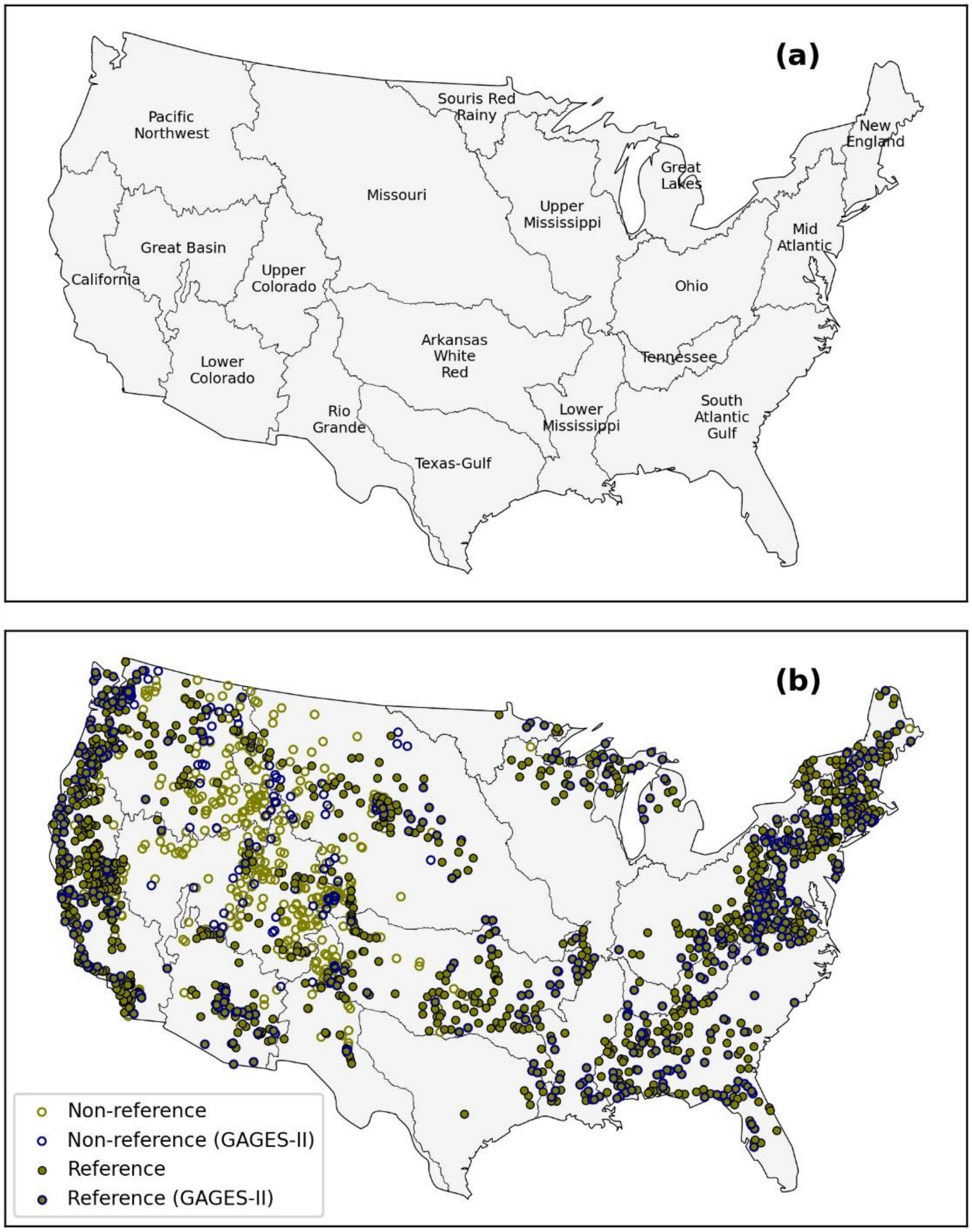

Figure F.3. Map showing (a) water resource divisions across the contiguous United States and (b) spatial distribution of streamgages selected for correlation analysis. The marker with blue outline indicates streamgages categorized as reference in GAGES-II dataset.

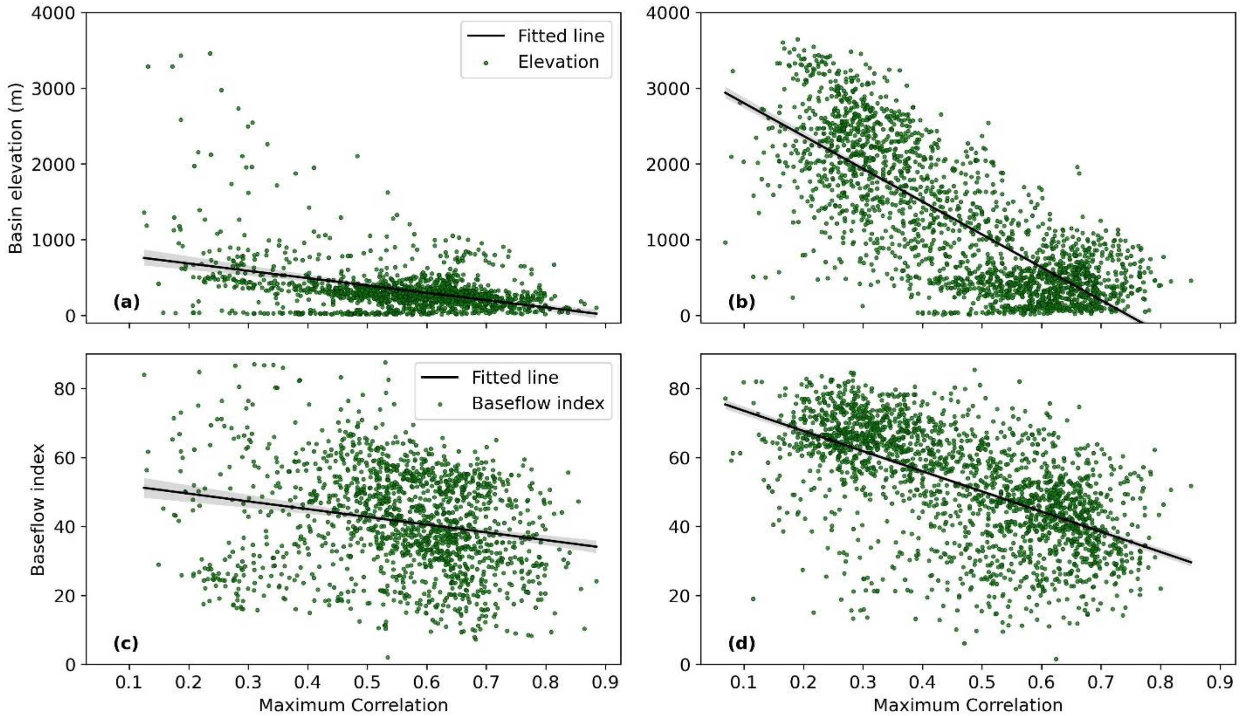

Figure F.4. Comparison of relationship of maximum precipitation-streamflow correlation coefficient with (a-b) basin elevation and (c-d) baseflow index for streamgages excluded (a and c) and selected (b and d) for correlation analysis.

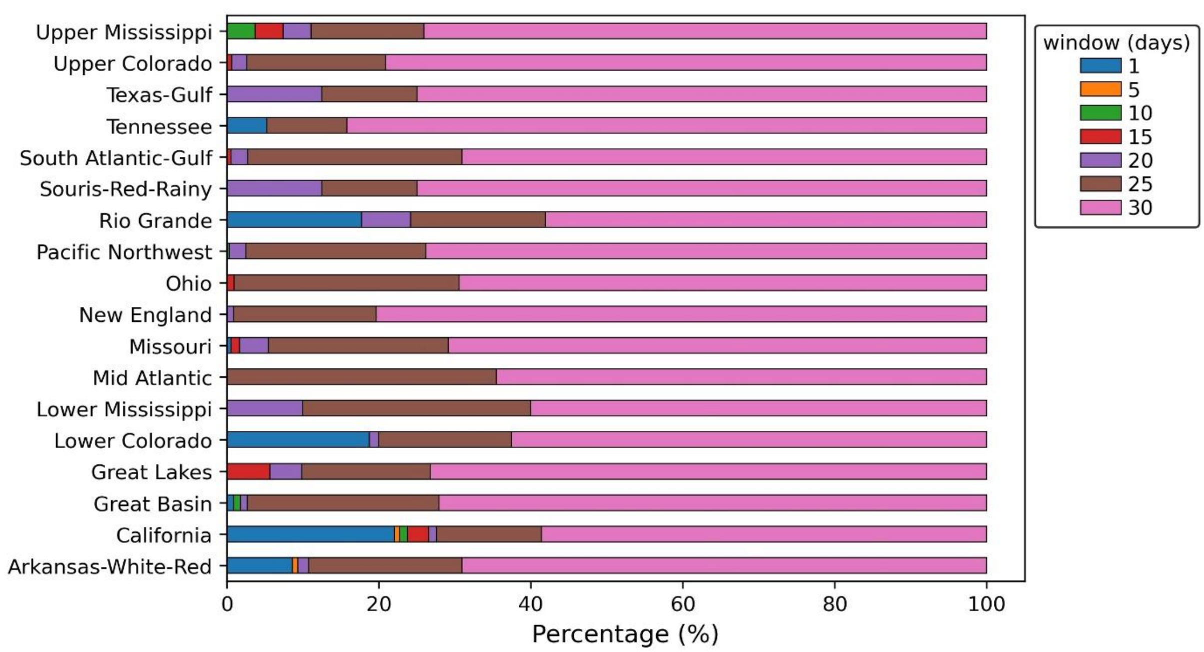

Figure F.5. Proportion of streamgages with maximum correlation obtained at the timescale of 1, 5, 10, 15, 20, 25, and 30 days for each water resource division.

Table F.1. Summary of streamgages selected as reference condition.

Region	Number of reference streamgages (total gages)	% of gages as GAGES-II reference (count)
Arkansas-White-Red	115	22 (25)
California	246	17 (42)
Great Basin	40	18 (7)
Great Lakes	69	30 (21)
Lower Colorado	65	32 (21)
Lower Mississippi	30	47 (14)
Mid Atlantic	200	32 (63)
Missouri	87	16 (14)
New England	110	28 (31)
Ohio	108	27 (29)
Pacific Northwest	188	30 (57)
Rio Grande	23	17 (4)
Souris-Red-Rainy	7	43 (3)
South Atlantic-Gulf	181	34 (61)
Tennessee	19	53 (10)
Texas-Gulf	8	38 (3)
Upper Colorado	22	0 (0)
Upper Mississippi	26	15 (4)

Note: “–” indicates that trends were not detected.

Bibliography

Abbaspour, K.C., Rouholahnejad, E., Vaghefi, S., Srinivasan, R., Yang, H., Kløve, B., 2015. A continental-scale hydrology and water quality model for Europe: Calibration and uncertainty of a high-resolution large-scale SWAT model. Journal of Hydrology 524, 733–752.

Addor, N., Newman, A.J., Mizukami, N., Clark, M.P., 2017. The CAMELS data set: catchment attributes and meteorology for large-sample studies. Hydrol. Earth Syst. Sci. 21, 5293–5313. https://doi.org/10.5194/hess-21-5293-2017

Agostini, F., Gregory, A.S., Richter, G.M., 2015. Carbon Sequestration by Perennial Energy Crops: Is the Jury Still Out? Bioenerg. Res. 8, 1057–1080. https://doi.org/10.1007/s12155-014-9571-0

Aldaya, M.M., Allan, J.A., Hoekstra, A.Y., 2010. Strategic importance of green water in international crop trade. Ecological Economics 69, 887–894. https://doi.org/10.1016/j.ecolecon.2009.11.001

Alexander, R.B., Smith, R.A., Schwarz, G.E., Boyer, E.W., Nolan, J.V., Brakebill, J.W., 2008. Differences in Phosphorus and Nitrogen Delivery to The Gulf of Mexico from the Mississippi River Basin. Environ. Sci. Technol. 42, 822–830. https://doi.org/10.1021/es0716103

Aliyari, F., Bailey, R.T., Tasdighi, A., Dozier, A., Arabi, M., Zeiler, K., 2019. Coupled SWAT-MODFLOW model for large-scale mixed agro-urban river basins. Environmental Modelling & Software 115, 200–210. https://doi.org/10.1016/j.envsoft.2019.02.014

Alley, W.M., Emery, P.A., 1986. Groundwater model of the Blue River basin, Nebraska—Twenty years later. Journal of Hydrology 85, 225–249. https://doi.org/10.1016/0022-1694(86)90058-2

Anderson, M., 1997. A Two-Source Time-Integrated Model for Estimating Surface Fluxes Using Thermal Infrared Remote Sensing. Remote Sensing of Environment 60, 195–216. https://doi.org/10.1016/S0034-4257(96)00215-5

Anderson, M.C., Kustas, W.P., Norman, J.M., Hain, C.R., Mecikalski, J.R., Schultz, L., González-Dugo, M.P., Cammalleri, C., d'Urso, G., Pimstein, A., Gao, F., 2011. Mapping daily evapotranspiration at field to continental scales using geostationary and polar orbiting satellite imagery. Hydrol. Earth Syst. Sci. 15, 223–239. https://doi.org/10.5194/hess-15-223-2011

Anderson-Teixeira, K.J., Davis, S.C., Masters, M.D., Delucia, E.H., 2009. Changes in soil organic carbon under biofuel crops. GCB Bioenergy 1, 75–96. https://doi.org/10.1111/j.1757-1707.2008.01001.x

Arnold, J.G., Srinivasan, R., Muttiah, R.S., Williams, J.R., 1998. Large area hydrologic modeling and assessment part I: model development 1. JAWRA Journal of the American Water Resources Association 34, 73–89. https://doi.org/10.1111/j.1752-1688.1998.tb05961.x

Arnold, J.G., Youssef, M.A., Yen, H., White, M.J., Sheshukov, A.Y., Sadeghi, A.M., Moriasi, D.N., Steiner, J.L., Amatya, D.M., Skaggs, R.W., 2015. Hydrological processes and model representation: Impact of soft data on calibration. Transactions of the ASABE 58, 1637–1660. https://doi.org/10.13031/trans.58.10726

Arundale, R.A., Dohleman, F.G., Heaton, E.A., Mcgrath, J.M., Voigt, T.B., Long, S.P., 2014. Yields of *Miscanthus* × *giganteus* and *Panicum virgatum* decline with stand age in the Midwestern USA. GCB Bioenergy 6, 1–13. https://doi.org/10.1111/gcbb.12077

Ashworth, A.J., Allen, F.L., Bacon, J.L., Sams, C.E., Hart, W.E., Grant, J.F., Moore, P.A., Pote, D.H., 2017. Switchgrass Cultivar, Yield, and Nutrient Removal Responses to Harvest Timing. Agronomy Journal 109, 2598–2605. https://doi.org/10.2134/agronj2017.01.0018

Aytaç, E., 2020. Unsupervised learning approach in defining the similarity of catchments: Hydrological response unit based k-means clustering, a demonstration on Western Black Sea Region of Turkey. International Soil and Water Conservation Research 8, 321–331. https://doi.org/10.1016/j.iswcr.2020.05.002

Bailey, R.T., Park, S., 2019. SWAT-MODFLOW Tutorial Version3—Documentation for Preparing and Running SWAT-MODFLOW Simulations. Department of Civil and Environmental Engineering, Colorado State University: Fort Collins, CO, USA.

Bailey, R.T., Wible, T.C., Arabi, M., Records, R.M., Ditty, J., 2016. Assessing regional-scale spatio-temporal patterns of groundwater--surface water interactions using a coupled SWAT-MODFLOW model. Hydrological Processes 30, 4420–4433. https://doi.org/10.1002/hyp.10933

Barlow, P.M., Leake, S.A., 2012. Streamflow depletion by wells: understanding and managing the effects of groundwater pumping on streamflow. US Geological Survey Circular 1376. Reston, VA.

Barnes, P.L., Kalita, P.K., 2001. Watershed monitoring to address contamination source issues and remediation of the contaminant impairments. Water Science and Technology 44, 51–56. https://doi.org/10.2166/wst.2001.0387

Bastiaanssen, W.G.M., Menenti, M., Feddes, R.A., Holtslag, A.A.M., 1998. A remote sensing surface energy balance algorithm for land (SEBAL). 1. Formulation. Journal of Hydrology 212–213, 198–212. https://doi.org/10.1016/S0022-1694(98)00253-4

Bathke, D.J., Oglesby, R.J., Rowe, C., Wilhite, D.A., 2014. Understanding and assessing climate change: implications for Nebraska. University of Nebraska-Lincoln, Nebraska, USA.

Beven, K., Freer, J., 2001. Equifinality, data assimilation, and uncertainty estimation in mechanistic modelling of complex environmental systems using the GLUE methodology. Journal of Hydrology 249, 11–29. https://doi.org/10.1016/S0022-1694(01)00421-8

Bieger, K., Arnold, J.G., Rathjens, H., White, M.J., Bosch, D.D., Allen, P.M., Volk, M., Srinivasan, R., 2017. Introduction to SWAT+, A Completely Restructured Version of the Soil and Water Assessment Tool. J Am Water Resour Assoc 53, 115–130. https://doi.org/10.1111/1752-1688.12482

Brown, R.A., Rosenberg, N.J., Hays, C.J., Easterling, W.E., Mearns, L.O., 2000. Potential production and environmental effects of switchgrass and traditional crops under current and greenhouse-altered climate in the central United States: a simulation study. Agriculture, Ecosystems & Environment 78, 31–47. https://doi.org/10.1016/S0167-8809(99)00115-2

Cai, X., Zhang, X., Wang, D., 2011. Land availability for biofuel production. Environmental science & technology 45, 334–339. https://doi.org/10.1021/es103338e

Carlisle, D., Wolock, D.M., Howard, J.K., Grantham, T.E., Fesenmyer, K., Wieczorek, M., 2016. Estimating natural monthly streamflows in California and the likelihood of anthropogenic modification (Report No. 2016–1189), Open-File Report. Reston, VA. https://doi.org/10.3133/ofr20161189

Carlisle, D.M., Falcone, J., Wolock, D.M., Meador, M.R., Norris, R.H., 2009. Predicting the natural flow regime: models for assessing hydrological alteration in streams. River Res. Applic. n/a-n/a. https://doi.org/10.1002/rra.1247

Carruthers, I., Rosegrant, M.W., Seckler, D., 1997. Irrigation and food security in the 21st century. Irrigation and Drainage Systems 11, 83–101. https://doi.org/10.1023/A:1005751232728

Chamberlain, J.F., Miller, S.A., Frederick, J.R., 2011. Using DAYCENT to quantify on-farm GHG emissions and N dynamics of land use conversion to N-managed switchgrass in the Southern U.S. Agriculture, Ecosystems & Environment 141, 332–341. https://doi.org/10.1016/j.agee.2011.03.011

Chen, L., Blanc-Betes, E., Hudiburg, T.W., Hellerstein, D., Wallander, S., DeLucia, E.H., Khanna, M., 2021. Assessing the Returns to Land and Greenhouse Gas Savings from Producing Energy Crops on Conservation Reserve Program Land. Environ. Sci. Technol. 55, 1301–1309. https://doi.org/10.1021/acs.est.0c06133

Chen, X., 2004. Streambed hydraulic conductivity for rivers in south-central Nebraska 1. JAWRA Journal of the American Water Resources Association 40, 561–573. https://doi.org/10.1111/j.1752-1688.2004.tb04443.x

Chen, Xunhong, Chen, Xi, 2004. Simulating the Effects of Reduced Precipitation on Ground Water and Streamflow in the Nebraska Sand Hills 1. JAWRA Journal of the American Water Resources Association 40, 419–430. https://doi.org/10.1111/j.1752-1688.2004.tb01040.x

Chen, Y., Marek, G.W., Marek, T.H., Brauer, D.K., Srinivasan, R., 2018. Improving SWAT auto-irrigation functions for simulating agricultural irrigation management using long-term lysimeter

field data. Environmental modelling & software 99, 25–38. https://doi.org/10.1016/j.envsoft.2017.09.013
Chen, Y., Marek, G.W., Marek, T.H., Brauer, D.K., Srinivasan, R., 2017. Assessing the efficacy of the SWAT auto-irrigation function to simulate irrigation, evapotranspiration, and crop response to management strategies of the Texas High Plains. Water 9, 509–509. https://doi.org/10.3390/w9070509
Cheng, C., Song, J., Chen, X., Wang, D., 2011. Statistical distribution of streambed vertical hydraulic conductivity along the Platte River, Nebraska. Water resources management 25, 265–285. https://doi.org/10.1007/s11269-010-9698-5
Choi, H.I., Kumar, P., Liang, X.-Z., 2007. Three-dimensional volume-averaged soil moisture transport model with a scalable parameterization of subgrid topographic variability. Water Resources Research 43. https://doi.org/10.1029/2006WR005134
Choi, H.I., Liang, X.-Z., Kumar, P., 2013. A Conjunctive Surface–Subsurface Flow Representation for Mesoscale Land Surface Models. Journal of Hydrometeorology 14, 1421–1442. https://doi.org/10.1175/JHM-D-12-0168.1
Choudhary, R., Athira, P., 2021. Effect of root zone soil moisture on the SWAT model simulation of surface and subsurface hydrological fluxes. Environ Earth Sci 80, 620. https://doi.org/10.1007/s12665-021-09912-z
Chum, H., Faaij, A., Moreira, J., Berndes, G., Dhamija, P., Dong, H., Gabrielle, B., Eng, A.G., Lucht, W., Mapako, M., Cerutti, O.M., McIntyre, T., Minowa, T., Pingoud, K., Bain, R., Chiang, R., Dawe, D., Heath, G., Junginger, M., Patel, M., Yang, J., Warner, E., Paré, D., Ribeiro, S.K., 2011. Renewable Energy Sources and Climate Change Mitigation: Special Report of the Intergovernmental Panel on Climate Change. Cambridge University Press, Cambridge. https://doi.org/10.1017/CBO9781139151153.006
Chun, J.A., Baik, J., Kim, D., Choi, M., 2018. A comparative assessment of SWAT-model-based evapotranspiration against regional-scale estimates. Ecological Engineering 122, 1–9. https://doi.org/10.1016/j.ecoleng.2018.07.015
Chunn, D., Faramarzi, M., Smerdon, B., Alessi, D., 2019. Application of an Integrated SWAT–MODFLOW Model to Evaluate Potential Impacts of Climate Change and Water Withdrawals on Groundwater–Surface Water Interactions in West-Central Alberta. Water 11, 110. https://doi.org/10.3390/w11010110
Cibin, R., Trybula, E., Chaubey, I., Brouder, S.M., Volenec, J.J., 2016. Watershed-scale impacts of bioenergy crops on hydrology and water quality using improved SWAT model. GCB Bioenergy 8, 837–848. https://doi.org/10.1111/gcbb.12307
Clifton-Brown, J., Harfouche, A., Casler, M.D., Dylan Jones, H., Macalpine, W.J., Murphy-Bokern, D., Smart, L.B., Adler, A., Ashman, C., Awty-Carroll, D., Bastien, C., Bopper, S., Botnari, V., Brancourt-Hulmel, M., Chen, Z., Clark, L.V., Cosentino, S., Dalton, S., Davey, C., Dolstra, O., Donnison, I., Flavell, R., Greef, J., Hanley, S., Hastings, A., Hertzberg, M., Hsu, T., Huang, L.S., Iurato, A., Jensen, E., Jin, X., Jørgensen, U., Kiesel, A., Kim, D., Liu, J., McCalmont, J.P., McMahon, B.G., Mos, M., Robson, P., Sacks, E.J., Sandu, A., Scalici, G., Schwarz, K., Scordia, D., Shafiei, R., Shield, I., Slavov, G., Stanton, B.J., Swaminathan, K., Taylor, G., Torres, A.F., Trindade, L.M., Tschaplinski, T., Tuskan, G.A., Yamada, T., Yeon Yu, C., Zalesny, R.S., Zong, J., Lewandowski, I., 2019. Breeding progress and preparedness for mass-scale deployment of perennial lignocellulosic biomass crops switchgrass, miscanthus, willow and poplar. GCB Bioenergy 11, 118–151. https://doi.org/10.1111/gcbb.12566
Clifton-Brown, J.C., Breuer, J., Jones, M.B., 2007. Carbon mitigation by the energy crop, Miscanthus. Global Change Biol 13, 2296–2307. https://doi.org/10.1111/j.1365-2486.2007.01438.x
Colaizzi, P.D., Gowda, P.H., Marek, T.H., Porter, D.O., 2009. Irrigation in the Texas High Plains: A brief history and potential reductions in demand. Irrigation and Drainage: The journal of the International Commission on Irrigation and Drainage 58, 257–274. https://doi.org/10.1002/ird.418

Coleman, J.S.M., Budikova, D., 2013. Eastern U.S. summer streamflow during extreme phases of the North Atlantic oscillation: EASTERN U.S. SUMMER STREAMFLOW AND NAO. J. Geophys. Res. Atmos. 118, 4181–4193. https://doi.org/10.1002/jgrd.50326

Creutzig, F., Ravindranath, N.H., Berndes, G., Bolwig, S., Bright, R., Cherubini, F., Chum, H., Corbera, E., Delucchi, M., Faaij, A., Fargione, J., Haberl, H., Heath, G., Lucon, O., Plevin, R., Popp, A., Robledo-Abad, C., Rose, S., Smith, P., Stromman, A., Suh, S., Masera, O., 2015. Bioenergy and climate change mitigation: an assessment. GCB Bioenergy 7, 916–944. https://doi.org/10.1111/gcbb.12205

Crosbie, R.S., Scanlon, B.R., Mpelasoka, F.S., Reedy, R.C., Gates, J.B., Zhang, L., 2013. Potential climate change effects on groundwater recharge in the High Plains Aquifer, USA. Water Resources Research 49, 3936–3951. https://doi.org/10.1002/wrcr.20292

Crow, W., Tobin, K., 2018. Smerge-Noah-CCI root zone soil moisture 0-40 cm L4 daily 0.125 x 0.125 degree V2.0. https://doi.org/10.5067/PAVQY1KHTMUT

Daggupati, P., Deb, D., Srinivasan, R., Yeganantham, D., Mehta, V.M., Rosenberg, N.J., 2016. Large-scale fine-resolution hydrological modeling using parameter regionalization in the Missouri River basin. JAWRA Journal of the American Water Resources Association 52, 648–666. https://doi.org/10.1111/1752-1688.12413

Dai, Y., Dickinson, R.E., Wang, Y.-P., 2004. A Two-Big-Leaf Model for Canopy Temperature, Photosynthesis, and Stomatal Conductance. J. Climate 17, 2281–2299. https://doi.org/10.1175/1520-0442(2004)017<2281:ATMFCT>2.0.CO;2

Dai, Y., Zeng, X., Dickinson, R.E., Baker, I., Bonan, G.B., Bosilovich, M.G., Denning, A.S., Dirmeyer, P.A., Houser, P.R., Niu, G., Oleson, K.W., Schlosser, C.A., Yang, Z.-L., 2003. The Common Land Model. Bulletin of the American Meteorological Society 84, 1013–1024. https://doi.org/10.1175/BAMS-84-8-1013

Daly, C., Neilson, R.P., Phillips, D.L., 1994. A Statistical-Topographic Model for Mapping Climatological Precipitation over Mountainous Terrain. J. Appl. Meteor. 33, 140–158. https://doi.org/10.1175/1520-0450(1994)033<0140:ASTMFM>2.0.CO;2

Danabasoglu, G., Lamarque, J. -F., Bacmeister, J., Bailey, D.A., DuVivier, A.K., Edwards, J., Emmons, L.K., Fasullo, J., Garcia, R., Gettelman, A., Hannay, C., Holland, M.M., Large, W.G., Lauritzen, P.H., Lawrence, D.M., Lenaerts, J.T.M., Lindsay, K., Lipscomb, W.H., Mills, M.J., Neale, R., Oleson, K.W., Otto-Bliesner, B., Phillips, A.S., Sacks, W., Tilmes, S., Van Kampenhout, L., Vertenstein, M., Bertini, A., Dennis, J., Deser, C., Fischer, C., Fox-Kemper, B., Kay, J.E., Kinnison, D., Kushner, P.J., Larson, V.E., Long, M.C., Mickelson, S., Moore, J.K., Nienhouse, E., Polvani, L., Rasch, P.J., Strand, W.G., 2020. The Community Earth System Model Version 2 (CESM2). J Adv Model Earth Syst 12, e2019MS001916. https://doi.org/10.1029/2019MS001916

Dangol, S., Zhang, X., Liang, X.-Z., Anderson, M., Crow, W., Lee, S., Moglen, G.E., McCarty, G.W., 2023. Multivariate Calibration of the SWAT Model Using Remotely Sensed Datasets. Remote Sensing 15, 2417. https://doi.org/10.3390/rs15092417

Dangol, S., Zhang, X., Liang, X.-Z., Miralles-Wilhelm, F., 2022. Agricultural Irrigation Effects on Hydrological Processes in the United States Northern High Plains Aquifer Simulated by the Coupled SWAT-MODFLOW System. Water 14, 1938. https://doi.org/10.3390/w14121938

Davis, S.C., Parton, W.J., Dohleman, F.G., Smith, C.M., Grosso, S.D., Kent, A.D., DeLucia, E.H., 2010. Comparative Biogeochemical Cycles of Bioenergy Crops Reveal Nitrogen-Fixation and Low Greenhouse Gas Emissions in a Miscanthus × giganteus Agro-Ecosystem. Ecosystems 13, 144–156. https://doi.org/10.1007/s10021-009-9306-9

Davis, S.C., Parton, W.J., Grosso, S.J. Del, Keough, C., Marx, E., Adler, P.R., DeLucia, E.H., 2012. Impact of second-generation biofuel agriculture on greenhouse-gas emissions in the corn-growing regions of the US. Frontiers in Ecology and the Environment 10, 69–74. https://doi.org/10.1890/110003

Del Grosso, S.J., Parton, W.J., Ojima, D.S., Keough, C.A., Riley, T.H., Mosier, A.R., 2008. DAYCENT Simulated Effects of Land Use and Climate on County Level N Loss Vectors in the USA, in:

Nitrogen in the Environment. Elsevier, pp. 571–595. https://doi.org/10.1016/B978-0-12-374347-3.00018-4
Dembélé, M., Hrachowitz, M., Savenije, H.H.G., Mariéthoz, G., Schaefli, B., 2020. Improving the Predictive Skill of a Distributed Hydrological Model by Calibration on Spatial Patterns With Multiple Satellite Data Sets. Water Resources Research 56. https://doi.org/10.1029/2019WR026085
Dethier, E.N., Sartain, S.L., Renshaw, C.E., Magilligan, F.J., 2020. Spatially coherent regional changes in seasonal extreme streamflow events in the United States and Canada since 1950. Sci. Adv. 6, eaba5939. https://doi.org/10.1126/sciadv.aba5939
Dieter, C.A., Maupin, M.A., Caldwell, R.R., Harris, M.A., Ivahnenko, T.I., Lovelace, J.K., Barber, N.L., Linsey, K.S., 2018. Estimated use of water in the United States in 2015 (Report No. 1441), Circular. Reston, VA. https://doi.org/10.3133/cir1441
Dolan, K.A., Stoy, P.C., Poulter, B., 2020a. Land management and climate change determine second-generation bioenergy potential of the US Northern Great Plains. GCB Bioenergy 12, 491–509. https://doi.org/10.1111/gcbb.12686
Dolan, K.A., Stoy, P.C., Poulter, B., 2020b. Land management and climate change determine second-generation bioenergy potential of the US Northern Great Plains. GCB Bioenergy 12, 491–509. https://doi.org/10.1111/gcbb.12686
Douglas-Mankin, K.R., Srinivasan, R., Arnold, J.G., 2010. Soil and Water Assessment Tool (SWAT) model: Current developments and applications. Transactions of the ASABE 53, 1423–1431. https://doi.org/10.13031/2013.34915
Dudley, R.W., Hirsch, R.M., Archfield, S.A., Blum, A.G., Renard, B., 2020. Low streamflow trends at human-impacted and reference basins in the United States. Journal of Hydrology 580, 124254. https://doi.org/10.1016/j.jhydrol.2019.124254
Duveiller, G., Caporaso, L., Abad-Viñas, R., Perugini, L., Grassi, G., Arneth, A., Cescatti, A., 2020. Local biophysical effects of land use and land cover change: towards an assessment tool for policy makers. Land Use Policy 91, 104382. https://doi.org/10.1016/j.landusepol.2019.104382
Easterling, D.R., Arnold, J.R., Knutson, T., Kunkel, K.E., LeGrande, A.N., Leung, L.R., Vose, R.S., Waliser, D.E., Wehner, M.F., 2017. Precipitation Change in the United States. Climate Science Special Report: Fourth National Climate Assessment, Volume I. Washington, DC. https://doi.org/10.7930/J0H993CC
Egbendewe-Mondzozo, A., Swinton, S.M., Izaurralde, C.R., Manowitz, D.H., Zhang, X., 2011. Biomass supply from alternative cellulosic crops and crop residues: A spatially explicit bioeconomic modeling approach. Biomass and Bioenergy 35, 4636–4647. https://doi.org/10.1016/j.biombioe.2011.09.010
Egbendewe-Mondzozo, A., Swinton, S.M., Izaurralde, R.C., Manowitz, D.H., Zhang, X., 2013. Maintaining environmental quality while expanding biomass production: Sub-regional U.S. policy simulations. Energy Policy 57, 518–531. https://doi.org/10.1016/j.enpol.2013.02.021
Eng, K., Carlisle, D., Grantham, T.E., Wolock, D.M., Eng, R.L., 2019. Severity and extent of alterations to natural streamflow regimes based on hydrologic metrics in the conterminous United States, 1980–2014 (Report No. 2019–5001), Scientific Investigations Report. Reston, VA. https://doi.org/10.3133/sir20195001
Essou, G.R.C., Sabarly, F., Lucas-Picher, P., Brissette, F., Poulin, A., 2016. Can Precipitation and Temperature from Meteorological Reanalyses Be Used for Hydrological Modeling? Journal of Hydrometeorology 17, 1929–1950. https://doi.org/10.1175/JHM-D-15-0138.1
Eyring, V., Bony, S., Meehl, G.A., Senior, C.A., Stevens, B., Stouffer, R.J., Taylor, K.E., 2016. Overview of the Coupled Model Intercomparison Project Phase 6 (CMIP6) experimental design and organization. Geosci. Model Dev. 9, 1937–1958. https://doi.org/10.5194/gmd-9-1937-2016
Faisol, A., Indarto, Novita, E., Budiyono, 2020. An evaluation of MODIS global evapotranspiration product (MOD16A2) as terrestrial evapotranspiration in East Java - Indonesia. IOP Conf. Ser.: Earth Environ. Sci. 485, 012002. https://doi.org/10.1088/1755-1315/485/1/012002
Falcone, J.A., 2011. GAGES-II: Geospatial Attributes of Gages for Evaluating Streamflow (Report). Reston, VA. https://doi.org/10.3133/70046617

Falcone, J.A., Carlisle, D.M., Wolock, D.M., Meador, M.R., 2010. GAGES: A stream gage database for evaluating natural and altered flow conditions in the conterminous United States: ***Ecological Archives*** **E091-045** . Ecology 91, 621–621. https://doi.org/10.1890/09-0889.1

FAO, 2011. The state of the world's land and water resources for food and agriculture: managing systems at risk. Food and Agriculture Organization. Rome: Earthscan.

Farsadnia, F., Rostami Kamrood, M., Moghaddam Nia, A., Modarres, R., Bray, M.T., Han, D., Sadatinejad, J., 2014. Identification of homogeneous regions for regionalization of watersheds by two-level self-organizing feature maps. Journal of Hydrology 509, 387–397. https://doi.org/10.1016/j.jhydrol.2013.11.050

Feng, Q., Chaubey, I., Cibin, R., Engel, B., Sudheer, K.P., Volenec, J., Omani, N., 2018. Perennial biomass production from marginal land in the Upper Mississippi River Basin. Land Degrad Dev 29, 1748–1755. https://doi.org/10.1002/ldr.2971

Feng, Q., Chaubey, I., Her, Y.G., Cibin, R., Engel, B., Volenec, J., Wang, X., 2015. Hydrologic and water quality impacts and biomass production potential on marginal land. Environmental Modelling & Software 72, 230–238. https://doi.org/10.1016/j.envsoft.2015.07.004

Ferguson, R.B., Shapiro, C.A., Dobermann, A.R., Wortmann, C.S., 2006. G87-859 Fertilizer Recommendations for Soybean (Revised August 2006). Historical Materials from University of Nebraska-Lincoln Extension.

Fernández-Martínez, M., Vicca, S., Janssens, I.A., Ciais, P., Obersteiner, M., Bartrons, M., Sardans, J., Verger, A., Canadell, J.G., Chevallier, F., Wang, X., Bernhofer, C., Curtis, P.S., Gianelle, D., Grünwald, T., Heinesch, B., Ibrom, A., Knohl, A., Laurila, T., Law, B.E., Limousin, J.M., Longdoz, B., Loustau, D., Mammarella, I., Matteucci, G., Monson, R.K., Montagnani, L., Moors, E.J., Munger, J.W., Papale, D., Piao, S.L., Peñuelas, J., 2017. Atmospheric deposition, CO2, and change in the land carbon sink. Sci Rep 7, 9632. https://doi.org/10.1038/s41598-017-08755-8

Ficklin, D.L., Robeson, S.M., Knouft, J.H., 2016. Impacts of recent climate change on trends in baseflow and stormflow in United States watersheds. Geophys. Res. Lett. 43, 5079–5088. https://doi.org/10.1002/2016GL069121

Fischer, G., Shah, M., Van Velthuizen, H., Nachtergaele, F.O., 2001. Global agro-ecological assessment for agriculture in the 21st century.

Frank, A.B., Berdahl, J.D., Hanson, J.D., Liebig, M.A., Johnson, H.A., 2004. Biomass and Carbon Partitioning in Switchgrass. Crop Sci. 44, 1391–1396. https://doi.org/10.2135/cropsci2004.1391

Gan, Y., Liang, X.-Z., Duan, Q., Choi, H.I., Dai, Y., Wu, H., 2015. Stepwise sensitivity analysis from qualitative to quantitative: Application to the terrestrial hydrological modeling of a Conjunctive Surface-Subsurface Process (CSSP) land surface model: Stepwise Sensitivity Analysis of LSMs. J. Adv. Model. Earth Syst. 7, 648–669. https://doi.org/10.1002/2014MS000406

Gao, L., Li, D., 2014. A review of hydrological/water-quality models. Frontiers of Agricultural Science and Engineering 1, 267–276. https://doi.org/10.15302/J-FASE-2014041

Garces-Restrepo, C., Vermillion, D., Muñoz, G., 2007. Irrigation management transfer. Worldwide efforts and results. FAO Water Reports 32. International Irrigation Management Institute, FAO, 62pp.

Garg, K.K., Bharati, L., Gaur, A., George, B., Acharya, S., Jella, K., Narasimhan, B., 2012. Spatial mapping of agricultural water productivity using the SWAT model in Upper Bhima Catchment, India. Irrigation and Drainage 61, 60–79. https://doi.org/10.1002/ird.618

Gassman, P.W., Arnold, J.J., Srinivasan, R., Reyes, M., 2010. The Worldwide Use of the SWAT Model: Technological Drivers, Networking Impacts, and Simulation Trends, in: 21st Century Watershed Technology: Improving Water Quality and Environment Conference Proceedings, 21-24 February 2010, Universidad EARTH, Costa Rica. Presented at the 21st Century Watershed Technology: Improving Water Quality and Environment Conference Proceedings, 21-24 February 2010, Universidad EARTH, Costa Rica, American Society of Agricultural and Biological Engineers. https://doi.org/10.13031/2013.29418

Gelfand, I., Sahajpal, R., Zhang, X., Izaurralde, R.C., Gross, K.L., Robertson, G.P., 2013a. Sustainable bioenergy production from marginal lands in the US Midwest. Nature 493, 514–517. https://doi.org/10.1038/nature11811

Gelfand, I., Sahajpal, R., Zhang, X., Izaurralde, R.C., Gross, K.L., Robertson, G.P., 2013b. Sustainable bioenergy production from marginal lands in the US Midwest. Nature 493, 514–517. https://doi.org/10.1038/nature11811

Gheewala, S.H., Berndes, G., Jewitt, G., 2011. The bioenergy and water nexus. Biofuels, Bioproducts and Biorefining 5, 353–360. https://doi.org/10.1002/bbb.295

Gopalakrishnan, G., Cristina Negri, M., Salas, W., 2012. Modeling biogeochemical impacts of bioenergy buffers with perennial grasses for a row-crop field in Illinois. Glob. Change Biol. Bioenergy 4, 739–750. https://doi.org/10.1111/j.1757-1707.2011.01145.x

Grell, G.A., Dévényi, D., 2002. A generalized approach to parameterizing convection combining ensemble and data assimilation techniques. Geophys. Res. Lett. 29, 38-1-38–4. https://doi.org/10.1029/2002GL015311

Guo, T., Cibin, R., Chaubey, I., Gitau, M., Arnold, J.G., Srinivasan, R., Kiniry, J.R., Engel, B.A., 2018a. Evaluation of bioenergy crop growth and the impacts of bioenergy crops on streamflow, tile drain flow and nutrient losses in an extensively tile-drained watershed using SWAT. Science of The Total Environment 613–614, 724–735. https://doi.org/10.1016/j.scitotenv.2017.09.148

Guo, T., Cibin, R., Chaubey, I., Gitau, M., Arnold, J.G., Srinivasan, R., Kiniry, J.R., Engel, B.A., 2018b. Evaluation of bioenergy crop growth and the impacts of bioenergy crops on streamflow, tile drain flow and nutrient losses in an extensively tile-drained watershed using SWAT. Science of The Total Environment 613–614, 724–735. https://doi.org/10.1016/j.scitotenv.2017.09.148

Gupta, H.V., Kling, H., Yilmaz, K.K., Martinez, G.F., 2009. Decomposition of the mean squared error and NSE performance criteria: Implications for improving hydrological modelling. Journal of Hydrology 377, 80–91. https://doi.org/10.1016/j.jhydrol.2009.08.003

Haacker, E.M.K., Kendall, A.D., Hyndman, D.W., 2016. Water level declines in the High Plains Aquifer: Predevelopment to resource senescence. Groundwater 54, 231–242. https://doi.org/10.1111/gwat.12350

Harbaugh, A.W., 2005. MODFLOW-2005, The U.S. Geological Survey modular ground-water model — the ground-water flow process: U.S. Geological Survey Techniques and Methods 6-A16, Modeling techniques. U.S. Geological Survey, Reston, VA.

Harris, W., Lubben, B., Novak, J., Sanders, L.D., 2008. The Food, Conservation, and Energy Act of 2008 summary and possible consequences. University of Georgia TS - DAERS-WP-1.

Hartigan, J.A., Wong, M.A., 1979. Algorithm AS 136: A K-Means Clustering Algorithm. Applied Statistics 28, 100. https://doi.org/10.2307/2346830

Hartman, J.C., Nippert, J.B., Springer, C.J., 2012. Ecotypic responses of switchgrass to altered precipitation. Functional Plant Biol. 39, 126. https://doi.org/10.1071/FP11229

He, J., 2013. Mixture model based multivariate statistical analysis of multiply censored environmental data. Advances in Water Resources 59, 15–24. https://doi.org/10.1016/j.advwatres.2013.05.001

He, Y., Jaiswal, D., Liang, X., Sun, C., Long, S.P., 2022. Perennial biomass crops on marginal land improve both regional climate and agricultural productivity. GCB Bioenergy 14, 558–571. https://doi.org/10.1111/gcbb.12937

Helgesen, J.O., 1996. Surface-water-quality assessment of the lower Kansas River basin, Kansas and Nebraska: Results of investigations, 1987-90. https://doi.org/10.3133/wsp2451

Her, Y., Frankenberger, J., Chaubey, I., Srinivasan, R., 2015. Threshold Effects in HRU Definition ofthe Soil and Water Assessment Tool. Trans. ASABE 367–378. https://doi.org/10.13031/trans.58.10805

Herman, M.R., Nejadhashemi, A.P., Abouali, M., Hernandez-Suarez, J.S., Daneshvar, F., Zhang, Z., Anderson, M.C., Sadeghi, A.M., Hain, C.R., Sharifi, A., 2018. Evaluating the role of evapotranspiration remote sensing data in improving hydrological modeling predictability. Journal of Hydrology 556, 39–49. https://doi.org/10.1016/j.jhydrol.2017.11.009

Hickman, G.C., Vanloocke, A., Dohleman, F.G., Bernacchi, C.J., 2010. A comparison of canopy evapotranspiration for maize and two perennial grasses identified as potential bioenergy crops. GCB Bioenergy no-no. https://doi.org/10.1111/j.1757-1707.2010.01050.x

Hodgkins, G.A., Dudley, R.W., Archfield, S.A., Renard, B., 2019. Effects of climate, regulation, and urbanization on historical flood trends in the United States. Journal of Hydrology 573, 697–709. https://doi.org/10.1016/j.jhydrol.2019.03.102

Holder, A.J., Rowe, R., McNamara, N.P., Donnison, I.S., McCalmont, J.P., 2019. Soil & Water Assessment Tool (SWAT) simulated hydrological impacts of land use change from temperate grassland to energy crops: A case study in western UK. GCB Bioenergy 11, 1298–1317. https://doi.org/10.1111/gcbb.12628

Hoque, Y.M., Raj, C., Hantush, M.M., Chaubey, I., Govindaraju, R.S., 2014. How Do Land-Use and Climate Change Affect Watershed Health? A Scenario-Based Analysis. Water Qual Expo Health 6, 19–33. https://doi.org/10.1007/s12403-013-0102-6

Hrozencik, R.A., Manning, D.T., Suter, J.F., Goemans, C., Bailey, R.T., 2017. The Heterogeneous Impacts of Groundwater Management Policies in the Republican River Basin of Colorado. Water Resources Research 53, 10757–10778. https://doi.org/10.1002/2017WR020927

Hua, L., Wang, H., Sui, H., Wardlow, B., Hayes, M.J., Wang, J., 2019. Mapping the spatial-temporal dynamics of vegetation response lag to drought in a semi-arid region. Remote Sensing 11, 1873–1873. https://doi.org/10.3390/rs11161873

Hudiburg, T.W., Davis, S.C., Parton, W., Delucia, E.H., 2015. Bioenergy crop greenhouse gas mitigation potential under a range of management practices. GCB Bioenergy 7, 366–374. https://doi.org/10.1111/gcbb.12152

Hudiburg, T.W., Wang, W., Khanna, M., Long, S.P., Dwivedi, P., Parton, W.J., Hartman, M., DeLucia, E.H., 2016. Impacts of a 32-billion-gallon bioenergy landscape on land and fossil fuel use in the US. Nat Energy 1, 15005. https://doi.org/10.1038/nenergy.2015.5

Huo, J., Liu, C., Yu, X., Jia, G., Chen, L., 2021. Effects of watershed char and climate variables on annual runoff in different climatic zones in China. Science of The Total Environment 754, 142157. https://doi.org/10.1016/j.scitotenv.2020.142157

Hutson, S.S., Barber, N.L., Kenny, J.F., Linsey, K.S., Lumia, D.S., Maupin, M.A., 2004. Estimated Use of Water in the United States in 2000 (No. 1268), Circular. https://doi.org/10.3133/cir1268

Immerzeel, W.W., Droogers, P., 2008. Calibration of a distributed hydrological model based on satellite evapotranspiration. Journal of Hydrology 349, 411–424. https://doi.org/10.1016/j.jhydrol.2007.11.017

IPCC, 2023. Summary for Policymakers. In: Climate Change 2022 – Impacts, Adaptation and Vulnerability: Working Group II Contribution to the Sixth Assessment Report of the Intergovernmental Panel on Climate Change, 1st ed. Cambridge University Press. https://doi.org/10.1017/9781009325844

IPCC (Ed.), 2014. Climate Change 2013 – The Physical Science Basis: Working Group I Contribution to the Fifth Assessment Report of the Intergovernmental Panel on Climate Change, 1st ed. Cambridge University Press. https://doi.org/10.1017/CBO9781107415324

Jarvis, A., Reuter, H.I., Nelson, A., Guevara, E., 2008a. Hole-filled SRTM for the globe Version 4. available from the CGIAR-CSI SRTM 90m Database (http://srtm. csi. cgiar. org) 15, 25–54.

Jarvis, A., Reuter, H.I., Nelson, A., Guevara, E., 2008b. Hole-filled SRTM for the globe Version 4. available from the CGIAR-CSI SRTM 90m Database (http://srtm. csi. cgiar. org) 15, 25–54.

Ji, P., Yuan, X., Liang, X.-Z., 2017. Do Lateral Flows Matter for the Hyperresolution Land Surface Modeling?: Do Lateral Flows Matter for Land Model? J. Geophys. Res. Atmos. 122, 12,077-12,092. https://doi.org/10.1002/2017JD027366

Jiang, R., Sun, L., Sun, C., Liang, X.-Z., 2021. CWRF downscaling and understanding of China precipitation projections. Clim Dyn 57, 1079–1096. https://doi.org/10.1007/s00382-021-05759-z

Jiang, Y., Xu, X., Huang, Q., Huo, Z., Huang, G., 2015. Assessment of irrigation performance and water productivity in irrigated areas of the middle Heihe River basin using a distributed agro-

hydrological model. Agricultural Water Management 147, 67–81. https://doi.org/10.1016/j.agwat.2014.08.003
Jin, X., Jin, Y., Mao, X., Zhai, J., Fu, D., 2021. Modelling the Impact of Vegetation Change on Hydrological Processes in Bayin River Basin, Northwest China. Water 13, 2787. https://doi.org/10.3390/w13192787
Jones, J.W., Hoogenboom, G., Porter, C.H., Boote, K.J., Batchelor, W.D., Hunt, L.A., Wilkens, P.W., Singh, U., Gijsman, A.J., Ritchie, J.T., 2003. The DSSAT cropping system model. European Journal of Agronomy 18, 235–265. https://doi.org/10.1016/S1161-0301(02)00107-7
Jung, J.Y., Lal, R., 2011. Impacts of nitrogen fertilization on biomass production of switchgrass (Panicum Virgatum L.) and changes in soil organic carbon in Ohio. Geoderma 166, 145–152. https://doi.org/10.1016/j.geoderma.2011.07.023
Kantola, I.B., Masters, M.D., Blanc-Betes, E., Gomez-Casanovas, N., DeLucia, E.H., 2022. Long-term yields in annual and perennial bioenergy crops in the Midwestern United States. GCB Bioenergy 14, 694–706. https://doi.org/10.1111/gcbb.12940
Karimi, P., Bastiaanssen, W.G.M., 2015. Spatial evapotranspiration, rainfall and land use data in water accounting – Part 1: Review of the accuracy of the remote sensing data. Hydrol. Earth Syst. Sci. 19, 507–532. https://doi.org/10.5194/hess-19-507-2015
Kendall, M.G., 1948. Rank correlation methods.
Kim, N.W., Chung, I.M., Won, Y.S., Arnold, J.G., 2008. Development and application of the integrated SWAT--MODFLOW model. Journal of hydrology 356, 1–16.
Kiniry, J.R., Schmer, M.R., Vogel, K.P., Mitchell, R.B., 2008. Switchgrass Biomass Simulation at Diverse Sites in the Northern Great Plains of the U.S. Bioenerg. Res. 1, 259–264. https://doi.org/10.1007/s12155-008-9024-8
Kisi, O., 2010. Wavelet regression model for short-term streamflow forecasting. Journal of Hydrology 389, 344–353. https://doi.org/10.1016/j.jhydrol.2010.06.013
Klocke, N.L., Hubbard, K., Kranz, W.L., Watts, D.G., 1990. G90-992 Evapotranspiration (ET) or Crop Water Use. Historical Materials from University of Nebraska-Lincoln Extension 1197–1197.
Kollet, S.J., Maxwell, R.M., 2006. Integrated surface–groundwater flow modeling: A free-surface overland flow boundary condition in a parallel groundwater flow model. Advances in Water Resources 29, 945–958. https://doi.org/10.1016/j.advwatres.2005.08.006
Kukal, M.S., Irmak, S., 2018. Climate-Driven Crop Yield and Yield Variability and Climate Change Impacts on the U.S. Great Plains Agricultural Production. Scientific Reports 8, 3450. https://doi.org/10.1038/s41598-018-21848-2
Kundu, D., Vervoort, R.W., van Ogtrop, F.F., 2017. The value of remotely sensed surface soil moisture for model calibration using SWAT. Hydrol. Process. 31, 2764–2780. https://doi.org/10.1002/hyp.11219
Kustu, M.D., Fan, Y., Robock, A., 2010. Large-scale water cycle perturbation due to irrigation pumping in the US High Plains: A synthesis of observed streamflow changes. Journal of Hydrology 390, 222–244. https://doi.org/10.1016/j.jhydrol.2010.06.045
Kustu, M.D., Fan, Y., Rodell, M., 2011. Possible link between irrigation in the U.S. High Plains and increased summer streamflow in the Midwest: PLAINS IRRIGATION AND INCREASED MIDWEST STREAMFLOW. Water Resour. Res. 47. https://doi.org/10.1029/2010WR010046
Lark, T.J., Hendricks, N.P., Smith, A., Pates, N., Spawn-Lee, S.A., Bougie, M., Booth, E.G., Kucharik, C.J., Gibbs, H.K., 2022. Environmental outcomes of the US Renewable Fuel Standard. Proc. Natl. Acad. Sci. U.S.A. 119, e2101084119. https://doi.org/10.1073/pnas.2101084119
Lark, T.J., Meghan Salmon, J., Gibbs, H.K., 2015. Cropland expansion outpaces agricultural and biofuel policies in the United States. Environ. Res. Lett. 10, 044003. https://doi.org/10.1088/1748-9326/10/4/044003
Larnaudie, V., Ferrari, M.D., Lareo, C., 2022. Switchgrass as an alternative biomass for ethanol production in a biorefinery: Perspectives on technology, economics and environmental sustainability. Renewable and Sustainable Energy Reviews 158, 112115. https://doi.org/10.1016/j.rser.2022.112115

Lawrence, D.M., Fisher, R.A., Koven, C.D., Oleson, K.W., Swenson, S.C., Bonan, G., Collier, N., Ghimire, B., Van Kampenhout, L., Kennedy, D., Kluzek, E., Lawrence, P.J., Li, F., Li, H., Lombardozzi, D., Riley, W.J., Sacks, W.J., Shi, M., Vertenstein, M., Wieder, W.R., Xu, C., Ali, A.A., Badger, A.M., Bisht, G., Van Den Broeke, M., Brunke, M.A., Burns, S.P., Buzan, J., Clark, M., Craig, A., Dahlin, K., Drewniak, B., Fisher, J.B., Flanner, M., Fox, A.M., Gentine, P., Hoffman, F., Keppel-Aleks, G., Knox, R., Kumar, S., Lenaerts, J., Leung, L.R., Lipscomb, W.H., Lu, Y., Pandey, A., Pelletier, J.D., Perket, J., Randerson, J.T., Ricciuto, D.M., Sanderson, B.M., Slater, A., Subin, Z.M., Tang, J., Thomas, R.Q., Val Martin, M., Zeng, X., 2019. The Community Land Model Version 5: Description of New Features, Benchmarking, and Impact of Forcing Uncertainty. J Adv Model Earth Syst 11, 4245–4287. https://doi.org/10.1029/2018MS001583

LeDuc, S.D., Zhang, X., Clark, C.M., Izaurralde, R.C., 2017. Cellulosic feedstock production on Conservation Reserve Program land: potential yields and environmental effects. GCB Bioenergy 9, 460–468. https://doi.org/10.1111/gcbb.12352

Lee, J., Pedroso, G., Linquist, B.A., Putnam, D., Kessel, C., Six, J., 2012. Simulating switchgrass biomass production across ecoregions using the DAYCENT model. Glob. Change Biol. Bioenergy 4, 521–533. https://doi.org/10.1111/j.1757-1707.2011.01140.x

Lee, S., Qi, J., Kim, H., McCarty, G.W., Moglen, G.E., Anderson, M., Zhang, X., Du, L., 2021. Utility of Remotely Sensed Evapotranspiration Products to Assess an Improved Model Structure. Sustainability 13, 2375. https://doi.org/10.3390/su13042375

Lee, S., Qi, J., McCarty, G.W., Anderson, M., Yang, Y., Zhang, X., Moglen, G.E., Kwak, D., Kim, H., Lakshmi, V., Kim, S., 2022. Combined use of crop yield statistics and remotely sensed products for enhanced simulations of evapotranspiration within an agricultural watershed. Agricultural Water Management 264, 107503. https://doi.org/10.1016/j.agwat.2022.107503

Li, M., Ma, Z., Du, J., 2010. Regional soil moisture simulation for Shaanxi Province using SWAT model validation and trend analysis. Sci. China Earth Sci. 53, 575–590. https://doi.org/10.1007/s11430-010-0031-1

Li, M., Zhang, Y., Wallace, J., Campbell, E., 2020. Estimating annual runoff in response to forest change: A statistical method based on random forest. Journal of Hydrology 589, 125168. https://doi.org/10.1016/j.jhydrol.2020.125168

Li, Q., Wang, T., Wang, F., Liang, X., Zhao, Chongbo, Dong, L., Zhao, Chunyu, Xie, B., 2021. Dynamical downscaling simulation of the East Asian summer monsoon in a regional CLIMATE-WEATHER Research and Forecasting model. Int J Climatol 41. https://doi.org/10.1002/joc.6800

Li, X., Petipas, R.H., Antoch, A.A., Liu, Y., Stel, H.V., Bell-Dereske, L., Smercina, D.N., Bekkering, C., Evans, S.E., Tiemann, L.K., Friesen, M.L., 2022. Switchgrass cropping systems affect soil carbon and nitrogen and microbial diversity and activity on marginal lands. GCB Bioenergy 14, 918–940. https://doi.org/10.1111/gcbb.12949

Li, Y., Grimaldi, S., Pauwels, V.R.N., Walker, J.P., 2018. Hydrologic model calibration using remotely sensed soil moisture and discharge measurements: The impact on predictions at gauged and ungauged locations. Journal of Hydrology 557, 897–909. https://doi.org/10.1016/j.jhydrol.2018.01.013

Li, Z., Ciais, P., Wright, J.S., Wang, Y., Liu, S., Wang, J., Li, L.Z.X., Lu, H., Huang, X., Zhu, L., Goll, D.S., Li, W., 2023. Increased precipitation over land due to climate feedback of large-scale bioenergy cultivation. Nat Commun 14, 4096. https://doi.org/10.1038/s41467-023-39803-9

Liang, K., Qi, J., Zhang, X., Deng, J., 2022. Replicating measured site-scale soil organic carbon dynamics in the U.S. Corn Belt using the SWAT-C model. Environmental Modelling & Software 158, 105553. https://doi.org/10.1016/j.envsoft.2022.105553

Liang, X.-Z., Sun, C., Zheng, X., Dai, Y., Xu, M., Choi, H.I., Ling, T., Qiao, F., Kong, X., Bi, X., Song, L., Wang, F., 2019. CWRF performance at downscaling China climate characteristics. Climate Dynamics 52. https://doi.org/10.1007/s00382-018-4257-5

Liang, X.-Z., Xu, M., Gao, W., Kunkel, K., Slusser, J., Dai, Y., Min, Q., Houser, P.R., Rodell, M., Schaaf, C.B., Gao, F., 2005. Development of land surface albedo parameterization based on

Moderate Resolution Imaging Spectroradiometer (MODIS) data. Journal of Geophysical Research: Atmospheres 110. https://doi.org/10.1029/2004JD005579
Liang, X.-Z., Xu, M., Yuan, X., Ling, T., Choi, H.I., Zhang, F., Chen, L., Liu, S., Su, S., Qiao, F., He, Y., Wang, J.X.L., Kunkel, K.E., Gao, W., Joseph, E., Morris, V., Yu, T.-W., Dudhia, J., Michalakes, J., 2012. Regional Climate–Weather Research and Forecasting Model. Bulletin of the American Meteorological Society 93, 1363–1387. https://doi.org/10.1175/BAMS-D-11-00180.1
Liebig, M.A., Schmer, M.R., Vogel, K.P., Mitchell, R.B., 2008. Soil Carbon Storage by Switchgrass Grown for Bioenergy. BioEnergy Research 1, 215–222. https://doi.org/10.1007/s12155-008-9019-5
Lin, P., Rajib, M.A., Yang, Z.-L., Somos-Valenzuela, M., Merwade, V., Maidment, D.R., Wang, Y., Chen, L., 2018. Spatiotemporal Evaluation of Simulated Evapotranspiration and Streamflow over Texas Using the WRF-Hydro-RAPID Modeling Framework. J Am Water Resour Assoc 54, 40–54. https://doi.org/10.1111/1752-1688.12585
Lins, H.F., 2012. USGS Hydro-Climatic Data Network 2009 (HCDN–2009): U.S. Geological Survey Fact Sheet 2012–3047 4.
Lins, H.F., Slack, J.R., 2005. Seasonal and Regional Characteristics of U.S. Streamflow Trends in the United States from 1940 to 1999. Physical Geography 26, 489–501. https://doi.org/10.2747/0272-3646.26.6.489
Liu, W., Bailey, R.T., Andersen, H.E., Jeppesen, E., Nielsen, A., Peng, K., Molina-Navarro, E., Park, S., Thodsen, H., Trolle, D., 2020. Quantifying the effects of climate change on hydrological regime and stream biota in a groundwater-dominated catchment: A modelling approach combining SWAT-MODFLOW with flow-biota empirical models. Science of The Total Environment 745, 140933. https://doi.org/10.1016/j.scitotenv.2020.140933
Liu, W., Park, S., Bailey, R.T., Molina-Navarro, E., Andersen, H.E., Thodsen, H., Nielsen, A., Jeppesen, E., Jensen, J.S., Jensen, J.B., Trolle, D., 2019. Comparing SWAT with SWAT-MODFLOW hydrological simulations when assessing the impacts of groundwater abstractions for irrigation and drinking water. Hydrology and Earth System Sciences Discussions 1–51. https://doi.org/10.5194/hess-2019-232
Lobell, D.B., Asner, G.P., 2003. Climate and Management Contributions to Recent Trends in U.S. Agricultural Yields. Science 299, 1032–1032. https://doi.org/10.1126/science.1078475
López, P., Sutanudjaja, E.H., Schellekens, J., Sterk, G., Bierkens, M.F.P., 2017. Calibration of a large-scale hydrological model using satellite-based soil moisture and evapotranspiration products. Hydrol. Earth Syst. Sci. 21, 3125–3144. https://doi.org/10.5194/hess-21-3125-2017
Lu, C., Zhang, J., Tian, H., Crumpton, W.G., Helmers, M.J., Cai, W.-J., Hopkinson, C.S., Lohrenz, S.E., 2020. Increased extreme precipitation challenges nitrogen load management to the Gulf of Mexico. Commun Earth Environ 1, 21. https://doi.org/10.1038/s43247-020-00020-7
Luke, A., Vrugt, J.A., AghaKouchak, A., Matthew, R., Sanders, B.F., 2017. Predicting nonstationary flood frequencies: Evidence supports an updated stationarity thesis in the U nited S tates. Water Resources Research 53, 5469–5494. https://doi.org/10.1002/2016WR019676
Luo, Y., He, C., Sophocleous, M., Yin, Z., Hongrui, R., Ouyang, Z., 2008. Assessment of crop growth and soil water modules in SWAT2000 using extensive field experiment data in an irrigation district of the Yellow River Basin. Journal of Hydrology 352, 139–156. https://doi.org/10.1016/j.jhydrol.2008.01.003
Madakadze, I.C., Coulman, B.E., Peterson, P., Stewart, K.A., Samson, R., Smith, D.L., 1998. Leaf Area Development, Light Interception, and Yield among Switchgrass Populations in a Short-Season Area. Crop Sci. 38, 827–834. https://doi.org/10.2135/cropsci1998.0011183X003800030035x
Mann, H.B., 1945. Nonparametric tests against trend. Econometrica: Journal of the econometric society 245–259.
Marek, G.W., Gowda, P.H., Marek, T.H., Porter, D.O., Baumhardt, R.L., Brauer, D.K., 2017. Modeling long-term water use of irrigated cropping rotations in the Texas High Plains using SWAT. Irrigation science 35, 111–123. https://doi.org/10.1007/s00271-016-0524-6

Markstrom, S.L., R. G., Regan, R.S., Prudic, D.E., Barlow, P.M., 2008. GSFLOW—Coupled groundwater and surface-water flow model based on the integration of the Precipitation-Runoff Modeling System (PRMS) and the Modular Ground-Water Flow Model (MODFLOW-2005). U.S. Geological Survey Techniques and Methods 6-D1, U.S. Geological Survey, Reston, Virginia.

Marti, M.K., Rydberg, K.R., 2023. Method for identification of reservoir regulation within U.S. Geological Survey streamgage basins in the Central United States using a decadal dam impact metric (Open-File Report No. 2023–1034), Open-File Report 2023–1034. U.S. Geological Survey, Reston, VA.

Martinez-Feria, R., Basso, B., 2020. Predicting soil carbon changes in switchgrass grown on marginal lands under climate change and adaptation strategies. GCB Bioenergy 12, 742–755. https://doi.org/10.1111/gcbb.12726

Martino, G.D., Fontana, N., Marini, G., Singh, V.P., 2013. Variability and Trend in Seasonal Precipitation in the Continental United States. J. Hydrol. Eng. 18, 630–640. https://doi.org/10.1061/(ASCE)HE.1943-5584.0000677

Massey, J., Antonangelo, J., Zhang, H., 2020. Nutrient Dynamics in Switchgrass as a Function of Time. Agronomy 10, 940. https://doi.org/10.3390/agronomy10070940

Maupin, M.A., Barber, N.L., 2005. Estimated withdrawals from principal aquifers in the United States, 2000. US Geological Survey Circular 1–51. https://doi.org/10.3133/cir1279

Mauritsen, T., Bader, J., Becker, T., Behrens, J., Bittner, M., Brokopf, R., Brovkin, V., Claussen, M., Crueger, T., Esch, M., Fast, I., Fiedler, S., Fläschner, D., Gayler, V., Giorgetta, M., Goll, D.S., Haak, H., Hagemann, S., Hedemann, C., Hohenegger, C., Ilyina, T., Jahns, T., Jimenéz-de-la-Cuesta, D., Jungclaus, J., Kleinen, T., Kloster, S., Kracher, D., Kinne, S., Kleberg, D., Lasslop, G., Kornblueh, L., Marotzke, J., Matei, D., Meraner, K., Mikolajewicz, U., Modali, K., Möbis, B., Müller, W.A., Nabel, J.E.M.S., Nam, C.C.W., Notz, D., Nyawira, S., Paulsen, H., Peters, K., Pincus, R., Pohlmann, H., Pongratz, J., Popp, M., Raddatz, T.J., Rast, S., Redler, R., Reick, C.H., Rohrschneider, T., Schemann, V., Schmidt, H., Schnur, R., Schulzweida, U., Six, K.D., Stein, L., Stemmler, I., Stevens, B., Von Storch, J., Tian, F., Voigt, A., Vrese, P., Wieners, K., Wilkenskjeld, S., Winkler, A., Roeckner, E., 2019. Developments in the MPI-M Earth System Model version 1.2 (MPI-ESM1.2) and Its Response to Increasing CO_2. J Adv Model Earth Syst 11, 998–1038. https://doi.org/10.1029/2018MS001400

McIsaac, G.F., David, M.B., Mitchell, C.A., 2010. Miscanthus and Switchgrass Production in Central Illinois: Impacts on Hydrology and Inorganic Nitrogen Leaching. J. Environ. Qual. 39, 1790–1799. https://doi.org/10.2134/jeq2009.0497

McLaughlin, S.B., Walsh, M.E., 1998. Evaluating environmental consequences of producing herbaceous crops for bioenergy. Biomass and Bioenergy 14, 317–324. https://doi.org/10.1016/S0961-9534(97)10066-6

McManamay, R.A., George, R., Morrison, R.R., Ruddell, B.L., 2022. Mapping hydrologic alteration and ecological consequences in stream reaches of the conterminous United States. Sci Data 9, 450. https://doi.org/10.1038/s41597-022-01566-1

McManamay, R.A., Orth, D.J., Dolloff, C.A., 2012. Revisiting the homogenization of dammed rivers in the southeastern US. Journal of Hydrology 424–425, 217–237. https://doi.org/10.1016/j.jhydrol.2012.01.003

Mehmood, M.A., Ibrahim, M., Rashid, U., Nawaz, M., Ali, S., Hussain, A., Gull, M., 2017. Biomass production for bioenergy using marginal lands. Sustainable Production and Consumption 9, 3–21. https://doi.org/10.1016/j.spc.2016.08.003

Meixner, T., Manning, A.H., Stonestrom, D.A., Allen, D.M., Ajami, H., Blasch, K.W., Brookfield, A.E., Castro, C.L., Clark, J.F., Gochis, D.J., Flint, A.L., Neff, K.L., Niraula, R., Rodell, M., Scanlon, B.R., Singha, K., Walvoord, M.A., 2016. Implications of projected climate change for groundwater recharge in the western United States. Journal of Hydrology 534, 124–138. https://doi.org/10.1016/j.jhydrol.2015.12.027

Menne, M.J., Durre, I., Korzeniewski, B., McNeill, S., Thomas, K., Yin, X., Anthony, S., Ray, R., Vose, R.S., Gleason, B.E., Houston, T.G., 2012. Global Historical Climatology Network - Daily (GHCN-Daily), Version 3. https://doi.org/10.7289/V5D21VHZ

Merz, R., Blöschl, G., 2009. A regional analysis of event runoff coefficients with respect to climate and catchment characteristics in Austria: REGIONAL ANALYSIS OF EVENT RUNOFF COEFFICIENTS. Water Resour. Res. 45. https://doi.org/10.1029/2008WR007163

Mesinger, F., DiMego, G., Kalnay, E., Mitchell, K., Shafran, P.C., Ebisuzaki, W., Jović, D., Woollen, J., Rogers, E., Berbery, E.H., Ek, M.B., Fan, Y., Grumbine, R., Higgins, W., Li, H., Lin, Y., Manikin, G., Parrish, D., Shi, W., 2006a. North American regional reanalysis. Bulletin of the American Meteorological Society 87, 343–360. https://doi.org/10.1175/BAMS-87-3-343

Mesinger, F., DiMego, G., Kalnay, E., Mitchell, K., Shafran, P.C., Ebisuzaki, W., Jović, D., Woollen, J., Rogers, E., Berbery, E.H., Ek, M.B., Fan, Y., Grumbine, R., Higgins, W., Li, H., Lin, Y., Manikin, G., Parrish, D., Shi, W., 2006b. North American regional reanalysis. Bulletin of the American Meteorological Society 87, 343–360. https://doi.org/10.1175/BAMS-87-3-343

Metherell, A.K., Harding, L.A., Cole, C.V., Parton, W.J., 1993. CENTURY Soil organic matter model environment. Technical documentation. Agroecosystem version 4.0. (Technical Report No. 4). Great Plains System Research Unit, USDA-ARS, Fort Collins, Colorado, USA.

Miguez, F.E., Maughan, M., Bollero, G.A., Long, S.P., 2012. Modeling spatial and dynamic variation in growth, yield, and yield stability of the bioenergy crops Miscanthus × giganteus and Panicum virgatum across the conterminous United States. Glob. Change Biol. Bioenergy 4, 509–520. https://doi.org/10.1111/j.1757-1707.2011.01150.x

Miller, W.P., Piechota, T.C., 2011. Trends in Western U.S. Snowpack and Related Upper Colorado River Basin Streamflow1: Trends in Western U.S. Snowpack and Related Upper Colorado River Basin Streamflow. JAWRA Journal of the American Water Resources Association 47, 1197–1210. https://doi.org/10.1111/j.1752-1688.2011.00565.x

Miralles, D.G., Jiménez, C., Jung, M., Michel, D., Ershadi, A., McCabe, M.F., Hirschi, M., Martens, B., Dolman, A.J., Fisher, J.B., Mu, Q., Seneviratne, S.I., Wood, E.F., Fernández-Prieto, D., 2016. The WACMOS-ET project – Part 2: Evaluation of global terrestrial evaporation data sets. Hydrol. Earth Syst. Sci. 20, 823–842. https://doi.org/10.5194/hess-20-823-2016

Molina-Navarro, E., Bailey, R.T., Andersen, H.E., Thodsen, H., Nielsen, A., Park, S., Jensen, J.S., Jensen, J.B., Trolle, D., 2019. Comparison of abstraction scenarios simulated by SWAT and SWAT-MODFLOW. Hydrological Sciences Journal 64, 434–454. https://doi.org/10.1080/02626667.2019.1590583

Monteith, J.L., 1965. Evaporation and environment, in: Symposia of the Society for Experimental Biology. Cambridge University Press (CUP) Cambridge, pp. 205–234.

Moriasi, D.N., Arnold, J.G., Van Liew, M.W., Bingner, R.L., Harmel, R.D., Veith, T.L., 2007. Model evaluation guidelines for systematic quantification of accuracy in watershed simulations. Transactions of the ASABE 50, 885–900.

Motovilov, Y.G., Gottschalk, L., Engeland, K., Rodhe, A., 1999. Validation of a distributed hydrological model against spatial observations. Agricultural and Forest Meteorology 98–99, 257–277. https://doi.org/10.1016/S0168-1923(99)00102-1

Mu, Q., Zhao, M., Running, S.W., 2013. MODIS global terrestrial evapotranspiration (ET) product (NASA MOD16A2/A3). Algorithm Theoretical Basis Document, Collection 5, 600.

Mu, Q., Zhao, M., Running, S.W., 2011. Improvements to a MODIS global terrestrial evapotranspiration algorithm. Remote Sensing of Environment 115, 1781–1800. https://doi.org/10.1016/j.rse.2011.02.019

Myers, D.T., Ficklin, D.L., Robeson, S.M., 2021. Incorporating rain-on-snow into the SWAT model results in more accurate simulations of hydrologic extremes. Journal of Hydrology 603, 126972. https://doi.org/10.1016/j.jhydrol.2021.126972

NADP, 2022. National Atmospheric Deposition Program (NRSP-3). NADP Program Office, Wisconsin State Laboratory of Hygiene, 465 Henry Mall, Madison, WI 53706.

Nangia, V., Gowda, P.H., Mulla, D.J., 2010. Effects of changes in N-fertilizer management on water quality trends at the watershed scale. Agricultural Water Management 97, 1855–1860. https://doi.org/10.1016/j.agwat.2010.06.023

Nash, J.E., Sutcliffe, J.V., 1970. River flow forecasting through conceptual models part I — A discussion of principles. Journal of Hydrology 10, 282–290. https://doi.org/10.1016/0022-1694(70)90255-6

National Research Council, 2009. Liquid transportation fuels from coal and biomass: technological status, costs, and environmental impacts. National Academies Press, Washington, D.C.

NDNR, 2016. 2017 Annual Evaluation of Availability of Hydrologically Connected Water Supplies. Nebraska Department of Natural Resources, Lincoln, Nebraska, USA.

Nebraska Department of Natural Resources., 2020. Groundwater Wells Database.

Neitsch, S.L., Arnold, J.G., Kiniry, J.R., Williams, J.R., 2011. Soil and water assessment tool theoretical documentation version 2009. Texas Water Resources Institute.

Nelson, R.G., Ascough, J.C., Langemeier, M.R., 2006. Environmental and economic analysis of switchgrass production for water quality improvement in northeast Kansas. Journal of Environmental Management 79, 336–347. https://doi.org/10.1016/j.jenvman.2005.07.013

Newman, A.J., Clark, M.P., Sampson, K., Wood, A., Hay, L.E., Bock, A., Viger, R.J., Blodgett, D., Brekke, L., Arnold, J.R., Hopson, T., Duan, Q., 2015. Development of a large-sample watershed-scale hydrometeorological data set for the contiguous USA: data set characteristics and assessment of regional variability in hydrologic model performance. Hydrol. Earth Syst. Sci. 19, 209–223. https://doi.org/10.5194/hess-19-209-2015

Ng, G.-H.C., McLaughlin, D., Entekhabi, D., Scanlon, B.R., 2010. Probabilistic analysis of the effects of climate change on groundwater recharge: EFFECTS OF CLIMATE CHANGE ON GROUNDWATER RECHARGE. Water Resour. Res. 46. https://doi.org/10.1029/2009WR007904

Ng, T.L., Eheart, J.W., Cai, X., Miguez, F., 2010. Modeling Miscanthus in the Soil and Water Assessment Tool (SWAT) to Simulate Its Water Quality Effects As a Bioenergy Crop. Environ. Sci. Technol. 44, 7138–7144. https://doi.org/10.1021/es9039677

Nocentini, A., Di Virgilio, N., Monti, A., 2015. Model Simulation of Cumulative Carbon Sequestration by Switchgrass (Panicum Virgatum L.) in the Mediterranean Area Using the DAYCENT Model. Bioenerg. Res. 8, 1512–1522. https://doi.org/10.1007/s12155-015-9672-4

Norman, J.M., Anderson, M.C., Kustas, W.P., French, A.N., Mecikalski, J., Torn, R., Diak, G.R., Schmugge, T.J., Tanner, B.C.W., 2003. Remote sensing of surface energy fluxes at 10^{1}-m pixel resolutions. Water Resour. Res. 39. https://doi.org/10.1029/2002WR001775

Nunes, A.N., De Almeida, A.C., Coelho, C.O.A., 2011. Impacts of land use and cover type on runoff and soil erosion in a marginal area of Portugal. Applied Geography 31, 687–699. https://doi.org/10.1016/j.apgeog.2010.12.006

Oki, T., Kanae, S., 2006. Global Hydrological Cycles and World Water Resources. Science 313, 1068 LP – 1072. https://doi.org/10.1126/science.1128845

Pan, S., Pan, N., Tian, H., Friedlingstein, P., Sitch, S., Shi, H., Arora, V.K., Haverd, V., Jain, A.K., Kato, E., Lienert, S., Lombardozzi, D., Nabel, J.E.M.S., Ottlé, C., Poulter, B., Zaehle, S., Running, S.W., 2020. Evaluation of global terrestrial evapotranspiration using state-of-the-art approaches in remote sensing, machine learning and land surface modeling. Hydrol. Earth Syst. Sci. 24, 1485–1509. https://doi.org/10.5194/hess-24-1485-2020

Panagopoulos, Y., Gassman, P.W., Kling, C.L., Cibin, R., Chaubey, I., 2017. Water Quality Assessment of Large-scale Bioenergy Cropping Scenarios for the Upper Mississippi and Ohio-Tennessee River Basins. JAWRA Journal of the American Water Resources Association 53, 1355–1367. https://doi.org/10.1111/1752-1688.12594

Parajuli, P.B., Jayakody, P., Ouyang, Y., 2018. Evaluation of Using Remote Sensing Evapotranspiration Data in SWAT. Water Resour Manage 32, 985–996. https://doi.org/10.1007/s11269-017-1850-z

Parton, W.J., Hartman, M., Ojima, D., Schimel, D., 1998. DAYCENT and its land surface submodel: description and testing. Global and Planetary Change 19, 35–48. https://doi.org/10.1016/S0921-8181(98)00040-X

Parton, W.J., Ojima, D.S., Cole, C.V., Schimel, D.S., 1994. A General Model for Soil Organic Matter Dynamics: Sensitivity to Litter Chemistry, Texture and Management, in: Bryant, R.B., Arnold, R.W. (Eds.), SSSA Special Publications. Soil Science Society of America, Madison, WI, USA, pp. 147–167. https://doi.org/10.2136/sssaspecpub39.c9

Paul, M., Dangol, S., Kholodovsky, V., Sapkota, A.R., Negahban-Azar, M., Lansing, S., 2020. Modeling the Impacts of Climate Change on Crop Yield and Irrigation in the Monocacy River Watershed, USA. Climate 8, 139. https://doi.org/10.3390/cli8120139

Paul, M., Rajib, A., Negahban-Azar, M., Shirmohammadi, A., Srivastava, P., 2021. Improved agricultural Water management in data-scarce semi-arid watersheds: Value of integrating remotely sensed leaf area index in hydrological modeling. Science of The Total Environment 791, 148177. https://doi.org/10.1016/j.scitotenv.2021.148177

Pervez, M.S., Brown, J.F., 2010a. Mapping Irrigated Lands at 250-m Scale by Merging MODIS Data and National Agricultural Statistics. Remote Sensing 2, 2388–2412. https://doi.org/10.3390/rs2102388

Pervez, M.S., Brown, J.F., 2010b. Mapping Irrigated Lands at 250-m Scale by Merging MODIS Data and National Agricultural Statistics. Remote Sensing 2, 2388–2412. https://doi.org/10.3390/rs2102388.

Peterson, S.M., Flynn, A.T., Traylor, J.P., 2016. Groundwater-flow model of the northern High Plains aquifer in Colorado, Kansas, Nebraska, South Dakota, and Wyoming (No. 2016–5153), Scientific Investigations Report. Reston, VA. https://doi.org/10.3133/sir20165153

Peterson, S.M., Traylor, J.P., Guira, M., 2020. Groundwater availability of the northern high plains aquifer in Colorado, Kansas, Nebraska, South Dakota, and Wyoming, US Geological Survey Professional Paper. https://doi.org/10.3133/pp1864

Piao, S., Ciais, P., Huang, Y., Shen, Z., Peng, S., Li, J., Zhou, L., Liu, H., Ma, Y., Ding, Y., Friedlingstein, P., Liu, C., Tan, K., Yu, Y., Zhang, T., Fang, J., 2010. The impacts of climate change on water resources and agriculture in China. Nature 467, 43–51. https://doi.org/10.1038/nature09364

Prathumratana, L., Sthiannopkao, S., Kim, K.W., 2008. The relationship of climatic and hydrological parameters to surface water quality in the lower Mekong River. Environment International 34, 860–866. https://doi.org/10.1016/j.envint.2007.10.011

Proulx, R.A., Hill, M.J., Laguette, S., 2022. Improved ALMANAC simulations of upland switchgrass ecotypes in the northern United States. Agronomy Journal 114, 508–523. https://doi.org/10.1002/agj2.20970

Qi, J., Du, X., Zhang, X., Lee, S., Wu, Y., Deng, J., Moglen, G.E., Sadeghi, A.M., McCarty, G.W., 2020a. Modeling riverine dissolved and particulate organic carbon fluxes from two small watersheds in the northeastern United States. Environmental Modelling & Software 124, 104601. https://doi.org/10.1016/j.envsoft.2019.104601

Qi, J., Lee, S., Du, X., Ficklin, D.L., Wang, Q., Myers, D., Singh, D., Moglen, G.E., McCarty, G.W., Zhou, Y., Zhang, X., 2021. Coupling terrestrial and aquatic thermal processes for improving stream temperature modeling at the watershed scale. Journal of Hydrology 603, 126983. https://doi.org/10.1016/j.jhydrol.2021.126983

Qi, J., Li, S., Li, Q., Xing, Z., Bourque, C.P.-A., Meng, F.-R., 2016. A new soil-temperature module for SWAT application in regions with seasonal snow cover. Journal of Hydrology 538, 863–877. https://doi.org/10.1016/j.jhydrol.2016.05.003

Qi, J., Zhang, X., McCarty, G.W., Sadeghi, A.M., Cosh, M.H., Zeng, X., Gao, F., Daughtry, C.S.T., Huang, C., Lang, M.W., Arnold, J.G., 2018. Assessing the performance of a physically-based soil moisture module integrated within the Soil and Water Assessment Tool. Environmental Modelling & Software 109, 329–341. https://doi.org/10.1016/j.envsoft.2018.08.024

Qi, J., Zhang, X., Yang, Q., Srinivasan, R., Arnold, J.G., Li, J., Waldholf, S.T., Cole, J., 2020b. SWAT ungauged: Water quality modeling in the Upper Mississippi River Basin. Journal of Hydrology 584, 124601. https://doi.org/10.1016/j.jhydrol.2020.124601

Qiao, F., Liang, X.-Z., 2017. Effects of cumulus parameterization closures on simulations of summer precipitation over the continental United States. Clim Dyn 49, 225–247. https://doi.org/10.1007/s00382-016-3338-6

Qiao, F., Liang, X.-Z., 2016. Effects of cumulus parameterization closures on simulations of summer precipitation over the United States coastal oceans: U.S. Coastal Ocean Summer Rainfall Simulation and the Cumulus Closure Effects. J. Adv. Model. Earth Syst. 8, 764–785. https://doi.org/10.1002/2015MS000621

Qiao, F., Liang, X.-Z., 2015. Effects of cumulus parameterizations on predictions of summer flood in the Central United States. Clim Dyn 45, 727–744. https://doi.org/10.1007/s00382-014-2301-7

Qin, Z., Zhuang, Q., Cai, X., 2015. Bioenergy crop productivity and potential climate change mitigation from marginal lands in the United States: An ecosystem modeling perspective. GCB Bioenergy 7, 1211–1221. https://doi.org/10.1111/gcbb.12212

Qin, Z., Zhuang, Q., Chen, M., 2012. Impacts of land use change due to biofuel crops on carbon balance, bioenergy production, and agricultural yield, in the conterminous United States. Glob. Change Biol. Bioenergy 4, 277–288. https://doi.org/10.1111/j.1757-1707.2011.01129.x

Rajib, A., Evenson, G.R., Golden, H.E., Lane, C.R., 2018. Hydrologic model predictability improves with spatially explicit calibration using remotely sensed evapotranspiration and biophysical parameters. Journal of Hydrology 567, 668–683. https://doi.org/10.1016/j.jhydrol.2018.10.024

Rajib, A., Kim, I.L., Golden, H.E., Lane, C.R., Kumar, S.V., Yu, Z., Jeyalakshmi, S., 2020. Watershed Modeling with Remotely Sensed Big Data: MODIS Leaf Area Index Improves Hydrology and Water Quality Predictions. Remote Sensing 12, 2148. https://doi.org/10.3390/rs12132148

Rajib, M.A., Merwade, V., Yu, Z., 2016. Multi-objective calibration of a hydrologic model using spatially distributed remotely sensed/in-situ soil moisture. Journal of Hydrology 536, 192–207. https://doi.org/10.1016/j.jhydrol.2016.02.037

Rasse, D.P., Rumpel, C., Dignac, M.-F., 2005. Is soil carbon mostly root carbon? Mechanisms for a specific stabilisation. Plant Soil 269, 341–356. https://doi.org/10.1007/s11104-004-0907-y

Rateb, A., Scanlon, B.R., Pool, D.R., Sun, A., Zhang, Z., Chen, J., Clark, B., Faunt, C.C., Haugh, C.J., Hill, M., Hobza, C., McGuire, V.L., Reitz, M., Müller Schmied, H., Sutanudjaja, E.H., Swenson, S., Wiese, D., Xia, Y., Zell, W., 2020. Comparison of Groundwater Storage Changes From GRACE Satellites With Monitoring and Modeling of Major U.S. Aquifers. Water Resources Research 56, e2020WR027556. https://doi.org/10.1029/2020WR027556

Reidmiller, D R, Avery, C W, Easterling, D R, Kunkel, K E, Lewis, K L M, Maycock, T K, Stewart, B C, Reidmiller, David R., Avery, Christopher W., Easterling, David R., Kunkel, Kenneth E., Lewis, Kristin L.M., Maycock, Thomas K., Stewart, Brooke C., 2018. Impacts, Risks, and Adaptation in the United States: The Fourth National Climate Assessment, Volume II. Washington, DC. https://doi.org/10.7930/NCA4.2018

Rogers, D.H., Aguilar, J., Kisekka, I., Barnes, P.L., Lamm, F.R., 2015. Agricultural crop water use.

Rossman, N.R., Zlotnik, V.A., Rowe, C.M., 2018. An approach to hydrogeological modeling of a large system of groundwater-fed lakes and wetlands in the Nebraska Sand Hills, USA. Hydrogeology Journal 26, 881–897. https://doi.org/10.1007/s10040-017-1691-0

Rost, S., Gerten, D., Bondeau, A., Lucht, W., Rohwer, J., Schaphoff, S., 2008. Agricultural green and blue water consumption and its influence on the global water system. Water Resources Research 44, W09405–W09405. https://doi.org/10.1029/2007WR006331

Rowe, C.M., Kuivinen, K.C., Flores-Mendoza, F., 1994. SENSITIVITY OF STREAMFLOW TO CLIMATE CHANGE: A CASE STUDY FOR NEBRASKA. Great Plains Research 4, 27–49.

Rumph Frederiksen, R., Molina-Navarro, E., 2021. The importance of subsurface drainage on model performance and water balance in an agricultural catchment using SWAT and SWAT-MODFLOW. Agricultural Water Management 255, 107058. https://doi.org/10.1016/j.agwat.2021.107058

Runkel, R.L., Crawford, C.G., Cohn, T.A., 2004. Load Estimator (LOADEST): A FORTRAN program for estimating constituent loads in streams and rivers (No. 2328–7055).
Running, S., Mu, Q., Zhao, M., 2019. MOD16A2GF MODIS/Terra Net Evapotranspiration 8-Day L4 Global 500m SIN Grid V006. NASA EOSDIS Land Processes DAAC. https://doi.org/10.5067/MODIS/MOD16A2.006
Ryberg, K.R., Akyüz, F.A., Wiche, G.J., Lin, W., 2016. Changes in seasonality and timing of peak streamflow in snow and semi-arid climates of the north-central United States, 1910–2012. Hydrol. Process. 30, 1208–1218. https://doi.org/10.1002/hyp.10693
Saad, D.A., Schwarz, G.E., Robertson, D.M., Booth, N.L., 2011. A Multi-Agency Nutrient Dataset Used to Estimate Loads, Improve Monitoring Design, and Calibrate Regional Nutrient SPARROW Models. JAWRA Journal of the American Water Resources Association 47, 933–949. https://doi.org/10.1111/j.1752-1688.2011.00575.x
Sainju, U.M., Allen, B.L., Lenssen, A.W., Ghimire, R.P., 2017. Root biomass, root/shoot ratio, and soil water content under perennial grasses with different nitrogen rates. Field Crops Research 210, 183–191. https://doi.org/10.1016/j.fcr.2017.05.029
Sando, S.K., McCarthy, P.M., 2018. Methods for peak-flow frequency analysis and reporting for streamgages in or near Montana based on data through water year 2015 (Report No. 2018–5046), Scientific Investigations Report. Reston, VA. https://doi.org/10.3133/sir20185046
Scanlon, B.R., Faunt, C.C., Longuevergne, L., Reedy, R.C., Alley, W.M., McGuire, V.L., McMahon, P.B., 2012. Groundwater depletion and sustainability of irrigation in the US High Plains and Central Valley. Proceedings of the National Academy of Sciences of the United States of America 109, 9320–9325. https://doi.org/10.1073/pnas.1200311109
Schaetzl, R.J., Krist, F.J., Miller, B.A., 2012. A Taxonomically Based Ordinal Estimate of Soil Productivity for Landscape-Scale Analyses. Soil Science 177, 288–299. https://doi.org/10.1097/SS.0b013e3182446c88
Schilling, K.E., Jha, M.K., Zhang, Y.-K., Gassman, P.W., Wolter, C.F., 2008a. Impact of land use and land cover change on the water balance of a large agricultural watershed: Historical effects and future directions. Water Resources Research 44. https://doi.org/10.1029/2007WR006644
Schilling, K.E., Jha, M.K., Zhang, Y.-K., Gassman, P.W., Wolter, C.F., 2008b. Impact of land use and land cover change on the water balance of a large agricultural watershed: Historical effects and future directions: IMPACT OF LULC CHANGE ON WATER BALANCE. Water Resour. Res. 44. https://doi.org/10.1029/2007WR006644
Schmer, M.R., Liebig, M.A., Vogel, K.P., Mitchell, R.B., 2011. Field-scale soil property changes under switchgrass managed for bioenergy. GCB Bioenergy 3, 439–448. https://doi.org/10.1111/j.1757-1707.2011.01099.x
Schneekloth, J., Andales, A., 2009. Seasonal water needs and opportunities for limited irrigation for Colorado crops.
Schnepf, R., Yacobucci, B.D., 2013. Renewable Fuel Standard (RFS): Overview and Issues (No. R40155). Congressional Research Service.
Searchinger, T., Heimlich, R., Houghton, R.A., Dong, F., Elobeid, A., Fabiosa, J., Tokgoz, S., Hayes, D., Yu, T.-H., 2008. Use of U.S. Croplands for Biofuels Increases Greenhouse Gases Through Emissions from Land-Use Change. Science 319, 1238–1240. https://doi.org/10.1126/science.1151861
Sen, P.K., 1968. Estimates of the regression coefficient based on Kendall's tau. Journal of the American statistical association 63, 1379–1389.
Senay, G.B., Friedrichs, M., Singh, R.K., Velpuri, N.M., 2016. Evaluating Landsat 8 evapotranspiration for water use mapping in the Colorado River Basin. Remote Sensing of Environment 185, 171–185. https://doi.org/10.1016/j.rse.2015.12.043
Shah, S., Duan, Z., Song, X., Li, R., Mao, H., Liu, J., Ma, T., Wang, M., 2021. Evaluating the added value of multi-variable calibration of SWAT with remotely sensed evapotranspiration data for improving hydrological modeling. Journal of Hydrology 603, 127046. https://doi.org/10.1016/j.jhydrol.2021.127046

Sharara, M.A., Sahoo, K., Reddy, A.D., Kim, S., Zhang, X., Dale, B., Jones, C.D., Izaurralde, R.C., Runge, T.M., 2020. Sustainable feedstock for bioethanol production: Impact of spatial resolution on the design of a sustainable biomass supply-chain. Bioresource Technology 302, 122896. https://doi.org/10.1016/j.biortech.2020.122896

Sheffield, J., Wood, E.F., Pan, M., Beck, H., Coccia, G., Serrat-Capdevila, A., Verbist, K., 2018. Satellite Remote Sensing for Water Resources Management: Potential for Supporting Sustainable Development in Data-Poor Regions. Water Resour. Res. 54, 9724–9758. https://doi.org/10.1029/2017WR022437

Sinistore, J.C., Reinemann, D.J., Izaurralde, R.C., Cronin, K.R., Meier, P.J., Runge, T.M., Zhang, X., 2015. Life Cycle Assessment of Switchgrass Cellulosic Ethanol Production in the Wisconsin and Michigan Agricultural Contexts. Bioenerg. Res. 8, 897–909. https://doi.org/10.1007/s12155-015-9611-4

Sirisena, T.A.J.G., Maskey, S., Ranasinghe, R., 2020. Hydrological Model Calibration with Streamflow and Remote Sensing Based Evapotranspiration Data in a Data Poor Basin. Remote Sensing 12, 3768. https://doi.org/10.3390/rs12223768

Sivakumar, B., 2011. Global climate change and its impacts on water resources planning and management: assessment and challenges. Stochastic Environmental Research and Risk Assessment 25, 583–600. https://doi.org/10.1007/s00477-010-0423-y

Smidt, S.J., Haacker, E.M.K., Kendall, A.D., Deines, J.M., Pei, L., Cotterman, K.A., Li, H., Liu, X., Basso, B., Hyndman, D.W., 2016. Complex water management in modern agriculture: Trends in the water-energy-food nexus over the High Plains Aquifer. Science of the Total Environment 566–567, 988–1001. https://doi.org/10.1016/j.scitotenv.2016.05.127

Song, J.X., Chen, X.H., Cheng, C., Wang, D.M., Wang, W.K., 2010. Variability of streambed vertical hydraulic conductivity with depth along the Elkhorn River, Nebraska, USA. Chinese Science Bulletin 55, 992–999. https://doi.org/10.1007/s11434-009-0640-2

Song, Y., Cervarich, M., Jain, A.K., Kheshgi, H.S., Landuyt, W., Cai, X., 2016. The interplay between bioenergy grass production and water resources in the United States of America. Environmental Science & Technology 50, 3010–3019. https://doi.org/10.1021/acs.est.5b05239

Sophocleous, M.A., Koelliker, J.K., Govindaraju, R.S., Birdie, T., Ramireddygari, S.R., Perkins, S.P., 1999. Integrated numerical modeling for basin-wide water management: The case of the Rattlesnake Creek basin in south-central Kansas. Journal of Hydrology 214, 179–196. https://doi.org/10.1016/S0022-1694(98)00289-3

Srinivasan, R., Zhang, X., Arnold, J., 2010. SWAT ungauged: Hydrological budget and crop yield predictions in the upper Mississippi River basin. Transactions of the ASABE 53, 1533–1546. https://doi.org/10.13031/2013.34903

Stahl, K., Hisdal, H., Hannaford, J., Tallaksen, L.M., Van Lanen, H.A.J., Sauquet, E., Demuth, S., Fendekova, M., Jódar, J., 2010. Streamflow trends in Europe: evidence from a dataset of near-natural catchments. Hydrol. Earth Syst. Sci. 14, 2367–2382. https://doi.org/10.5194/hess-14-2367-2010

Strauch, K.R., Linard, J.I., 2009. Streamflow Simulations and Percolation Estimates Using the Soil and Water Assessment Tool for Selected Basins in North-Central Nebraska, 1940-2005. U. S. Geological Survey, Scientific Investigations Report 2009–5075.

Strauch, M., Volk, M., 2013. SWAT plant growth modification for improved modeling of perennial vegetation in the tropics. Ecological Modelling 269, 98–112. https://doi.org/10.1016/j.ecolmodel.2013.08.013

Sullivan, T.P., Gao, Y., 2016. Assessment of nitrogen inputs and yields in the Cibolo and Dry Comal Creek watersheds using the SWAT model, Texas, USA 1996–2010. Environ Earth Sci 75, 725. https://doi.org/10.1007/s12665-016-5546-0

Sun, C., Liang, X.-Z., 2020. Improving US extreme precipitation simulation: sensitivity to physics parameterizations. Climate Dynamics 54. https://doi.org/10.1007/s00382-020-05267-6

Sun, L., Anderson, M.C., Gao, F., Hain, C., Alfieri, J.G., Sharifi, A., McCarty, G.W., Yang, Yun, Yang, Yang, Kustas, W.P., McKee, L., 2017. Investigating water use over the C hoptank R iver W

atershed using a multisatellite data fusion approach. Water Resources Research 53, 5298–5319. https://doi.org/10.1002/2017WR020700
Sutanudjaja, E.H., van Beek, L.P.H., de Jong, S.M., van Geer, F.C., Bierkens, M.F.P., 2011. Large-scale groundwater modeling using global datasets: a test case for the Rhine-Meuse basin. Hydrol. Earth Syst. Sci. 15, 2913–2935. https://doi.org/10.5194/hess-15-2913-2011
Szilagyi, J., Harvey, F.E., Ayers, J.F., 2005. Regional estimation of total recharge to ground water in Nebraska. Ground Water 43, 63–69. https://doi.org/10.1111/j.1745-6584.2005.tb02286.x
Taylor, R.G., Scanlon, B., Döll, P., Rodell, M., van Beek, R., Wada, Y., Longuevergne, L., Leblanc, M., Famiglietti, J.S., Edmunds, M., Konikow, L., Green, T.R., Chen, J., Taniguchi, M., Bierkens, M.F.P., MacDonald, A., Fan, Y., Maxwell, R.M., Yechieli, Y., Gurdak, J.J., Allen, D.M., Shamsudduha, M., Hiscock, K., Yeh, P.J.-F., Holman, I., Treidel, H., 2013. Ground water and climate change. Nature Climate Change 3, 322–329. https://doi.org/10.1038/nclimate1744
Theil, H., 1992. A Rank-Invariant Method of Linear and Polynomial Regression Analysis, in: Raj, B., Koerts, J. (Eds.), Henri Theil's Contributions to Economics and Econometrics, Advanced Studies in Theoretical and Applied Econometrics. Springer Netherlands, Dordrecht, pp. 345–381. https://doi.org/10.1007/978-94-011-2546-8_20
Tilman, D., Balzer, C., Hill, J., Befort, B.L., 2011. Global food demand and the sustainable intensification of agriculture. Proceedings of the National Academy of Sciences 108, 20260–20264. https://doi.org/10.1073/pnas.1116437108
Tobin, K.J., Crow, W.T., Dong, J., Bennett, M.E., 2019. Validation of a New Root-Zone Soil Moisture Product: Soil MERGE. IEEE J. Sel. Top. Appl. Earth Observations Remote Sensing 12, 3351–3365. https://doi.org/10.1109/JSTARS.2019.2930946
Tobin, K.J., Torres, R., Crow, W.T., Bennett, M.E., 2017. Multi-decadal analysis of root-zone soil moisture applying the exponential filter across CONUS. Hydrol. Earth Syst. Sci. 21, 4403–4417. https://doi.org/10.5194/hess-21-4403-2017
Trenberth, K., 2011. Changes in precipitation with climate change. Climate Research 47, 123–138. https://doi.org/10.3354/cr00953
Troy, T.J., Kipgen, C., Pal, I., 2015. The impact of climate extremes and irrigation on US crop yields. Environmental Research Letters 10, 054013. https://doi.org/10.1088/1748-9326/10/5/054013
Trybula, E.M., Cibin, R., Burks, J.L., Chaubey, I., Brouder, S.M., Volenec, J.J., 2015. Perennial rhizomatous grasses as bioenergy feedstock in SWAT : parameter development and model improvement. GCB Bioenergy 7, 1185–1202. https://doi.org/10.1111/gcbb.12210
United States Bureau of Reclamation, (USBR), 2019. Hydromet. https://www.usbr.gov/pn/hydromet/ (accessed 5 March 2019).
Uniyal, B., Dietrich, J., Vasilakos, C., Tzoraki, O., 2017. Evaluation of SWAT simulated soil moisture at catchment scale by field measurements and Landsat derived indices. Agricultural Water Management 193, 55–70. https://doi.org/10.1016/j.agwat.2017.08.002
US Army Corps of Engineers, (USACE), 2013. Annual report of reservoir regulation activities: Summary for 2011-2012. US Army Corps of Engineers, Kansas City District, Engineering Division, Hydrologic Engineering Branch, Water Management Section.
U.S. EPA, 2022. Biofuels and the Environment: Third Triennial Report to Congress (External Review Draft). , (No. EPA/600/R-22/273). U.S. EPA.
US Geological Survey, 2016. National water information system data available on the world wide web (USGS water data for the nation). https://waterdata.usgs.gov/nwis? (accessed 8 March 2019).
USDA, 2016. Statistics by State. U.S. Department of Agriculture National Agricultural Statistics Service.
USDA NASS Cropland Data Layer, 2008. Published crop-specific data layer [Online]. Available at https://nassgeodata.gmu.edu/CropScape/. USDA-NASS,. Washington, DC. (accessed March 2018).
USDA-NASS, 2010. Field Crops Usual Planting and Harvesting Dates (October 2010) (No. Agricultural Handbook Number 628). US Department of Agriculture National Agriculture Statistics Service.
USDA-NRCS, 1994a. State Soil Geographic (STATSGO) database – Data User Guide. U.S. Department of Agriculture, Natural Resources Conservation Service, Misc. Publ. 1492, Washington, D.C.

USDA-NRCS, 1994b. State Soil Geographic (STATSGO) database – Data User Guide. U.S. Department of Agriculture, Natural Resources Conservation Service, Misc. Publ. 1492, Washington, D.C.

Van Liew, M.W., Feng, S., Pathak, T.B., 2012. Climate change impacts on streamflow, water quality, and best management practices for the Shell and Logan Creek Watersheds in Nebraska, USA. International Journal of Agricultural and Biological Engineering 5, 13–34. https://doi.org/10.3965/j.ijabe.20120501.003

Vanloocke, A., Bernacchi, C.J., Twine, T.E., 2010. The impacts of Miscanthus×giganteus production on the Midwest US hydrologic cycle: IMPACTS OF MISCANTHUS ON US HYDROLOGIC CYCLE. GCB Bioenergy no-no. https://doi.org/10.1111/j.1757-1707.2010.01053.x

VanLoocke, A., Twine, T.E., Kucharik, C.J., Bernacchi, C.J., 2017. Assessing the potential to decrease the Gulf of Mexico hypoxic zone with Midwest US perennial cellulosic feedstock production. GCB Bioenergy 9, 858–875. https://doi.org/10.1111/gcbb.12385

Velpuri, N.M., Senay, G.B., Singh, R.K., Bohms, S., Verdin, J.P., 2013. A comprehensive evaluation of two MODIS evapotranspiration products over the conterminous United States: Using point and gridded FLUXNET and water balance ET. Remote Sensing of Environment 139, 35–49. https://doi.org/10.1016/j.rse.2013.07.013

Wallander, S., Claassen, R., Nickerson, C., 2011. The Ethanol Decade: An Expansion of U.S. Corn Production, 2000-09. USDA-ERS Economic Information Bulletin. https://doi.org/10.2139/ssrn.2131399

Wang, Q., Qi, J., Qiu, H., Li, J., Cole, J., Waldhoff, S., Zhang, X., 2021. Pronounced Increases in Future Soil Erosion and Sediment Deposition as Influenced by Freeze–Thaw Cycles in the Upper Mississippi River Basin. Environ. Sci. Technol. 55, 9905–9915. https://doi.org/10.1021/acs.est.1c02692

Wang, Q., Qi, J., Wu, H., Zeng, Y., Shui, W., Zeng, J., Zhang, X., 2020. Freeze-Thaw cycle representation alters response of watershed hydrology to future climate change. CATENA 195, 104767. https://doi.org/10.1016/j.catena.2020.104767

Wang, T., Istanbulluoglu, E., Lenters, J., Scott, D., 2009. On the role of groundwater and soil texture in the regional water balance: An investigation of the Nebraska Sand Hills, USA. Water Resources Research 45, W10413–W10413. https://doi.org/10.1029/2009WR007733

Wayman, S., Bowden, R.D., Mitchell, R.B., 2014. Seasonal Changes in Shoot and Root Nitrogen Distribution in Switchgrass (Panicum virgatum). Bioenerg. Res. 7, 243–252. https://doi.org/10.1007/s12155-013-9365-9

Wei, X., Bailey, R.T., 2019. Assessment of system responses in intensively irrigated stream-aquifer systems using SWAT-MODFLOW. Water (Switzerland) 11, 1576–1576. https://doi.org/10.3390/w11081576

Wen, F., Chen, X., 2006. Evaluation of the impact of groundwater irrigation on streamflow in Nebraska. Journal of Hydrology 327, 603–617. https://doi.org/10.1016/j.jhydrol.2005.12.016

Wieczorek, M.E., Wolock, D.M., McCarthy, P.M., 2021. Dam impact/disturbance metrics for the conterminous United States, 1800 to 2018. https://doi.org/10.5066/P92S9ZX6

Williams, J.R., Jones, C.A., Kiniry, J.R., Spanel, D.A., 1989. The EPIC Crop Growth Model. Transactions of the ASAE 32, 0497–0511. https://doi.org/10.13031/2013.31032

Woznicki, S.A., Nejadhashemi, A.P., 2012. Sensitivity Analysis of Best Management Practices Under Climate Change Scenarios1: Sensitivity Analysis of Best Management Practices Under Climate Change Scenarios. JAWRA Journal of the American Water Resources Association 48, 90–112. https://doi.org/10.1111/j.1752-1688.2011.00598.x

Wu, M., Demissie, Y., Yan, E., 2012a. Simulated impact of future biofuel production on water quality and water cycle dynamics in the Upper Mississippi river basin. Biomass and Bioenergy 41, 44–56. https://doi.org/10.1016/j.biombioe.2012.01.030

Wu, M., Demissie, Y., Yan, E., 2012b. Simulated impact of future biofuel production on water quality and water cycle dynamics in the Upper Mississippi river basin. Biomass and Bioenergy 41, 44–56. https://doi.org/10.1016/j.biombioe.2012.01.030

Wu, X., Zhou, J., Wang, H., Li, Y., Zhong, B., 2015. Evaluation of irrigation water use efficiency using remote sensing in the middle reach of the Heihe river, in the semi-arid Northwestern China. Hydrol. Process. 29, 2243–2257. https://doi.org/10.1002/hyp.10365

Xia, Y., Mitchell, K., Ek, M., Sheffield, J., Cosgrove, B., Wood, E., Luo, L., Alonge, C., Wei, H., Meng, J., 2009. NLDAS primary forcing data L4 hourly 0.125× 0.125 degree V002. Goddard Earth Sciences Data and Information Services Center (GES DISC), Greenbelt, MD, USA, Rep. NASA/GSFC/HSL. https://doi.org/10.5067/6J5LHHOHZHN4

Xu, M., Liang, X.-Z., Samel, A., Gao, W., 2014. MODIS Consistent Vegetation Parameter Specifications and Their Impacts on Regional Climate Simulations. Journal of Climate 27, 8578–8596. https://doi.org/10.1175/JCLI-D-14-00082.1

Yang, Q., Zhang, X., 2016. Improving SWAT for simulating water and carbon fluxes of forest ecosystems. Science of The Total Environment 569–570, 1478–1488. https://doi.org/10.1016/j.scitotenv.2016.06.238

Yang, Yang, Anderson, M.C., Gao, F., Wardlow, B., Hain, C.R., Otkin, J.A., Alfieri, J., Yang, Yun, Sun, L., Dulaney, W., 2018. Field-scale mapping of evaporative stress indicators of crop yield: An application over Mead, NE, USA. Remote Sensing of Environment 210, 387–402. https://doi.org/10.1016/j.rse.2018.02.020

Yang, Yanmin, Yang, Yonghui, Liu, D., Nordblom, T., Wu, B., Yan, N., 2014. Regional Water Balance Based on Remotely Sensed Evapotranspiration and Irrigation: An Assessment of the Haihe Plain, China. Remote Sensing 6, 2514–2533. https://doi.org/10.3390/rs6032514

Yapo, P.O., Gupta, H.V., Sorooshian, S., 1998. Multi-objective global optimization for hydrologic models. Journal of Hydrology 204, 83–97. https://doi.org/10.1016/S0022-1694(97)00107-8

Yasarer, L.M.W., Taylor, J.M., Rigby, J.R., Locke, M.A., 2020. Trends in Land Use, Irrigation, and Streamflow Alteration in the Mississippi River Alluvial Plain. Front. Environ. Sci. 8, 66. https://doi.org/10.3389/fenvs.2020.00066

Yonts, C.D., Melvin, S.R., Eisenhauer, D.E., 2008. Predicting the last irrigation of the season. NebGuide G1871.

Yuan, X., Liang, X.-Z., 2011. Evaluation of a Conjunctive Surface–Subsurface Process Model (CSSP) over the Contiguous United States at Regional–Local Scales. Journal of Hydrometeorology 12. https://doi.org/10.1175/2010JHM1302.1

Zan, C.S., Fyles, J.W., Girouard, P., Samson, R.A., 2001. Carbon sequestration in perennial bioenergy, annual corn and uncultivated systems in southern Quebec. Agriculture, Ecosystems & Environment 86, 135–144. https://doi.org/10.1016/S0167-8809(00)00273-5

Zeng, R., Cai, X., 2014. Analyzing streamflow changes: irrigation-enhanced interaction between aquifer and streamflow in the Republican River basin. Hydrology and Earth System Sciences 18, 493–502. https://doi.org/10.5194/hess-18-493-2014

Zeng, X., Schnier, S., Cai, X., 2021. A data-driven analysis of frequent patterns and variable importance for streamflow trend attribution. Advances in Water Resources 147, 103799. https://doi.org/10.1016/j.advwatres.2020.103799

Zhang, B., Xia, Y., Long, B., Hobbins, M., Zhao, X., Hain, C., Li, Y., Anderson, M.C., 2020. Evaluation and comparison of multiple evapotranspiration data models over the contiguous United States: Implications for the next phase of NLDAS (NLDAS-Testbed) development. Agricultural and Forest Meteorology 280, 107810. https://doi.org/10.1016/j.agrformet.2019.107810

Zhang, G., Su, X., Ayantobo, O.O., Feng, K., Guo, J., 2020. Remote-sensing precipitation and temperature evaluation using soil and water assessment tool with multiobjective calibration in the Shiyang River Basin, Northwest China. Journal of Hydrology 590, 125416. https://doi.org/10.1016/j.jhydrol.2020.125416

Zhang, J., Campana, P.E., Yao, T., Zhang, Y., Lundblad, A., Melton, F., Yan, J., 2018. The water-food-energy nexus optimization approach to combat agricultural drought: a case study in the United States. Applied Energy 227, 449–464. https://doi.org/10.1016/j.apenergy.2017.07.036

Zhang, J., Felzer, B.S., Troy, T.J., 2016. Extreme precipitation drives groundwater recharge: the Northern High Plains Aquifer, central United States, 1950–2010. Hydrological Processes 30, 2533–2545. https://doi.org/10.1002/hyp.10809

Zhang, X., 2018. Simulating eroded soil organic carbon with the SWAT-C model. Environmental Modelling & Software 102, 39–48. https://doi.org/10.1016/j.envsoft.2018.01.005

Zhang, X., Beeson, P., Link, R., Manowitz, D., Izaurralde, R.C., Sadeghi, A., Thomson, A.M., Sahajpal, R., Srinivasan, R., Arnold, J.G., 2013a. Efficient multi-objective calibration of a computationally intensive hydrologic model with parallel computing software in Python. Environmental Modelling & Software 46, 208–218. https://doi.org/10.1016/j.envsoft.2013.03.013

Zhang, X., Harvey, K.D., Hogg, W.D., Yuzyk, T.R., 2001. Trends in Canadian streamflow. Water Resour. Res. 37, 987–998. https://doi.org/10.1029/2000WR900357

Zhang, X., Izaurralde, R.C., Arnold, J.G., Sammons, N.B., Manowitz, D.H., Thomson, A.M., Williams, J.R., 2011a. Comment on "Modeling Miscanthus in the Soil and Water Assessment Tool (SWAT) to Simulate Its Water Quality Effects As a Bioenergy Crop." Environ. Sci. Technol. 45, 6211–6212. https://doi.org/10.1021/es201463x

Zhang, X., Izaurralde, R.C., Arnold, J.G., Williams, J.R., Srinivasan, R., 2013b. Modifying the Soil and Water Assessment Tool to simulate cropland carbon flux: Model development and initial evaluation. Science of the Total Environment 463–464, 810–822. https://doi.org/10.1016/j.scitotenv.2013.06.056

Zhang, X., Izaurralde, R.C., Manowitz, D., West, T.O., Post, W.M., Thomson, A.M., Bandaru, V.P., Nichols, J., Williams, J.R., 2010. An integrative modeling framework to evaluate the productivity and sustainability of biofuel crop production systems. GCB Bioenergy 2, 258–277. https://doi.org/10.1111/j.1757-1707.2010.01046.x

Zhang, X., Liang, F., Yu, B., Zong, Z., 2011b. Explicitly integrating parameter, input, and structure uncertainties into Bayesian Neural Networks for probabilistic hydrologic forecasting. Journal of Hydrology 409, 696–709. https://doi.org/10.1016/j.jhydrol.2011.09.002

Zhang, X., Srinivasan, R., Bosch, D., 2009a. Calibration and uncertainty analysis of the SWAT model using Genetic Algorithms and Bayesian Model Averaging. Journal of Hydrology 374, 307–317. https://doi.org/10.1016/j.jhydrol.2009.06.023

Zhang, X., Srinivasan, R., Van Liew, M., 2008. Multi-Site Calibration of the SWAT Model for Hydrologic Modeling. Transactions of the ASABE 51, 2039–2049. https://doi.org/10.13031/2013.25407

Zhang, X., Srinivasan, R., Zhao, K., Van Liew, M., 2009b. Evaluation of global optimization algorithms for parameter calibration of a computationally intensive hydrologic model. Hydrological Processes 23, 430–441. https://doi.org/10.1002/hyp.7152

Zhang, Y., Suyker, A., Paustian, K., 2018. Improved Crop Canopy and Water Balance Dynamics for Agroecosystem Modeling Using DayCent. Agronomy Journal 110, 511–524. https://doi.org/10.2134/agronj2017.06.0328

Zhou, X., Zhang, Y., Beck, H.E., Yang, Y., 2021. Divergent negative spring vegetation and summer runoff patterns and their driving mechanisms in natural ecosystems of northern latitudes. Journal of Hydrology 592, 125848. https://doi.org/10.1016/j.jhydrol.2020.125848